# Mise au point d'un outil de diagnostic pour révéler les microthrombi

Charlène Jacqmarcq

Charlène Jacqmarcq. Mise au point d'un outil de diagnostic pour révéler les microthrombi. Médecine humaine et pathologie. Normandie Université, 2022. Français. NNT : 2022NORMC412 . tel-03880864

HAL Id: tel-03880864
https://theses.hal.science/tel-03880864

Submitted on 1 Dec 2022

# THÈSE

## Pour obtenir le diplôme de doctorat

### Spécialité SCIENCES DE LA VIE ET DE LA SANTE

### Préparée au sein de l'Université de Caen Normandie

# Mise au point d'un outil de diagnostic pour révéler les microthrombi

## Présentée et soutenue par
## CHARLENE JACQMARCQ

**Thèse à caractère confidentiel soutenue le 15/11/2022**
**devant le jury composé de**

| | | |
|---|---|---|
| MME EMMANUELLE CANET-SOULAS | Professeur des universités, Université Lyon 1 Claude Bernard | Rapporteur du jury |
| M. SÉBASTIEN MERIAUX | Directeur de recherche, Université Paris Saclay | Rapporteur du jury |
| M. THOMAS GABEREL | Professeur des universités PraticienHosp, Université de Caen Normandie | Membre du jury |
| MME FLORENCE GAZEAU | Professeur des universités, CNRS PARIS | Membre du jury |
| M. DENIS VIVIEN | Professeur des universités PraticienHosp, Université de Caen Normandie | Président du jury |
| M. THOMAS BONNARD | Maître de conférences, Université de Caen Normandie | Directeur de thèse |

**Thèse dirigée par THOMAS BONNARD (Physiopathologie et imagerie des troubles neurologiques)**

# Résumé

Les traitements actuels de l'AVC ischémique ont pour but la restauration de la perfusion cérébrale en éliminant le thrombus qui occlut l'artère par injection d'un agent thrombolytique (thrombolyse) ou mécaniquement, en retirant le caillot par voie endovasculaire (thrombectomie). Les études cliniques ont montré la présence de thrombi au niveau de la microcirculation chez les patients, même après une recanalisation réussie de l'artère occlue. Ce phénomène est par ailleurs associé à l'apparition de déclins cognitifs et de démences. Cependant les outils de diagnostics habituellement utilisés dans l'imagerie à la phase aigüe de l'AVC ne permettent pas d'établir précisément la présence et l'étendue de cette microthrombose. Nous proposons, dans ce travail de thèse, l'utilisation de l'IRM moléculaire pour le diagnostic de la microthrombose. Nous avons développé un agent de contraste basé sur des nanoparticules superparamagnétiques d'oxydes de fer conglomérées dans une matrice de polydopamine biodégradable. Nos résultats suggèrent un ciblage spécifique de l'agent de contraste aux microthrombi *in vitro*, sur des microthrombi formés à partir de sang humain de volontaires sains, et *in vivo* sur un modèle d'AVC thromboembolique murin. Nous avons montré son efficacité pour l'IRM moléculaire de la microthrombose en préclinique, et mis en évidence l'apport diagnostic que représente le suivi des microthrombi dans le cadre de la thrombolyse. Nous avons enfin observé la biodégradabilité de ce nouvel agent de contraste, ce qui nous permet d'envisager la translation de cette approche en clinique, pour améliorer la prise en charge des patients victimes d'AVC ischémiques.

Mots-Clés : Microparticules d'Oxydes de Fer ; IRM ; modèle murin d'AVC ; Microthrombi

# Summary

Current treatments of ischemic stroke consist in restoring cerebral perfusion by removing the thrombus occluding the artery with a thrombolytic agent injection (thrombolysis) or mechanically with an endovascular approach (thrombectomy). Clinical studies have demonstrated the presence of thrombi localized in the microcirculation, even after a successful recanalization. Those microthrombi are associated with further dementia and cognitive decline. Unfortunately, current imaging tool for the diagnosis of acute stroke cannot provide information on this microthrombosis. In this work, we propose to use molecular MRI for the diagnosis of microthrombosis and, to this end, we developed a superparamagnetic iron oxide-based contrast agent clusterized in a polydopamine matrix. Our results shows specific targeting of the contrast agent *in vitro* to microthrombi formed with human blood, and *in vivo* in a thromboembolic mouse model. We demonstrated the efficacy of the contrast agent to provide molecular MRI of microthrombosis, and highlighted its ability to follow-up microthrombi degradation during thrombolysis. Finally, we observed the biodegradation of the contrast agent, allowing us to consider a future clinical translation to improve stroke patient care.

Keywords : Microparticles of Iron Oxide ; MRI ; Mouse Model of Stroke ; Microthrombi

# Remerciements

Je souhaite remercier chaleureusement les Pr. Emmanuelle Canet-Soulas et Dr. Sébastien Mériaux pour avoir accepté d'être les rapporteurs de mon travail de thèse. Merci d'avoir pris le temps d'évaluer ce travail et de m'avoir apporté des remarques constructives et encourageantes. Merci également au Pr Florence Gazeau d'avoir accepté d'être membre du Jury et examinatrice de ce travail.

Merci au Pr Thomas Gaberel d'avoir officiellement encadrer ma thèse au début, d'avoir accepté d'être examinateur et d'avoir toujours porté un intérêt à mon travail.

Merci au Pr Denis Vivien, de m'avoir accueillie au laboratoire d'abord en stage de Licence, puis de Master, puis de m'avoir proposé de continuer en thèse. Merci de m'avoir fait confiance sur ces projets et de me faire encore confiance pour la suite.

Merci à mon directeur de thèse, Dr Thomas Bonnard. J'ai appris beaucoup de choses pendant ces quatre ans. Je retiens beaucoup de tes conseils qui m'ont permis de me sentir autonome et confiante en mon travail et moins stressée. Merci pour ta bienveillance, ta patience et pour m'avoir mise en avant lors des collaborations. En général, merci pour la confiance que tu m'as montré.

Je tiens également à remercier les Dr Isabelle Bardou et Antoine Drieu, mes premiers encadrants pour mon stage de Master 1. Ce stage a été déterminant dans mes études et a contribué au fait que je soutienne ma thèse aujourd'hui.

Merci aux personnes extérieures au laboratoire avec qui j'ai eu la chance de collaborer pendant ma thèse, en particulier aux Dr Didier Goux et Benoit Bernay, qui m'ont aidé sur ces travaux.

Un grand merci à toute la « team imagerie ». A Swannie et Audrey, pour vos petits mots d'encouragements. Un grand merci à Sara et Maxime, pour vos précieux conseils scientifiques et vos précieux conseils en général. Vous avez toujours pris le temps de m'aider et toujours eu des réponses aux questions que je me posais.

Je tiens à remercier de manière général le personnel du laboratoire et de Cyceron. Merci au personnel du CURB. Merci à Yannick, Laurent, Jean-Michel, Sandrine, Manue et Marion. Merci à Mikael, pour m'avoir formée à l'utilisation des IRM et à l'analyse d'images.

Merci à toute l'équipe, aux doctorants et post-doctorants du bureau de gauche, du bureau de droite, et du petit bureau du fond. Merci à Jo et Carine de passer prendre de nos nouvelles dans l'aquarium ☺.

Pour tous les apéros, les remontages de moral, les chocolats, les pauses cafés qui sont plus que des pauses cafés, ces moments d'escapades à la plage et en ballades, merci à vous les filles : Amandine (ptit café ?), Léonie (notre confidente à tous), Caro (tu réchauffes mon petit cœur de meow-meow), Zita, Fatima et Hélène.

Merci à mes amis pour m'avoir soutenue et encouragée, et remonté le moral, et tout en fait ! A ces soirées de l'été 2021 à l'Hédoniste qui m'ont été presque vitales. Et une mention particulière à Lucie et Julien, vous êtes les meilleurs !

A ma famille : merci pour vos encouragements à tous ! A mes parents qui sont toujours prêts à me soutenir dans mes projets (même si je n'ai pas les meilleures idées des fois), qui m'ont tout donné, je sais que j'ai de la chance de vous avoir. A ma grande sœur qui est toujours là quand j'en ai besoin, j'espère que j'arrive à en faire autant malgré les 1200 km qui nous séparent. A mes grands-parents et à ma tante, qui me donnent beaucoup d'amour.

Et enfin, à Guillaume (dit « le coloc' »). Merci d'être dans ma vie. Maintenant que le « projet thèse » est terminé, pleins d'autres nous attendent, j'ai trop hâte !

*“It has long been an axiom of mine that the little things are infinitely the most important.”*

– from "The Memoirs of Sherlock Holmes"

Sir Arthur Conan Doyle

# Table des matières

# Liste des figures

# Liste des abréviations

**ACI** : Artère carotide interne

**ADC** : coefficient apparent de diffusion

**AIT** : Accident Ischémique Transitoire

**ASPECTS** : Alberta Stroke Program CT Scale

**AVC** : Accident Vasculaire Cérébral

**BHE** : Barrière Hémato-Encéphalique

**BSA** : albumine sérique bovine

**CDR** : classification de la démence clinique

**CP** : couronne de protéines

**DLS** : diffusion dynamique de la lumière

**DSA** : Angiographie par substraction digitale

**DWI** : Diffusion-Weighted Imaging

**EPR** : Enhanced Permeability and Retention

**FDA** : Food and Drug Administration (Agence fédérale américaine des produits alimentaires et médicamenteux)

**FLAIR** : Fluid Attenuated Inversion Recovery

**HSA** : hémorragie sous-arachnoïdienne

**IRM** : Imagerie par Résonance Magnétique

**LCR** : liquide céphalo-rachidien

**LRP** : protéines de récepteur de lipoprotéine

**MPI** : l'imagerie par particules magnétiques

**MPIO** : Microparticules d'Oxydes de Fer

**mRS** : échelle modifiée de Rankin

**NIHSS** : National Institute of Health Stroke Scale

**NMDA** : N-methyl-D-aspartate

**PDA** : Polydopamine

**PDF** : Produits de Dégradation de la Fibrine

**rtPA** : tPA recombinant

**SPIO** : superparamagnetic iron oxide

**SRE** : système réticulo-endothélial

**TDM** : Tomodensitométrie

**TEP** : Tomographie par Emission de Positons

**TICI** : Thrombolysis in Cerebral Infarction scale

**Tmax** : temps au maximum de la fonction résiduelle

**TNK** : ténectéplase

**TOF** : Time-of-Flight

**tPA** : activateur tissulaire du plasminogène

**UH** : Unité Hounsfield

**USPIO** : ultrasmall superparamagnetic iron oxide

# INTRODUCTION

# 1. Les Accidents Vasculaires Cérébraux

## 1.1 Epidémiologie

L’accident vasculaire cérébral (AVC) est une pathologie d’origine soudaine, provoquée par un manque d’oxygénation du cerveau suite à l’obstruction ou la rupture de la paroi des vaisseaux sanguins cérébraux. Selon les dernières données de la « Word Stroke Organization » (WSO), on estime que plus de 12,2 millions d’AVC sont déclarés chaque année, soit un AVC toutes les 3 secondes. Une personne sur quatre âgée de plus de 25 ans aura un AVC dans sa vie. Ce nombre a augmenté de 50% dans les 17 dernières années et est dû en partie au vieillissement de la population, qui entraîne une augmentation du risque de pathologies liées à l’âge, dont l’AVC (Feigin *et al.*, 2022).

Il existe deux grands types d’AVC aux physiopathologies très différentes : l’AVC hémorragique et l’AVC ischémique (Figure 1).

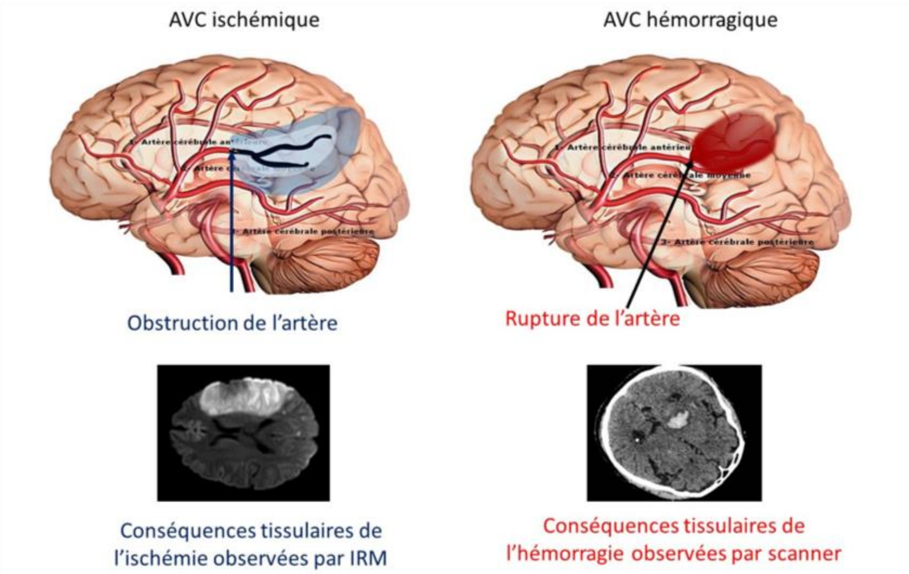

**Figure 1 Schéma d’illustration des AVC de type ischémique et hémorragique et leurs conséquences tissulaires visibles en imagerie.**
L’AVC ischémique est dû à l’occlusion par un caillot d’une artère qui induit la mort tissulaire de la zone irriguée. L’AVC hémorragique est la conséquence de la rupture d’une artère, s’ensuit une hémorragie visible au scanner. Source : Institut de la moelle et du cerveau.

Les AVC hémorragiques représentent entre 20 et 30% des AVC et se divisent en plusieurs catégories selon la localisation de l’hémorragie. Il s’agit principalement d’hémorragies intracérébrales et d'hémorragies sous-arachnoïdiennes. Ils entraînent une perte de la perfusion cérébrale et des fonctions neurologiques associées.

On parle d'AVC ischémique lorsque le vaisseau a été obstrué par un caillot sanguin, empêchant ou diminuant ainsi la circulation du sang dans une partie du cerveau (la région ischémique) et donc de la perfusion nécessaire au fonctionnement normal du parenchyme cérébral. Ils représentent entre 70 et 80% des AVC.

L'Accident Ischémique Transitoire (AIT) est un type particulier d'AVC ischémique, décrit par l'apparition brutale de troubles neurologiques passagers (dont la durée ne dépasse pas 1h), et sans lésions visibles en imagerie. Environ 800 000 personnes sont diagnostiquées par an. Selon plusieurs études de grandes cohortes, l'apparition d'un AIT induit des risques à court et long terme de survenue d'un AVC. Effectivement, 10% des personnes atteintes d'AIT vont présenter un AVC dans les trois mois (Johnston *et al.*, 2007). L'AIT est également associé à une altération des fonctions cognitives à long terme, bien que difficiles à mettre en évidence au regard des nombreux facteurs de risques (Sivakumar *et al.*, 2014).

### 1.2 Symptômes de l'AVC

Les symptômes de l'AVC sont très variés car ils dépendent de la localisation de l'AVC et de l'étendue des territoires vasculaires impactés (Figure 2). A titre d'exemple, le territoire artériel le plus souvent touché (dans un cas sur deux) est l'artère cérébrale moyenne (Ng *et al.*, 2007). Or ce territoire est le lieu de beaucoup de fonctions cérébrales motrices et cognitives.

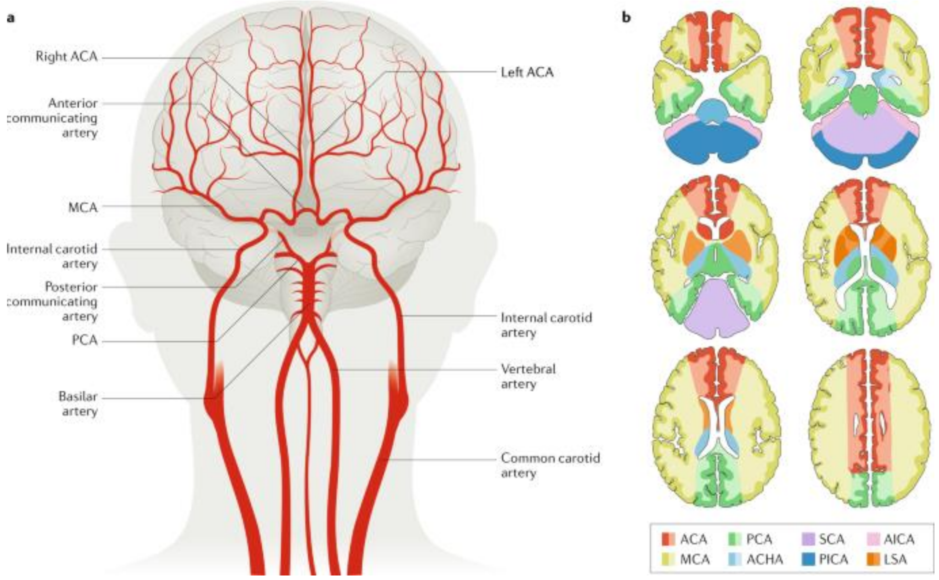

**Figure 2 Principales artères irriguant le cerveau et les territoires artériels associés.**
Le cerveau est irrigué par 4 grandes artères : les artères carotides internes et vertébrales. Elles se rejoignent à la base du cerveau pour former le polygone de Willis. Les artères provenant du polygone de Willis sont les artères cérébrales antérieures, moyennes et postérieures et irriguent différents territoires vasculaires. ACA = artère cérébrale antérieure, PCA = artère cérébrale postérieure, MCA = artère cérébrale moyenne. D'après (Campbell *et al.*, 2019)

De plus, dans les deux types d'AVC, un facteur très important à prendre en compte est le temps. La diminution de la perfusion sanguine et le manque d'oxygénation du parenchyme cérébral entraîne rapidement des conséquences très graves, voire bien souvent fatales. Deux millions de neurones sont perdus par minute écoulée depuis le début de l'AVC (Saver, 2006). Cette perte se manifeste par des déficits moteurs et cognitifs :

- Paralysie brutale ou faiblesse musculaire au niveau du visage ou d'un membre, le plus souvent d'un seul côté (hémiplégie) ;
- Trouble soudain de la parole et difficulté à s'exprimer clairement (aphasie). Le langage devient incompréhensible ;
- Troubles de la vision ou perte de la vision d'un œil ou des deux yeux ;
- Troubles de l'équilibre ;
- Violentes céphalées, migraines.

C'est pourquoi il est capital de pouvoir reconnaître rapidement les signes cliniques d'un AVC. Afin d'alerter la population sur la détection des symptômes de l'AVC, un acronyme a été créé pour reconnaître rapidement les principales manifestations cliniques et l'importance de la rapidité de la prise en charge (Figure 3).

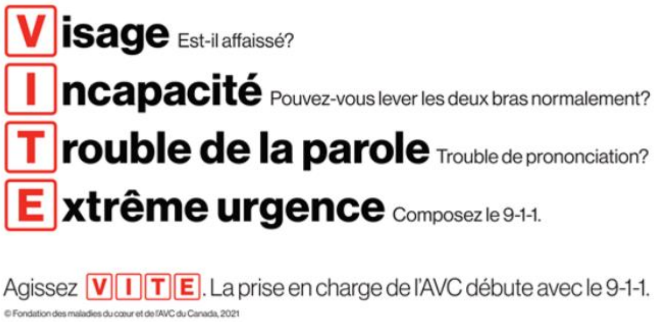

**V**isage Est-il affaissé?
**I**ncapacité Pouvez-vous lever les deux bras normalement?
**T**rouble de la parole Trouble de prononciation?
**E**xtrême urgence Composez le 9-1-1.

Agissez VITE. La prise en charge de l'AVC débute avec le 9-1-1.
© Fondation des maladies du cœur et de l'AVC du Canada, 2021

**Figure 3 Acronyme « VITE » utilisé pour la détection des principaux symptômes cliniques de l'AVC et pour augmenter la rapidité de la prise en charge des patients.**

Par la suite, nous développerons uniquement l'AVC ischémique et la physiopathologie de la thrombose.

## 1.3 AVC ischémique

### 1.3.1 Etiologie

On compte cinq types d'AVC ischémiques selon la classification TOAST (Trial of Org 10172 in Acute Stroke Treatment Subtype (Adams *et al.*, 1993)) : l'athérosclérose des larges artères, l'embolie cardiaque, l'occlusion des petites artères (lacunaires), les causes autres d'origines connues et d'origines inconnues (Figure 4).

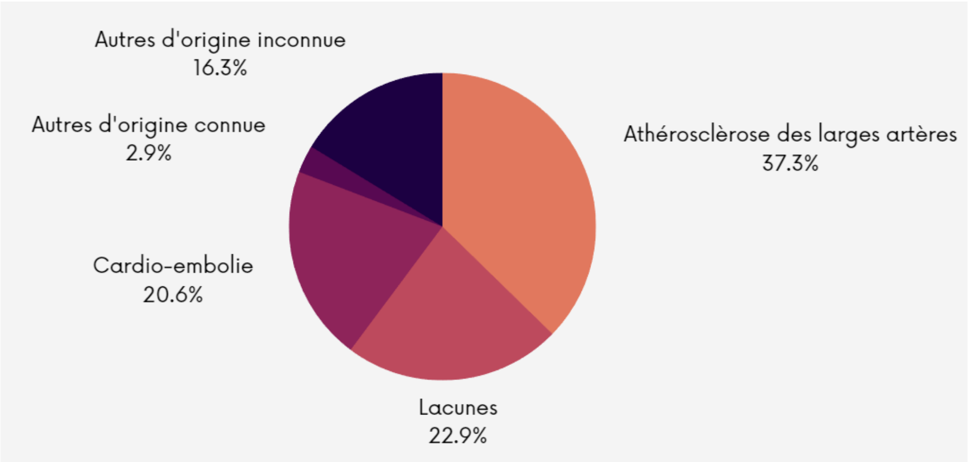

**Figure 4 Etiologie des AVC ischémiques selon la classification TOAST.**
Données extraites de Chung *et al.*, 2014.

- L'**athérosclérose** est l'installation d'une plaque d'athérome (accumulation lipidique dans la paroi du vaisseau et recrutement de cellules inflammatoires), ce qui a pour conséquence le rétrécissement de la lumière artérielle. La progression de cette pathologie peut aller jusqu'à l'obstruction complète du vaisseau (ischémie cardiaque, plus couramment appelé infarctus du myocarde). Dans une partie des cas, un morceau de la plaque d'athérome se détache sous la pression sanguine et va obstruer un vaisseau en aval de la circulation et former un caillot sanguin dans les artères cérébrales, entrainant un AVC. L'athérosclérose est à l'origine de la majorité des AVC (37 %) (Chung *et al.*, 2014)

- Les AVC d'origine **cardio-embolique** sont provoqués par l'embolisation d'un caillot sanguin venant du cœur, le plus souvent suite à une fibrillation auriculaire. L'origine cardio-embolique est associée à une issue moins favorable pour les patients (Lamassa *et al.*, 2001).

- Les AVC de types **lacunaires** se définissent par un petit infarctus (< 1,5cm), dû le plus souvent à l'obstruction d'une seule artère perforante (Wardlaw, 2005).

- Les autres étiologies d'AVC ischémiques d'origine connue sont nombreuses. Les plus courantes sont l'infarctus migraineux, la dissection vasculaire ou encore le lupus érythémateux.

- L'origine des AVC ischémiques reste inconnue dans 15 à 20% des cas, selon les études (Sanna *et al.*, 2014). Cela peut être dû à un examen clinique incomplet, ou complet mais n'ayant pas permis de démontrer l'origine de l'AVC, alors appelé AVC cryptogénique.

### 1.3.2 Facteurs de risques

Afin de réduire le nombre d'AVC, il est important de comprendre quels sont les facteurs de risques associés. Certains facteurs de risques sont modifiables et permettraient, en les contrôlant, d'éviter 80 % des AVC (O'Donnell *et al.*, 2010). Les facteurs de risques **modifiables** regroupent :

- L'hypertension artérielle : c'est un facteur de risque modifiable majeur. Il a été montré une corrélation directe entre une pression artérielle élevée et le risque d'AVC. C'est pourquoi le traitement de l'hypertension fait partie des stratégies thérapeutiques de l'AVC (Suchy-Dicey *et al.*, 2013).

- La consommation de tabac est associée à une augmentation du risque d'AVC, ainsi que la consommation d'alcool en grande quantité (Falkstedt *et al.*, 2017).

- L'obésité contribue fortement à l'augmentation du risque de développer des maladies cardio-vasculaires (fibrillation auriculaire, infarctus du myocarde), dont l'AVC. D'autre part, l'obésité contribue à l'inhibition de la fibrinolyse. En partie à cause de la part importante de tissu adipeux qui produit des inhibiteurs de l'activation du plasminogène ; PAI-1 (cf 1.4.1 Hémostase).

- L'inactivité physique est associée à un risque plus grand d'AVC. Elle peut d'autant plus être la cause d'une augmentation de la pression artérielle, du poids et de diabète (Boehme *et al.*, 2017).

D'autres facteurs de risques sont **non-modifiables** :

- L'âge est le plus important des facteurs de risques non-modifiables. Le risque d'avoir un AVC double chaque année après 55 ans (Roger *et al.*, 2012). De plus, la prévalence de l'AVC va augmenter avec le vieillissement de la population (Krishnamurthi *et al.*, 2013).

- Le sexe : les AVC sont plus courant chez les hommes, mais les femmes ont statistiquement plus de risque de décéder des suites d'un AVC (Goldstein *et al.*, 2001). Cependant le risque de développer un AVC selon le sexe dépend également de l'âge. En effet, à un âge jeune, les femmes ont autant de risque de faire un AVC que les hommes (Kapral *et al.*, 2005).

- L'ethnicité : les personnes d'origines africaines, ont un risque doublé de faire un AVC par rapport aux personnes caucasiennes (Cruz-Flores *et al.*, 2011), et un risque accrue de décès.

- L'existence d'antécédents familiaux augmente également de risque d'AVC. En particulier les antécédents de maladies cardiovasculaires (principalement la fibrillation atriale qui peut provoquer une cardioembolie).

### 1.3.3 Handicap post-AVC

On estime à 63 millions le nombre d'années de bonne santé perdues chaque année dû à la mort ou au handicap après un AVC ischémique ("Global, regional, and national burden of stroke and its risk factors, 1990–2019," 2021). Après un AVC ; la proportion de patients décédés est de 30%, celle de patients dits « dépendants » (perte d'autonomie) est de 25%, et celle de patients souffrant de démences de 30% (Sun *et al.*, 2014). C'est donc un coût sociétal très important. Les séquelles de l'AVC sont de types motrices (hémiplégie, aphasie, héminégligence) et cognitives (dépression, fatigue, troubles de l'attention, crises d'angoisse, démences) et dépendent de l'étiologie de l'AVC et des territoires artériels touchés par l'ischémie, comme vu précédemment.

Ces séquelles sont mesurées par différentes échelles telle que l'échelle du National Institutes of Health Stroke Scale (NIHSS) en première intention, pour évaluer les déficits après un AVC (Figure 5). Une autre échelle fréquemment utilisée est l'échelle modifiée de Rankin (modified Rankin Scale ou mRS). Elle est notamment employée dans les études cliniques pour établir les séquelles des patients après administration d'un nouveau traitement, mais aussi pour guider les mesures de rééducation (Kasner, 2006).

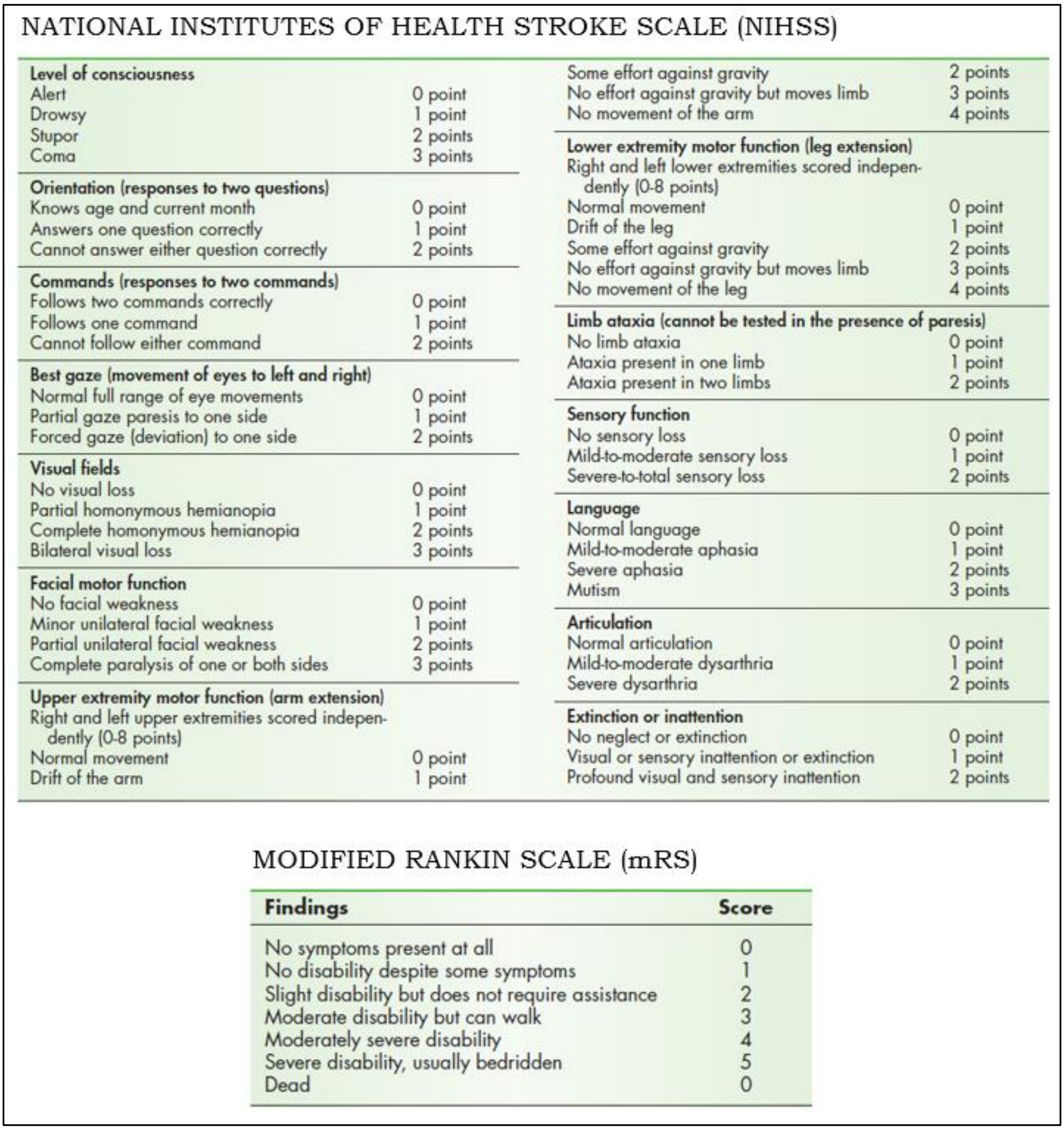

NATIONAL INSTITUTES OF HEALTH STROKE SCALE (NIHSS)

| | |
|---|---|
| **Level of consciousness** | |
| Alert | 0 point |
| Drowsy | 1 point |
| Stupor | 2 points |
| Coma | 3 points |
| **Orientation (responses to two questions)** | |
| Knows age and current month | 0 point |
| Answers one question correctly | 1 point |
| Cannot answer either question correctly | 2 points |
| **Commands (responses to two commands)** | |
| Follows two commands correctly | 0 point |
| Follows one command | 1 point |
| Cannot follow either command | 2 points |
| **Best gaze (movement of eyes to left and right)** | |
| Normal full range of eye movements | 0 point |
| Partial gaze paresis to one side | 1 point |
| Forced gaze (deviation) to one side | 2 points |
| **Visual fields** | |
| No visual loss | 0 point |
| Partial homonymous hemianopia | 1 point |
| Complete homonymous hemianopia | 2 points |
| Bilateral visual loss | 3 points |
| **Facial motor function** | |
| No facial weakness | 0 point |
| Minor unilateral facial weakness | 1 point |
| Partial unilateral facial weakness | 2 points |
| Complete paralysis of one or both sides | 3 points |
| **Upper extremity motor function (arm extension)** | |
| Right and left upper extremities scored independently (0-8 points) | |
| Normal movement | 0 point |
| Drift of the arm | 1 point |
| Some effort against gravity | 2 points |
| No effort against gravity but moves limb | 3 points |
| No movement of the arm | 4 points |
| **Lower extremity motor function (leg extension)** | |
| Right and left lower extremities scored independently (0-8 points) | |
| Normal movement | 0 point |
| Drift of the leg | 1 point |
| Some effort against gravity | 2 points |
| No effort against gravity but moves limb | 3 points |
| No movement of the leg | 4 points |
| **Limb ataxia (cannot be tested in the presence of paresis)** | |
| No limb ataxia | 0 point |
| Ataxia present in one limb | 1 point |
| Ataxia present in two limbs | 2 points |
| **Sensory function** | |
| No sensory loss | 0 point |
| Mild-to-moderate sensory loss | 1 point |
| Severe-to-total sensory loss | 2 points |
| **Language** | |
| Normal language | 0 point |
| Mild-to-moderate aphasia | 1 point |
| Severe aphasia | 2 points |
| Mutism | 3 points |
| **Articulation** | |
| Normal articulation | 0 point |
| Mild-to-moderate dysarthria | 1 point |
| Severe dysarthria | 2 points |
| **Extinction or inattention** | |
| No neglect or extinction | 0 point |
| Visual or sensory inattention or extinction | 1 point |
| Profound visual and sensory inattention | 2 points |

MODIFIED RANKIN SCALE (mRS)

| Findings | Score |
|---|---|
| No symptoms present at all | 0 |
| No disability despite some symptoms | 1 |
| Slight disability but does not require assistance | 2 |
| Moderate disability but can walk | 3 |
| Moderately severe disability | 4 |
| Severe disability, usually bedridden | 5 |
| Dead | 0 |

**Figure 5 Échelles de mesure de la sévérité de l'AVC (NIHSS) et d'évaluation des séquelles post-AVC (mRS).**

(Adams, 2011)

## 1.4 Physiopathologie de l'AVC ischémique

### 1.4.1 L'hémostase

L'hémostase est l'ensemble des mécanismes biochimiques et cellulaires qui assurent la prévention des saignements spontanés et l'arrêt des hémorragies en cas de lésion vasculaire. Elle se divise en trois étapes successives : (i) l'hémostase primaire avec formation du clou plaquettaire, (ii) l'hémostase secondaire ou coagulation plasmatique qui entraîne l'arrêt du saignement et la cicatrisation de la paroi (Figure 6), puis (iii) la fibrinolyse pour dissoudre ce caillot et retrouver l'intégrité de la paroi vasculaire.

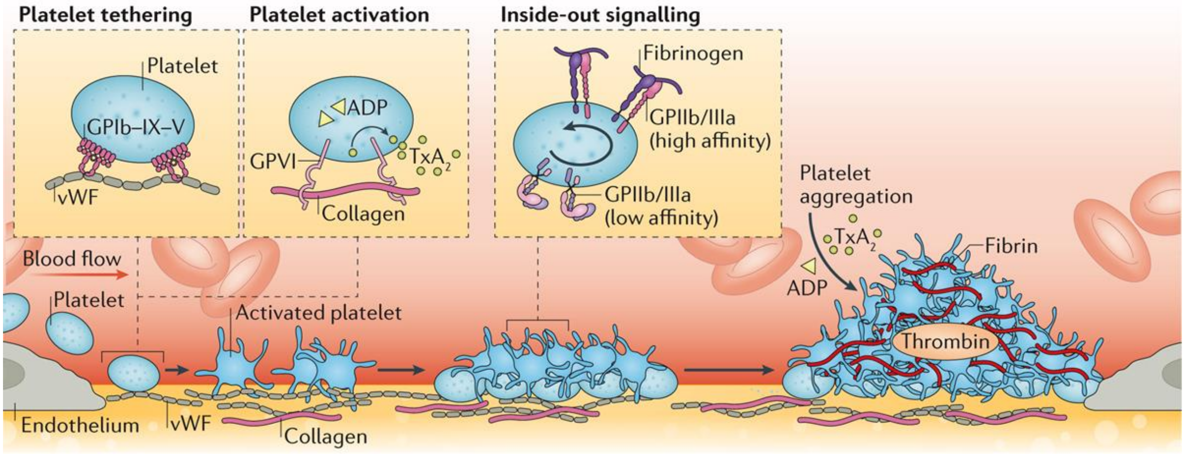

**Figure 6 Mécanismes physiologiques de l'hémostase.**
L'hémostase primaire consiste en l'activation et la fixation des plaquettes au niveau de la brèche vasculaire, formant le clou plaquettaire. La cascade de la coagulation entraîne la solidification du caillot grâce à l'interaction de la thrombine et de la fibrine. (McFadyen *et al.*, 2018)

- **L'hémostase primaire** :

Elle fait intervenir la paroi vasculaire, les facteurs plasmatiques de la coagulation et les plaquettes. Lorsque qu'il y a une lésion vasculaire, les éléments du sous-endothélium sont exposés à la lumière du vaisseau et recrutent les plaquettes de la circulation pour se fixer et former le clou plaquettaire. Dans cette première partie, les plaquettes adhèrent au collagène sous-endothélial par le facteur von Willebrand et les glycoprotéines GPIb-IX-V. Celles-ci entraînent leur activation, qui se traduit par un changement de conformation et l'expression à leur surface de récepteurs membranaires comme la forme activée de la glycoprotéine GP IIb-

IIIa, récepteur responsable de l'agrégation des plaquettes entre elles, reliées par un pont fait de fibrinogène (Varga-Szabo *et al.*, 2008).

- **L'hémostase secondaire ou coagulation plasmatique**:

C'est la consolidation du clou plaquettaire faisant intervenir en cascade les facteurs de la coagulation. On distingue la voie dépendante du facteur tissulaire et la voie dépendante du collagène (Figure 7).

La voie dépendante du facteur tissulaire est déclenchée lorsque le facteur tissulaire (FT), présent dans le sous-endothélium, rentre en contact avec la circulation sanguine. Le facteur VII va se fixer au FT. Leur association va activer les facteurs IX et X.

Dans la voie dépendante du collagène, le facteur de von Willebrand se lie au collagène sous-endothélial (Hoylaerts et al., 1997), ce qui active le facteur XIII, puis XI et rejoint la voie commune.

L'activation de ces deux voies amènent à l'activation d'une voie commune de la coagulation. Le facteur X activé (FXa) forme un complexe avec le facteur V, pour former la prothrombinase. Celle-ci va ensuite activer la prothrombine en thrombine qui transforme le fibrinogène soluble en fibrinogène insoluble, et active également la cascade de la coagulation et l'activation plaquettaire. Ces étapes aboutissent à la formation d'un caillot composé de fibrine insoluble, piégeant les érythrocytes (Palta *et al.*, 2014).

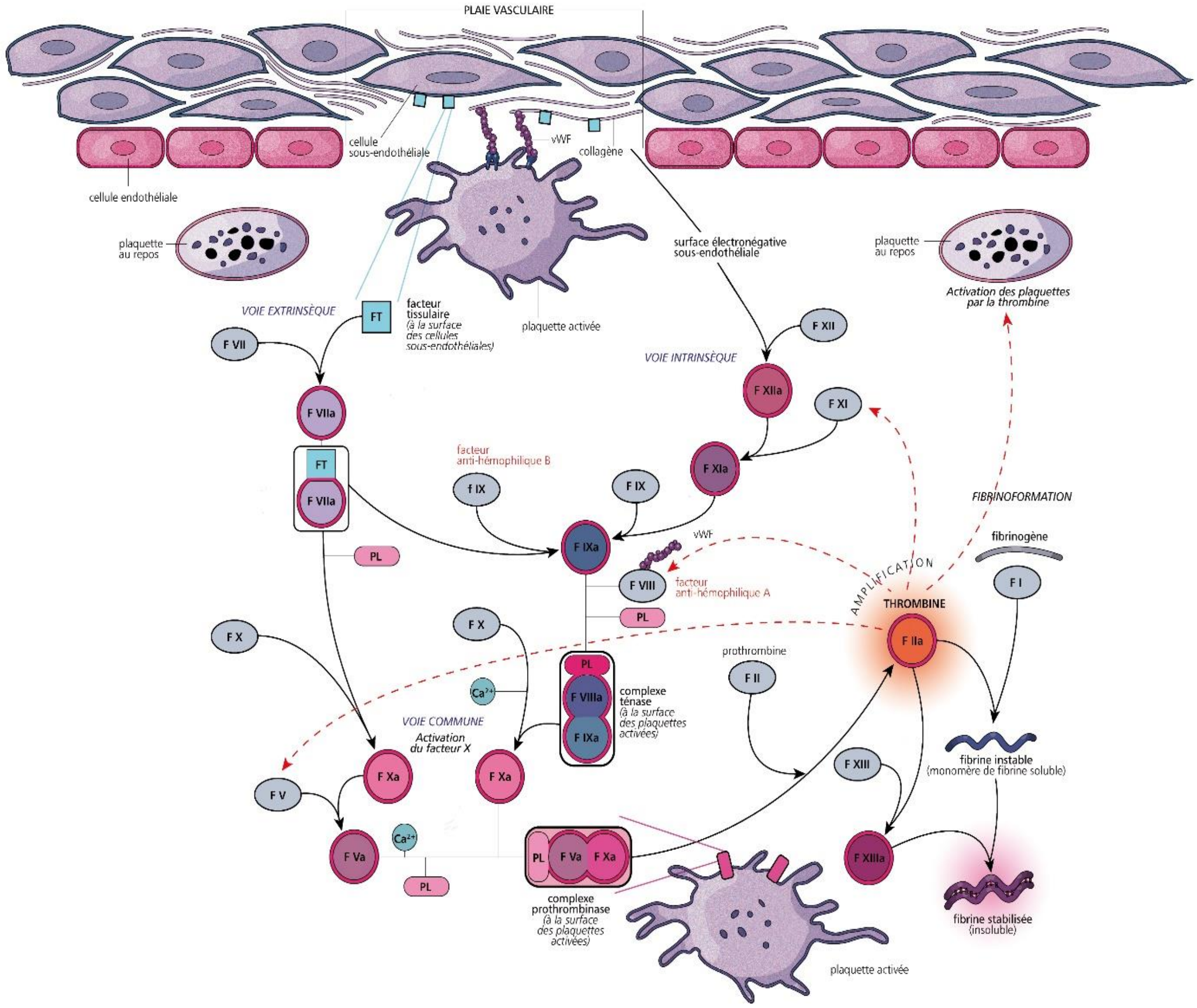

**Figure 7 Cascade de la coagulation.**
Une brèche au niveau de la paroi vasculaire expose le sous-endothelium aux constituants du sang et enclenche les deux voies d'activation de la coagulation : la voie dépendante du collagène (intrinsèque) et la voie dépendante du facteur tissulaire (extrinsèque). ("Physiologie de l'hémostase," https://mhemo.fr/les-pathologies/physiologie-de-lhemostase/)

- **La fibrinolyse** :

Lorsqu'un caillot dû à l'hémostase secondaire est présent dans la circulation, ce sont les mécanismes de la fibrinolyse qui permettent de l'éliminer et de restaurer l'intégrité de la paroi vasculaire. Ce mécanisme est centré sur l'activation de la plasmine, enzyme capable de dégrader les chaînes de fibrine et possédant une affinité pour la fibrine, le fibrinogène et les protéines de la coagulation (V et VIII). La plasmine est produite par le foie sous sa forme inactive : le plasminogène. Il existe deux activateurs du plasminogène : l'activateur tissulaire du plasminogène (tPA) qui est stocké dans les corps de Weibel-Palade des cellules endothéliales, et va activer le plasminogène fixé au niveau de l'incident vasculaire (Huber *et al.*, 2002), et l'urokinase (activateur du plasminogène de type urokinase ou uPA). Afin d'éviter une fibrinolyse exacerbée, ou hyperfibrinolyse, des mécanismes d'inhibition de la fibrinolyse interviennent pour la réguler (Figure 8): l'inhibition de la plasmine par l'antiplasmine α2, et l'inactivation de l'uPA et du tPA par les inhibiteurs du plasminogène PAI-1 et PAI-2 (Wun and Capuano, 1987).

Les mécanismes de l'hémostase montrent donc un équilibre fragile entre la coagulation et la fibrinolyse. La perturbation de cet équilibre est à l'origine d'hémorragies ou de thromboses.

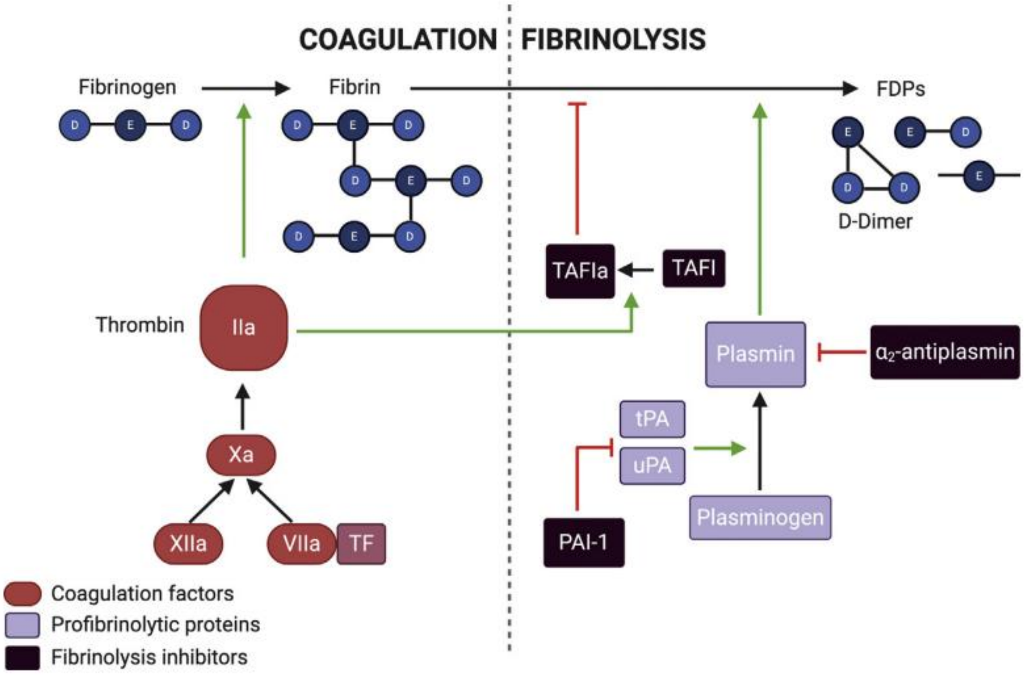

**Figure 8 Principales protéines et leurs inhibiteurs impliqués dans la coagulation et fibrinolyse.** Le tPA endogène active le plasminogène en plasmine. Celle-ci dégrade le caillot de fibrine en produits de dégradation de la fibrine (FDPs). (May *et al.*, 2021)

### 1.4.2 La thrombose

La formation d'un thrombus dépend donc de l'activation des plaquettes, du système de coagulation et de la fibrinolyse. Les thrombi peuvent être composés majoritairement de plaquettes, fibrine ou d'érythrocytes et présentent différentes propriétés physiques (taille, solidité, friabilité) qui vont déterminer la nature du traitement à appliquer (Marder *et al.*, 2006). Leur composition va dépendre de l'origine du caillot, ils peuvent être classés en thrombi riches en fibrine ou riches en érythrocytes (Yuki *et al.*, 2012).

Par exemple, dans l’athérosclérose, l’accumulation lipidique dans la paroi vasculaire entraîne une réduction de la lumière vasculaire (Figure 9). La rupture de cette plaque lipidique expose le collagène et le FT aux éléments sanguins et entraîne l’activation plaquettaire et la cascade de la coagulation (Borissoff *et al.*, 2011). Le caillot formé au niveau de la plaque va se détacher puis emboliser les artères distales en aval de la circulation. Ces thrombi sont donc riches en plaquettes, stabilisés par des liaisons fortes de fibrine.

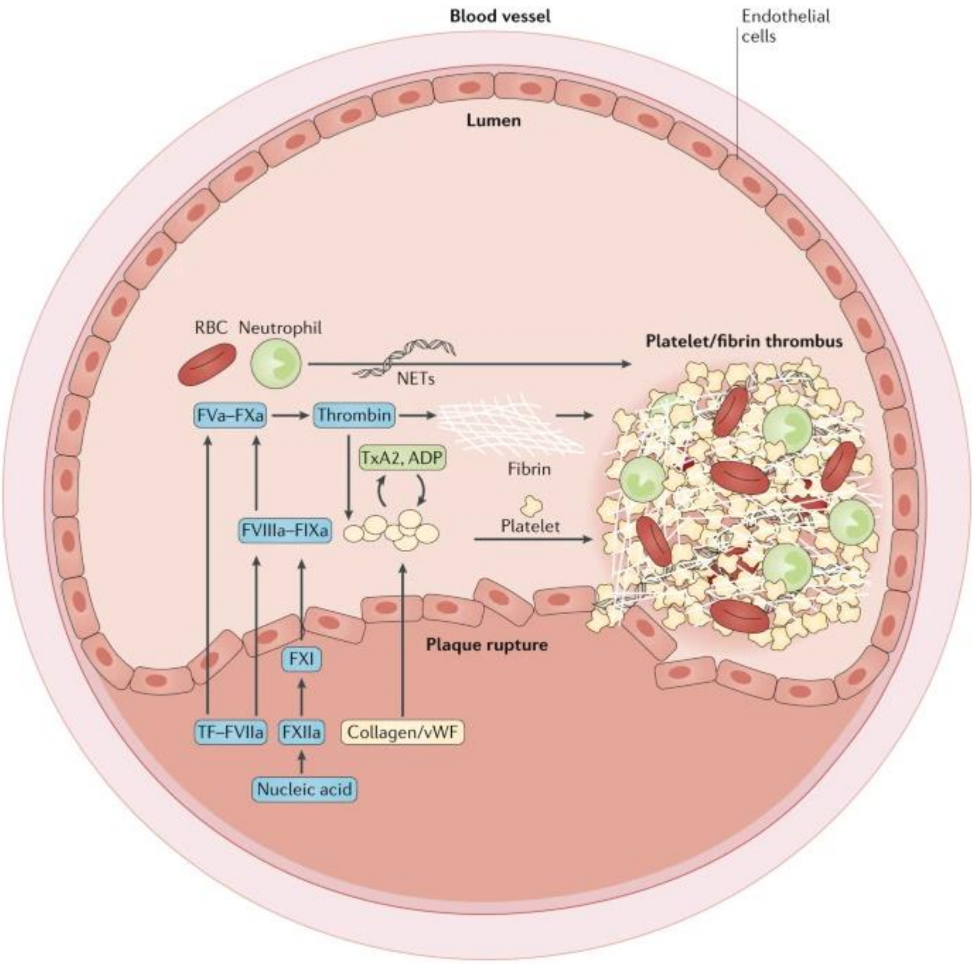

**Figure 9 Formation d’un thrombus riche en fibrine et plaquettes après rupture de la plaque athérosclérotique.**
D’après Mackman *et al.*, 2020.

La demande énergétique des tissus nerveux est très élevée, et nécessite un apport sanguin constant et suffisant. En effet, le cerveau consomme environ 20% de l’oxygène du corps. Lorsqu’un caillot empêche l’apport en énergie au cerveau, le territoire irrigué par l’artère occlue est en hypoperfusion. On distingue dans le cadre de l'AVC trois types de zones hypo-perfusées (Figure 10) :

- Le cœur ou **foyer ischémique** : tissu proche de l'occlusion. Les lésions provoquées sont irréversibles.

- La **pénombre ischémique** : tissu sévèrement hypoperfusé présentant un risque d'ischémie. La réduction du débit sanguin est moins importante dans cette zone grâce à la circulation collatérale. Les lésions progressent moins rapidement et la zone peut être récupérée si une reperfusion à lieu dans le temps imparti.

- L'**oligémie** : tissu avec hypoperfusion modérée qui n'est pas à risque.

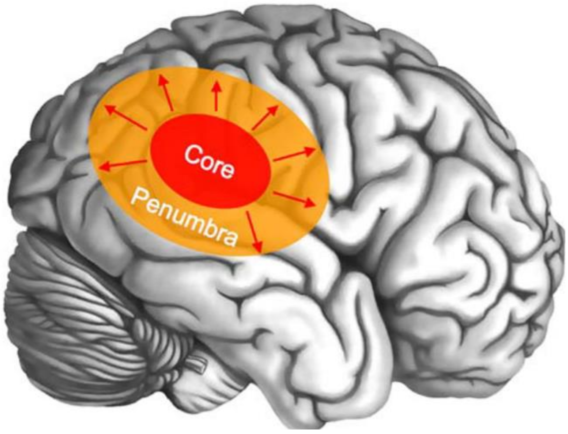

**Figure 10 Zones d'hypoperfusions cérébrales lors d'une ischémie cérébrale.**
On distingue trois zones : le foyer ischémique (core), la pénombre (penumbra) et l'oligémie (non représentée). D'après (Kloska *et al.*, 2010)

### 1.5 Traitements de l'AVC ischémique

Le traitement de référence depuis 2015 pour l'obstruction d'une artère proximale (artère cérébrale moyenne, artère carotide interne, tronc basilaire), est l'association de la thrombolyse intraveineuse et de la thrombectomie mécanique.

### 1.5.1 Thrombolyse

Les activateurs du plasminogène ont été introduit en clinique dans les années 90. Le traitement pharmaceutique de référence encore actuellement utilisé est l'activateur tissulaire du plasminogène recombinant (rtPA), avec une autorisation de mise sur le marché pour le traitement des AVC ischémiques aux Etats-Unis en 1995. Le rtPA est produit de façon synthétique par recombinaison à partir du tPA endogène, protéine intervenant dans le processus de fibrinolyse. Il possède une affinité forte pour la fibrine, qui compose le thrombus, et transforme sélectivement le plasminogène, lié au thrombus, en plasmine. La plasmine va ensuite dégrader la matrice fibrineuse et lysera le caillot (Figure 11).

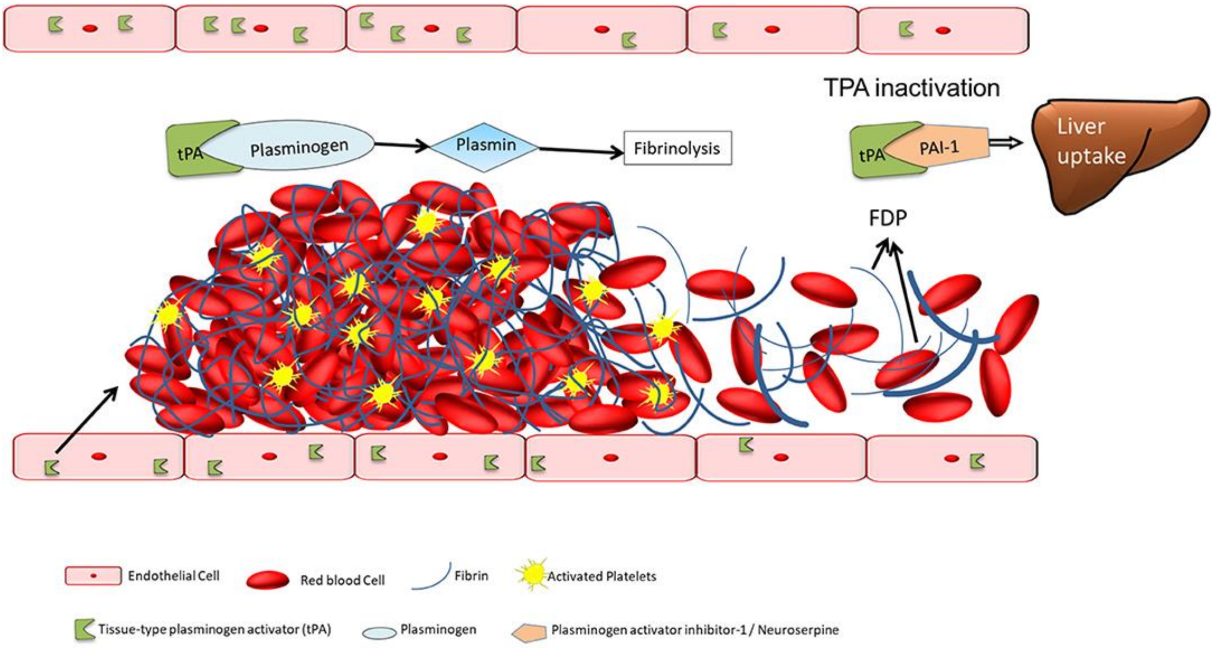

**Figure 11 Action thrombolytique du rtPA.**
Le rtPA active le plasminogène circulant en plasmine. La plasmine va alors dégrader la fibrine en produits de dégradation (FDP) et dissoudre le caillot. D'après (Pan and Shi, 2021)

L'utilisation du rtPA pour le traitement de l'AVC ischémique par injection intraveineuse fait suite à un essai clinique de grande envergure ayant démontré que 30 % des patients ayant reçu du rtPA présentait un handicap minime ou nul, par comparaison aux patients ayant reçu un placebo ("Tissue Plasminogen Activator for Acute Ischemic Stroke," 1995). A l'origine, il était indiqué dans les AVC datant de moins de 3h. Mais cette fenêtre thérapeutique rendait le traitement inaccessible pour beaucoup de patients, et il est estimé que seul 2% des patients présentant un AVC ischémqiue ont pu recevoir ce traitement dans les années qui ont suivis (Grond *et al.*, 1998). Depuis, grâce au progrès des techniques d'imagerie, d'autres essais cliniques ont permis de démontrer son efficacité sur les AVC survenu dans les 4h30 (“Association of outcome with early stroke treatment,” 2004), et jusqu’à 9h (Ma *et al.*, 2019). Ces avancées ont ainsi élargi l’utilisation à d’autres patients.

Mais la thrombolyse présente beaucoup de contre-indications. La dégradation de la fibrine par le tPA entraîne une dérégulation de l’hémostase entraînant un risque majeur d’hémorragie. De plus, les études sur le tPA ont montré qu’il perturbe la barrière hémato-encéphalique (BHE), par interaction avec les protéines de récepteurs de lipoprotéines (LRP) des cellules endothéliales (Suzuki *et al.*, 2011), ce qui favorise également le risque d’hémorragies. Le tPA a aussi montré un effet pro-excitotoxique en potentialisant le signal des récepteurs glutamatergiques par interaction avec le récepteur N-methyl-D-aspartate (NMDA) (Nicole *et al.*, 2001), ce qui impact la survie neuronale. Tous ces éléments font que seulement 5% des patients diagnostiqués AVC peuvent bénéficier du traitement (Demaerschalk *et al.*, 2016).

Bien que le l’altéplase (rtPA) soit à ce jour le seul traitement thrombolytique approuvé pour l’AVC ischémique, une alternative potentielle est l’utilisation de la ténectéplase (TNK-tPA). La TNK est une protéine recombinante fibrino-spécifique de l’activateur tissulaire du plasminogène. Elle se distingue du tPA endogène par mutation de 3 sites dans sa structure protéique. Elle possède de nombreux avantages par rapport à l’altéplase tels qu’une plus grande affinité pour la fibrine (diminue le risque hémorragique), une demi-vie d’élimination plus longue (administration en bolus donc traitement plus rapide), une plus grande résistance à l’inactivation par PAI-1, et un coût moindre. Pourtant, les essais cliniques sur la TNK n’ont pas montré de différences significatives entre les groupes que ce soit pour l’amélioration neurologique ou pour les risques de transformation hémorragique (Huang *et al.*, 2015).

D’autres approches de types endovasculaires ont été développées pour désobstruer le vaisseau et obtenir la recanalisation des vaisseaux, sans encourir les effets secondaires des thrombolytiques.

### 1.5.2 Traitements endovasculaires

En 2014 et 2015, cinq essais cliniques majeurs ont démontré l’efficacité d’une approche mécanique sur les patients présentant une occlusion des artères proximales : l’introduction par voie endoscopique d'un dispositif pour retirer le caillot appelé « stent retriever ». Le nom de cette pratique endovasculaire est la thrombectomie. Ces essais avaient pour objectif d'évaluer l'efficacité du traitement endovasculaire associé à la thrombolyse, par rapport à la thrombolyse seule. Ils différaient toutefois dans les critères d'inclusions des patients, la fenêtre thérapeutique, les dispositifs utilisés pour la thrombectomie et les modalités d'imagerie pour attester de la recanalisation des artères (Tableau 1).

| **Nom de l'essai clinique** | **Conditions et Modalités d'imagerie** | **Fenêtre thérapeutique** | **Dispositif** | **Références** |
|---|---|---|---|---|
| MR CLEAN | Occlusion distale de la carotide interne, du premier ou second segment de l'ACM (M1 ou M2) ou de l'artère cérébrale antérieure (A1 ou A2) diagnostiqués par angioscanner, angio-IRM ou artériographie. | 6 premières heures de l'infarctus cérébral | Dispositifs approuvés par la Food and Drug Administration (FDA) ou par la réglementation européenne (dispositif CE) | (Fransen *et al.*, 2014) |
| EXTEND-IA | Occlusion de l'ACI ou occlusion de l'ACM (M1 ou M2), infarctus < 70 mLet volume de pénombre ischémique (T max > 6sec) visible sur scanner de perfusion | 4h30 après l'occlusion cérébrale | Stent Solitaire ™ | (Campbell *et al.*, 2014) |
| ESCAPE | Angioscanner multiphase qui permet de sélectionner rapidement les patients sur une cartographie de collatéralité. Zone d'infarctus réduite, occlusion intracrânienne proximale | 12h après le début des symptômes | Dispositifs approuvés par la FDA ou CE. | (Goyal *et al.*, 2015) |
| SWIFT PRIME | Occlusion d'un gros vaisseau (ACM M1, occlusion ACI intracrânienne) dignostiquée par angioscanner CT, CTA | 6h après le début des symptômes | Stent Solitaire ™ | (Saver *et al.*, 2015) |
| REVASCAT | Occlusion artérielle proximale antérieure confirmée sur imagerie imagerie ACI (occlusion ACI distale ou T), segment ACM-M1 | 8h après le début des symptômes | Stent Solitaire ™ | (Molina *et al.*, 2015) |

**Tableau 1 Essais cliniques majeurs publiés en 2014 et 2015 sur l'évaluation des traitements endovasculaires**. Extraits du rapport d'évaluation de la thrombectomie des artères intracrâniennes (Haute Autorité de la Santé).

Ces études ont prouvé l'efficacité de la thrombectomie pour la recanalisation des artères proximales dans les 6 heures après le début des symptômes. Depuis, d'autres essais cliniques ont permis d'étendre le temps de traitement jusqu'à 24 heures après le début des symptômes grâce à une surveillance accrue par imagerie (Nogueira *et al.*, 2018).

Par la suite, d'autres études ont cherché à évaluer si le traitement associant thrombolyse et thrombectomie présente un avantage par rapport à la thrombectomie seule. L'étude récente « DIRECT MT » ne montre pas de différence au niveau de la récupération fonctionnelle et du risque hémorragique entre les patients des deux groupes (Yang *et al.*, 2020).

Bien que la thrombectomie permet d'obtenir une recanalisation complète des artères dans 60% des cas (Nikoubashman *et al.*, 2019), cette méthode est limitée aux artères proximales et, par conséquent, les patients avec un AVC au niveau d'artère sinueuses ou présentant des occlusions dans des branches plus distales, tels que les branches M3 et M4 de l'ACM (fréquemment touchées), ne sont pas éligibles.

Ainsi, dans les guides de pratique pour le traitement des AVC ischémiques, il est aujourd'hui recommandé de traiter les patients par thrombolyse, thrombectomie ou association des deux, selon leur éligibilité.

### 1.5.3 Traitements de prévention primaires et secondaires

Les autres principaux traitements utilisés dans l'AVC ischémique sont les antiagrégants plaquettaires et les anticoagulants. Ce sont des traitements de prévention primaires secondaires : ils ne permettent pas de restaurer le flux sanguin cérébral en dégradant le caillot mais pourrons réduire le risque de survenue d'un AVC, ou la récidive ("Collaborative overview of randomised trials of antiplatelet therapy," 1994).

L'antiagrégant plaquettaire utilisé principalement après un AVC est l'aspirine à faible dose. L'aspirine, par inhibition de la cyclooxygenase-1 (enzyme intervenant dans l'agrégation plaquettaire) permet de réduire de 20 % le risque de récidive de l'AVC (Collaboration *et al.*, 2009). Il est donc utilisé à titre préventif, à condition de s'assurer qu'il n'entraine par un risque de perturbation de l'hémostase, et donc d'hémorragie, par réalisation de bilans sanguins.

Selon le tableau clinique, les anticoagulants sont à privilégier par rapport aux antiagrégants plaquettaires. Jusqu'en 2009, l'anticoagulant de référence était la warfarine qui cible la synthèse des facteurs de coagulation II, VII, IX et X. Depuis, d'autres anticoagulants comme les inhibiteurs du facteur Xa (l'apixaban, rivaroxaban, et edoxaban) ainsi que l'inhibiteur direct de la thrombine (dabigatran) ont démontré une efficacité similaire à la warfarine.

Ainsi, ces traitements ont pour objectif principal la recanalisation des vaisseaux obstrués, ou la prévention de la formation de caillots sanguins. Mais beaucoup de patients, malgré qu'ils démontrent une recanalisation de l'artère obstruée, ne montre pas d'améliorations cliniques (Dalkara and Arsava, 2012).

### 1.6 Microthrombose

La microcirculation cérébrale se distingue des autres vaisseaux cérébraux par la structure des parois des vaisseaux et leur capacité à ajuster l'apport d'oxygène et de nutriments pour répondre aux exigences métaboliques des cellules du parenchyme, par ajustement du tonus vasculaire et en libérant différentes substances vasoactives (Gutterman *et al.*, 2016).

Lorsque les artères carotides internes rejoignent le polygone de Willlis, à la base du crâne, la circulation sanguine se divise en artères cérébrales (MCA, ACA, PCA), puis en artères pénétrantes pour enfin rejoindre la microcirculation. Cette dernière correspond aux artérioles, aux capillaires et aux veinules (Pappano and Gil Wier, 2013). Les artérioles ont une taille comprise entre 10 et 100 µm. Elles possèdent une couche de cellules musculaires lisses, un adventice et une couche de cellules endothéliales, et donnent directement naissance aux capillaires. Les capillaires ont un diamètre compris entre 10 et 20 µm et leur paroi est uniquement composée des cellules endothéliales et d'une membrane basale associée (Figure 12). Les capillaires forment un très grand réseau interconnecté, et leur longueur totale dans le système cardiovasculaire serait comprise entre 100 et 160 000 km (à titre de comparaison, le tour de la Terre mesure 40 000 km), ce qui facilite les échanges métaboliques (Myers and Lam, 2021). Enfin, les veinules sont similaires aux artérioles, mais n'ont pas de cellules musculaires lisses. Elles connectent les capillaires aux veines.

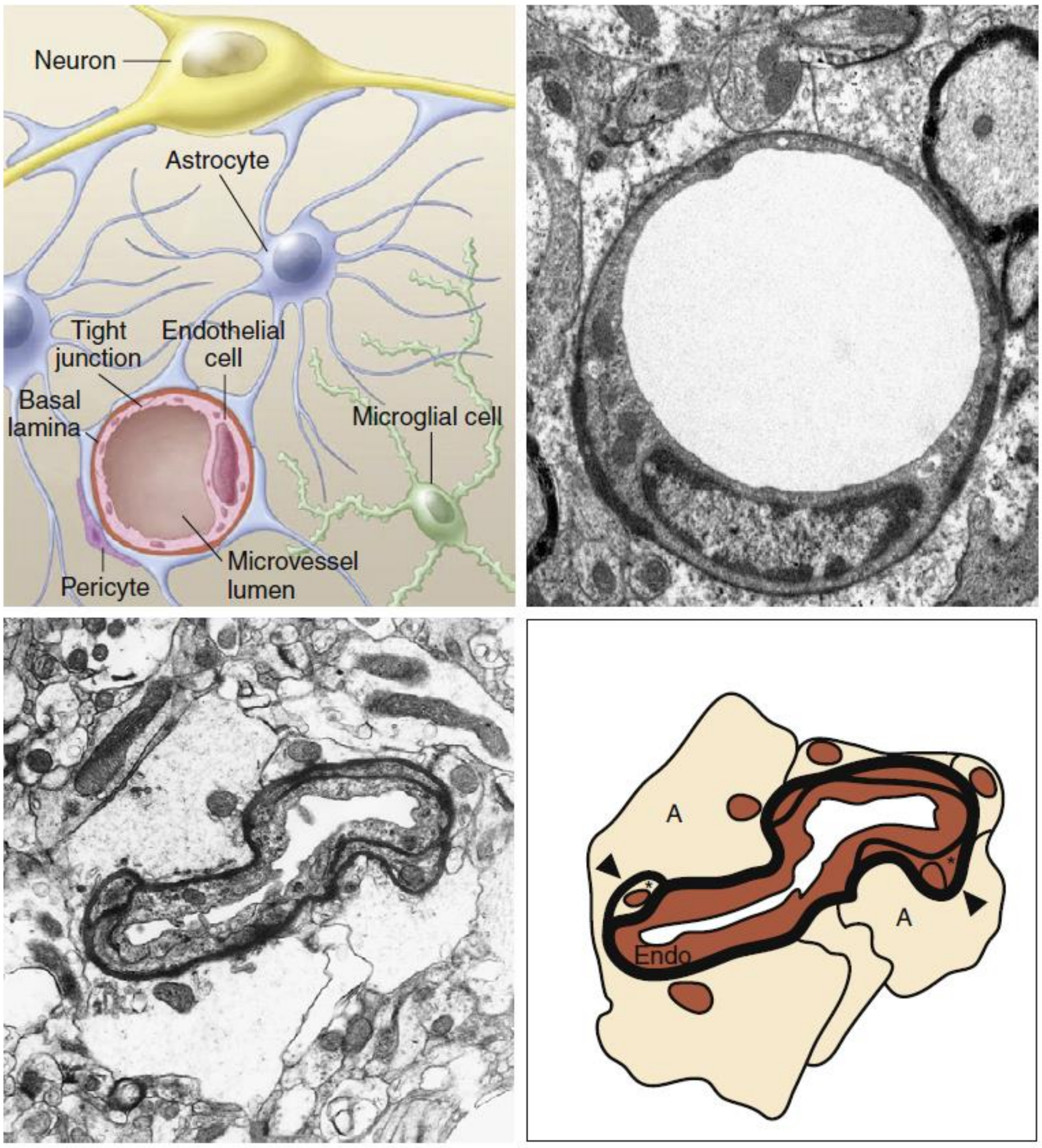

**Figure 12 La microcirculation cérébrale.**
Cellules du système nerveux impliquée dans la microcirculation (haut gauche), et capillaires cérébraux observés en microscopie électronique. (A : astrocytes, Endo : cellules endothéliales). (Del Zoppo, 2006)

La microthrombose (ou thrombose microvasculaire) désigne les thrombi de petites tailles (<100 µm), les microthrombi, qui obstrue les artérioles et capillaires sanguins. Ce mécanisme est impliqué dans différents contextes pathologiques : AVC ischémique et hémorragique, infarctus du myocarde, coagulation intravasculaire disséminée, septicémie. Dans cette partie, nous développerons uniquement la microthrombose observée après un AVC ischémique.

Les thérapies endovasculaires et thrombolytiques visent à restaurer la zone de pénombre en éliminant le thrombus en amont (la recanalisation) tout en restaurant la perfusion microvasculaire en aval (la reperfusion). Ces deux mots sont le plus souvent utilisés de manière interchangeable dans beaucoup de publications. Cependant il est nécessaire de distinguer ces deux phénomènes, car la recanalisation de l'artère proximale ne signifie pas nécessairement une reperfusion au niveau de la microcirculation. Des études cliniques ont rapporté la présence de microthrombi après une recanalisation spontanée, ou une apparition des microthrombi dite iatrogène, par thrombolyse ou par thrombectomie du vaisseau proximal, pouvant expliquer ce manque de reperfusion distale (Goyal *et al.*, 2021).

### 1.6.1 Origine de la microthrombose dans l'AVC

Les microthrombi retrouvés lors d'un AVC ischémique ont plusieurs origines. Ils peuvent survenir après traitement du caillot proximal par thrombolyse ou thrombectomie, ou encore apparaître spontanément après une recanalisation, par ce qu'on appelle le phénomène de *no-reflow* (Figure 13). Par ailleurs, dans une étude de 2015, l'analyse d'images par résonance magnétique (IRM) acquises avant traitement a également montré la présence de multiples thrombi distaux en plus d'un caillot proximal chez 8 % des patients inclus (Gratz *et al.*, 2015).

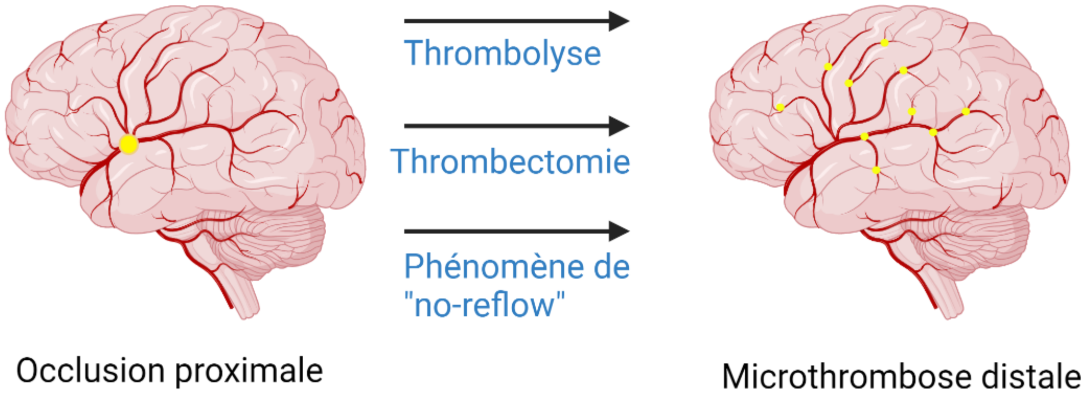

**Figure 13 Formation de microthrombi distaux après recanalisation par thrombolyse, thrombectomie ou no-reflow**

- **Microthrombose après thrombolyse**

La thrombolyse par injection intraveineuse de rtPA est le traitement de référence pour les AVC depuis les années 90. Cependant, même lorsque la thrombolyse permet une recanalisation des vaisseaux, des fragmentations puis migrations du thrombus proximal ont été observées dans un patient sur quatre après thrombolyse (Alves *et al.*, 2019).

- **Microthrombose après thrombectomie**

De nombreuses évolutions des traitements endovasculaires ont eu lieues depuis 2015, en passant de dispositifs de stent retrievers, à des dispositifs plus évolués d'aspiration ou combinaison des deux (Figure 14). Cela a augmenté le taux de recanalisation chez les patients de près de 50% (Ospel *et al.*, 2020).

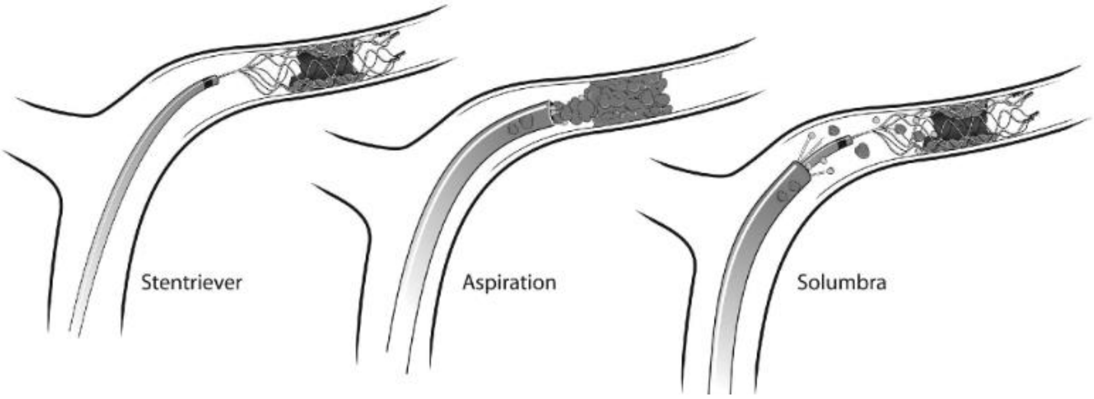

**Figure 14 Différents dispositifs utilisés pour extraire le caillot par thrombectomie.**
(Munich *et al.*, 2019)

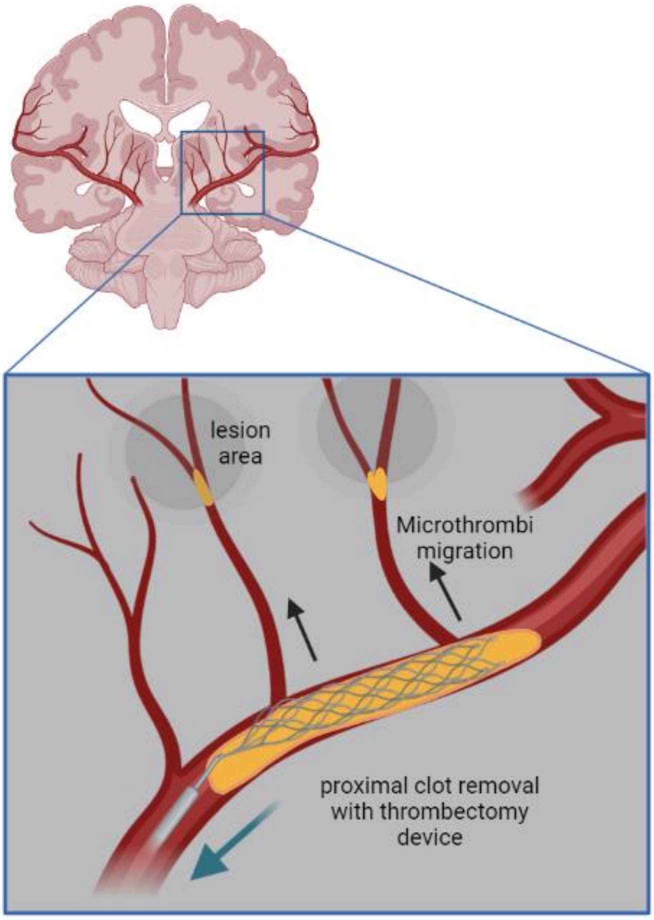

**Figure 15 Migration du thrombus dans les artères perforantes après thrombectomie.**
Le dispositif de thrombectomie permet la recanalisation de l'artère proximale. Cependant il peut provoquer la fragmentation et migration de microthrombi dans la circulation distale.

Ainsi, bien que la thrombectomie entraîne une recanalisation réussie chez beaucoup de patients, la présence de microthrombi est observée dans 9 à 22 % des cas (Berkhemer *et al.*, 2015). Ce résultat varie selon les études cliniques et dépend des conditions d'inclusion des patients, et des techniques d'imagerie utilisées. Dans l'étude MR CLEAN, qui inclue 500 patients, la migration du thrombus est un phénomène qui a été remarqué dans 22% des cas. L'une des raisons est la fragmentation du thrombus primaire pendant la thrombectomie, puis la migration des fragments du caillot dans la circulation en aval (Figure 15). Ces résultats ont été retrouvés également dans une étude préclinique, dans un modèle d'ischémie chez le rat, dans lequel des microsphères de différentes tailles (15-50 µm) ont été injectées par voie intraveineuse après recanalisation de l'artère occlue, pour marquer les microthrombi. De nombreuses zones d'hypoperfusion sont observées à proximité des microsphères marquant les microthrombi (Georgakopoulou *et al.*, 2021 ; Figure 16).

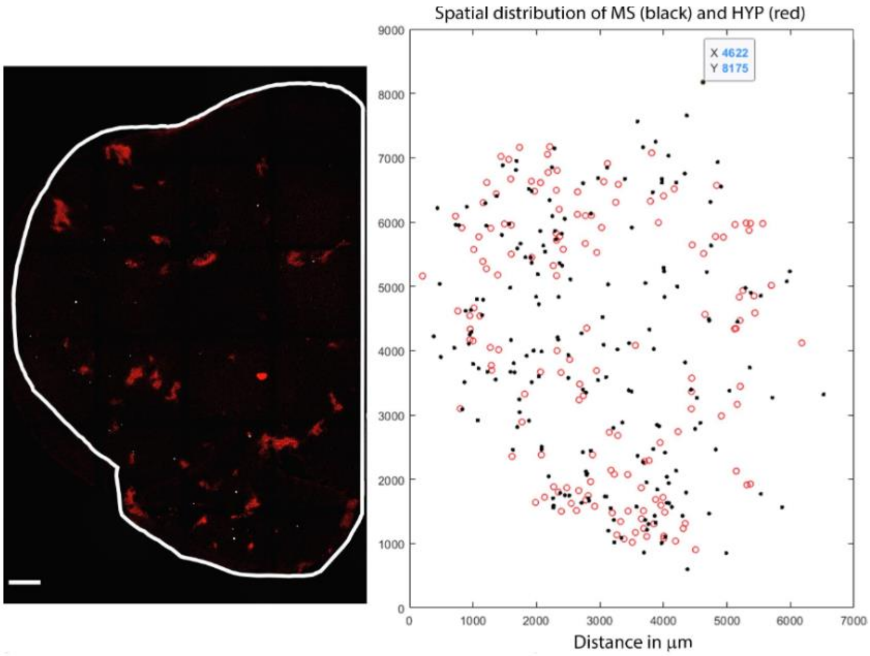

**Figure 16 Microembolisation après reperfusion cérébrale observée dans un modèle d'ischémie chez le rat.**
D'après (Georgakopoulou *et al.*, 2021)

Ces résultats ont soulevé l'hypothèse d'un potentiel effet délétère du traitement par thrombolyse avant traitement par thrombectomie. Des études montrent que le traitement par thrombolyse précédant une thrombectomie augmente le nombre d'embolisations du caillot proximal et est corrélée à un taux de reperfusion inférieur (Kaesmacher *et al.*, 2017 ; Figure 16). Mais, malgré cela, la thrombolyse précédant la thrombectomie est associée à un meilleur pronostic fonctionnel (Flint *et al.*, 2020).

L'évolution des dispositifs de thrombectomie rend également possible l'extraction de thrombus ayant migré dans des artères plus distales (Hofmeister *et al.*, 2018). Cependant, leur utilisation est limitée aux thrombi distaux présents au niveau des deuxièmes et troisièmes fractions de l'ACM, ACP et ACA.

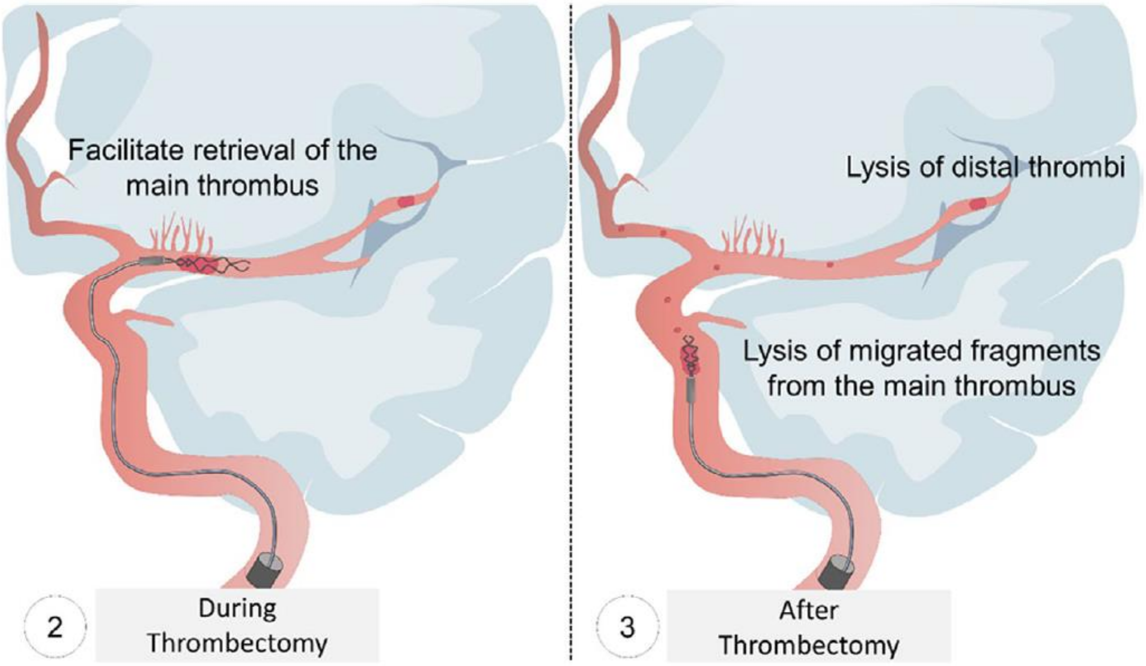

**Figure 17 Formation de microthrombi après traitements endovasculaire**
D'après (Gauberti *et al.*, 2021)

D'autres études ont été menées pour déterminer si la thrombolyse en amont ou pendant la thrombectomie pourrait réduire le risque de microthrombi formés par fragmentation (Broocks *et al.*, 2021, Figure 17) et n'a pas démontrée de différence entre les patients traité par thrombectomie sur la présence de microthrombi, qu'ils aient reçu du rtPA ou non. La disparité de ces résultats met en évidence l'intérêt de diagnostiquer clairement la présence de microthromboses dans l'AVC ischémique.

- **Phénomène de *no-reflow***

La reperfusion incomplète de la microcirculation a été décrite en 1968 par Ames et collaborateurs, dans le cas d'une ischémie globale chez le lapin, sous le terme de *no-reflow* (Ames *et al.*, 1968). Ce phénomène transcrit le manque de reperfusion après une recanalisation de la zone ischemiée et le développement continue de la lésion ischémique, aussi décrit comme lésion d'ischémie-reperfusion. Par la suite, del Zoppo et collaborateurs ont montré que cette reperfusion incomplète du flux sanguin est accompagnée d'un gonflement des pieds astrocytaires, une contraction des péricytes et un rétrécissement de la lumière des microvaisseaux (del Zoppo and Mabuchi, 2003). L'hypoperfusion entraîne l'expression de molécules d'adhésion à la surface des cellules endothéliales, suivi de l'adhésion de leucocytes polymorphonucléaires et une accumulation de dépôts de fibrine et de plaquettes activées, formant des microthrombi secondaires à l'ischémie (Figure 18).

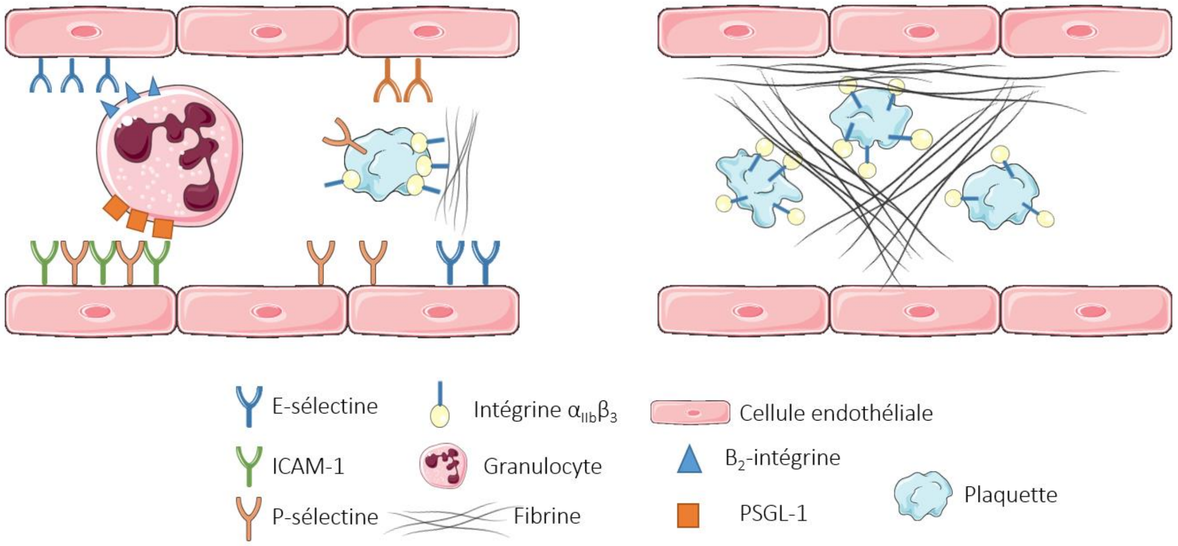

**Figure 18 Réponse microvasculaire après occlusion de l'ACM.**
Les leucocytes polymorphonucléaires vont adhérer à l'endothélium par liaison aux molécules d'adhésion (VCAM-1, P-sélectine), puis transmigrer à travers les cellules endothéliales (A). La formation de fibrine et d'agrégats fibrine-plaquettes contribue au phénomène de « no-reflow » après occlusion de l'ACM (B). (Adaptation de del Zoppo *et al.*, 2003).

L'étude de la microthrombose est particulièrement étendue dans les pathologies cardiaques. Le terme de *no-reflow* décrit par ailleurs le manque de reperfusion après traitement dans l'ischémie du myocarde et peut atteindre 40% des patients traités (Chettibi *et al.*, 2015). La formation de microthrombi dans la microcirculation cardiaque est associée au phénomène de *no-reflow,* entrainant des nécroses focales du muscle et a donc un rôle important dans la pathologie de l'ischémie du myocarde (Bekkers *et al.*, 2010). Ces resultats laissent supposer que le *no-reflow* est un phénomène sous-évalué dans l'ischémie cérébrale et nécessite de plus amples investigations.

### 1.6.2 Conséquences pathologiques de la microthrombose

Des microlésions cérébrales ont été retrouvées dans les autopsie de patients atteints de démences. Ainsi, plusieurs études neuropathologiques ont permis de déterminer que la quantité de microlésions observées en autopsie par coloration histologique (hématoxyline et éosine) était plus élevée chez les patients atteints de démences et de déficits cognitifs mesurés par une échelle clinique, la Clinical Dementia Rating (CDR) (Smith *et al.*, 2012).

Une reperfusion incomplète des microvaisseaux, dû à la présence de microthrombi, est en outre associée à une lésion de taille supérieure (Soares *et al.*, 2010). Dans une étude de Gratz *et al.*, l'imagerie IRM de susceptibilité pondérée a permis d'identifier la présence de microthrombi chez une partie des patients avant traitement, et a montré que celle-ci induit un pronostic plus défavorable à 3 mois que les patients sans microthrombose (Gratz *et al.*, 2015).

D'autre part l'installation d'une microlésion peut avoir un impact sur les fibres nerveuses de la matière blanche à proximité (van Veluw *et al.*, 2017), ce qui engendre des déficits cognitifs à long terme (Figure 19).

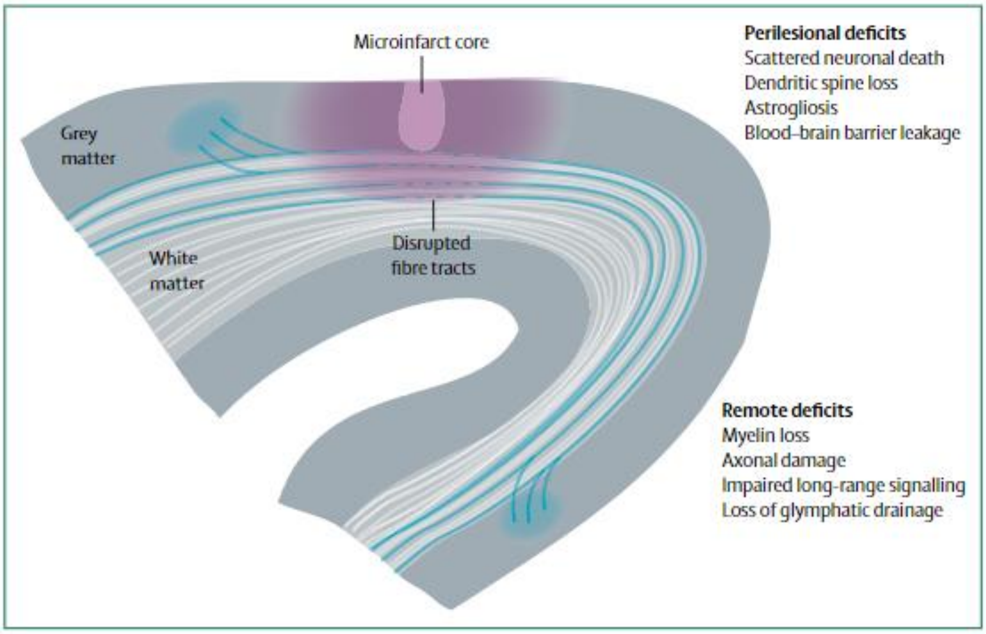

**Figure 19 Les microlésions corticales endommagent les fibres nerveuses, à l'origine de déficits cognitifs.**
D'après (van Veluw *et al.*, 2017)

Ainsi la reperfusion est un meilleur indice de diminution de la lésion ischémique que la recanalisation. Or, la reperfusion de la microcirculation dans la zone de pénombre ischémique varie en fonction de la circulation collatérale. Celle-ci assure l'apport en oxygène et en métabolites au niveau de la zone ischemiée mais la présence d'artères collatérales varie d'une personne à l'autre (Leng *et al.*, 2016).

**Figure 20 Impact des collatérales et du niveau de reperfusion sur le pronostic fonctionnel.** Dans l'ischémie cérébrale, la viabilité du tissu et les séquelles cognitives vont dépendre de la restauration de la perfusion des capillaires et de la perfusion dû aux artères collatérales. (Soares *et al.*, 2009)

C'est pourquoi chez les patients présentant une reperfusion incomplète après traitement, certains montrent un meilleur pronostic fonctionnel à 3 mois, grâce à la présence de nombreuses artères collatérales qui viennent irriguer la zone de pénombre (Figure 20).

De manière générale, la raison pour laquelle une reperfusion incomplète est associée à un mauvais pronostic peut s'expliquer par les mécanismes cellulaires qui se mettent en place pour réagir à l'hypoperfusion. L'hypoperfusion cérébrale entraine la production excessive de radicaux oxygénés, un stress oxydatif qui entraine à son tour une perturbation de la BHE et la détérioration des cellules endothéliales de la microcirculation (Yu *et al.*, 2017). Or ces dommages créés au niveau de la BHE ont pour conséquence l'infiltration leucocytaire, l'activation plaquettaire, activation des facteurs du complément, et rupture de la BHE qui mène à la formation d'un œdème ou à l'hémorragie (Figure 21).

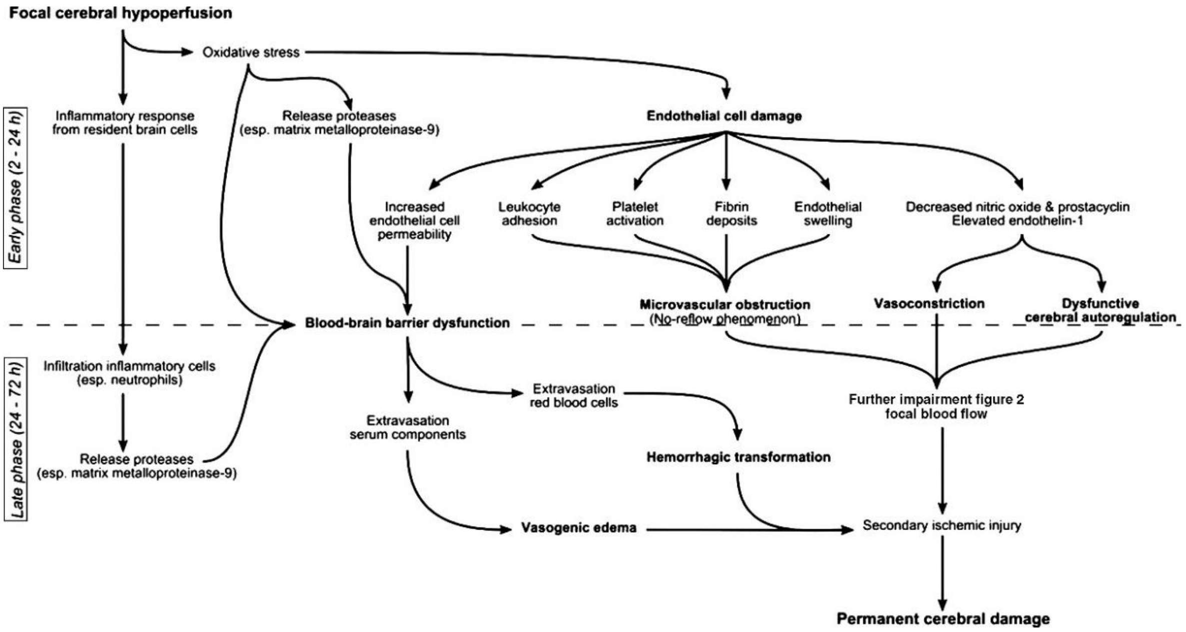

**Figure 21 Représentation des évènements suivant une hypoperfusion lors d'un AVC ischémique et conséquences sur la microcirculation.**
D'après (Brouns and De Deyn, 2009)

Ainsi, toutes ces réactions cellulaires sont de potentiels cibles pour le traitement de la microthrombose vasculaire.

### 1.6.3 Traitements de la microthrombose

L'activation des plaquettes joue un rôle important dans le phénomène de *no-reflow*. Le traitement par antiagrégants plaquettaires a été testé en préclinique pour le traitement de la microthrombose distale (Ye *et al.*, 2010). Or, même si ce traitement permet une meilleure reperfusion des artères distales, ce qui représente un espoir pour le traitement en clinique, le risque de transformations hémorragiques est trop important.

Une publication de El Amki *et al.*, parue en 2020 montre le rôle des neutrophiles dans microthrombose vasculaire. En effet, dans un modèle d'ischémie par insertion puis retrait d'un filament au niveau de l'artère cérébrale moyenne, l'occlusion secondaire à la recanalisation est induite à 75 % par les neutrophiles dans le cœur ischémique, et 60 % dans la pénombre ischémique. L'utilisation anti-Ly6G, traitement qui entraine la déplétion des neutrophiles, a eu pour conséquence une meilleure reperfusion de la microcirculation, après recanalisation.

Pour toutes ces raisons, il est nécessaire de diagnostiquer la microthrombose après un AVC, afin de pouvoir traiter au mieux les patients et possiblement diminuer les conséquences qu'elle engendre à court et long termes.

# 2. Imagerie de la thrombose dans l'AVC

Le diagnostic fiable de l'AVC ischémique repose en priorité sur l'imagerie par scanner et/ou IRM. La HAS recommande l'utilisation de l'IRM au possible ou, à défaut, un scanner cérébral.

Dans ce chapitre, les différentes techniques d'imagerie de l'AVC ischémique sont décrites, en évoquant les principaux paramètres permettant de visualiser les thromboses vasculaires. Dans un second temps, les différents agents de contraste utilisés en IRM seront développés, ainsi que leur rôle dans l'imagerie moléculaire.

## 2.1 Techniques d'imagerie

### 2.1.1 Artériographie

L'artériographie, aussi appelée angiographie cérébrale, est une technique développée depuis plus d'un siècle, reposant sur le principe de la radiographie. L'étude de la vascularisation cérébrale est possible après injection d'un agent de contraste iodé et permet d'observer les occlusions et sténoses artérielles (Figure 22). De plus, la méthode de soustraction digitale des images d'angiographie en temps réel est utilisée pour la surveillance de la recanalisation lors de traitements endovasculaires et/ou de la thrombolyse.

Mais l'artériographie est une technique invasive qui nécessite une sédation et l'injection intra-artérielle de l'agent de contraste, ce qui entraîne des complications de natures ischémiques dans 0.2% des cas (Kaufmann *et al.*, 2007). De plus, l'observation de la présence de microthrombi en aval de l'occlusion proximale est difficile en artériographie car elle nécessite que l'agent de contraste injecté passe le thrombus proximal en quantité suffisante, pour mettre en évidence les obstructions dans la microcirculation.

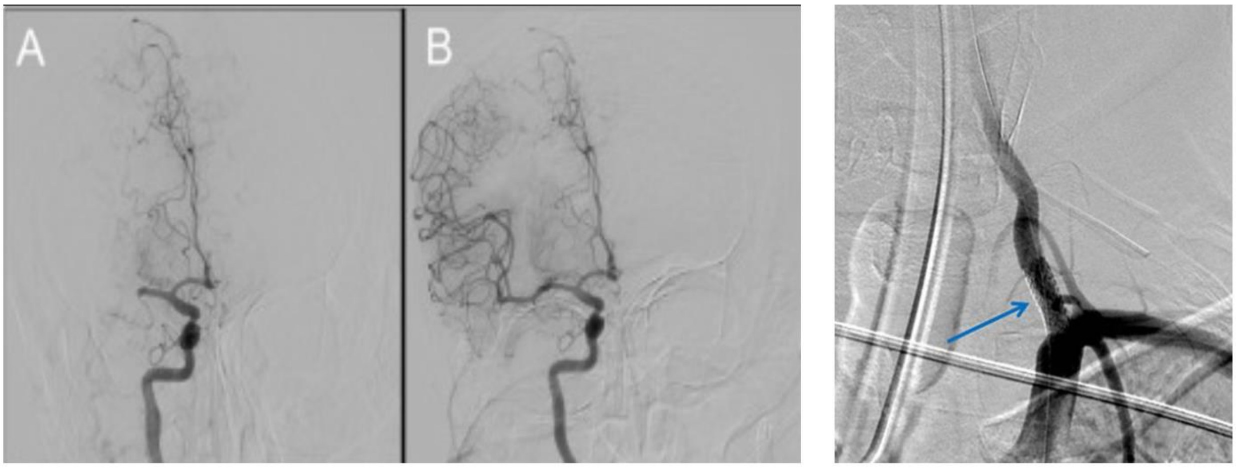

**Figure 22 Artériographie cérébrale d'un patient présentant une occlusion de ACM droite avant et après recanalisation de l'artère (A, B) et dispositif de thrombectomie visible en artériographie (droite).**
Images de Shimonaga *et al.*, 2020 (gauche) et Evans *et al.*, 2017 (droite).

### 2.1.2 Doppler transcrânien

Le doppler transcrânien est souvent utilisé en complément du scanner et de l'IRM, ou lorsque ceux-ci ne sont pas disponibles. C'est un examen non-invasif, qui se fait généralement au lit du patient (Figure 23). Il peut être fait de façon répété et en temps réel. Le principe du doppler transcrânien repose sur l'envoi d'ultrasons à travers les différentes fenêtre crâniennes telles que la fenêtre temporale pour observer les branches proximales de l'ACM (Aaslid *et al.*, 1982). Il permet notamment la surveillance de la recanalisation dans les heures suivant un AVC ischémique (Burgin *et al.*, 2000). L'échelle de thrombolyse dans l'ischémie cérébrale (Thrombolysis in Brain Ischemia ou TIBI) pour le doppler transcrânien est utilisée pour le diagnostic d'occlusions et évaluer la recanalisation (Tsivgoulis *et al.*, 2013).

Le doppler transcrânien est d'ailleurs l'examen de référence pour l'observation en temps réel d'embolisation. Ainsi, des microemboli cérébrales peuvent apparaître au doppler chez les patients atteins des maladies cardio-vasculaires (Kargiotis *et al.*, 2019). Elle permet donc de diagnostiquer la présence de microemboli, ce qui permet notamment d'établir l'étiologie de l’AVC ischémique. Cependant, cette technique est limitée à l’étude des branches proximales des artères intracrâniennes et ne permet pas d’observer les microthrombi formés au niveau de la microcirculation.

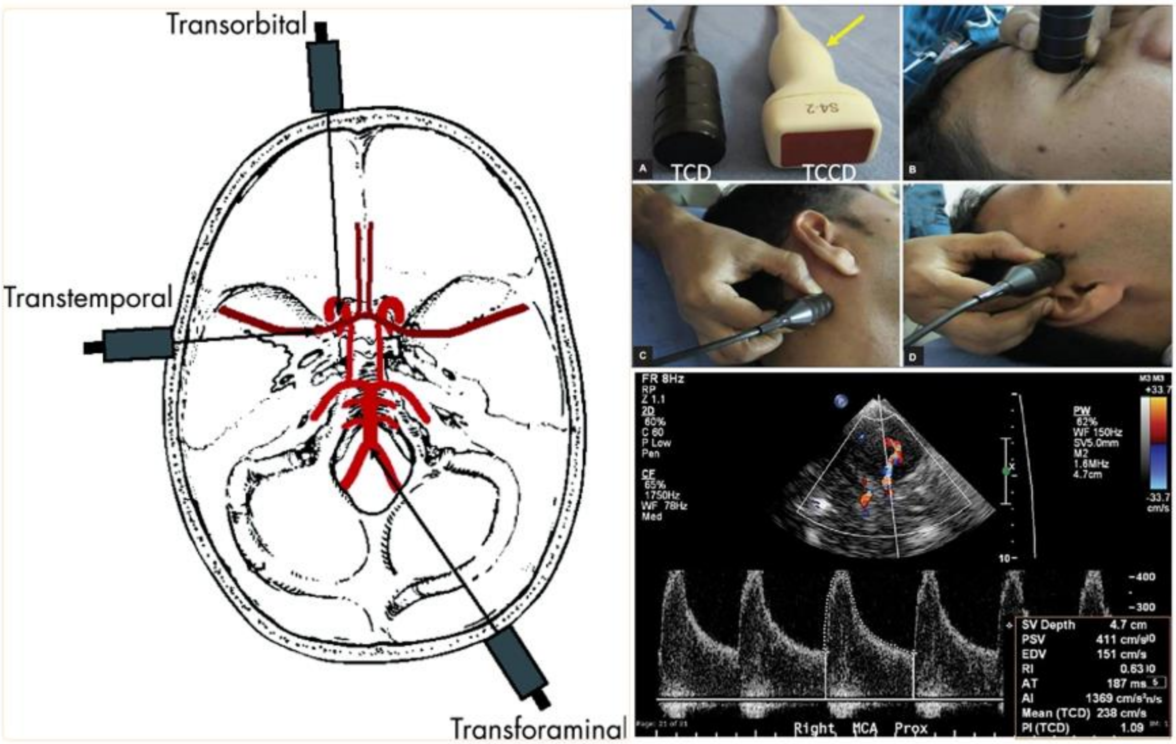

**Figure 23 Utilisation du doppler transcranien pour l’imagerie de l’AVC.**
Basée sur l’émission d’ultrasons, le doppler permet d’observer les signaux emboliques par les fenêtre trans-orbitales, trans-temporales et trans-foraminales du crâne. (Pan *et al.*, 2022)

### 2.1.3 Scanner

Lorsqu’un patient est amené aux urgences pour suspicion d’AVC, le scanner, aussi appelé tomodensitométrie (TDM), est l’examen de premier recours (Benjamin *et al.*, 2017), car c’est la technique d’imagerie la plus simple d’accès et qui offre des temps d’acquisition courts. C’est une technique multimodale dont le principe repose sur l’atténuation des rayons X envoyés par les tissus, elle est donc quantitative et la mesure du signal se fait en Unité Hounsfield (UH). On distingue la TDM sans injection d’agents de contraste, l’angioscanner, et le scanner de perfusion.

- **Scanner sans injection d’agents de contraste**

Le scanner sans injection permet rapidement de distinguer si l’AVC est de nature ischémique ou hémorragique (Figure 24). Un AVC hémorragique est caractérisé par une hyperdensité de l’hématome intra ou extra-cérébral, dû à la grande quantité de protéines contenues dans l’hématome (Merino and Warach, 2010). Alors que les artères occluses apparaissent hyperdenses (Barber *et al.*, 2001), l’AVC ischémique en phase aigüe va se caractériser au scanner par des hypodensités corticales (zone ischémique). En effet, l’œdème cytotoxique formé à un temps très précoce de l’AVC est produit par une entrée d’eau intracellulaire, après défaillance des canaux ioniques des cellules (Dzialowski *et al.*, 2004). Ce déplacement du liquide du compartiment intravasculaire vers le compartiment parenchymateux, réduit la densité du tissu, ce qui se traduit par la perte d’atténuation des rayons X, soit une hypodensité au scanner.

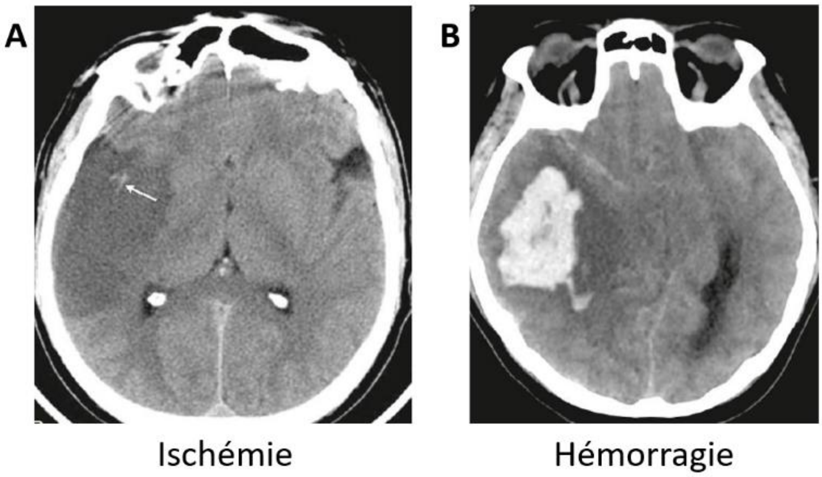

**Figure 24 Scanner sans injection démontrant une ischémie cérébrale (A) et une hémorragie cérébrale (B), avec hyperdensités de la MCA (flèche blanche).**
Images du livre Imagerie médicale et radiologique, 2015

D’autre part, les artères qui apparaissent en hyperdensité démontrent la présence d’un thrombus intraluminal. Leur détection va dépendre de la composition du thrombus, plus ou moins riche en érythrocytes (Viltuznik *et al.*, 2021). Les transformations hémorragiques après ischémie sont également visibles en hyperdensité. L’évaluation de la sévérité de l’ischémie observée au scanner repose sur un score : l’Alberta Stroke Program CT Scale (ASPECTS), qui augmente en fonction du nombre de territoires tissulaires lésés (Figure 25). Cette échelle est utilisée pour standardiser l'évaluation de l'étendue des lésions.

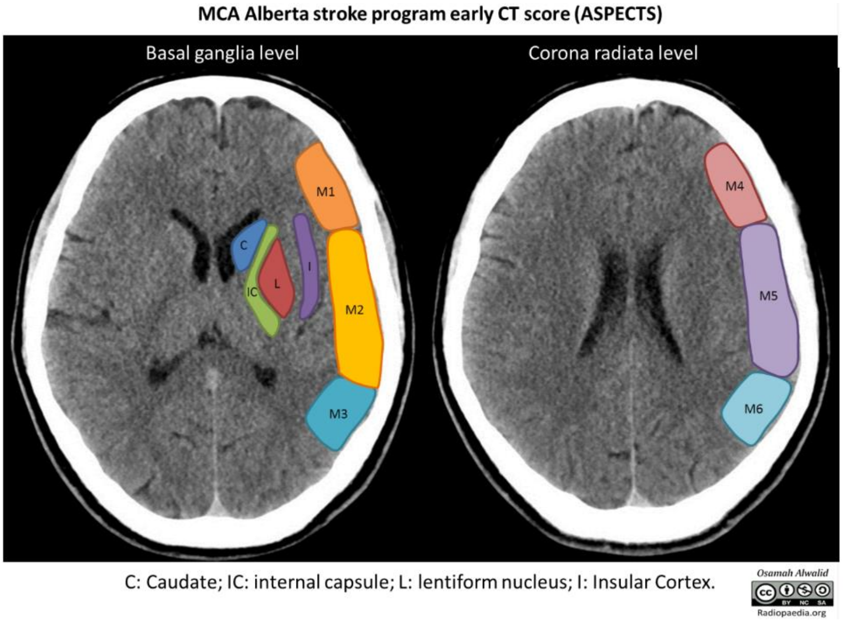

**Figure 25 Représentation de différents territoires artériels utilisés pour déterminer le score ASPECTS.**
Plus le score est élevé, plus la lésion est étendue. (Dr Osamah A. A. Alwalid, Radiopaedia.org)

- **Angioscanner**

L'angioscanner consiste en l'injection d'un agent de contraste iodé en bolus pour visualiser la vascularisation depuis l'aorte jusqu'aux branches cérébrales distales des artères intracrâniennes (Pomerantz *et al.*, 2006). Il possède une très bonne résolution spatiale, supérieure à beaucoup de séquence d'angiographie IRM. La présence d'un thrombus est identifiée par l'interruption de la progression du produit de contraste dans la vascularisation en aval (Figure 26). Cela permet de localiser précisément le caillot mais également de déterminer si le caillot est occlusif ou non (Lubezky *et al.*, 1998). Par ailleurs, lorsque l'occlusion est établie, et qu'un traitement thrombolytique ou endovasculaire est possible, l'angioscanner pré et post-traitement témoigne d'une recanalisation réussie ou non (Figure 26).

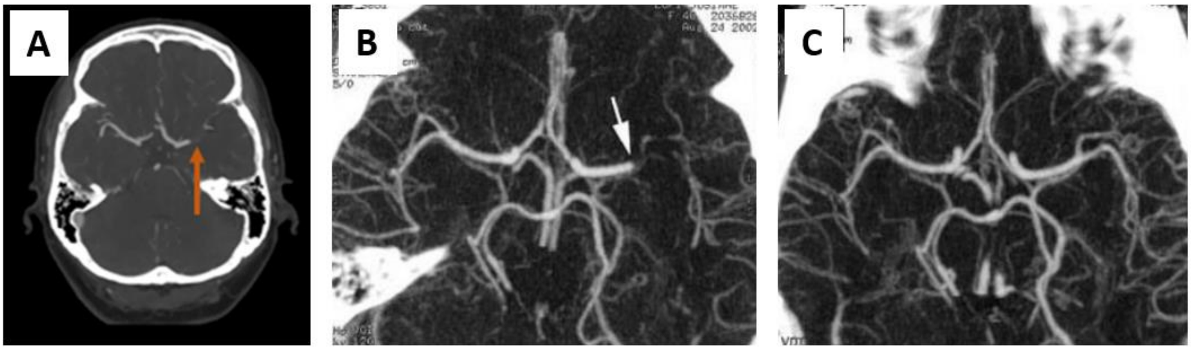

**Figure 26 Angioscanner.**
Angioscanner d'un patient avec occlusion de l'ACM gauche (A). Images avant (B) et après (C) recanalisation de l'artère. (Ledezma and Wintermark, 2009)

- **Le scanner de perfusion**

Le scanner de perfusion est une technique quantitative de traçage de la cinétique d'un agent de contraste, similaire à l'angioscanner. Les images de perfusion sont acquises après injection intraveineuse d'un agent de contraste iodé, de façon dynamique. Le niveau de rehaussement des tissus, associé à la concentration d'agent de contraste injecté et des données de perfusion artérielle, donnent la possibilité d'établir de façon quantitative des cartes de perfusion cérébrale (Wintermark *et al.*, 2006). Ces cartes sont construites en analysant différents paramètres de la perfusion (Figure 27, 28) : le débit sanguin cérébral (CBF), le volume sanguin cérébral (CBV) , le *mean transit time* (MTT ou temps moyen de transit), le *time to peak* (TTP ou temps pour arriver au signal maximal avec le produit de contraste) ou encore le *time to maximum* (Tmax ou temps au maximum de la fonction résiduelle).

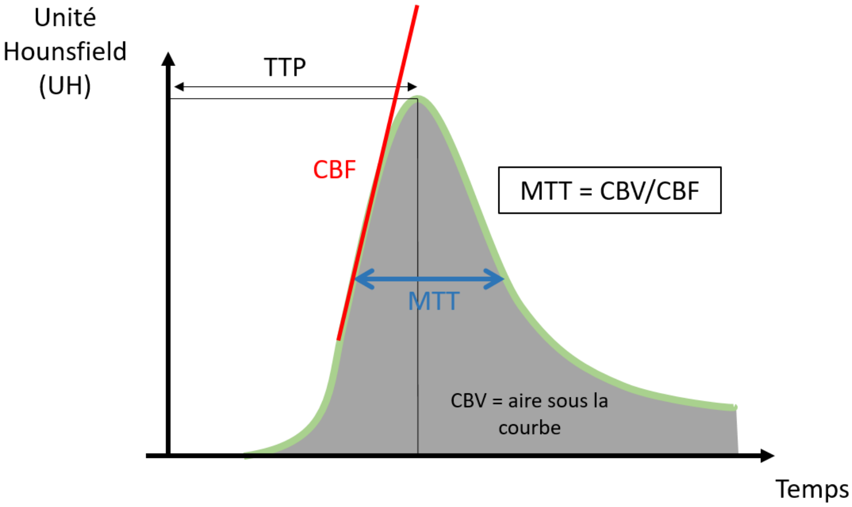

**Figure 27 Paramètres de perfusion calculés après injection du produit de contraste.** L'imagerie de perfusion permet d'obtenir d'important paramètres hémodynamiques, comme le TTP, MTT, CBV et CBF. Modifié de radiopaedia.org

Le scanner de perfusion met en évidence les zones d'hypoperfusion cérébrale, par comparaison de la réduction du flux sanguin cérébral (CBF) et des zones hypoperfusées révélées avec le paramètre Tmax. On appelle cette différence entre le Tmax et le CBF le *mismatch*. Il correspond à la zone de pénombre ischémique, zone qui peut encore être sauvée si la perfusion est rétablie par traitement thrombolytique ou thrombectomie. Cette technique d'imagerie a notamment permis d'élargir les critères d'éligibilité pour la thrombectomie, en mettant en évidence les bénéfices d'une thrombectomie pour sauver la zone de pénombre (Albers *et al.*, 2018).

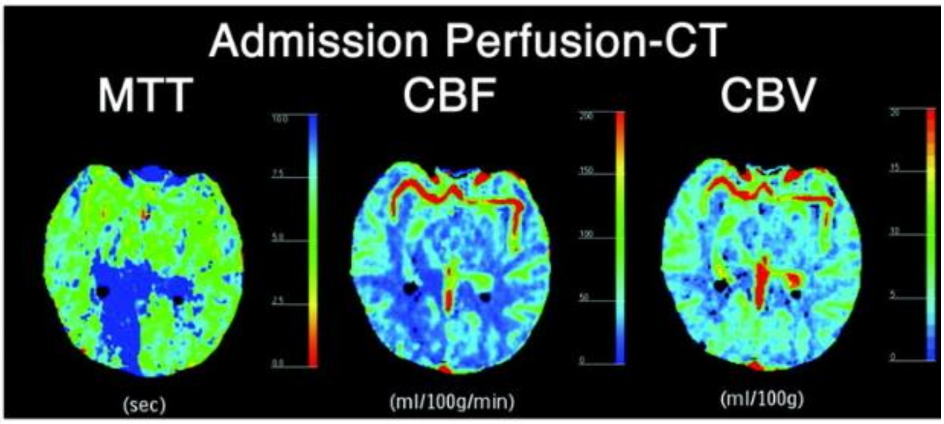

**Figure 28 Cartes de perfusions cérébrales de patients admis pour un AVC ischémique.** D'après (Wintermark *et al.*, 2006)

Cependant, l'utilisation du scanner a montré quelques limitations dans la visualisation des lésions ischémiques à un temps aigüe (< 6 heures). L'apport de l'IRM, et particulièrement la séquence de diffusion IRM, présente une plus grande sensibilité pour visualiser la lésion de moins de 6 heures.

### 2.1.4 IRM

L'IRM est l'examen recommandé en cas de suspicion d'AVC, lorsque cela est possible (Haute Autorité de la Santé). Elle permet dans l'AVC ischémique de détecter la localisation, la taille et l'étendue de l'ischémie, ainsi que l'identification les tissus hypoperfusés. Le protocole d'imagerie IRM pour suspicion d'AVC ischémique comprend généralement l'imagerie pondérée en diffusion (diffusion weighted imaging ou DWI), imagerie par écho de gradient, imagerie pondérée en T2 avec inversion-récupération (Fluid Attenuated Inversion Recovery ou FLAIR), et l'angiographie par résonance magnétique (MRA).

- **IRM de diffusion**

La séquence IRM pondérée en diffusion permet un diagnostic sensible des lésions d'apparitions récentes. Dans les premières minutes de l'AVC, l'hypoperfusion après l'occlusion du vaisseau entraîne une perturbation des pompes ioniques présentes à la surface des cellules neuronales. Il y a alors une augmentation du liquide intracellulaire et diminution du liquide extracellulaire. Les molécules d'eau présentes dans l'espace extracellulaire ne diffusent plus aussi librement. Or, la séquence de diffusion est sensible aux mouvements des protons et donc des molécules d'eau (Figure 29). Elle est ainsi particulièrement utilisée pour révéler l'œdème cytotoxique après l'occlusion, à des temps très courts après l'occlusion. Elle peut également montrer les premiers évènements lors d'un AIT (Awad *et al.*, 1986).

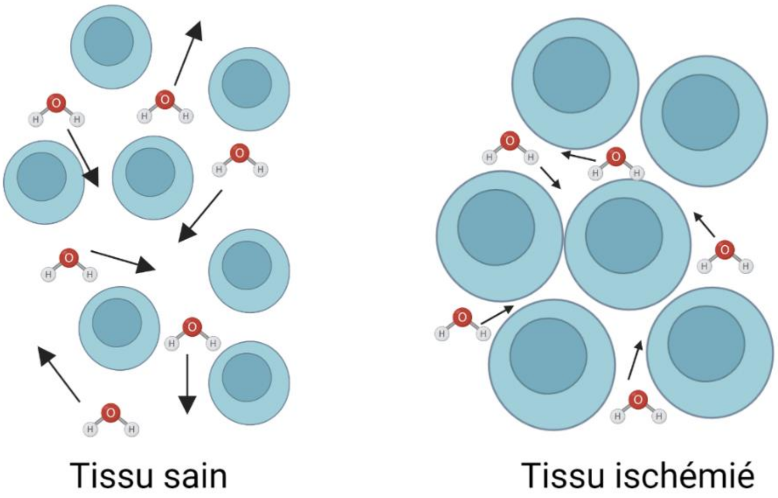

**Figure 29 Principe de l'imagerie de diffusion.**
Les molécules d'eau diffusent librement dans l'espace extracellulaire dans un tissu sain. Cette diffusion est limitée dans un tissu ischémié. La réduction des mouvements des molécules d'eau est le phénomène observé en IRM de diffusion.

L 'IRM de diffusion permet de calculer un paramètre appelé coefficient apparent de diffusion (Apparent Diffusion Coefficient ou ADC). Les lésions ischémiques observées en séquence pondérée en diffusion apparaitront hyperintenses et les hypointenses sur les cartes ADC (Figure 30).

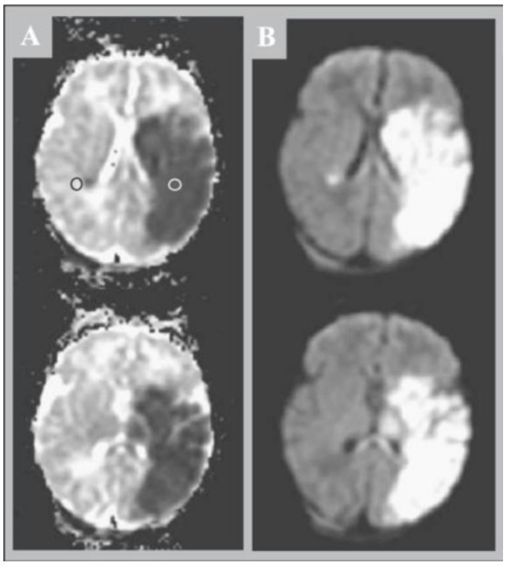

**Figure 30 Carte ADC avec hyposignaux dans la zone ischémiée (A) et IRM de diffusion montrant la zone ischémiée en hypersignal (B).**
(Seghier *et al.*, 2004)

- **IRM de perfusion**

La séquence IRM pondérée en perfusion étudie les paramètres hémodynamiques cérébraux. Le principe de l'IRM de perfusion est l'acquisition dynamique d'images, pendant 60 secondes environ, immédiatement après l'injection d'un agent de contraste en bolus. Lorsque l'agent de contraste parvient au cerveau, il fait chuter le signal. Une perturbation de l'hémodynamique du tissu cérébral sera alors visible dans le cas d'un AVC ischémique. L'imagerie pondérée en perfusion, couplée à l'IRM de diffusion, permet d'évaluer la zone de pénombre via la différence entre les deux (*mismatch*) qui, comme expliqué précédemment, correspond aux zones de tissu parenchymateux qui peuvent être sauvés. Cette analyse a un intérêt dans la sélection des patients pour lesquels un traitement par thrombectomie et/ou thrombolyse serait bénéfique (Heiss, 2011).

- **IRM d'inversion-récupération FLAIR (T2)**

C'est une séquence pondérée en T2 dans laquelle les signaux liquidiens sont supprimés. Ainsi, le signal provenant du liquide céphalo-rachidien (LCR), qui apparaît normalement en hypersignal en séquence pondérée en T2, est atténué pour apparaître en hyposignal. Les artères apparaissent en séquence FLAIR avec une faible intensité, similaire à l'intensité du LCR. Lors d'un accident vasculaire à la phase hyperaigüe, les vaisseaux impactés peuvent apparaître en hypersignal. D'autre part, les tissus cérébraux ischémiés apparaissent en hyposignal environ 6 heures après l'occlusion (Sorensen *et al.*, 1996). Ainsi, les disparités entre l'hypersignal visible en IRM de diffusion et l'hyposignal apparaissant en séquence FLAIR donnent une estimation du temps écoulé depuis l'occlusion (Thomalla *et al.*, 2011, Figure 31).

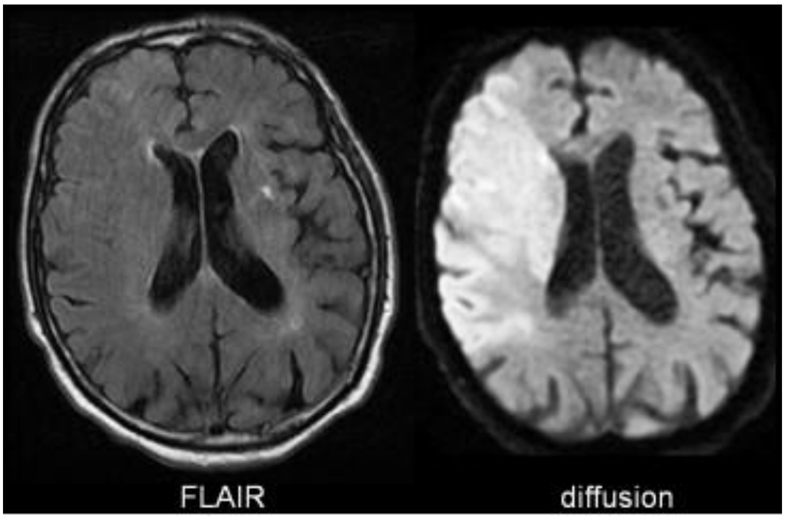

**Figure 31 Séquences FLAIR et de diffusion.**

Une ischémie est visible sur la séquence de diffusion, mais pas sur la séquence FLAIR. Ces images sont caractéristiques d'une lésion datant de moins de 4,5 heures. (Tisserand *et al.*, 2014)

De plus, elle peut mettre en évidence la perte d'étanchéité de la BHE, après injection d'un chélate de gadolinium qui va passer au travers de celle-ci (Lee *et al.*, 2016). Or, ce phénomène est prédicateur d'un risque hémorragique pour les patients traités par thrombolyse.

- **Angio-IRM**

L'angio-IRM est utilisée pour observer la vascularisation et la présence d'une occlusion, d'une sténose ou encore d'une dissection des vaisseaux cérébraux. On distingue l'angio-IRM avec injection d'agent de contraste (Contrast-Enhanced MRA), et l'angio-IRM par temps de vol (Time Of Flight ou TOF-MRA). La TOF-MRA, sans injection de produit de contraste, utilise la direction et vélocité du flux sanguin pour observer la vascularisation cérébrale (Figure 32). Cette dernière présente des limitations car elle ne permet pas de voir les artères dont le niveau de perfusion est fortement diminué, et peut induire un faux diagnostic d'occlusion de l'artère. C'est pourquoi l'angio-IRM avec injection de produit de contraste est le plus souvent utilisée pour évaluer la circulation cérébrale après un AVC. L'échelle « Thrombolysis in Cerebral Infarction » (TICI) permet de standardiser l'évaluation de cette perfusion après traitement (Higashida and Furlan, 2003).

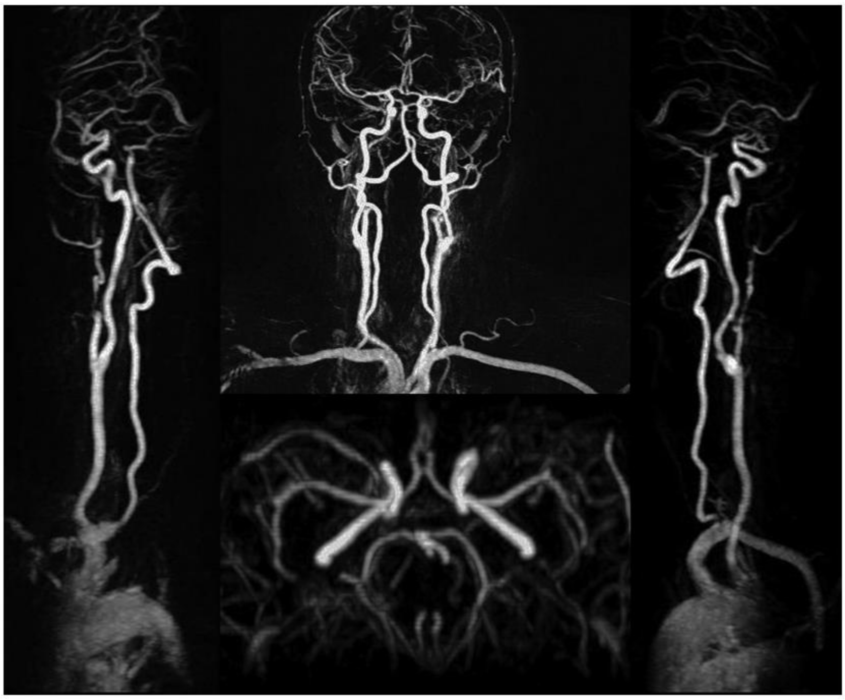

**Figure 32 Images sous différents axes du système cardiovasculaire par angio-IRM** (González, 2017)

- **IRM pondérée en écho de gradient (T2*)**

La séquence pondérée en écho de gradient permet de discriminer les ischémies et les hémorragies. Cette séquence est pondérée en T2*, elle est donc sensible aux inhomogénéités de champs magnétiques locaux induits par la présence de fer dans le sang (Hayman *et al.*, 1991). De cette façon les hémorragies vont apparaître sous forme d'hyposignaux et il est donc facile de différencier AVC ischémiques et AVC hémorragiques (Figure 33). Cette séquence peut révéler les thrombi intraluminaux en raison de leur composition riche en désoxyhémoglobine paramagnétique (visibles en hyposignal en pondération T2*). Par ailleurs, l'utilisation d'agent de contraste dits « ferromagnétiques », composés de fer, offre de nombreuses possibilités dans l'imagerie biomédicale pour le ciblage moléculaire (voir 2.2.2 Imagerie moléculaire).

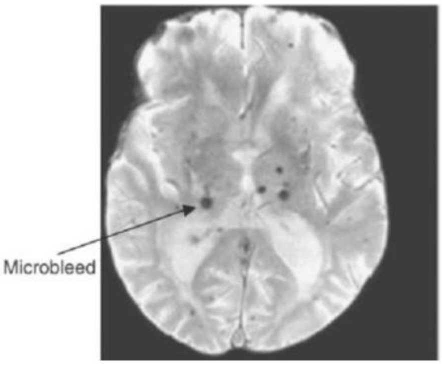

**Figure 33 Image pondérée en écho de gradient d'un patient avec microhémorragies cérébrales.**
(Li *et al.*, 2018)

- **IRM pondérée de susceptibilité**

C'est également une séquence pondérée en T2*. Les images sont produites en accentuant les différences de susceptibilité magnétique (Figure 34). Sa haute sensibilité pour diagnostiquer la présence de thrombus permet d'observer la présence de thrombi plus distaux dans les artères cérébrales et d'étudier leurs conséquences sur le devenir du patient (Gratz *et al.*, 2015).

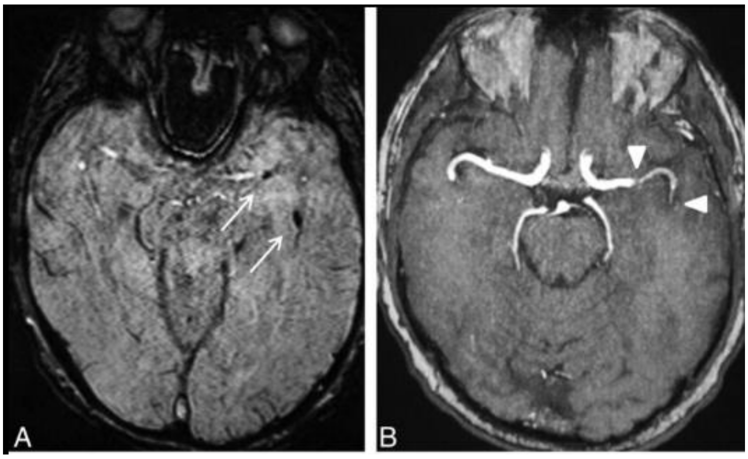

**Figure 34 Imagerie de susceptibilité magnétique.**
Les images montrent les signaux de susceptibilité du vaisseau au niveau du segment M1-M2 de l'ACM (A). L'angio-IRM confirme la diminution de la perfusion distale du site d'occlusion (B). (Gratz *et al.*, 2015)

L'IRM est une technique de choix pour l'observation des microlésions et les évènements microvasculaires, notamment par les séquences pondérées en diffusion et de susceptibilité magnétique (T2*) qui permettent d'observer des évènements microvasculaires de l'orde du millimètre. Cependant, il reste difficile de distinguer la présence de microthrombi d'autres évènements microvasculaires tels que les microhémorragies, et des signaux physiologiques comme les espaces périvasculaires et les vaisseaux sanguins (Figure 35 ; van Veluw *et al.*, 2017). Par conséquent, l'utilisation d'une technique permettant le ciblage spécifique des évenements microvasculaires, l'imagerie moléculaire, serait plus appropriée.

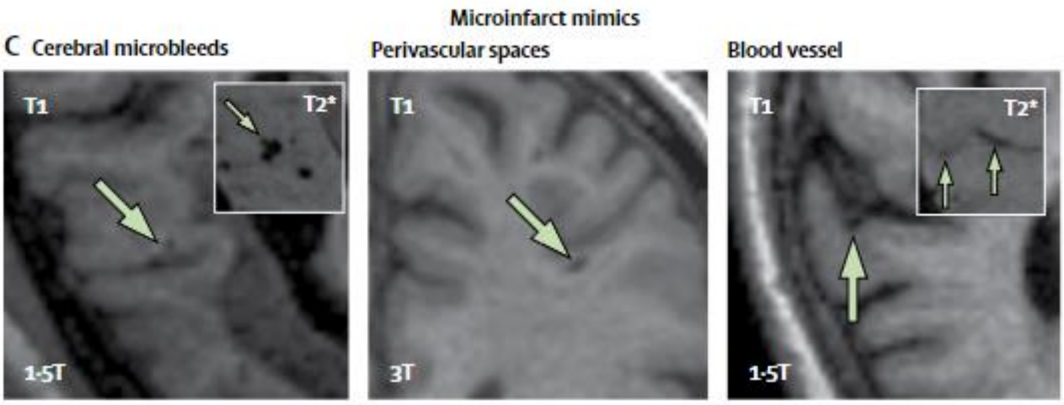

**Figure 35 Signaux physiologiques ressemblants à la microthrombose. Microhémorragies (A), Espaces périvasculaires (B), Vaisseaux sanguins (C).**

Extrait de (van Veluw *et al.*, 2017).

## 2.2 Imagerie moléculaire et agents de contraste IRM

### 2.2.1 Imagerie moléculaire

L'imagerie moléculaire a été développée tout d'abord en médecine nucléaire par Tomographie par Emission de Positons (TEP). La TEP est une technique d'imagerie qui nécessite l'utilisation d'agents de contrastes radiomarqués (radiopharmaceutiques). Les rayonnements utilisés en TEP proviennent de la désintégration de l'isotope radioactif injecté qui conduira à l'émission de deux photons gamma dans deux directions opposées (Figure 36), c'est la détection en coïncidence de ces deux photons qui permet de localiser l'origine du signal et permet d'étudier de façon quantitative différents processus physiopathologiques.

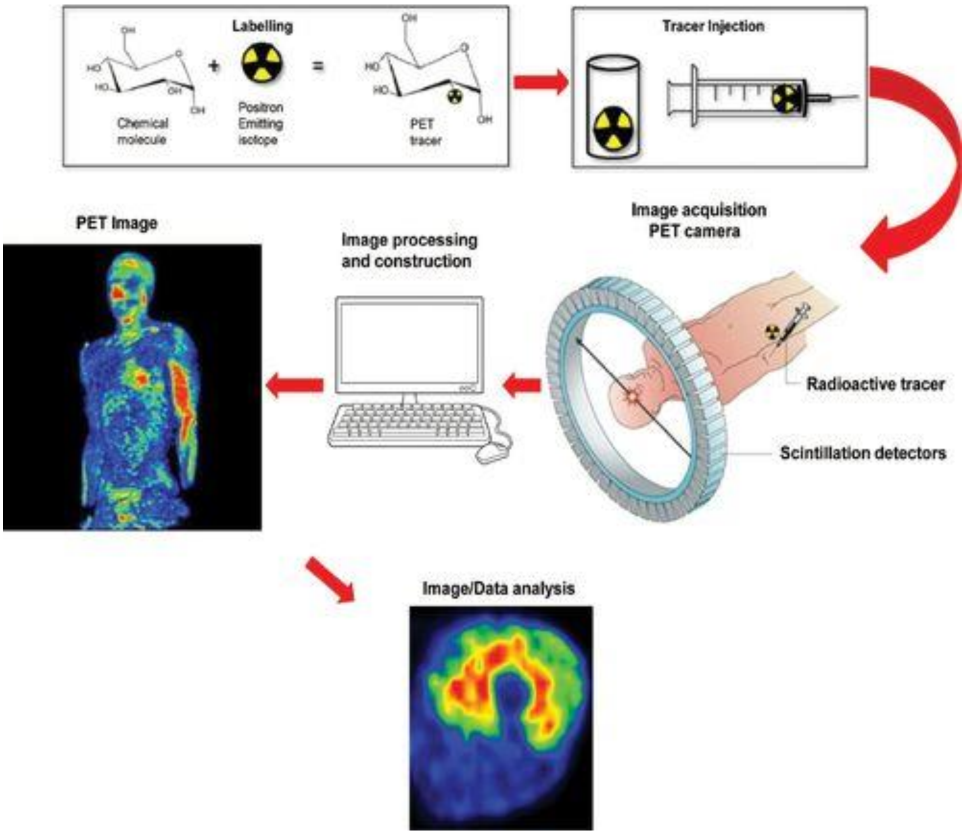

**Figure 36 Principe de la Tomographie par Emission de Positons**
(Rudroff *et al.*, 2015)

De façon classique, les isotopes radioactifs sont greffés à une protéine d'intérêt, afin d'observer un processus physiologique ou pathologique en particulier. L'exemple le plus commun est l'utilisation du Fluor 18 ($^{18}$F, isotope radioactif) inséré dans une molécule de glucose, formant le fluoro-déoxyglucose marqué au fluor 18 ($^{18}$FDG) et synthétisé à la fin des années 1970 (Reivich *et al.*, 1979). L'injection du $^{18}$FDG met en évidence les cellules tumorales dans le corps, grâce à leur grande consommation en glucose.

La TEP est également utilisée pour l'exploration dans les pathologies cérébrales (Figure 37): la perfusion cérébrale, la consommation métabolique ou encore la neurotransmission noradrénergique (Guedj, 2018). Et d'autres complexes formés avec des isotopes radioactifs ont par la suite été développés pour le ciblage direct de molécules. C'est le cas du radiotraceur composé B de Pittsburg marqué au Carbone 11 (carbon-11-labelled Pittsburgh compound B ou $^{11}$C-PiB) qui se fixe aux dépôts fibrillaires du peptide β-amyloïde, utilisés pour révéler les plaques amyloïdes dans la maladie d'Alzheimer (Rinne *et al.*, 2010; Figure ).

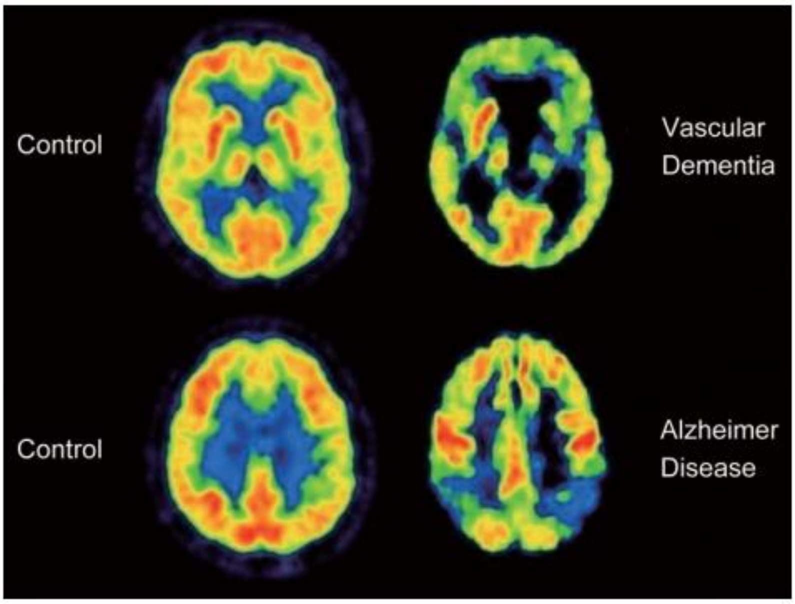

**Figure 37 Utilisation de la TEP dans différentes pathologies cérébrales.**
(Dreuille *et al.*, 2004).

La TEP reste la technique de choix pour l'imagerie moléculaire chez l'Homme et le petit animal, grâce à sa sensitivité et sa haute résolution temporelle. Cependant, l'utilisation de rayonnements ionisants, la faible résolution spatiale et la nécessité de synthétiser des radiopharmaceutiques peut freiner la généralisation de son utilisation en clinique, notamment pour des pathologies telles que l'AVC, qui nécessite une prise en charge dans l'urgence. Cependant, l'imagerie moléculaire n'est pas limitée à la TEP et de nombreuses avancées ont été faite dans le domaine de l'imagerie moléculaire IRM, destinées à une application clinique courante (Hengerer and Grimm, 2006). Elle reste pour l'instant, à l'état de recherche préclinique.

L'IRM présente de nombreux avantages pour l'imagerie moléculaire. C'est une technique non-ionisantes, avec une très haute résolution spatiale de l'ordre du millimètre en IRM clinique (1.5T et 3T) et jusqu'à 50 µm avec les IRM de haut champs magnétique (7T et 9T), et une grande profondeur de pénétration dans les tissus. Mais l'IRM a une sensibilité intrinsèque faible, c'est-à-dire qu'elle nécessite une amplification du signal ou l'utilisation de fortes concentrations d'agents de contraste (Gauberti *et al.*, 2018).

La visualisation de cibles moléculaires impliquées dans les processus pathologiques de l'AVC nécessitera donc l'utilisation d'agents de contraste en IRM. En résumé, ces agents de contraste modifie le temps de relaxation des protons tissulaires, c'est leur interaction avec ceux-ci qui modifie le signal IRM (Figure 38). Il existe différents types d'agents de contraste utilisés classiquement en IRM : les paramagnétiques (rehaussement du signal) et superparamagnétiques (diminution du signal).

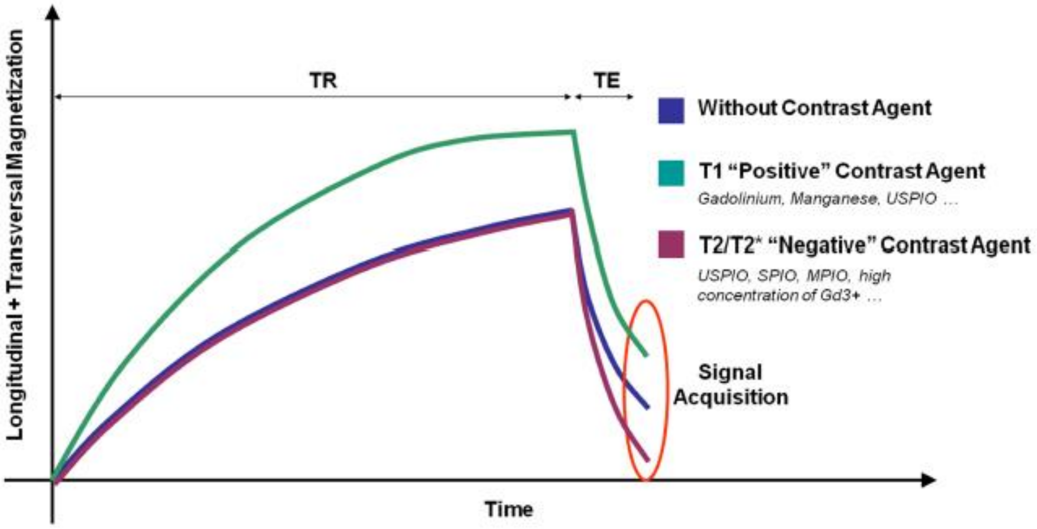

**Figure 38 Effets de relaxation des paramètres T1 et T2 en IRM par les différents types d'agents de contraste.**
D'après (Gauberti *et al.*, 2014)

### 2.2.2 Agents de contraste paramagnétiques

Les agents de contrastes paramagnétiques agissent en diminuant le temps de relaxation, en T1, des noyaux d'hydrogène de l'eau présents à proximité. Ils sont également appelés agents de contraste « positifs » car ils entrainent le rehaussement du signal pondéré en T1. L'utilisation d'agents de contraste paramagnétiques est courante en clinique et ils se composent de métaux lourds, dont le principal utilisé est le gadolinium ($Gd^{3+}$). Le gadolinium appartient à la famille d'éléments chimiques des lanthanides. Sous sa forme ionique libre, il est hautement toxique pour l'organisme et n'est pas administrable à l'Homme. Il est nécessaire de séquestrer les ions $Gd^{3+}$ dans des molécules ligands, les polyaminocarboxylates linéaires ou macrocycliques, pour être ainsi injecté en imagerie sous formes de **chélates de gadolinium**.

Les chélates de gadolinium sont les plus courant en IRM, et sont utilisés dans environ 27 % des examens IRM (Rasschaert, 2019). Leur application principale se fait par injection intraveineuse, pour rehausser le signal au niveau des artères et des veines (Figure 39).

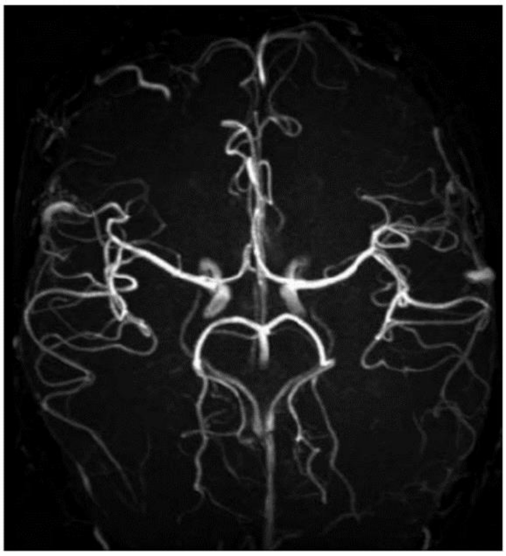

**Figure 39 Amélioration du signal IRM par injection de gadolinium pour obsrever la vascularisation cérébrale.**
D'après (Ozsarlak *et al.*, 2004)

En IRM moléculaire, des nanoparticules de perfluoro-carbone contenant de grandes quantité de gadolinium et fonctionnalisées avec un ligand pour la fibrine ont été synthétisés pour le marquage spécifique des microthrombi formés à la surface de plaques d'athérosclérose (Flacke *et al.*, 2001). Une équipe de recherche a également synthétisé un agent de contraste basé sur les chélates de gadolinium, pour l'IRM moléculaire des thrombi, en ciblant la fibrine (Overoye-Chan *et al.*, 2008; Uppal *et al.*, 2010; Figure 40). Néanmoins, ces techniques d'IRM moléculaire du thrombus ne présentent pas la sensibilité nécessaire pour observer de plus petits évenements vasculaires comme la microthrombose, et nécessiterait d'augmenter les doses injectées.

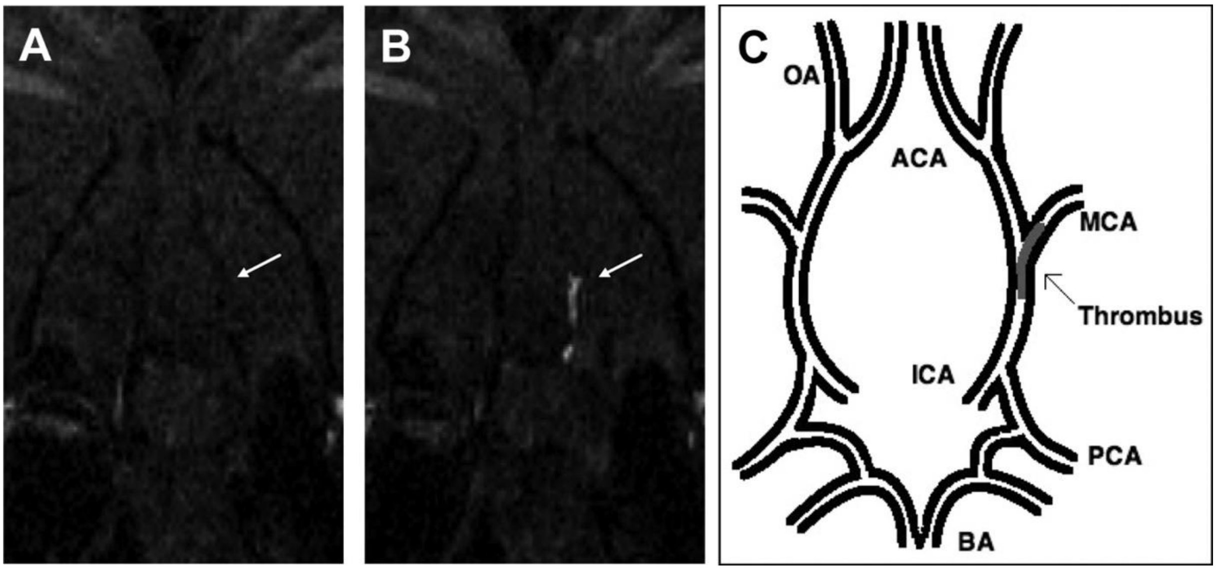

**Figure 40 Observation à l'IRM de la thrombose dans un modèle animal d'AVC, après injection d'un agent de contraste paramagnétiques ciblant la fibrine.**
D'après (Uppal *et al.*, 2010)

Les chélates de Gadolinium ont longtemps été considérés comme un agent de contraste pour l'IRM sûr et sans danger. Mais en 2006, plusieurs études ont mis en relation l'apparition de scléroses cutanées appelée fibrose systémique néphrogénique chez les patients dialysés et les insuffisants rénaux et hépatiques (Marckmann *et al.*, 2006; Rogosnitzky and Branch, 2016). Plus récemment, il a également été mis en évidence l'accumulation de gadolinium dans le foie, les os, la peau et le tissu cérébral, après des injections répétées chez les patients sans dysfonction rénale (Kanda *et al.*, 2015). Bien que le mécansime responsable de cette accumulation ne soit pas encore bien identifié, il est supposé que l'accumulation soient dû à une « déchélation » des complexes de gadolinium, moins stable sous leur forme linéaire que macrocycliques. A l'heure actuelle, seul les chélates de gadolinium macrocyclique sont encore utilisés chez l'Homme. Les chélates linéaires se sont vu retirer leur AMM par l'agence européenne des médicaments (EMA) en 2018. Ces résultats suscitent un regain d'intérêt pour la recherche d'agents de contraste alternatif pour un usage à l'IRM.

### 2.2.3 Agents de contraste superparamagnétiques

A l'inverse des agents de contraste paramagnétique, les superparamagnétiques diminuent le temps de relaxation des noyaux autours en T2. Ainsi, ils entrainent une diminution du signal en pondération T2 et T2*, ils sont dits « négatifs ».

Ils sont composés d'oxydes de fer ferreux (magnémite ; gamma-$Fe_2O_3$) et ferrique (magnétite ; $Fe_3O_4$). En fonction de leur taille, les nanoparticules peuvent être distinguées en *superparamagnetic iron oxide* (SPIO) et *ultrasmall superparamagnetic iron oxide* (USPIO). Leurs mécanismes d'élimination sont légèrement différents, car les SPIO sont éliminer par le système réticulo-endothélial (SRE) au niveau du foie et de la rate, et les USPIO se retrouvent pour une faible part dans les nœuds lymphatiques (Bourrinet *et al.*, 2006). Le seuil de détection des nanoparticules composées d'oxydes de fer est très bas car il sont très riche en fer (une particule de 10 à 20 nm contient 5000 atomes de fer (Wang *et al.*, 2001)). Ils présentent également d'autres caractéristiques intéressantes pour l'IRM moléculaire, comme de nombreuses méthodes de synthèse, avec des procédés de fabrication simples et peu coûteux.

Après injection des (U)SPIO dans la circulation, et leur capture par les macrophages du SRE, ils se retrouvent en majorité dans le foie et la rate. C'est ainsi que s'est développée leur utilisation en clinique pour observer des tumeurs hépatiques et spléniques (imperméable à l'entrée des SPIO) (Hamm *et al.*, 1994, Figure 41). Une autre utilité est d'observer l'inflammation des plaques d'athérosclérose. Dans ce contexte, les macrophages capturent les SPIO et sont ensuite dirigés près des plaques d'athérosclérose pour répondre à l'inflammation (Kooi *et al.*, 2003).

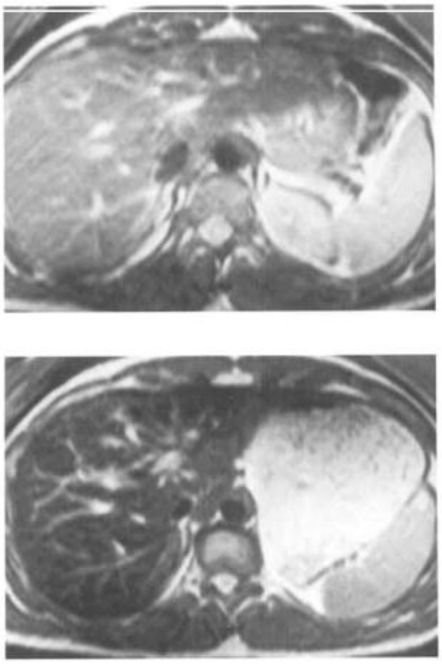

**Figure 41 IRM du foie avant (haut) et après (bas) injection de SPIO.**
Les SPIO injecté apparessent en hyposignal, après capture par les macrophages du foie.
D'après (Hamm *et al.*, 1994)

Dans la sclérose en plaques, maladie auto-immune du système nerveux central, les différents stades de la maladie peuvent être caractérisés par le niveau d'inflammation, marquée par l'infiltration des macrophages après capture des SPIO (Maarouf *et al.*, 2016).

En alternative aux chélates de gadolinium, les SPIO peuvent être injectés par voie intraveineuse pour étudier les vaisseaux sanguins, grâce à leur effet (plus léger) sur la relaxation en T1 (Goyen, 2008). Cependant, les chélates de gadolinium macrocycliques restent très efficaces pour cette application et sont à l'heure actuelle le produit de contraste de référence pour cette application.

Au cours des 30 dernières années, de nombreux agents de contraste superparamagnétiques ont été approuvés pour l'application clinique. Mais la plupart sont maintenant retirés du marché dû à un manque d'efficacité en comparaison à d'autres agents de contraste (Tableau 2).

| *Nom commercial* | *Cible clinique* | *Mise sur le marché* | *Statut* |
|---|---|---|---|
| *Lumirem/Gastromark* | Tractus gastrointestinal | Approuvée par la FDA (1996) | Commercialisation |
| *Sinerem/Combidex* | Foie/ Nœuds lymphatiques | / | Retrait de la demande d'autorisation |
| *Feridex* | Foie | Approuvée par la FDA (1996) | Retiré (2008) |
| *Resovist/Cliavist* | Foie | Approuvée pour le marché europpéen | Retiré (2009) |
| *Clariscan* | Foie | / | Retiré (2009) |

**Tableau 2 Autorisation et commercialisation des oxydes de fer pour l'imagerie.**

### 2.2.4 Mécanismes de ciblage moléculaire

De façon similaire aux agents de contrastes utilisés en TEP pour l'imagerie moléculaire, il est possible d'adresser les agents de contrastes à base d'oxydes de fer vers une cible moléculaire (Crețu *et al.*, 2021). Dans ce but, il existe de nombreux types de revêtement des particules, et autant de cibles moléculaires impliquées dans des pathologies diverses. Les principales approches sont décrites dans la Figure 42 et les avantages et inconvénients sont résumés dans le tableau 3.

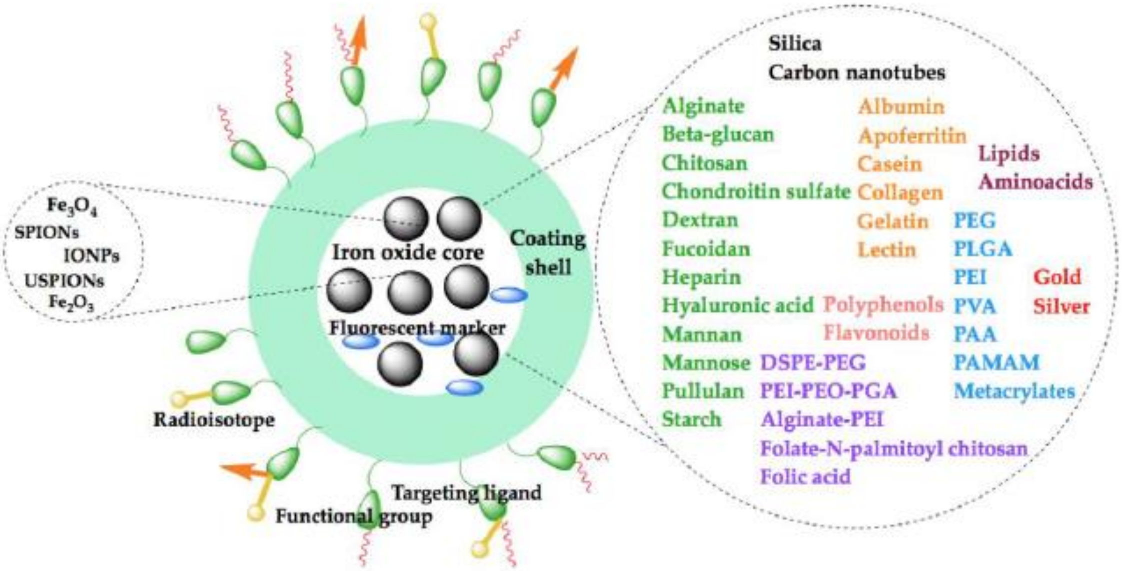

**Figure 42 Principaux revêtements utilisés pour la fonctionnalisation des particules d'oxydes de fer.**

D'après (Cretu *et al.*, 2021)

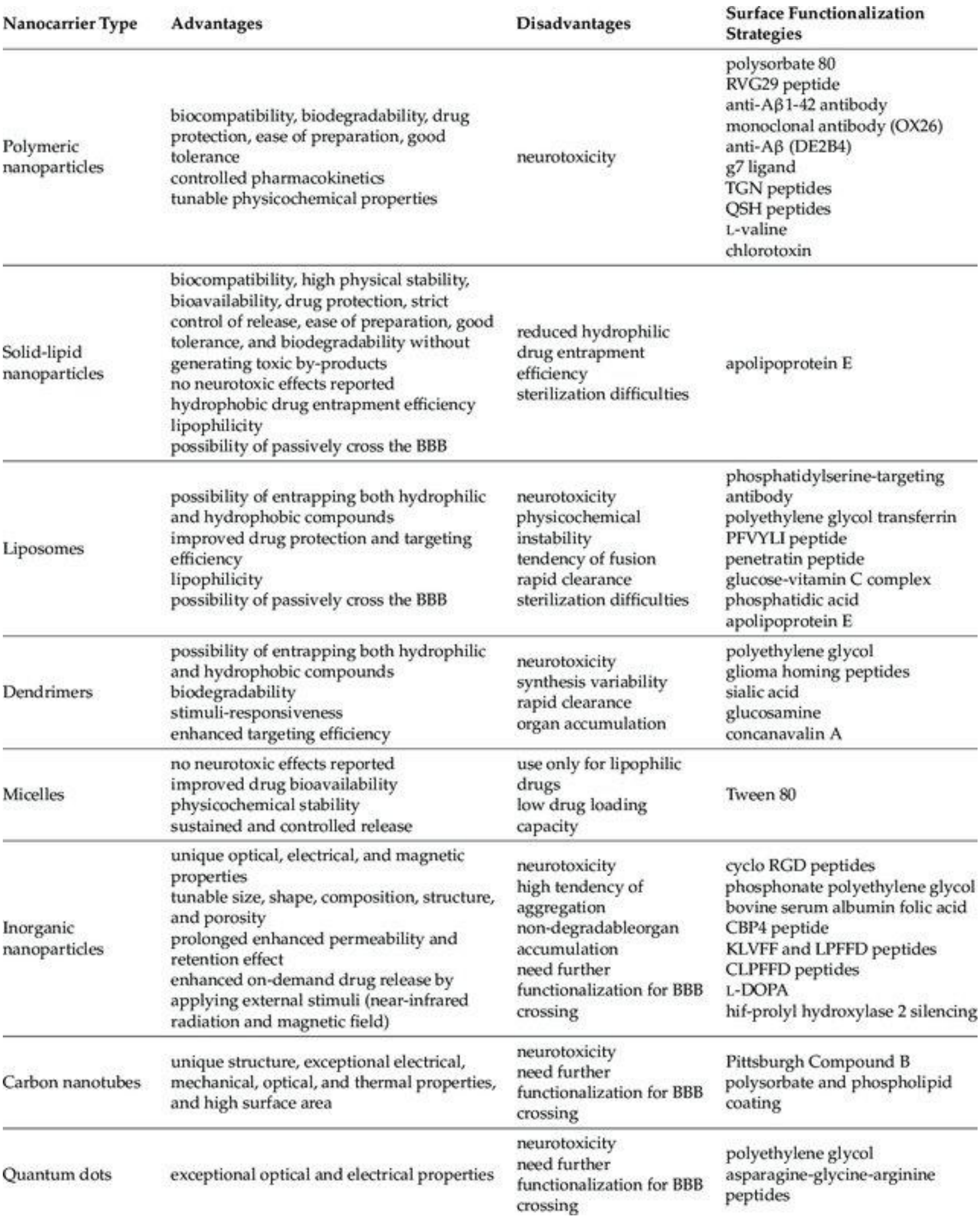

| Nanocarrier Type | Advantages | Disadvantages | Surface Functionalization Strategies |
|---|---|---|---|
| Polymeric nanoparticles | biocompatibility, biodegradability, drug protection, ease of preparation, good tolerance<br>controlled pharmacokinetics<br>tunable physicochemical properties | neurotoxicity | polysorbate 80<br>RVG29 peptide<br>anti-Aβ1-42 antibody<br>monoclonal antibody (OX26)<br>anti-Aβ (DE2B4)<br>g7 ligand<br>TGN peptides<br>QSH peptides<br>L-valine<br>chlorotoxin |
| Solid-lipid nanoparticles | biocompatibility, high physical stability, bioavailability, drug protection, strict control of release, ease of preparation, good tolerance, and biodegradability without generating toxic by-products<br>no neurotoxic effects reported<br>hydrophobic drug entrapment efficiency<br>lipophilicity<br>possibility of passively cross the BBB | reduced hydrophilic drug entrapment efficiency<br>sterilization difficulties | apolipoprotein E |
| Liposomes | possibility of entrapping both hydrophilic and hydrophobic compounds<br>improved drug protection and targeting efficiency<br>lipophilicity<br>possibility of passively cross the BBB | neurotoxicity<br>physicochemical instability<br>tendency of fusion<br>rapid clearance<br>sterilization difficulties | phosphatidylserine-targeting antibody<br>polyethylene glycol transferrin<br>PFVYLI peptide<br>penetratin peptide<br>glucose-vitamin C complex<br>phosphatidic acid<br>apolipoprotein E |
| Dendrimers | possibility of entrapping both hydrophilic and hydrophobic compounds<br>biodegradability<br>stimuli-responsiveness<br>enhanced targeting efficiency | neurotoxicity<br>synthesis variability<br>rapid clearance<br>organ accumulation | polyethylene glycol<br>glioma homing peptides<br>sialic acid<br>glucosamine<br>concanavalin A |
| Micelles | no neurotoxic effects reported<br>improved drug bioavailability<br>physicochemical stability<br>sustained and controlled release | use only for lipophilic drugs<br>low drug loading capacity | Tween 80 |
| Inorganic nanoparticles | unique optical, electrical, and magnetic properties<br>tunable size, shape, composition, structure, and porosity<br>prolonged enhanced permeability and retention effect<br>enhanced on-demand drug release by applying external stimuli (near-infrared radiation and magnetic field) | neurotoxicity<br>high tendency of aggregation<br>non-degradableorgan accumulation<br>need further functionalization for BBB crossing | cyclo RGD peptides<br>phosphonate polyethylene glycol<br>bovine serum albumin folic acid<br>CBP4 peptide<br>KLVFF and LPFFD peptides<br>CLPFFD peptides<br>L-DOPA<br>hif-prolyl hydroxylase 2 silencing |
| Carbon nanotubes | unique structure, exceptional electrical, mechanical, optical, and thermal properties, and high surface area | neurotoxicity<br>need further functionalization for BBB crossing | Pittsburgh Compound B<br>polysorbate and phospholipid coating |
| Quantum dots | exceptional optical and electrical properties | neurotoxicity<br>need further functionalization for BBB crossing | polyethylene glycol<br>asparagine-glycine-arginine peptides |

**Tableau 3 Principaux avantages, inconvéniants et stratégies de fonctionnalisation de surface de particules organique et inorganiques.**

D'après (Daniel Mihai *et al.*, 2019)

Par exemple, dans une publication de 2014, des nanoparticules composées d'oxydes de fer revêtus d'un peptide présentant une forte affinité pour la fibrine (CREKA) ont permis d'observer les microthrombi dans un modèle d'ischémie-reperfusion chez le rat (Song *et al.*, 2014).

Les nombreuses possibilités de fonctionnalisation des nanoparticules associées aux revêtements utilisés, ont permis le développement des recherches sur l'association d'agent pharmacologiques à ces particules. Les oxydes de fer, conjugués à la fois à un ligand d'une cible moléculaire (pour le diagnostic), et à une molécule pour traiter un agent thérapeutique sont à la base d'une nouvelle approche médicale, appelée théragnostique. C'est le cas des SPIO conjugués avec du rtPA (agent thrombolytique), qui ciblent la fibrine pour le traitement de la thrombose (Heid *et al.*, 2017).

### 2.2.5 Microparticules d'oxydes de fer (MPIO)

Les nanoparticules d'oxydes de fer ont donc été très utilisées dans des approches d'imagerie moléculaires, notamment pour le marquage de cellules telles que les macrophages, pour suivre la réaction inflammatoire impliquée dans plusieurs pathologies. Cependant, ce marquage n'est détectable en IRM que lorsqu'une grande quantité de nanoparticules est accumulée dans les cellules. Ainsi, afin d'augmenter la sensibilité du signal, des particules de fer de taille micrométriques (MPIO) ont été synthétisées.

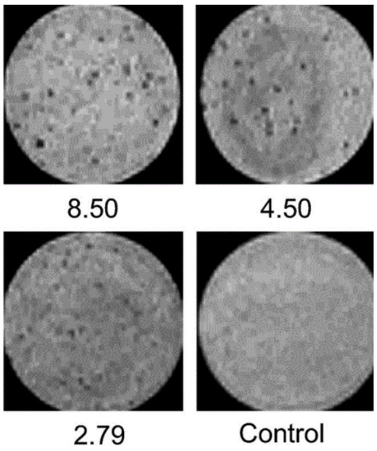

**Figure 43 MPIO de différentes tailles (8.5, 4.5, 2.79 µm) visible en imagerie de susceptibilité magnétique.**

D'après (Shapiro *et al.*, 2005)

.

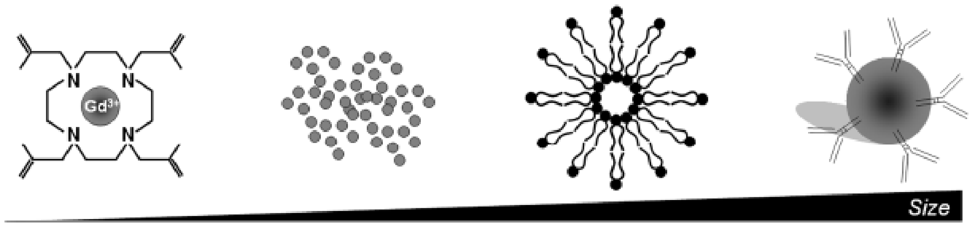

| | Gadolinium labeled contrast agent | USPIO | Loaded-Liposomes | MPIO |
|---|---|---|---|---|
| Diameter | 1 – 7 nm | 10-50 nm | 80-300 nm | 1000 - 4000 nm |
| T1 Effect | +++ | + | +++ or ~0 | ~0 |
| T2 Effect | +/- | + | + | + |
| T2* Effect | +/- | + | + or +++ | +++ |

| Contrast Agent | Contrast Unit | Minimum Detectable Concentration | | | |
|---|---|---|---|---|---|
| | | Per Contrast Unit | | Per Contrast Agent | |
| Iron Oxide NPs | Iron | 821 | nM | 91 | pM |
| $MnCl_2$* | Manganese | 2.3 | µM | 2.3 | µM |
| MnTPPS | | 1.6 | µM | 1.6 | µM |
| Dotarem | Gadolinium | 3.1 | µM | 3.1 | µM |
| Gadovist | | 2.5 | µM | 2.5 | µM |
| Magnevist | | 2.6 | µM | 2.6 | µM |
| Omniscan | | 3.0 | µM | 3.0 | µM |
| Prohance | | 3.1 | µM | 3.1 | µM |
| Poly-D-Lysine | Amide | 25 | mM | 567 | µM |
| Salmon Protamine | Arginine | 672 | µM | 32 | µM |

**Figure 44 Effets des différents agents de contraste sur les pondérations IRM, et concentration minimale détectable des principaux agents de contraste.**
D'après Gauberti *et al.*, 2014 (haut) et extrait de Alvares et al., 2017 (bas)

Dû à leur concentration très riche en fer, les MPIO peuvent créer un signal jusqu'à 50 fois leur taille réelle sur une séquence pondérée en T2*, c'est le « blooming effect » (Figure 43,44), ce qui rend possible la visualisation d'une microparticule unique en IRM de haut champs (Shapiro *et al.*, 2005).

Shapiro et collaborateurs ont ainsi montré que le marquage des hépatocytes *in vitro* par les MPIO améliorait considérablement l'intensité du signal.

De plus, la taille des MPIO (>1µm) empêche leur capture non-spécifique par les cellules endothéliales de la paroi vasculaire et permet un meilleur ciblage des molécules endovasculaires. Cela représente un avantage considérable pour l'IRM moléculaire des maladies cardiovasculaires. D'autre part, les SPIO injectés dans l'imagerie de pathologies cérébrales ont montrés des problèmes d'accumulation au niveau du parenchyme cérébral proche des sites d'inflammations, car la BHE y est détériorée et laisse passer les particules de petites tailles (Debatisse *et al.*, 2020). Ce n'est pas le cas pour les MPIO qui ne peuvent atteindre le parenchyme même lorsque la BHE est endommagée. La demi-vie des MPIO (<5 min) est également avantageuse car elle est beaucoup plus courte que celle des SPIO (Yang *et al.*, 2010). L'accumulation dans le tissu cérébral *via* ce qui est appelé le phénomène d'augmentation de la rétention et de la perméabilité (Enhanced Permeability and Retention ou EPR), est donc impossible (Maeda, 2001).

L'application des MPIO en imagerie moléculaire fût ensuite étendue à l'observation de l'inflammation dans les pathologies cérébrales telles que la maladie d'Alzheimer, la sclérose en plaques et l'ischémie cérébrale. Les MPIO sont ici conjugués avec un anticorps anti-VCAM1, molécules d'adhésion des cellules endothéliales, exprimées en cas d'inflammation (Montagne *et al.*, 2012).

Comme vu précédemment, le ciblage des thrombus des pathologies cardio-vasculaires a fait l'objet de développement de nanoparticules pour l'imagerie moléculaire. La faible intensité du signal cependant, a mené au développement de MPIO fonctionnalisés avec un anticorps ciblant un récepteur moléculaire des plaquettes (von zur Muhlen *et al.*, 2008; Figure 45). Des MPIO fonctionnalisé avec un anticorps anti-LIBS (sites de liaison induits par les ligands au récepteurs GP IIb-IIIa) se fixent aux plaquettes des thrombi *in vitro* fixés dans l'agarose à l'IRM.

Cette étude a démontré le potentiel des MPIO pour la visualisation d'un thrombus en IRM moléculaire.

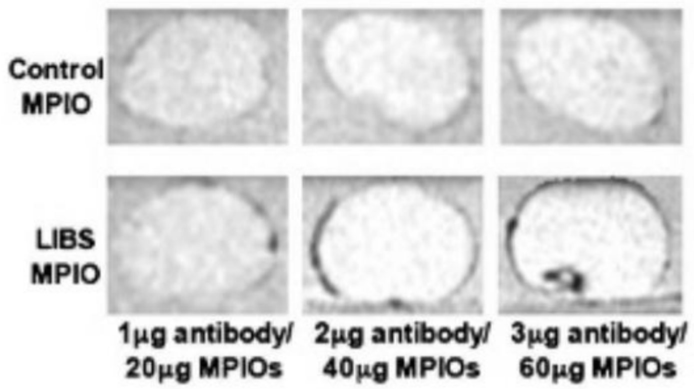

**Figure 45 MPIO fonctionnalisé avec des anticorps anti-LIBS dirigés contre les plaquettes de caillots fixés dans l'agarose à l'IRM.**
D'après (von zur Muhlen *et al.*, 2008)

Mais les MPIO utilisés dans les précédentes études présentent un inconvénient majeur, ils ne sont pas biodégradables. Les MPIO commerciaux possèdent un revêtement composé de polyuréthane et polystyrène, qui empêche leur assimilation par l'organisme. Pendant leur élimination au niveau des macrophages spécifiques du foie, les cellules de Kupffer (Ilium *et al.*, 1982), les MPIO s'accumulent car ils ne peuvent pas être dégradés comme les SPIO par les lysosomes. C'est pour cette raison qu'une partie de mon projet de thèse a été portée sur le développement de MPIO biodégradables, qui pourrait permettre leur utilisation en clinique (Nkansah *et al.*, 2011).

### 2.2.6 MPIO biodégradables

Selon cet objectif, plusieurs équipes ont mis au point la synthèse de MPIO en utilisant uniquement des composés compatibles à l'injection chez l'Homme, et déjà approuvé par la FDA dans d'autres composés pharmacologiques ou de diagnostic (Hamoudeh and Fessi, 2006).

Dans une publication de Perez-Balderas et collaborateurs, la synthèse de microparticules par assemblage de SPIO a été proposée. L'objectif est de rendre possible la réduction des microparticules en nanoparticules pour qu'elles soient dégradées dans les lysosomes des cellules de Kupffer (Figure 46 ; Perez-Balderas *et al.*, 2017). Les nanoparticules sont reliées entre elles par des séquences peptidiques, sensible aux enzymes de dégradation présentes dans le foie.

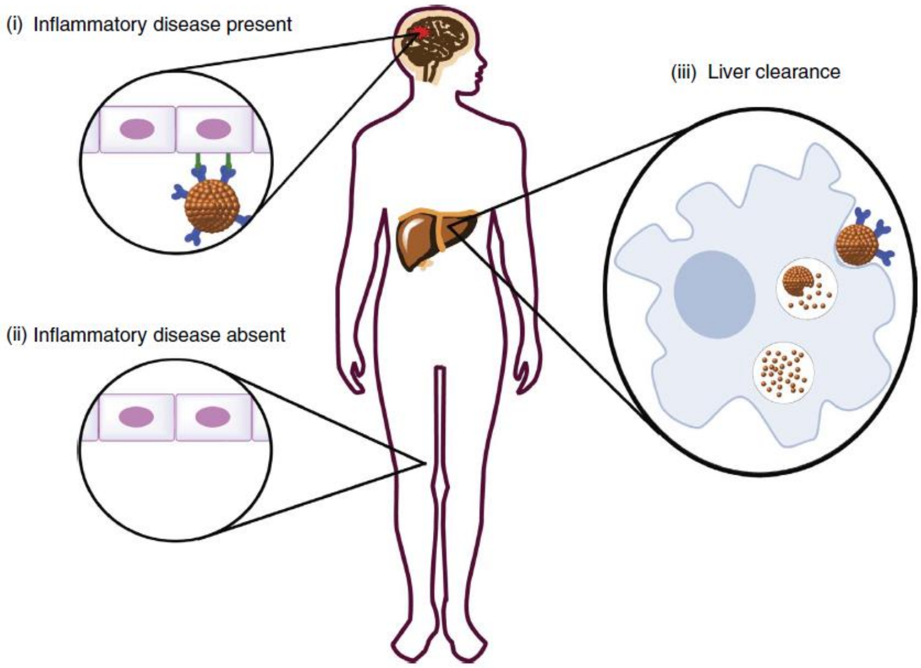

**Figure 46 IRM moléculaire de l'inflammation cérébrale par injection de microparticules d'oxydes de fer biodégradables et leur devenir dans l'organisme.**
D'après (Perez-Balderas *et al.*, 2017)

Les polymères biodégradables pour la synthèse de MPIO par ce procédé d'assemblage présentent donc l'avantage d'être compatible à l'utilisation clinique, mais également une meilleure relaxivité des particules par rapport au SPIO, à dose de fer équivalente, et une demi-vie courte qui permet une élimination rapide et la possibilité de réaliser des injections répétées.

La polydopamine (PDA) est un polymère très employé dans la synthèse de nanoparticules. La dopamine est une molécule qui présente à ses terminaisons des groupes catéchols et des groupes amines. L'idée d'utiliser ce polymère pour former un revêtement de nanoparticules provient de l'observation de ces groupes amines chez les protéines d'adhésions de la moule (Lee *et al.*, 2007). La polymérisation de la dopamine se fait en condition alcaline et forme un film de PDA à la surface des nanoparticules. La PDA présente également l'avantage de permettre la conjugaison de ligands pour l'imagerie moléculaire via les amines primaires (Lee *et al.*, 2009).

La synthèse de tels complexes est simple et peu coûteuse et crée des matériaux biocompatibles. Particulièrement, la synthèse de nanoparticules de PDA seules, est largement décrite dans la littérature et les méthodes permettent de contrôler la taille des particules sont connus (Zmerli *et al.*, 2020). La PDA possède des régions sensibles au pH environnant, ainsi elle peut se dégrader après capture dans les lysosomes (Gu *et al.*, 2015, Figure 47).

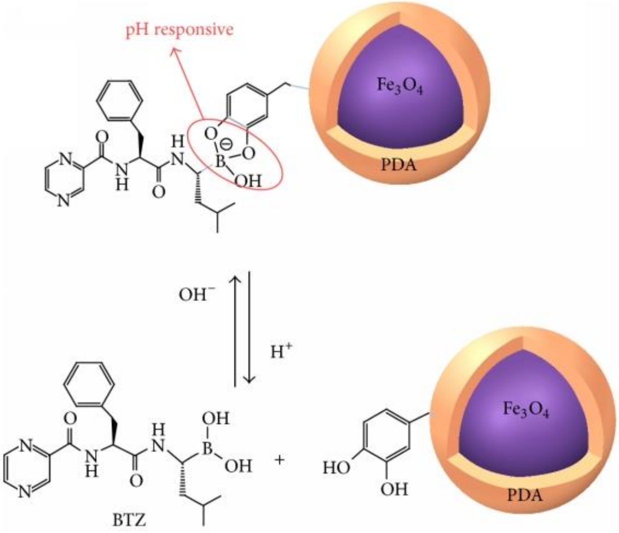

**Figure 47 Nanoparticules d'oxydes de fer encapsulées dans la polydopamine.**
D'après (Gu *et al.*, 2015)

Les différentes propriétés de la PDA décrites ci-dessus en font le candidat idéal pour être utilisé comme matrice biodégradable pour la synthèse de MPIO, et ainsi développer un agent de contraste d'IRM moléculaire qui combine une forte sensibilité de signal et la biocompatibilité, condition nécessaire pourl'administration en intraveineux chez l'homme.

# OBJECTIFS

# Objectifs

La microthrombose peut entraîner des dommages à long terme dans l'AVC ischémique. Les données sur la microthrombose sont pourtant faibles, une des raisons étant que les méthodes d'imagerie actuelles ne sont pas assez sensibles pour la détecter. Les avancées dans l'utilisation de l'imagerie moléculaire et le développement des agents de contrastes offrent la possibilité de cibler spécifiquement les microthrombi pour les diagnostiquer, puis les traiter.

L'objectif principal de ma thèse est le développement de microparticules biodégradables, composées d'oxydes de fer, pour l'imagerie moléculaire de la microthrombose à l'IRM.

Pour remplir cet objectif, l'agent de contraste synthétisé doit répondre à trois contraintes principales :

- Le ciblage spécifique des thrombi et microthrombi ;
- Présenter un signal suffisant pour limiter la dose d'oxydes de fer à injecter ;
- Être composé de matériaux biodégradables, pour permettre la bonne élimination des particules.

Dans ce but, la première partie de mes travaux de thèse a consisté à évaluer les caractères physico-chimiques (taille, charge à la surface, relaxivité) des microparticules synthétisées, puis le suivi des microparticules injectées chez des souris saines pour évaluer leur biodégradation.

La seconde partie de mes travaux s'est concentrée sur le mécanisme de ciblage *in vitro* des microparticules, et la comparaison entre différentes microparticules, dans une chambre microfluidique, mimant les conditions hémodynamiques de formation de la microthrombose.

Enfin la dernière partie fût centrer sur l'utilisation des microparticules pour l'imagerie moléculaire de la microthrombose en IRM, en utilisant un modèle murin d'AVC thromboembolique. Cette étude a pour but d'évaluer la cinétique des particules lorsqu'elles sont fixées au microthrombi, mais également d'observer la microthrombose et ses effets dans le modèle animal. J'ai ensuite observé la dynamique de la microthrombose lors d'un traitement par thrombolyse avec de l’activateur tissulaire du plasminogène recombinant (rtPA), qui est le traitement de référence pour cette indication chez l’Homme.

# METHODOLOGIE

## 1) Caractéristiques physico-chimiques

Pour répondre aux objectifs de ces travaux de thèse, la caractérisation des paramètres physico-chimiques a tout d’abord consisté à mesurer le diamètre hydrodynamique et le potentiel zêta par diffusion dynamique de la lumière (Dynamic Light Scattering ou DLS). La relaxivité des microparticules a été mesurée en réalisant des fantômes : les microparticules à différentes concentrations en fer sont fixées dans un gel d’agarose, puis le signal IRM est mesuré selon différentes modalités (pondération en T1, T2, et T2*). Les temps de relaxation T1 et T2 de chaque échantillon ont été mesurés et les valeurs de relaxivité calculées ensuite selon la formule :

$$R = R0 + r \times [Fe]$$

R = taux de relaxation (1/T) (dans chaque échantillons)
R0 = taux de relaxation dans une solution aqueuse (absence de particules)
r = valeur de relaxivité
[Fe] = concentration en fer de l’échantillon

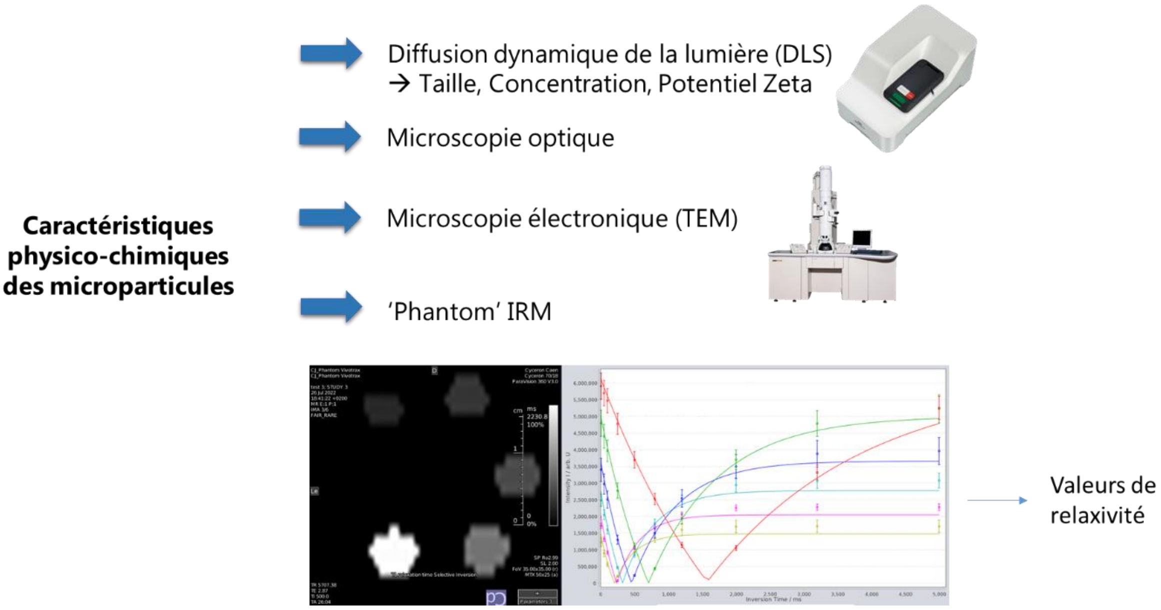

La biodégradation des particules synthétisées a été mesurée en IRM corps entier, à différents temps après injection par voie intraveineuse. A chaque temps (1h, 2 jours, 7 jours et 31 jours après injection), les tissus du foie ont été prélevés pour être observés en microscopie électronique et observer plus finement la dégradation des particules au sein de ceux-ci.

La deuxième étape a consisté en l'évaluation de la fixation *in vitro* des microparticules synthétisées. Pour cela, j'ai mis en place un système de microfluidique dans le laboratoire, selon les méthodes vues dans la littérature, qui permet de recréer des caillots dans une chambre microfluidique, à partir de sang humain de volontaires sains (partenariat avec l'EFS). L'injection de PHySIOMIC sans conjugaison à un ligand spécifique pour cibler les microthrombi, et observés par microscopie à fluorescence, a montré une fixation aux caillots dans la chambre et nous a amené à nous demander par quels méchanismes les microparticules se fixent aux microthrombi. Afin de répondre à cette question nous avons émis l'hypothèse que la couronne de protéine créée autour des microparticules lorsqu'elles sont en contact du sang humain pourrait jouer un rôle dans cette fixation.

Or, d'après la littérature, nous savons que les groupes à la surface des particules modifient la couronne de protéine à la surface. C'est pourquoi nous utilisons dans cette expérimentation des particules formées à partir de résine de mélamine, pour leur similarité en terme de taille avec nos particules, fonctionnalisées soit avec des groupements amines ($NH_2$) similaires aux PHySIOMIC, soit carboxyliques (COOH). Les principales caractéristiques des différentes particules sont résumées dans le tableau 2.

| **Microparticules** | *PHySIOMIC* | *Melamine-NH2* | *Melamine-COOH* |
|---|---|---|---|
| **Diamètre Hydrodynamique** | 700 nm | 1 µm | 1 µm |
| **Fonctionnalisation** | NH2 | NH2 | COOH |
| **Fluo** | BSA-555 | Rhodamine | Nile's Blue |
| **Potentiel Zêta** | -36,37 ± 2,45 mV | -10,84 ± 0,58 mV | -15,93 ± 0.33 mV |

## 2) Modèles animaux

La troisième étape fut l'injection in vivo dans différents modèles d'AVC pratiqués dans notre laboratoire, chez la souris.

- **Modèle par injection de thrombine dans l'ACM** : Il a déjà été décrit dans la littérature que le modèle par injection de thrombine forme, en plus d'un caillot proximal au niveau de l'ACM, une multitude de microthrombi distaux dans les artères.

- **Modèle par application de chlorure d'aluminium** : L'altération de la paroi de ACM, par application de chlorure d'aluminium, conduit à la formation d'un caillot. Le chlorure d'aluminium a été choisi en comparaison au chlorure de fer, afin d'éviter l'apparition d'artéfacts dû aux résidus de fer pouvant se déposer au moment de la chirurgie. Ce modèle nous servira de contrôle négatif, car celui-ci n'engendre pas la formation de microthrombi.

- **Modèle par insertion d'un monofilament jusqu'à l'ACM** : Le monofilament est introduit par la carotide interne et remonté jusqu'à la bifurcation de l'ACM. Selon la littérature, ce modèle induit la formation d'une microthrombose secondaire pouvant correspondre au phénomène de no-reflow décrit plus tôt dans l'introduction.

- **Modèle de compression de l'ACM ou modèle d'AIT** : ce modèle a été envisagé pour déterminer si celui-ci induit une microthrombose secondaire. Il est également intéressant car nous avons vu que les AIT, bien qu'ils ne présentent pas de lésion ischémique, sont associées à l'apparition de troubles cognitifs et de démences.

- **Modèle d'apoptose par injection intrastriatale de staurosporine** : est également utilisé, dans le but de montrer que les particules sont capables de marquer la thrombose générée par une voie différente de la thrombine.

### 3) Imagerie

Pour chacun de ces modèles, la microthrombose sera observée par imagerie IRM, avec l'utilisation d'une séquence pondérée en T2*, sensible au fer. Dans les protocoles où nous cherchons à observer la taille de lésion, une séquence pondérée en T2 est utilisée et l'occlusion et la restauration du flux sanguin de l'ACM est observée par angiographie.

- **Séquence pondérée en T2* (PHySIOMIC)** : Nous réaliserons une acquisition avant et après injection des microparticules afin de discriminer les hyposignaux induits spécifiquement par les PHYSIOMIC, d'autres hyposignaux pouvant apparaître après chirurgie (comme la présence de déoxyhémoglobine dans les vaisseaux). Dans tous les modèles murins utilisées, l'injection des PHYSIOMIC se fera 30 min après la chirurgie, excepté pour le modèle par insertion de filament, pour lequel nous testerons l'injection de PHySIOMIC à différents temps, ne sachant pas à quel temps précis nous pourrons observer la microthrombose secondaire.

- **Séquence pondérée en T2 (Taille de lésion)** : La taille de lésion est un paramètre important dans les modèles d'AVC car elle représente la zone du cerveau impactée par l'occlusion. Elle est mesurée dans beaucoup d'études pour l'évaluation de nouveaux traitements. Nous la mesurerons à l'aide d'une séquence pondérée en T2, 24h après la chirurgie.

- **Angiographie IRM (Flux sanguin)** : Enfin, des angiographies IRM seront réalisées parallèlement aux autres acquisitions IRM. Le but est d'observer le flux sanguin au niveau de l'ACM pour évaluer la recanalisation.

-

# RESULTATS

Les travaux présentés dans cette partie sont en cours de finalisation et feront l'objet d'une publication intitulée :

# Synthesis and preclinical validation of a novel biocompatible MRI contrast agent that reveals brain microvascularthrombosis

**Charlène Jacqmarcq**[1], Florent Lebrun[1], Jules Flon[1], Mikaël Naveau[2], Sara Martinez de Lizarrondo[1], Didier Goux[3], Marina Rubio[1], Cyrille Orset[1], Aurélie Malzert Fréon[4], Maxime Gauberti[1,5], Denis Vivien[1,6], Thomas Bonnard[1]

[1] Normandie Université, UNICAEN, INSERM U1237, PhIND 'Physiopathology and Imaging of Neurological Disorders', Caen, France

[2] Normandie Université, UNICAEN, CNRS UMS 3408, Caen, France

[3] Normandie Université, UNICAEN, SF 4206 ICORE, CMAbio3 : Centre de Microscopie Appliquée à la Biologie, Caen, France

[4] Normandie Université, UNCAEN, EA 4258, CERMN : Centre d'études et de recherche sur le médicament de normandie, Caen, France

[5] Centre Hospitalier Universitaire Caen, Department of Diagnostic Imaging and Interventional Radiology, Caen, France

[6] Centre Hospitalier Universitaire Caen, Department of Clinical Research, Caen, France

## Abstract

The aim of current ischemic stroke treatments is to achieve reperfusion of the occluded vessels via thrombolysis, combined or not with thrombectomy. However, even when a full recanalisation is obtained, incomplete reperfusion of the downstream vascularisation is often observed. This is correlated with the presence of microthrombi in the vessels of the infarcted area. Microthrombi are suspected to contribute to dementia and cognitive decline and are currently misdiagnosed due to the absence of precise methods. Our purpose is to design a novel contrast agent to detect microthrombi during acute ischemic stroke in magnetic resonance imaging (MRI). Microparticles were synthesized using SPIO clustered in a polydopamine matrix. The PHySIOMIC microparticles (Polydopamine Hybridized Self-assembled Iron Oxide Mussel Inspired Clusters) obtained were characterized with dynamic Light Scattering, Optical and Transmission Electron Microscopy and microthrombi targeting was studied in microfluidic chambers. The PHySIOMIC contrast agent was then tested in a mouse model of ischemic stroke, induced by intra-arterial thrombin injection. Susceptibility weighted sequence (T2*) was used in a preclinical MRI scanner to detect the particles in the brain microvasculature and study the evolution of the signal over time, as well as its variation during thrombolysis. Biodegradability was investigated with MRI and histology of the liver and spleen. Our results demonstrate that PHySIOMIC generate a hyposignal on T2*-weighted sequences indicating the presence of microthrombi, confirmed with histological findings. The signal void area formed correlates with lesion sizes observed at 24h. Mice injected with a thrombolytic agent showed a hyposignal loss, suggesting a degradation of some microthrombi with thrombolysis. Biocompatibility study demonstrate that the particles are taken up by the Mononuclear phagocyte system. Progressive degradation is observed in the liver and spleen over 1 month. PHySIOMIC particles enable the detection of microthrombi during the acute phase of ischemic stroke with a molecular MRI strategy. They constitute a promising tool to monitor thrombolysis and assess a successful reperfusion of microvessels.

## Introduction

Acute ischemic stroke (AIS) is caused by the occlusion of a cerebral artery by a thrombus and is the leading cause of acquire disability among adults and the second cause of dementia worldwide. Current strategy for recanalisation of the occluded artery are thrombolysis and mechanical thrombectomy (MT). Thrombolysis consist in the administration of recombinant tissue-type Plasminogen Activator (rtPA, ACTILYSE®) and is mostly limited to a 4.5 hours therapeutic window after symptoms onset. Due to its many contraindications and side effects (in particular hemorrhagic transformations), rtPA is only available to less than 10% of the patients admitted in the hospital for AIS[1]. Since 2015 and the publication of numerous clinical trials that prove the benefit of recanalisation with MT[2–5], this treatment has now been incorporated into the standard of care for patients with AIS. MT can be used either in combination or as an alternative of thrombolysis, thereby increasing the number of AIS patients eligible to treatment. However, microembolic signals are found in patients treated with thrombolysis[6,7], and for 14 to 20% of patients who underwent MT we observe a microfragmentation of the proximal thrombus, i.e. microthrombi, that moves in the distal microvascularisation[8]. The presence of microthrombi despite a successful recanalisation of the occluded artery is associated with a risk of dementia and poor outcome[9–11]. In addition, it has been demonstrated in animal models, that reperfusion of the microvascularisation improve stroke outcome[12]. These elements revive the debate on the need to visualize microthrombi after AIS to guide the treatment. Unfortunately, visualization of microthrombi in the cerebral vascularization with standard imaging method remains challenging because of their small size, even with recent development of high-resolution diffusion weighted imaging (DWI) in MRI to visualize distal emboli or the use of transcranial Doppler[13]. Although recently new contrast agents have been synthesized to better visualize thrombi in MRI and CT[14,15], they are not sensitive enough to reveal microthrombi.

Superparamagnetic iron oxide nanoparticles (SPIO) are a contrast agent in MRI, approved for human administration mainly for patient with iron-deficient anemia (Feraheme®)[16], in development for lymph node imaging[17], in hyperthermia for cancer therapy[18] and in a large number of clinical trials. Their long half-life, low toxicity and biocompatible properties are engaging for microthrombi-targeted imaging.

However, the size of the particles limits their use for target-specific binding combined to a good signal in MRI[19].

Polydopamine is a bio-inspired polymer of interest in the bioengineering and biomedical field. Under alkaline condition, and in presence of oxygen, dopamine polymerize into polydopamine. Its properties are investigated since a decade as potential tool for anti-cancer drug delivery and diagnostic imaging[20–22]. Beside its biocompatible properties, polydopamine offers many advantages for microparticles design such as a high affinity for metal oxide[23], an easy functionalization of the surface due to its numerous functional groups for targeting moieties, and it has simple preparation protocols. All of its characteristics shows a perfect candidate for microparticles synthesis with high loading capacity.

In this paper, we use polydopamine to encapsulate commercial SPIO and detect microthrombosis in MRI, in different mouse models of AIS. We demonstrate that Polydopamine Hybridized Self-assembled Iron Oxide Clusters (PHySIOMIC) fixate on microthrombi and efficiently reveal their presence in AIS models on T2* weighted MRI scans. The obtained MRI hyposignal is predictive of lesion size. We evaluate microvascular thrombosis after a reference treatment and verify the biocompatibility and biodegradability of the PHySIOMIC particles.

## Materials and Methods

### Preparation and characterization of PHySIOMIC microparticles

*Microparticles synthesis and surface functionalization*

PHySIOMIC microparticles were synthetized in a self-assembly method by mixing SPIO and dopamine. SPIO particles (Vivotrax, Magnetic Insight Inc.) are composed of iron oxide with a dextran coating, the same composition as Resovist contrast agent, clinically authorized SPIO particles until 2009. Briefly, 200 µL of a SPIO nanoparticle solution (5.5 mg.mL$^{-1}$) is mixed with dopamine (10 mg.mL$^{-1}$, Sigma Aldrich) in a TRIS buffer (10 mM, pH 8.8). A reaction of polymerisation of dopamine into polydopamine occurs under constant agitation at room temperature for 24h, as described elsewhere[24]. Polymerization reaction is stopped by washing microparticles in a phosphate buffer (10 mM, pH 8.8) using a separating magnet (PolyATtract® System 1000 Magnetic Separation Stand, Promega). The solution is placed under sonication (Ultrasonic Probe Sonicator, Hielscher®) at high intensity during 10 min to obtain microparticles of requested size. For *in vivo* injection, microparticles are washed and resuspended in a mannitol buffer (0.3 M, pH 7.4).

PHySIOMIC were functionalized for *in vitro* experiment with Bovine Serum Albumine (BSA) conjugated with Alexa Fluor™ 555 (0.5 mg.mL$^{-1}$M, Invitrogen™). PHySIOMIC are washed in a phosphate buffer 0.1 M and BSA is added at an 1:5 volume ratio. The reaction is left overnight, under constant agitation at 37°C. The particles are washed and resuspended in PB 10 mM. All microparticles solution are kept under agitation at 4°C until used.

Commercial microparticles based on melamine resin (Sigma-Aldrich) with amine (Rhodamine B-marked) or carboxylic termaisons (Nile Blue-marked) are prepared for the microfluidic experiment at 1:100 volume ratio.

*Size, particle concentration and zeta potential measurement*

Dynamic light scattering (DLS) measurements were carried out on a Zeta sizer Ultra (Malvern Panalytical®). Microparticles are diluted in a phosphate buffer (10 mM) and average hydrodynamic diameter, polydispersity index (PDI) and particle concentration measurements were determined at 25°C. Zeta potential measurements were acquired using the same equipment, with a detection angle of 17° in a $10^{-3}$ M KCl sample dispersion.

*Determination of iron concentration with ferrozine assay*

Total iron was quantified using a modified version of the ferrozine colorimetric assay[25]. 500 µL of 2N HCL was added to 500 µL of sample lysate. The iron standards were prepared using growing concentrations of $FeCl_2$. Samples were incubated overnight and mixed with iron detection reagent (37.5 µL of 5mM ferrozine, 60 µL of ammonium acetate 30% and 30µL of ascorbic acid 30% ; Sigma-Aldrich). Equal volumes of the test and standard samples were deposited into a 96-well microplate in duplicates and absorbance was read at 560 nm using a microplate reader (ELx808 Absorbance Reader, Biotek Instruments).

*Transmission Electron Microscopy*

For observation of SPIO or PHysIOMIC in suspension, a droplet of particles was deposited on a hydrophilized 400-mesh grid. For observation of liver sections, small samples were harvested from the biocompatibility study were fixated in a 2.5% glutaraldehyde in 0.1M cacodylate buffer (Sigma), then dehydrated in progressive bath of ethanol (5, 40, 60, 80, 100%), replaced finally by acetone and embedded in a Epon resin mixture. After 20 hours of polymerization at 60°C, the coverslip were then separated from the cell's resin bloc and polymerization continued for 28 hours. Slices of 250 nm were obtained using an ultramicrotome (Leica ultracut R). SPIO, PHysIOMIC and liver sections images were taken an ORIUS 200 digital camera on a JEM 1011 transmission electron microscope. Samples treatment and image acquisition were performed at CMAbio3 (Centre de Microscopie Appliquée à la Biologie, Biological Microscopy Facility Center UFR des Sciences, SF 4206 ICORE, University of Caen Normandie).

### *Relaxivity measurements*

Samples of PHySIOMIC and SPIO at growing concentrations (0, 0.72, 1.43, 2.15, 2.86, 3.58 mM) were prepared. Samples are diluted in a TAE buffer (40 mM Tris-acetate, 1mM EDTA) with 2% agarose after heating until boiling of the solution, and dispose in 500µL eppendorf. Device with particles samples was place at the center of a BioSpec 7-T TEP-MRI (Bruker, Germany). R1 relaxivity was calculated from T1 mapping using flow-sensitive alternating inversion recovery–rapid acquisition with relaxation enhancement (FAIR-RARE) sequence with repetition time (TR) = 3000 ms and inversion time ranging from 6.5 to 2000 ms, R2 relaxivity was obtained from T2 mapping using multislice multiecho (MSME) sequence with TR = 4000 ms and echo time (TE) ranging from 3.65 to 51.11 ms, and R2* relaxivity from T2* mapping using multigradient echo sequence with TR = 4000 ms and TE ranging from 2 to 17.47 ms.

### *Microfluidic experiment*

Microfluidic experiment was conducted using an ibidi pump system to control the blood flow through a microfluidic channel (µ-slide VI 0.4, ibidi) to reproduce microthrombosis *in vitro*. First, the microfluidic channel was incubated with collagen from calf skin (Sigma) and left at room temperature for an hour. Whole blood collected on citrate from healthy volunteers was provided by Etablissement Français du Sang (EFS, Caen, France). Platelets of collected blood were stained using $DiOC_6$ intracellular probe (1 µg.mL$^{-1}$, Abcam). Blood was perfused through the microfluidic channel, reproducing an endothelial damage in the vasculature, at a shear rate of 500 s$^{-1}$ according to previous study[26]. The collagen coating induced platelet aggregation, and the formation of microthrombi that could be observed in the AF488 channel with a confocal microscope (Leica). After extended washing of the blood, 200 µL of a preparation of microparticles (PHySIOMIC or melamine microparticles) suqpended in either phosphate buffer or blood was injected into the chamber with concentrations calculated to 1 mg[Fe].kg$^{-1}$ , for PHySIOMIC, and observed in the corresponding fluorescence channel.

## Animals

All studies were conducted on male Swiss mice (age 8-10 weeks ; weight 35-45g ; CURB, Caen, France) in accordance with European communities Council (Directives of November 24, 1986 (86/609/EEC) and French Legislation (act no, 87-848) on Animal Experimentation and validated by the local ethical committee of Normandy (CENOMEXA). Mice were housed in a temperature-controlled room on a 12-hour light/12-hour dark cycle with food and water *ad libitum*. Before surgery, mice were deeply anesthetized with isoflurane 5% in a 70/30 gas mixture ($NO_2/O_2$) and maintained under anaesthesia with 2% isoflurane in a 50/50 gas mixture ($NO_2/O_2$). To avoid any pain due to surgery, mice were injected subcutaneously with buprenorphine (Buprecare®, 0.1 mg/kg), 20 minutes before. Animals' temperature was maintained at 37 ± 0.5°C throughout the surgical procedures using a feedback-regulated heating system with a rectal probe. A catheter was inserted into the tail vein of mice for intravenous administration of contrast agent or treatments. After surgery, animals were allowed to recover in a clean heated cage.

### *In vivo biodegradation of PHySIOMIC and SPIO*

PHySIOMIC or SPIO particles were administered to naïve male Swiss mice (8 weeks, n = 5 per group). At different time after injection (1 hour, 2, 7 and 31 days), T2-weighted images (RARE sequence, FOV : 4 x 4 mm, TR/TE = 3000 ms/50 ms) were acquired on a BioSpec 7-T TEP-MRI system with a volume coil resonator (Bruker, Germany). At each steps, mice were deeply anesthetized with 5% isoflurane (in a 70/30 gaz mixture $N_2O/O_2$) and transcardiacly perfused with saline. Organs of interest (lungs, liver, kidneys, spleen) were harvested and post-fixated in paraformaldehyde for 24h and stored for transmission electron microscopy.

## Mouse Models

### *Middle Cerebral Artery Occlusion (MCAO) with thrombin or $AlCl_3$*

As described in Orset *et al* [27], mice were placed in a stereotaxic device, the skin between the right eye and the right ear was incised and the temporal muscle was retracted. We performed a small craniotomy followed by the excision of the dura, to expose the middle cerebral artery (MCA). A home-made glass micropipette was introduced into the lumen of the MCA and 1µL of purified murine alpha-thrombin (1 UE ; Stago BNL) was pneumatically injected to induce the *in situ* formation of the clot. The pipette is removed 10 minutes after the injection at which time the clot was stabilized. For the aluminium chloride model ($AlCl_3$), the MCA was exposed and $AlCl_3$ (Sigma-Aldrich) was topically applied on the artery (as previously described [28]). To study the effects of thrombolysis on microthrombosis, mice received intravenous administration of rtPA (10mg.kg$^{-1}$ in 200µL ; Actilyse) as 10% bolus and 90% perfusion over 40 minutes. The control group received the same volume of saline under the same conditions.

*Exclusion criteria*

Mie were excluded in case of death during the experimental procedure, technical problems, or heamorrage, or if mice presented a lesion size superior to 35 mm² or inferior to 10 mm² (without injection of a thrombolytic agent).

### Magnetic Resonance Imaging (MRI)

*In vivo* experiments on stroke imaging were carried out on a Pharmascan 7 T/12 cm system with surface coils (Brüker, Germany). Magnetic resonance angiographies (MRA) were performed using a 2D-TOF sequence (TE/TR 5/12ms). A T1-weighted rapid acquisition with relaxation enhancement (RARE) sequence was used to obtain anatomical images (TE/TR 9/1200ms, with 70 x 70 x 500 µm$^3$ spatial resolution. T2-weighted images were acquired using a multi-slice multi-echo (MSME) sequence (TE/TR 50/3000ms with 70 x 70 x 500 µm$^3$ spatial resolution. 3D T2*-weighted gradient echo imaging with flow compensation (GEFC, spatial resolution of 93 x 70 x 70 µm interpolated to an isotropic resolution of 70µm) with TE/TR 9/50 ms and a flip angle of 15° was performed to visualize PhySIOMICs. Diffusion-weighted images (DWI) were acquired using a standard spin echo imaging modified with a Stejskal-Tanner gradient scheme (TE/TR 38ms/2000ms, with 75 x 75 x 500 µm$^3$ spatial resolution, giving an in plane resolution of 100x78mm, slice thickness of 0.75mm, one direction diffusion gradient (in the frequency encoding direction) with a b factor of 1000s/mm2 and one averaging. For perfusion-weighted imaging, a gradient-echo fast imaging with steady-state precession sequence was used, with TR/TE, 10/5 ms (FA of 8°), temporal resolution of 911 ms and spatial resolution of 100 x 100 x 75 µm$^3$ (half-scan). Mice were injected with 30µL of 0.5M solution of Dotarem (Guerbet, France) during repetitive image acquisitions [29].

### Image Analysis

All MRI analysis were performed blinded to the experimental data. Analysis of the MCA MRA were performed using the score : 2 : normal appearance, 1 : partial occlusion, 0 : complete occlusion of the MCA. All T2*-weighted images presented in this study are minimum intensity projections of 4 consecutive slices (yielding a Z resolution of 600 µm), obtained with Image J software. Perfusion index was calculated by measurement of the ratio of ipsilateral and contralateral intensities as described previously[30], using a in-house-created macro, and signal intensity ratios were measured by drawing the region of interest in the liver, spleen, kidney, over the signal intensity of paravertebral muscles as reference, in ImageJ. Lesion sizes on T2-weighted images and signal void on T2*-weighted images were quantified using Slicer software (v1.45r). Signal void quantification on 3D T2*-weighted images, and 3D representation of PhySIOMIC-induced hyposignal were realised using the segmentation and thresholding module on Slicer software (v4.11). Results are presented as volume of particles-induced signal void, or area of signal void (in mm$^3$).

### Immunohistochemistry

Deeply anesthetized mice were perfused transcardially with saline followed by a fixative solution (4% paraformaldehyde in phosphate buffer) at a physiological rate (8 mL.min$^{-1}$) with a peristaltic pump. Brains and liver were post-fixed (24h, 4°C) and cryoprotected (20% sucrose, 24h, 4°C) before freezing in Tissue-Tek (Miles Scientific). Coronal brain sections (10µm) were co-incubeted with anti-fibrinogen/fibrin (1:1000 ; sheep antiserum againt fibrinogen prepared at the National institute for agronomic research, France), platelet-specific marker anti-CD41 (1:1000 ; BD Biosciences), and anti-vWF (1:800 ; Fisher). Primary antibodies were revealed using Fab’2 fragments of donkey anti-rat, goat, sheep IgG linked to FITC, TRITC or DyLight 629 (1:800, Jackson ImmunoResearch, USA). The specificity of immunostainings was checked by showing the absence of staining when primary antibodies were omitted. Images were digitally captured using a Leica DM6000 microscope-coopled coolsnap camera, visualized with MetaVue 5.0 software.

### Histological Preparation of Heart, Lung, Spleen, Liver, and Kidney

Perls' Prussian Blue Iron Kit stains (Leica Biosystems) were used to detect and identify ferric ($Fe^{3+}$) iron residue of PhySIOMIC particles in brain sections (10µm). Images were further processed using QuPath and ImageJ.

### Statistical Analysis

All results are presented as mean ± Standard Error of the Mean (SEM). Statistical analysis were performed blinded to the experimental groups, using Graph Pad Prism software (v8.0). We assumed normality of the data distribution with Shapiro-Wilk test. Independent samples *t*-tests or one-tailed paired *t*-test were used for comparisons between two groups. Non-parametric data were analysed by Mann-Whitney and Wilcoxon test. One-way ANOVA, Kruskal-Wallis and Friedman test, with Tukey's multiple comparisons test were used for comparing more than two groups. Linear regression was used to model relationship between variables. Differences were considered statistically significant if probability value $p < 0.05$.

## Results and Discussion

### 1. PHySIOMICs synthesis and physico-chemical properties determination

We designed microparticles of superparamagnetic iron oxide (SPIO) clustered in polydopamine by employing a self-polymerization process as described in Figure 1A. The SPIO are clustered in the polydopamine matrix during the polymerization step in alkaline conditions. The sonication of the solution creates microparticles we called Polydopamine Hybridized Self-assemble Iron Oxide Clusters or PHySIOMIC. We verified the clusterization of SPIO into PHySIOMIC by measuring the hydrodynamic diameter (HD) of the particles (Table 1). Dynamic Light Scattering (DLS) measurement of PHySIOMIC shows an average HD of 753.7 ± 47.5 nm and a Polydispersity Index (PDI) of 0.22 ± 0.19 and SPIO an average HD of 78.53 ± 11.30 nm and PDI of 0.21 ± 0.04 (Table 1). PHySIOMIC particles structure were observed by Transmission Electron Microscopy (TEM) confirming the clusterization of SPIO inside the polydopamine matrix (Fig 1B). Iron quantification in equal volume and dilution of either SPIO or PHySIOMIC shows no differences (Table 1) and suggest that the majority of iron is conserved through the process of microparticles synthesis. PHySIOMIC exhibit a negative zeta potential of -36.37 ± 2.45 mV (Table 1), in agreement with what has been observed experimentally in the literature with polydopamine particles[22], and lead to less particle aggregation, whilst zeta potential of SPIO in less negative (-11.09 ± 1.56 mV). This difference can be attributed to the presence of carboxyl groups on the dextran perimeter of the SPIO particles[31]. The potential of PHySIOMIC as a T2*-weighted MRI contrast agent was evaluated by measuring relaxation rate and establish the relaxivity (R2*) with a 7T magnet. PHySIOMIC appear more hypointense than SPIO particles while iron contents are kept equal (Fig 1D) and translate in a relaxivity value almost two fold than SPIO particles (Table 1) for T2*-weighted imaging. This result shows that PHySIOMIC are highly sensitive to T2*-weighted MRI imaging, even at small concentration, and is attributed to the fact that larger particles creates greater magnetic moment[32]. Regarding T1 and T2-weighted imaging, PHySIOMIC relaxation rates are respectively lower and equal to SPIO (Fig S1, Table1).

## 2. MRI and TEM follow-up of PHySIOMIC degradation

Our next concern was to evaluate the correct biodegradation of PHySIOMIC in the body. To this aim we injected a high concentration of particles (4 mg of iron.kg$^{-1}$), and compared it to biodegradation of the SPIO particles (Vivotrax, Magnetic Insight Inc.). Whole-body MRI was performed before and shortly after injection of PHySIOMIC or SPIO suspensions. Signal enhancement was monitored in the liver, spleen and kidney at 2, 7 and 31 days after injection. Both PHySIOMIC and SPIO particles induced a strong hyposignal within the liver and the spleen (Fig 2A) which is in line with a rapid elimination of particles from the blood compartment, captured by the mononuclear phagocyte system ; in the Kupffer cells of the liver[19] and resident macrophages of the spleen. As no significant differences between PHySIOMIC and SPIO are observed, the results are leading toward a successful bioelimination of PHySIOMIC, as well as SPIO particles, inside the liver and spleen at one month after injection. There is a residual hyposignal after 31D post injection in the spleen for both type of particles that may be explained by the degradation of iron oxide into iron-rich ferritin proteins, mainly accumulated in the spleen[18]. After the injection of SPIO particles, we can observe a decrease of the signal in the kidneys, while no change was observed with PHySIOMIC (Fig 2B). PHySIOMIC presenting a larger hydrodynamic diameter do not pass through the renal clearance barrier for elimination.[33] This might implicate that PHySIOMIC particles would not be contraindicated for patients with kidney deficiencies, as it was the case for some SPIO nanoparticles.

For further investigation of PHySIOMIC biotransformation in the liver, the liver of the mice were collected at the same time points as MRI and observed in transmission electron microscopy (TEM) (Fig 2C). As expected, PHySIOMIC are found in the Kupffer cells of the liver after injection and the biotransformation can be witnessed in the lysosome of the cells. Over time, we can see a degradation of the structure of the particles inside the lysosomes, consistent with the loss of superparamagnetic properties seen in MRI images. Altogether, the results of the biodegradation study indicate a deterioration of the polydopamine matrix due to the low pH, and enzymes presence in the lysosomes[19] and subsequent elimination of iron oxide into iron-rich ferritin proteins, hence a restoration to the iron pool of the body.

### 3. In vitro test and investigation on particle fixation on microthrombi

For in vitro investigation of PHySIOMIC fixation on microthrombi, we used microfluidics as described in Fig 3A. PHySIOMIC were labelled with bovine serum albumin conjugated with an Alexa Fluor 555 dye (PHySIOMIC@BSA-555) on the surface to be observed in fluorescence. The result shows that PHySIOMIC@BSA-555 fixate on the *in vitro*-created microthrombi formed into the microfluidic chamber (Fig 3B) when injected with human blood. For a better understanding of the targeting mechanism, we used commercial micrometric particles in order to have a clear fluorescence signal and a clean surface functionalisation. We worked with microparticles composed of resin melamine (with surface amine groups), described here as Melamine-$NH_2$, or carboxylate-modified resin melamine (with surface carboxylic groups), described as Melamine-COOH. Previous studies have reported that surface functionalization on nanoparticles influence their properties, related to the adsorption of plasma proteins present in the blood onto their surface, forming a protein corona (PC)[34]. First, we injected both type of melamine microparticles in a phosphate buffer (PB). The result shows no significant differences between Melamine-$NH_2$ and Melamine-COOH. When injected microparticles in whole human blood, the number of Melamine-$NH_2$ attached to microthrombi exhibit a 2-fold increase (95 per $mm^2$) compared to Melamine-COOH (34 per $mm^2$) (Fig 3C), showing that surface functional group impact microparticles fixation, only when injected in blood. Hence, we can infer that the PC on the surface of PHySIOMIC plays a role in the fixation of the particles on microthrombi. Further investigations should be done on the composition of different protein coronas on PHySIOMIC, Melamine-NH2 and Melamine-COOH, to understand which proteins influence the fixation on microthrombi in our study, using liquid chromatography mass spectrometry (LC MS)[35].

### 4. Revealing microthrombosis in a stroke mouse model using PHySIOMIC injection in MRI

The presence of microthrombosis in ischemic stroke was studied *in vivo* in a mouse model of thromboembolic stroke. The thrombin injected in the middle cerebral artery (MCA) in order to create a thrombus at the bifurcation of the artery also flows in the downstream microvasculature and induce the formation of microthrombi.[27] We compared it to another stroke model where thrombosis was induced *in situ*, by the damage of the endothelial wall of the artery via deposition of a filter paper soaked with aluminium chloride ($AlCl_3$), leading to thrombus formation at the bifurcation. We performed $T_1$, $T_2$, $T_2$* and DWI in MRI and observed no differences between the thrombin and the $AlCl_3$ model (Fig S2 A,B). We injected a gadolinium-based contrast agent while acquiring dynamic perfusion images and made a reconstruction of the perfusion maps ; similar perfusion default was observed in the ischemic area for both models. The perfusion index measured inside the cortex, along with mean angiographic scores (MAS) obtained from magnetic resonance angiography (Fig S2 C) confirms a diminution of perfusion in the ipsilateral cortex (56,40% and 53,11% of perfusion for thrombin and $AlCl_3$ models, respectively) and does not show any statistical differences. After MRI acquisitions, the brain of the mice are collected and observed in fluorescence after immunohistochemistry (IHC). Colocalisation of anti-platelets and anti-fibrin antibody confirm the presence of microthrombi in the cortex of the thrombin-induced animals, but no microthrombi could be found in the $AlCl_3$ induced animals (Fig S2 D). All together, these results suggest that although the two models are strongly different due to the presence of multiple microthrombi in the thrombin model, no differences are observed using standard MRI modalities without a microthrombi-targeted contrast agent.

We tested an approach of molecular imaging to reveal the presence of microthrombi in the thrombin model, with the PHySIOMIC particles that have favourable relaxivity and efficient targeting properties to microthrombi, as confirmed by the *in vitro* studies. The mice were scanned with $T_2$*-weighted MRI before and after injections of PHySIOMIC suspensions (Fig 4A). Post-injection images shows a strong hyposignal formed in the ipsilateral cortex within the ischemic area (Fig 4B). Perls' staining of the iron revealed in histology the presence of PHySIOMIC particles around microthrombi (Fig 4 G). MRI images were acquired 10 min after PHySIOMIC injection, suggesting a short half-life of the particles as described in previous study on microparticles[36,37], and observed in Fig S3. $T_2$-weighted images were acquired 24 hours after the thrombin injection to measure the lesion size. Comparison of the area of hyposignal in the mice brains and lesion size at 24h exhibits a significant linear correlation (Fig 4 D,E), with a $R^2$ of 0.9329. The 3D representation of PHySIOMIC-induced hyposignal shows the repartition of hyposignal in the lesion area (Fig 4E). Our findings shows that in addition to reveal microthrombosis in a stroke model, our particles could predict the lesion size at 24 hours. It also highlights the role of microthrombosis in stroke models and suggests that a particular attention should be given to their impact on the lesion size for future treatment study. One of the major concern with contrast agent is the time of elimination once injected. We performed dynamic MRI imaging during PHySIOMIC injection and we observed a very short half-life compared to SPIO (Fig S3). Those results are consistent with previous evaluation of micrometric particles half-life and highlights the advantage of micrometric particles over SPIO for rapid and repeated imaging[19]. To assess the kinetic of the PHySIOMIC-induced hyposignal after injection associated with microthrombi, repeated MRI were acquired every 6 hours during 24 hours (Fig 5A). Images shows a decrease of the hyposignal over 24 hour (Fig 5B), until restauration to the baseline signal at 24 hours. The experiment demonstrates the loss of hyposignal volume over time until no hyposignal could be detected, at 24 hours after injection (Fig 5C). Those results are in line with spontaneous reperfusion observe with MR angiography in this model[38], suggesting that the signal loss is associated with a slow and spontaneous microthrombi degradation.

We also evaluated the PHySIOMIC signal obtained according to the time between the induction of the stroke and the injection of particles (Fig S4A). The hyposignal is strongest when injected at 30 min post stroke onset and diminish with the extension of the delay between the stroke induction and the injection time. We evaluated that PHySIOMIC can successfully reveals microthrombosis up to 2 hours after stroke onset, as it is not significantly different at 3 and 6 hours (Fig S4 B,C).

### 5. Monitoring of microthrombosis using PHySIOMIC during thrombolysis

The thrombin-induced stroke model is commonly used to evaluate the efficacy of new thrombolytic treatments [38,39]. Our aim was to evaluate the efficacy of recombinant tissue-type Plasminogen Activator or rtPA (Alteplase®) - the gold standard for thrombolytic therapy in ischemic stroke patients - on microthrombosis, using the PHySIOMIC contrast agent to monitor microthrombi on $T_2$*-weighted MRI scans (Fig 6A). While pre-treatment images exhibits a strong hyposignal, the $T_2$*-weighted images after rtPA administration shows significantly lower signal, in accordance to a reduction of the microthrombosis (Fig 6B). In mice treated with saline, no differences were measured between the hyposignal obtained pre and post-treatment. Magnetic resonance angiographies display a restoration of the blood flow in the MCA and downstream vasculature for rtPA-treated mice (Fig 6D). Previous studies using the thrombin model have demonstrated that there is a spontaneous partial restoration of the blood flow on angiography from 6 hours after stroke onset, a full restoration at 24 hours[40], and a faster restoration of the blood flow when the mice were treated with rtPA. All these characteristics were observed in our study, which confirms a correlation between blood flow recovery and reduction of microthrombosis.

## Conclusion

The developed PHySIOMIC contrast agent combines strong magnetic and thrombosis targeting properties. We demonstrated its ability to reveal in an ultra-sensitive and high-resolution manner the presence of cortical microthrombi in an ischemic stroke mouse model in MRI. The PHySIOMIC contrast agent also exhibit a good biocompatibility, similar to FDA-approved SPIO nanoparticles. Although the mechanism of targeting on microthrombosis needs further investigation, we demonstrated that the protein corona formed at the surface is involve in the process of fixation. *In vivo* injection of PHySIOMIC in a thrombin-induced stroke models reveals microthrombosis in T2*-weighted images shortly after the stroke onset. Induced targeted hyposignal is disappearing after 24 hours. Furthermore, PHySIOMIC used in the context of a thrombolytic study shows good ability to monitor microthrombosis degradation. Overall, this contrast agent could help to reveal and monitor microthrombosis in stroke patients, and guide treatment strategies.

## References

1. de los Ríos la Rosa, F. *et al.* Eligibility for Intravenous Recombinant Tissue-Type Plasminogen Activator Within a Population. *Stroke* **43**, 1591–1595 (2012).
2. Berkhemer, O. A. *et al.* A Randomized Trial of Intraarterial Treatment for Acute Ischemic Stroke. *N. Engl. J. Med.* **372**, 11–20 (2015).
3. Goyal, M. *et al.* Randomized assessment of rapid endovascular treatment of ischemic stroke. *N. Engl. J. Med.* **372**, 1019–1030 (2015).
4. Molina, C. A. *et al.* REVASCAT: a randomized trial of revascularization with SOLITAIRE FR device vs. best medical therapy in the treatment of acute stroke due to anterior circulation large vessel occlusion presenting within eight-hours of symptom onset. *Int. J. Stroke Off. J. Int. Stroke Soc.* **10**, 619–626 (2015).
5. Saver, J. L. *et al.* Stent-retriever thrombectomy after intravenous t-PA vs. t-PA alone in stroke. *N. Engl. J. Med.* **372**, 2285–2295 (2015).
6. Idicula, T. T., Naess, H. & Thomassen, L. Microemboli-monitoring during the acute phase of ischemic stroke: Is it worth the time? *BMC Neurol.* **10**, 79 (2010).
7. Broocks, G. *et al.* Impact of intravenous alteplase on sub-angiographic emboli in high-resolution diffusion-weighted imaging following successful thrombectomy. *Eur. Radiol.* **31**, 8228–8235 (2021).
8. Alves, H. C. *et al.* Thrombus Migration Paradox in Patients With Acute Ischemic Stroke. *Stroke* **50**, 3156–3163 (2019).
9. Hilal, S. *et al.* Cortical cerebral microinfarcts on 3T MRI: A novel marker of cerebrovascular disease. *Neurology* **87**, 1583–1590 (2016).
10. Shih, A. Y. *et al.* The smallest stroke: occlusion of one penetrating vessel leads to infarction and a cognitive deficit. *Nat. Neurosci.* **16**, 55–63 (2013).
11. Zaidat, O. O. *et al.* Primary Results of the Multicenter ARISE II Study (Analysis of Revascularization in Ischemic Stroke With EmboTrap). *Stroke* **49**, 1107–1115 (2018).

12. Desilles Jean-Philippe *et al.* Alteplase Reduces Downstream Microvascular Thrombosis and Improves the Benefit of Large Artery Recanalization in Stroke. *Stroke* **46**, 3241–3248 (2015).

13. Gratz, P. P. *et al.* Whole-Brain Susceptibility-Weighted Thrombus Imaging in Stroke: Fragmented Thrombi Predict Worse Outcome. *AJNR Am. J. Neuroradiol.* **36**, 1277–1282 (2015).

14. Uppal, R. *et al.* Molecular MRI of intracranial thrombus in a rat ischemic stroke model. *Stroke* **41**, 1271–1277 (2010).

15. Kim, J.-Y. *et al.* Direct Imaging of Cerebral Thromboemboli Using Computed Tomography and Fibrin-targeted Gold Nanoparticles. *Theranostics* **5**, 1098–1114 (2015).

16. Shah, A. & Dobrovolskaia, M. A. Immunological Effects of Iron Oxide Nanoparticles and Iron-based Complex Drug Formulations: Therapeutic Benefits, Toxicity, Mechanistic Insights, and Translational Considerations. *Nanomedicine Nanotechnol. Biol. Med.* **14**, 977–990 (2018).

17. Muehe, A. M. *et al.* Differentiation of benign and malignant lymph nodes in pediatric patients on ferumoxytol-enhanced PET/MRI. *Theranostics* **10**, 3612–3621 (2020).

18. Kolosnjaj-Tabi, J. *et al.* Heat-generating iron oxide nanocubes: subtle ‘destructurators’ of the tumoral microenvironment. *ACS Nano* **8**, 4268–4283 (2014).

19. Perez-Balderas, F. *et al.* Covalent assembly of nanoparticles as a peptidase-degradable platform for molecular MRI. *Nat. Commun.* **8**, 14254 (2017).

20. Li, B. *et al.* Improved Stability and Photothermal Performance of Polydopamine-Modified Fe3 O4 Nanocomposites for Highly Efficient Magnetic Resonance Imaging-Guided Photothermal Therapy. *Small Weinh. Bergstr. Ger.* **16**, e2003969 (2020).

21. Zhong, X. *et al.* Polydopamine as a Biocompatible Multifunctional Nanocarrier for Combined Radioisotope Therapy and Chemotherapy of Cancer. *Adv. Funct. Mater.* **25**, 7327–7336 (2015).

22. Shu, G. *et al.* Sialic acid-engineered mesoporous polydopamine nanoparticles loaded with SPIO and Fe3+ as a novel theranostic agent for T1/T2 dual-mode MRI-guided combined chemo-photothermal treatment of hepatic cancer. *Bioact. Mater.* **6**, 1423–1435 (2020).

23. Lee, H., Scherer, N. F. & Messersmith, P. B. Single-molecule mechanics of mussel adhesion. *Proc. Natl. Acad. Sci. U. S. A.* **103**, 12999–13003 (2006).

24. Ju, K.-Y., Lee, Y., Lee, S., Park, S. B. & Lee, J.-K. Bioinspired Polymerization of Dopamine to Generate Melanin-Like Nanoparticles Having an Excellent Free-Radical-Scavenging Property. *Biomacromolecules* **12**, 625–632 (2011).

25. Gupta, A., Pratt, R. D. & Crumbliss, A. L. Ferrous iron content of intravenous iron formulations. *Biometals Int. J. Role Met. Ions Biol. Biochem. Med.* **29**, 411–415 (2016).

26. Bonnard, T. *et al.* Low-Fouling and Biodegradable Protein-Based Particles for Thrombus Imaging. *ACS Nano* **12**, 6988–6996 (2018).

27. Orset, C. *et al.* Mouse Model of In Situ Thromboembolic Stroke and Reperfusion. *Stroke* **38**, 2771–2778 (2007).

28. Karatas, H. *et al.* Thrombotic distal middle cerebral artery occlusion produced by topical FeCl3 application: a novel model suitable for intravital microscopy and thrombolysis studies. *J. Cereb. Blood Flow Metab.* **31**, 1452–1460 (2011).

29. Gauberti, M., Lizarrondo, S. M. de, Orset, C. & Vivien, D. Lack of secondary microthrombosis after thrombin-induced stroke in mice and non-human primates. *J. Thromb. Haemost.* **12**, 409–414 (2014).

30. Gauberti, M. *et al.* Thrombotic stroke in the anesthetized monkey (Macaca mulatta): characterization by MRI--a pilot study. *Cerebrovasc. Dis. Basel Switz.* **33**, 329–339 (2012).

31. Khalkhali, M. *et al.* Synthesis and characterization of dextran coated magnetite nanoparticles for diagnostics and therapy. *BioImpacts BI* **5**, 141–150 (2015).

32. Hinds, K. A. *et al.* Highly efficient endosomal labeling of progenitor and stem cells with large magnetic particles allows magnetic resonance imaging of single cells. *Blood* **102**, 867–872 (2003).

33. Ehlerding, E. B., Chen, F. & Cai, W. Biodegradable and Renal Clearable Inorganic Nanoparticles. *Adv. Sci.* **3**, 1500223 (2016).

34. Sakulkhu, U., Mahmoudi, M., Maurizi, L., Salaklang, J. & Hofmann, H. Protein Corona Composition of Superparamagnetic Iron Oxide Nanoparticles with Various Physico-Chemical Properties and Coatings. *Sci. Rep.* **4**, 5020 (2015).

35. Lundqvist, M. *et al.* Nanoparticle size and surface properties determine the protein corona with possible implications for biological impacts. *Proc. Natl. Acad. Sci.* **105**, 14265–14270 (2008).

36. Montagne, A. *et al.* Ultra-sensitive molecular MRI of cerebrovascular cell activation enables early detection of chronic central nervous system disorders. *NeuroImage* **63**, 760–770 (2012).

37. Gauberti, M. *et al.* Ultra-Sensitive Molecular MRI of Vascular Cell Adhesion Molecule-1 Reveals a Dynamic Inflammatory Penumbra After Strokes. *Stroke* **44**, 1988–1996 (2013).

38. Ansar, S. *et al.* Characterization of a New Model of Thromboembolic Stroke in C57 black/6J mice. *Transl. Stroke Res.* **5**, 526–533 (2014).

39. Arkelius, K., Vivien, D., Orset, C. & Ansar, S. Validation of a stroke model in rat compatible with rt-PA-induced thrombolysis: new hope for successful translation to the clinic. *Sci. Rep.* **10**, (2020).

40. Martinez de Lizarrondo, S. *et al.* Potent Thrombolytic Effect of N-Acetylcysteine on Arterial Thrombi. *Circulation* **136**, 646–660 (2017).

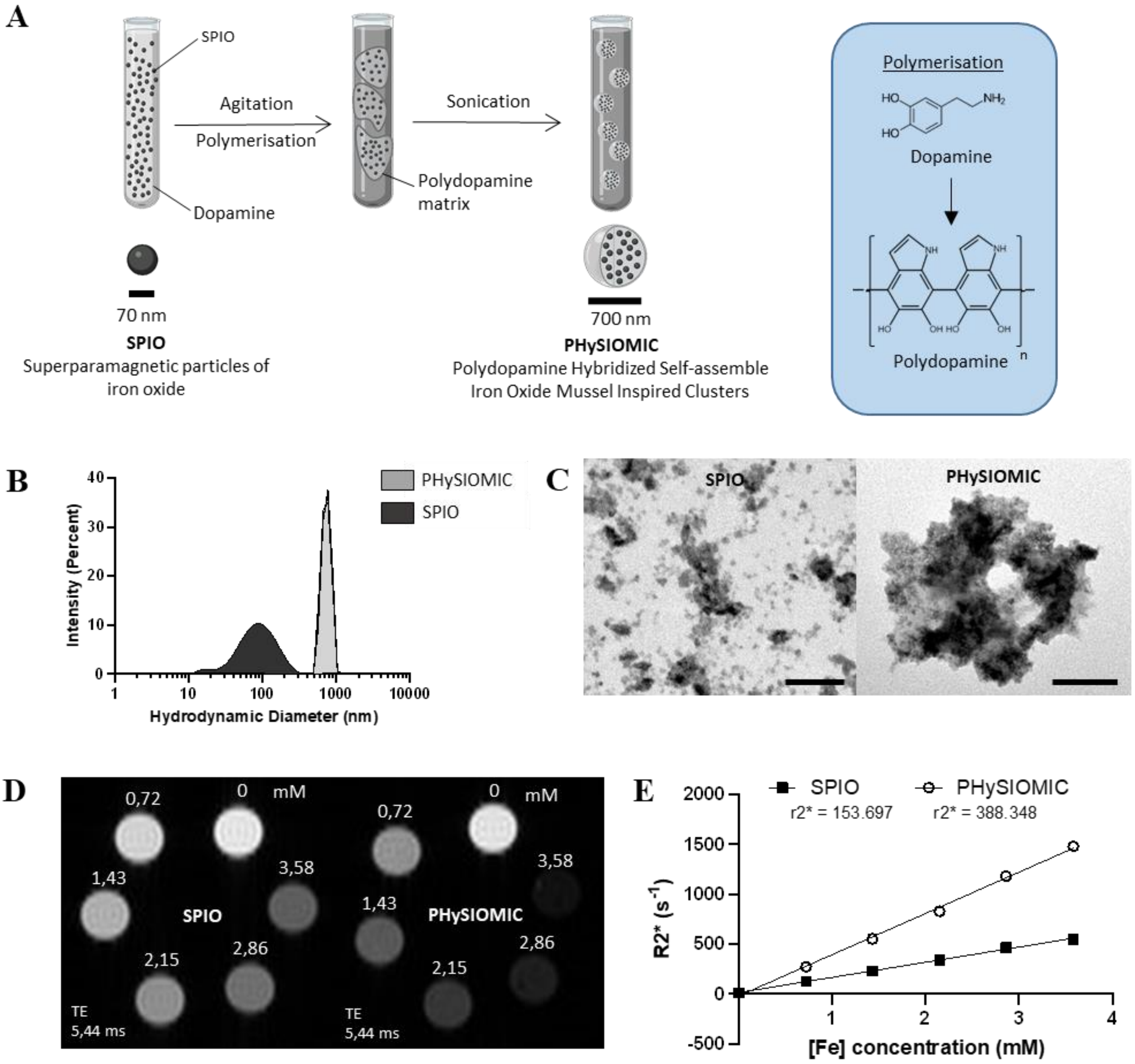

**Figure 1. PHySIOMIC synthesis and physico-chemical caracteristics**. Mechanism of PHySIOMIC synthesis with SPIO particles (**A**). Dynamic light scattering analysis of PHySIOMIC and SPIO particles mean hydrodynamic diameter (**B**) and morphological and core size observation with TEM. Scale bar = 100 nm (**C**). MR imaging (**D**) and measurement of relaxivities (**E**) on a $T_2$*-weighted sequence of PHySIOMIC and SPIO. T1 and T2 relaxivities are shown in supplementary data.

| | SPIO | PHySIOMIC |
|---|---|---|
| Hydrodynamic diameter (nm) ± SD | 78.53 ± 11.3 | 753.7 ± 47,5 *** |
| Polydispersity index ± SD | 0.22 ± 0.04 | 0.22 ± 0.19 |
| Zeta potential (mV) ± SD | -11.09 ± 1.56 | -36.37 ± 2.45 *** |
| Iron concentration (mg.mL$^{-1}$) ± SD | 0.481 ± 0.024 | 0.417 ± 0.017 |
| Particle Concentration (u.mL$^{-1}$) | 1,151 e$^{10}$ | 9,968 e$^{06}$ |
| Relaxivity r1 (mM$^{-1}$.s$^{-1}$) | 0.801 | 0.486 |
| Relaxivity r2 (mM$^{-1}$.s$^{-1}$) | 121.133 | 119.558 |
| Relaxivity r2* (mM$^{-1}$.s$^{-1}$) | 153.697 | 388.348 |

**Table 1**. Summary of physico-chemical properties of SPIO and PHySIOMIC. *** Statistical differences with p-value < 0,001

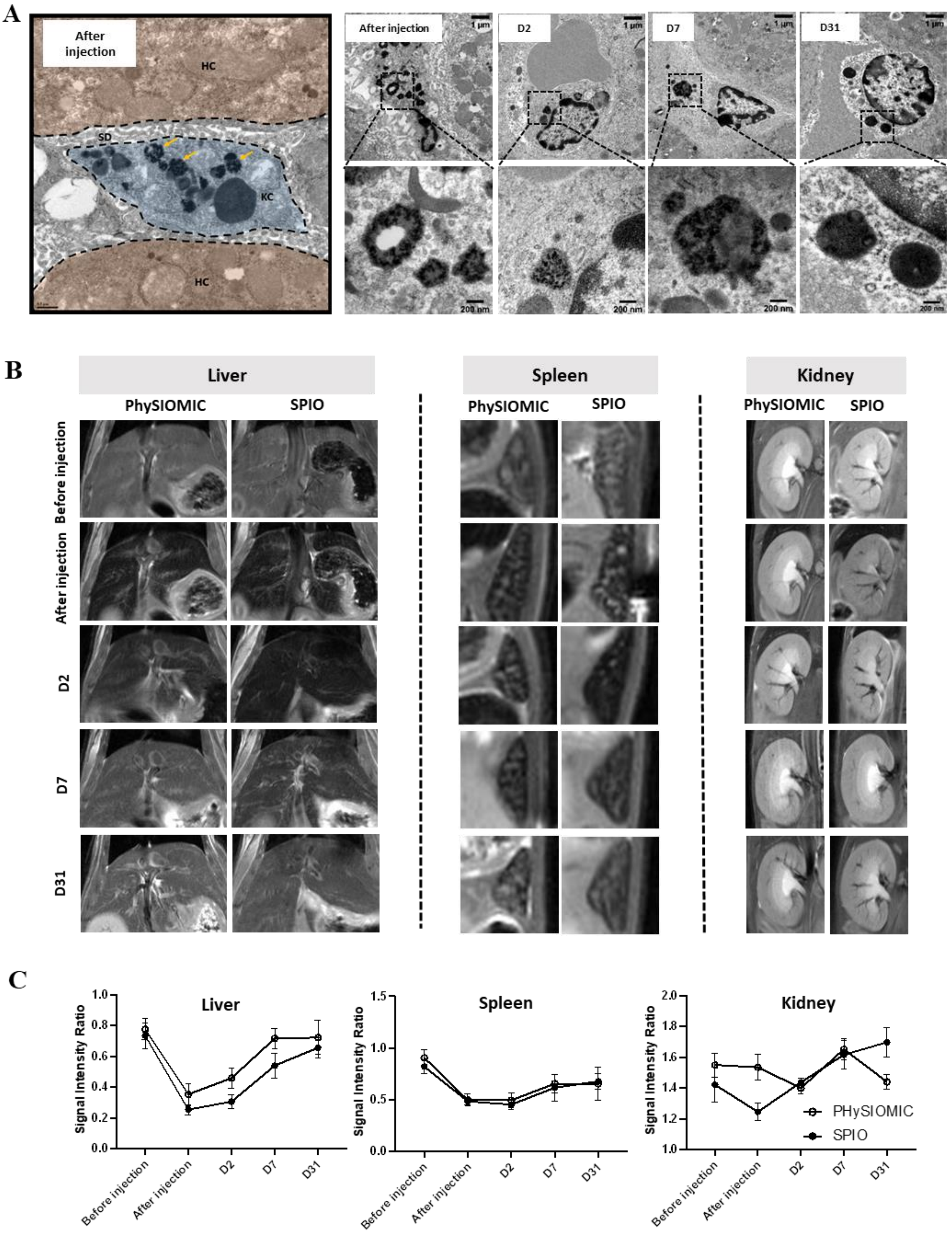

**Figure 2. PHySIOMIC microparticles show a biodistribution and a biodegradation in the liver and spleen in full body MRI and TEM**. TEM images of the degradation of PHySIOMIC in the Kupffer cells (KC) located inside the Space of Diss (SD) between hepatocytes (HC) the of the liver (**A**). $T_2$-weighted images were acquired before and after injection of PHySIOMIC and SPIO (4 mg.kg$^{-1}$), and longitudinaly at 2, 7 and 31 days (**A**). Quantification of $T_2$-values in the liver, spleen and kidneys (**C**).

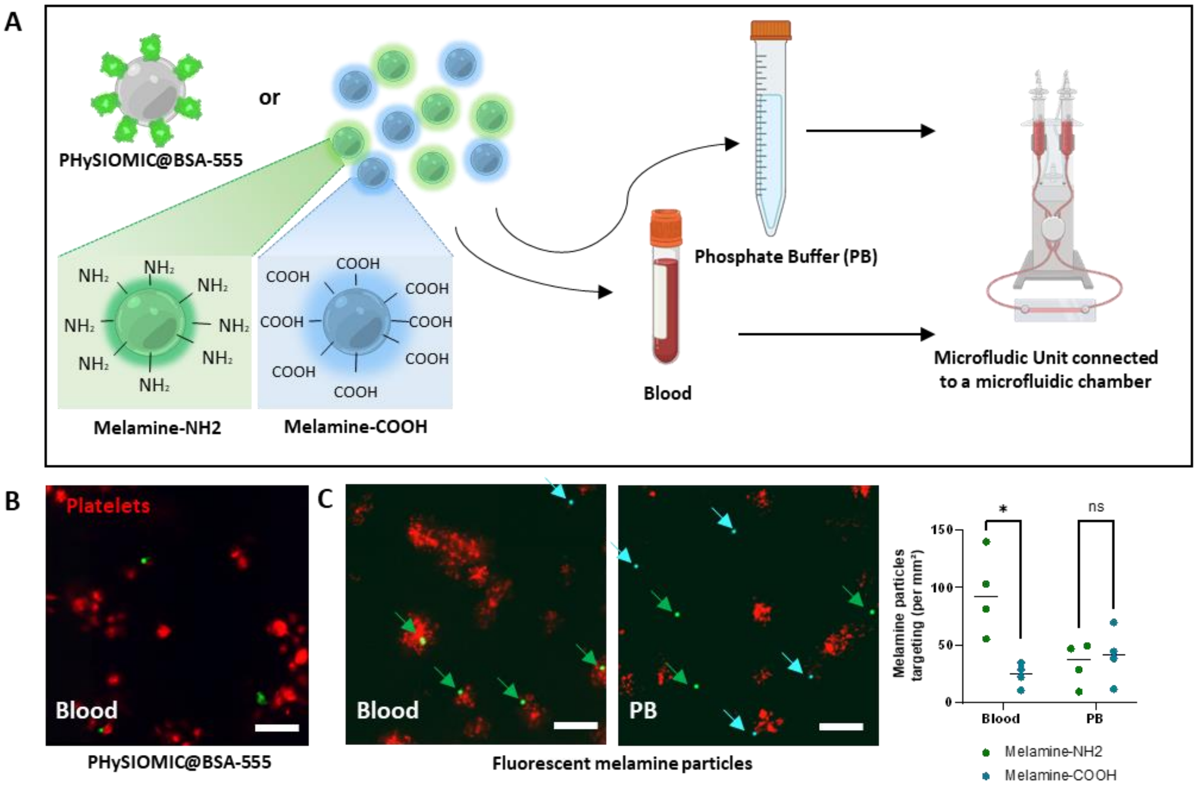

**Figure 3 Implication of surface functionnalizations of particles on microthrombi targeting.** PHySIOMIC graphed with BSA-555 and commercial melamine microparticules with different functionnalizations ($NH_2$ or COOH) were incubated either with phosphate Buffer (PB) or human blood and injected in the microfluidic chamber with microthrombi (**A**). PHySIOMIC@BSA-555 are found in the microfluidic chamber at the edges of microthrombi (**B**, video in supplementary data). Melamine-$NH_2$ and Melamine-COOH are found at the same number on microthrombi (around 50 per mm²). Whereas 95 ± 36 per mm² of Melamine-$NH_2$ injected in human blood were found on microthrombi, and only 24 ± 10 per mm² for Melamine-COOH. Scale bar = 10 µm.

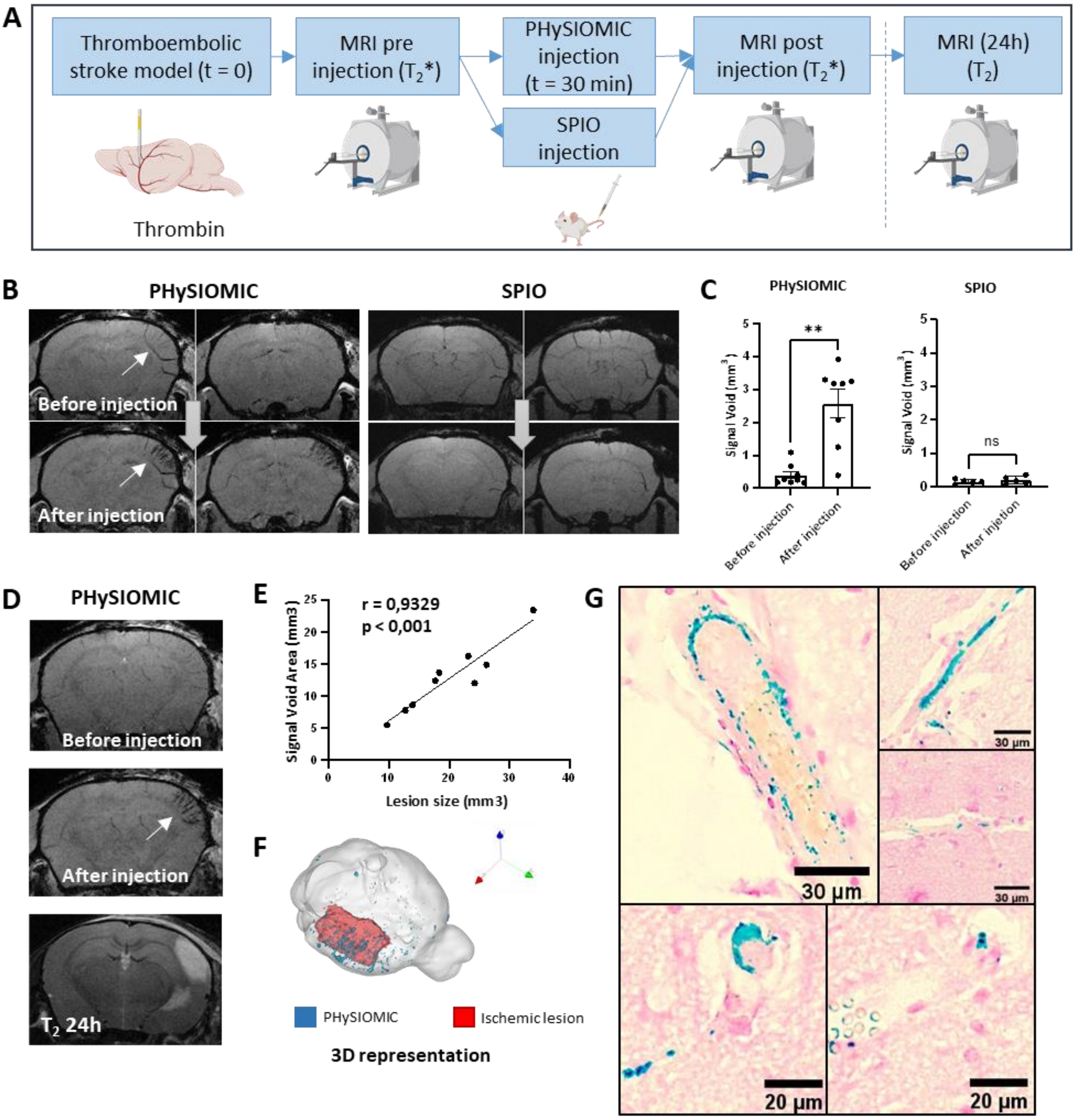

**Figure 4. Intravenous injection of PHySIOMIC reveals microthrombosis during the acute phase of stroke in a thromboembolic stroke models induced by injection of thrombin and induced hyposignal correlates with the lesion size at 24h.** PHySIOMIC or SPIO were injected intravenously in a thrombin-induced stroke model and T2*-weighted images were acquired in MRI (**A**). PHySIOMIC particles induce hyposignals in T2*-weighted images in the brain cortex whereas no hyposignal is seen with SPIO (**B**). Quantification of signal void in mm$^3$ before and after PHySIOMIC (n=8) or SPIO injection injection (n=5) (**C**). Signal void area observed right after the occlusion in a $T_2$*-weighted sequence is predictive of the lesion size observed at 24h after occlusion in a $T_2$-weighted sequence (**D**). Signal void area measures show a significant correlation to lesion size at 24h with p-value = 0,0007 (**E**). 3D representation of PHySIOMIC-induced hyposignal and lesion hypersignal in MRI (**F**). Perls' staining of ferric iron (blue) in PHySIOMIC in the brain cortex, counterstained with nuclear fast red. (**G**).

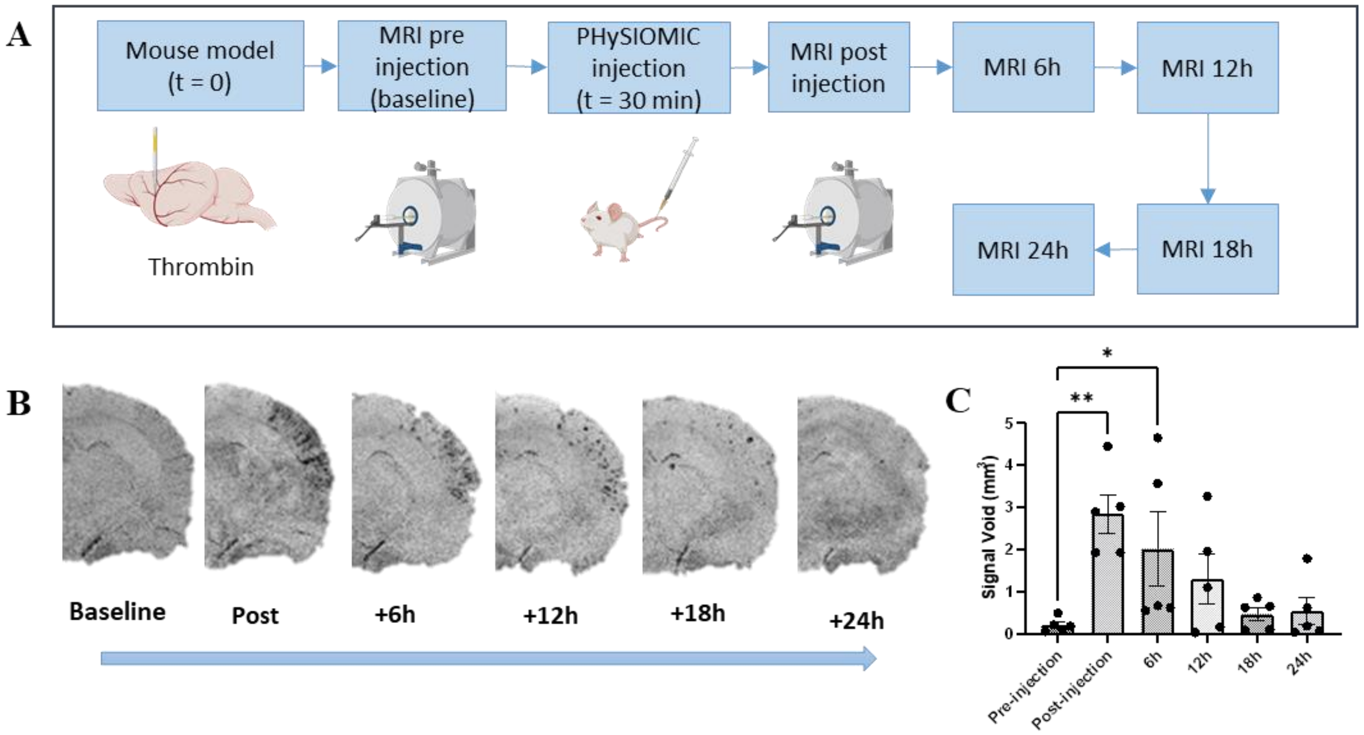

**Figure 5. PHySIOMIC injected in a thromboembolic stroke model induce an hyposignal that disappear spontaneously with time**. T2*-weighted images were acquired before and after PHySIOMIC injection and followed at 6, 12, 18 and 24 hours (**A**). Hyposignal decreases althrough 24 hours (**B**). Same animals were longitudinally imaged (n = 5), so statistical analysis is a one-way ANOVA with Dunnett's multiple comparisons test with Pre-injection as reference (**C**).

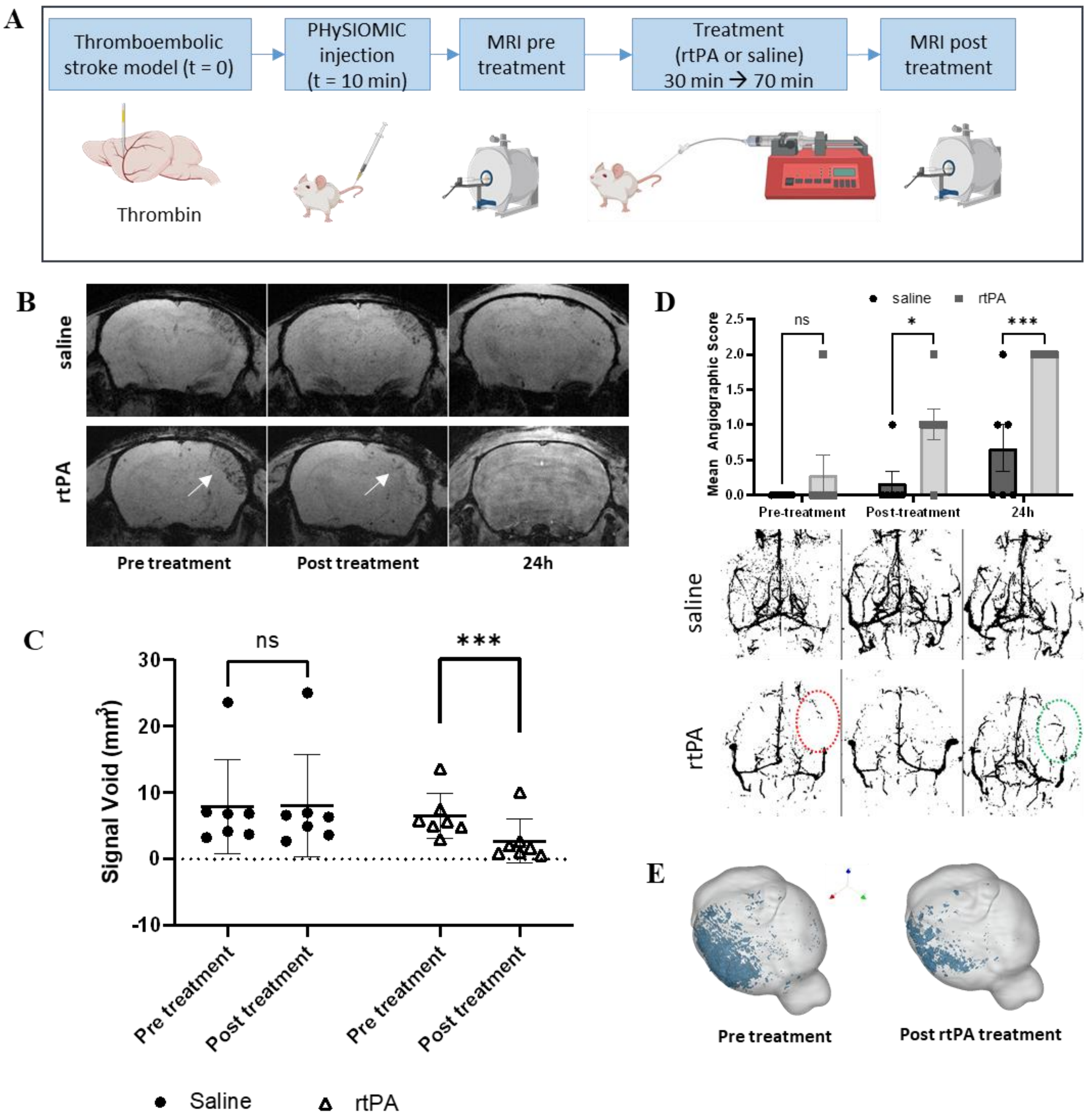

**Figure 6. PHySIOMIC-induced hyposignal decreases in thrombolysed mice**. PHySIOMIC were injected 10 min after occlusion and T2*-weighted sequence were acquired before and after treatment either with tPA or saline (**A**). MRI images shows a decrease of the hyposignal only in rtPA treated mice (**B**). Quantification of induced hyposignal reveals a diminution in the treated group and no changes for the saline group (n = 7) (**C**). Magnetic resonance angiography display a restoration of the blood flow in the MCA and downstream vasculature for r-tPA-treated mice (**D**). 3D representation of PHySIOMIC in the brain of one animal before and after treatment with rtPA (**E**).

# Supplementary data

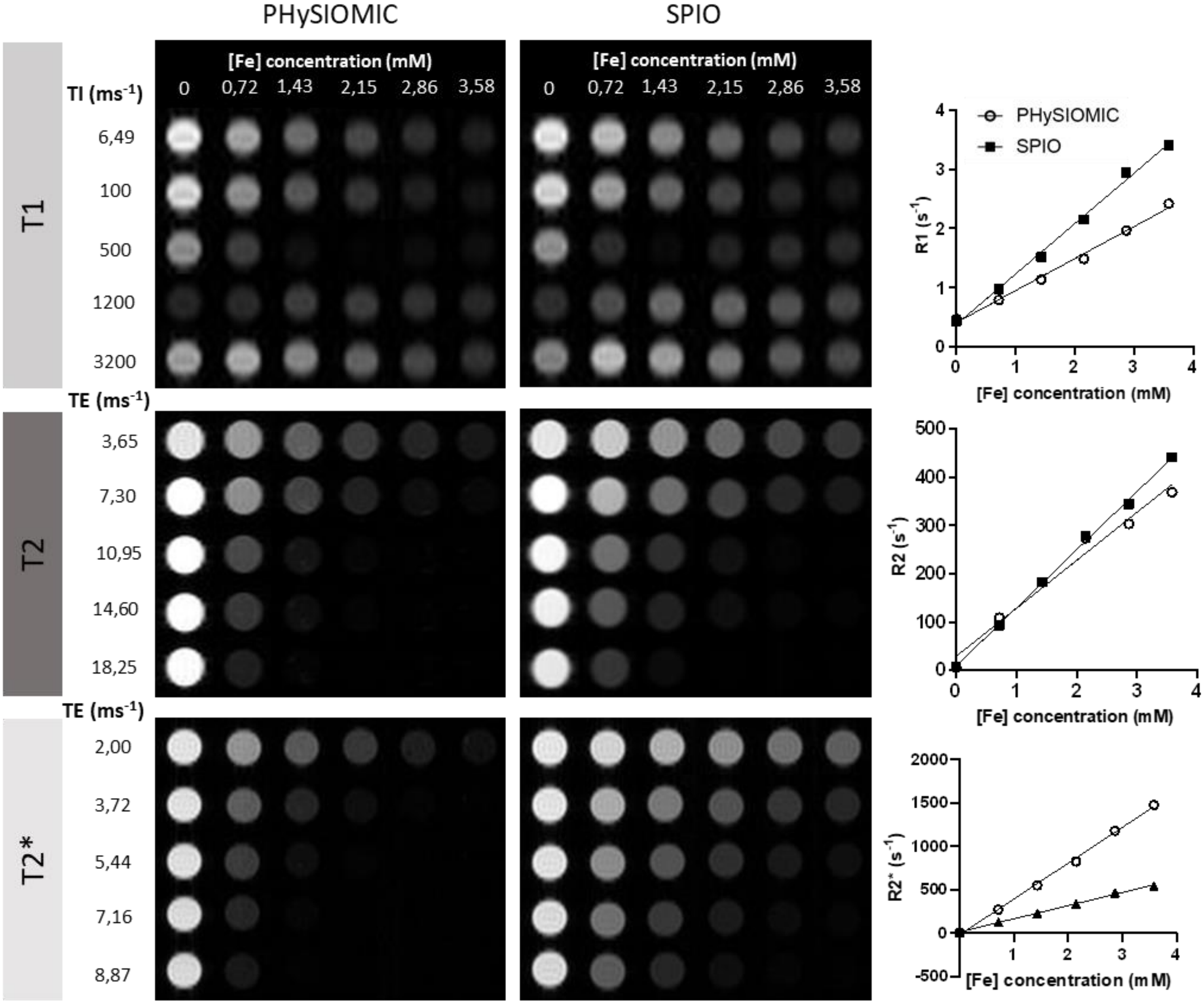

**Figure S1. Evaluation of PHySIOMIC relaxivity over SPIO on T1, T2 and T2*-weighted MRI.** T1, T2 and T2*-weighted MRI of PHySIOMIC and SPIO particles at different concentrations with the corresponding relaxation values (R1, R2, R2*). PHySIOMIC shows a lower relaxivity in T1-weighted, similar in T2-weighted, and two-fold higher in T2*-weighted images.

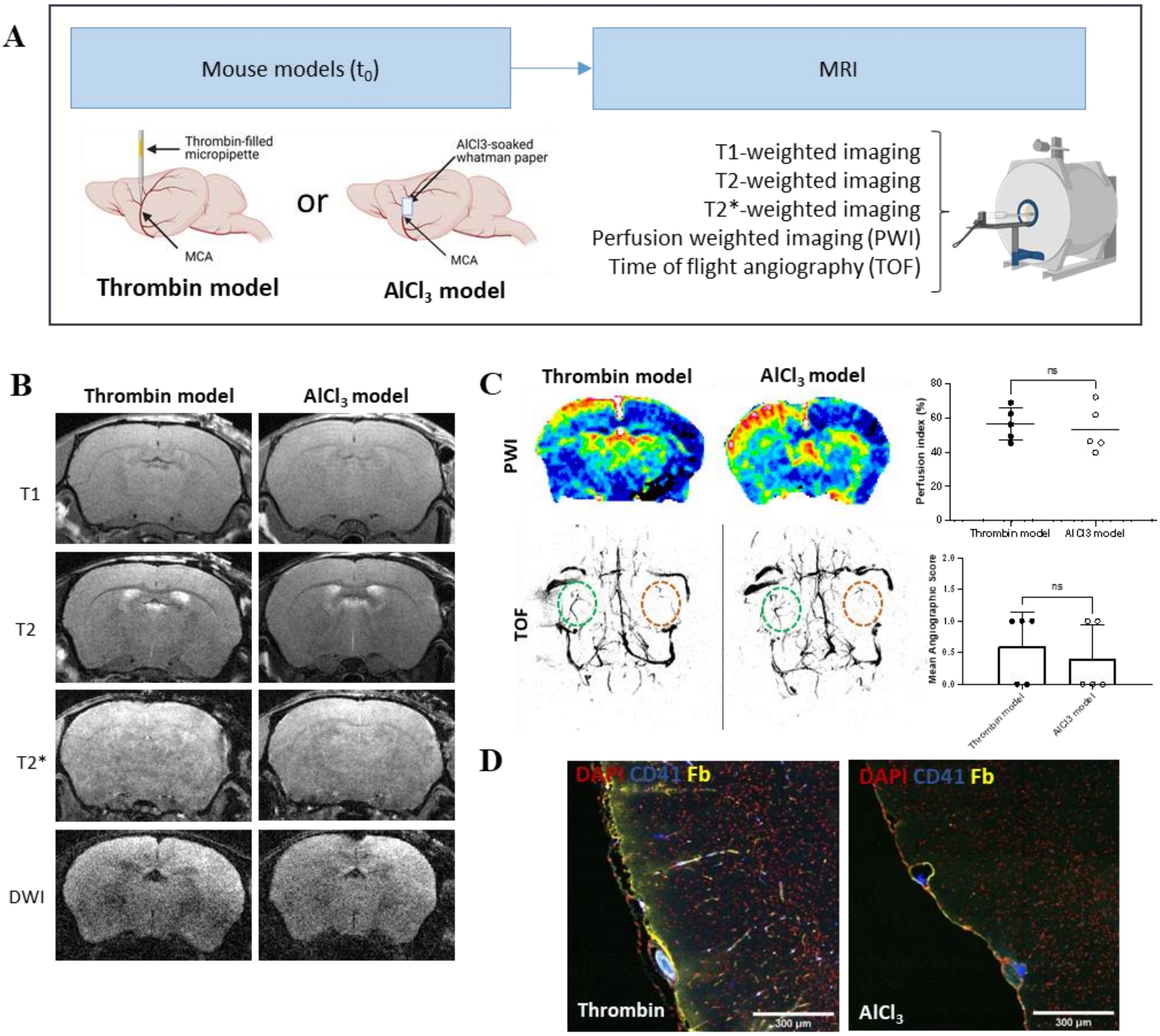

**Figure S2. There are no differences between a stroke model with microthrombosis (thrombin model) and a thromboembolic stroke model without ($AlCl_3$ model, control) at MRI.** Protocole (A). Comparative MRI sequences showing no differrences between the two stroke models (B). Perfusion and angiography images and analysis showing no differences (C). Immunohistological staining demonstrates microthrombi in thrombin model (CD41/Fb) in the ipsilateral cortex, and showing CD41+ thrombi only in the $AlCl_3$ model (D).

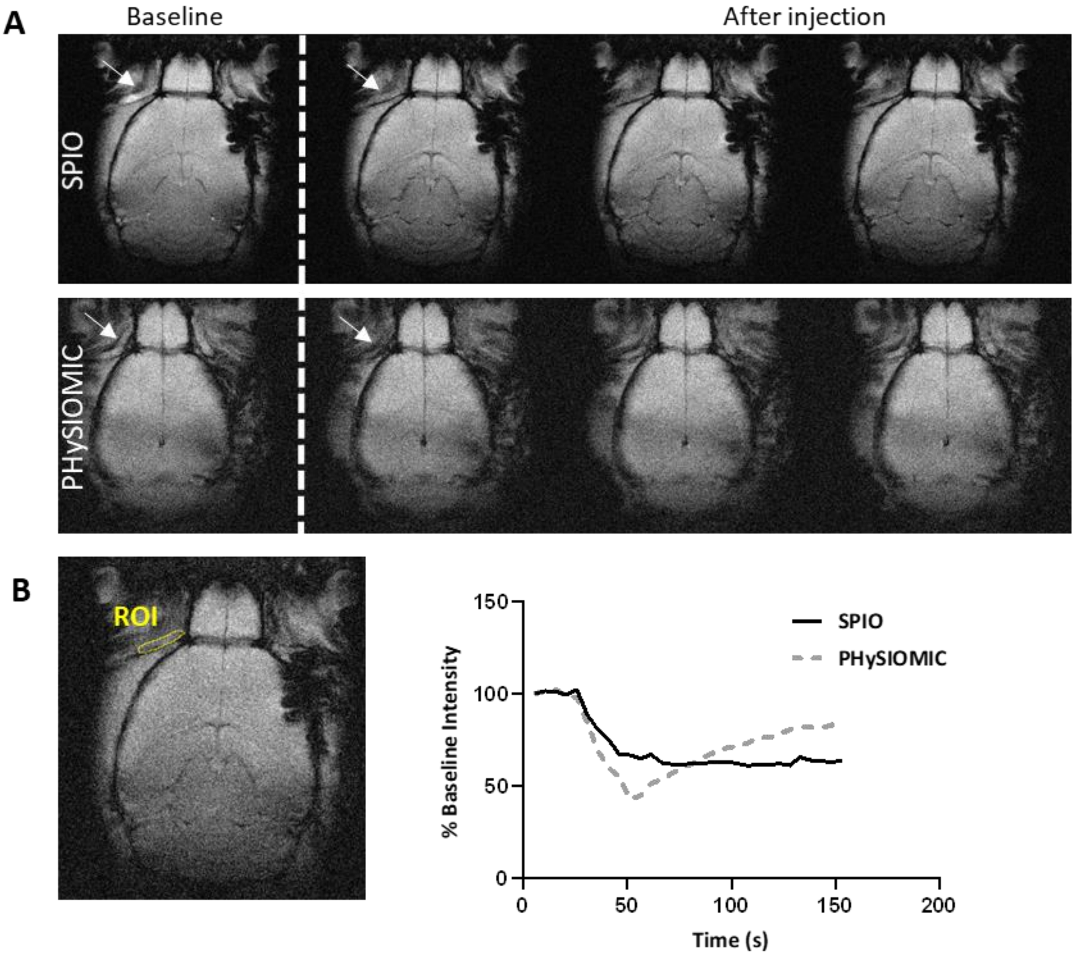

**Figure S3. Blood circulation time of SPIO and PHySIOMIC.** Dynamic T2*-weighted MRI acquisitions of mouse brain during intravenous injection of SPIO or PHYSIOMIC (**A**). Quantification of particles-induced signal over time in the supraorbital vein (**B**).

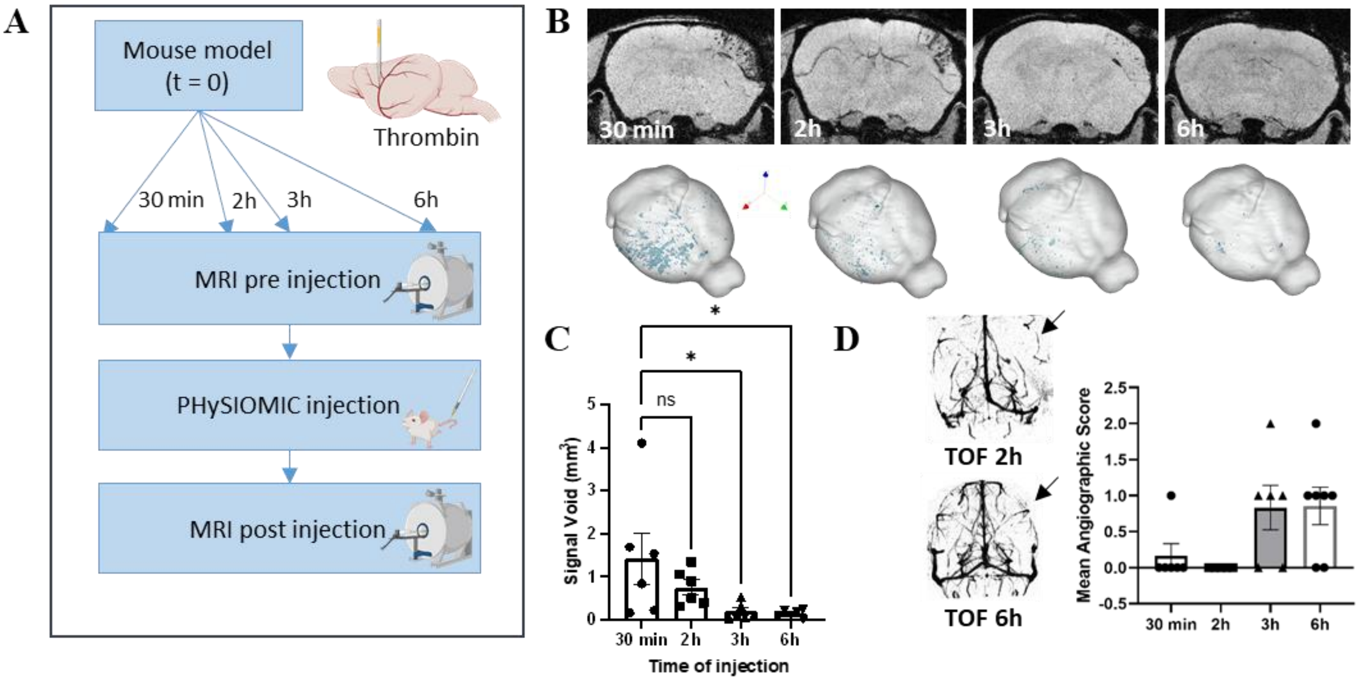

**Figure S4. Microthrombosis follow-up using PHySIOMIC in MRI.** PHySIOMIC were injected intraveneously at 30 min, 2h, 3h and 6h after stroke onset (**A**). MRI images and 3D representation of of PHySIOMIC-induced hyposignal (**B**), and quantification showing a decrease of microthrombosis over time (**C**), in line with spontaneous reperfusion observed in TOF angiograhy (**D**).

# DISCUSSION

# Discussion

La microthrombose après un AVC ischémique est associée à l'apparition de démences et de déficits cognitifs à long-terme (Dalkara and Arsava, 2012). Ce chiffre est probablement sous-estimé car les techniques d'imagerie des microthrombi sont limitées, leur sensitivité étant trop faible. Récemment, l'émergence de nouvelles nanoparticules composées d'oxydes de fer pour l'IRM moléculaire ont permis d'augmenté la sensibilité et le marquage de thrombi. Les particules d'oxydes de fer de taille micrométrique présentent l'avantage de ne pas pouvoir traverser la BHE, impactée après l'AVC, et ne se déposent pas dans le parenchyme. Dans cette étude, nous avons montré un procédé de synthèse de MPIO biodégradables formés à partir de SPIO pouvant cibler les microthrombi dans un modèle thromboembolique murin.

## 1. Ciblage de la microthrombose par les microparticules PHySIOMIC

Par un procédé d'auto-assemblage des SPIO en PHySIOMIC, nous avons combiné les avantages présentés par les SPIO : un moment magnétique qui permet un signal élevé en IRM pondérée en T2*, et une faible toxicité ; avec ceux offerts par les MPIO : une relaxivité deux fois supérieur en IRM (Perez-Balderas et al., 2017), une large aire de surface qui permet la conjugaison avec des ligands, et un champ d'action restreint aux cibles endovasculaire. A travers la caractérisation des particules par diffusion dynamique de la lumière (Dynamic Light-Scattering ou DLS) et par microscopie électronique, nous avons montré que les SPIO sont agglomérés avec succès et encapsulés dans une matrice formée de PDA.

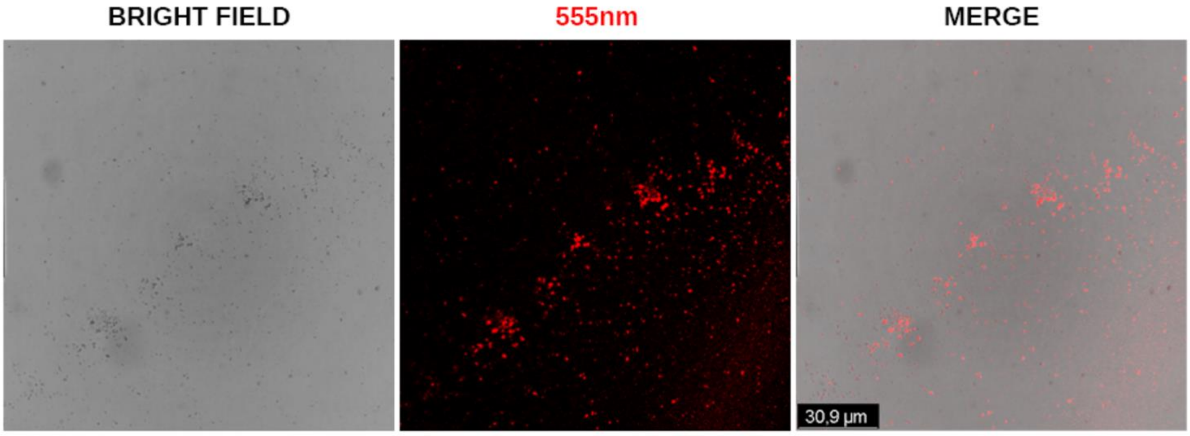

**Figure 48 PHySIOMIC fonctionnalisés avec de la BSA conjuguée au fluorochrome Alexa 555.**

Grâce aux propriétés de surface de la PDA nous avons, réussi à montrer la fonctionnalisation des PHySIOMIC avec l'albumine sérique bovine (BSA) conjuguée avec un fluorochrome Alexa-555 (Figure 48). Cependant, ne connaissant pas les effets de la fonctionnalisation avec la BSA sur le ciblage des microthrombi, nous avons observé par la suite comment les groupes fonctionnels à la surface de particules micrométriques commerciales pouvait influencer le ciblage de la microthrombose. Notre étude s'est concentrée sur les microparticules avec terminaisons avec des groupes fonctionnels de type amine ($NH_2$), similaire au PHySIOMIC, ou carboxylique (COOH). Les microparticules, composée de résine de mélamine, se fixent de manière équivalente aux microthrombi lorsqu'elles sont injectées dans un tampon PB. Nous avons également observé que les particules avec terminaisons $NH_2$ se fixent de manière plus significative que les particules COOH lorsqu'elles sont injectées dans du sang, suggérant un impact de l'incubation des microparticules dans du sang humain.

Le phénomène d'adsorption de protéines sériques à la surface de nanoparticules en présence de sang est bien décrit dans la littérature (Monopoli *et al.*, 2012 ; Figure 49). La couronne de protéines (CP) formée en surface de nanoparticules participe à leur biodistribution, leur reconnaissance par le système immunitaire, leur capture intracellulaire, et leur toxicité (Wolfram *et al.*, 2014). Elle se compose de deux couches : une couche à la surface directe des nanoparticules avec des protéines serrées appelée « hard corona », et une couche externe formée de protéines plus lâches, la « soft corona » (Lundqvist *et al.*, 2008). Les protéines qui la composent sont généralement classées en apolipoprotéines, immunoglobulines, fateurs du complément, facteurs de la coagulation et protéines de la réponse inflammatoire à la phase aigüe (Tenzer *et al.*, 2011). La formation de la CP dépend des intéractions protéines-protéines se formant une fois les nanoparticules en contact avec le plasma humain. Sa présence dépend des caractéristiques des particules. A la fois, plusieurs études ont décrit que la CP influencait le diamètre hydrodynamique des particules, leur charge à la surface mais également leurs formes (Cedervall *et al.*, 2007).

Dans un article de Corbo et collaborateurs, il a été montré que la modification des groupes fonctionnels à la surface de nanoparticules a pour résultat la modulation de l'activation du système de complément (Corbo *et al.*, 2016). Ce dernier correspond aux protéines de surfaces cellulaires qui ont pour rôle le ciblage, l'opsonisation (qui favorise la phagocytose) et l'élimination de micro-organismes ou corps étrangers. C'est pourquoi il est important de réaliser des évaluations physico-chimiques des particules seules, mais aussi après formation de la CP. Il a été par exemple été montré que la modification de la CP à la surface de liposomes entraîne une modification du ciblage des particules qui adoptent une distribution intracérébrale (Zhang *et al.*, 2019).

Conventionnellement, l'identification des protéines plasmatiques impliquées dans la composition de la CP se fait avec l'analyse dite « protéomique » par spectrométrie de masse (Schöttler *et al.*, 2016). Nous avons donc débuté une étude par chromatographie en phase liquide couplée à la spectrométrie de masse avec les PHySIOMIC, mais également avec les particules micrométriques commerciales avec terminaisons amines et carboxyliques, afin de déterminer les modifications qui interviennent au niveau de la CP pouvant être à l'origine d'un ciblage spécifique des microthrombi.

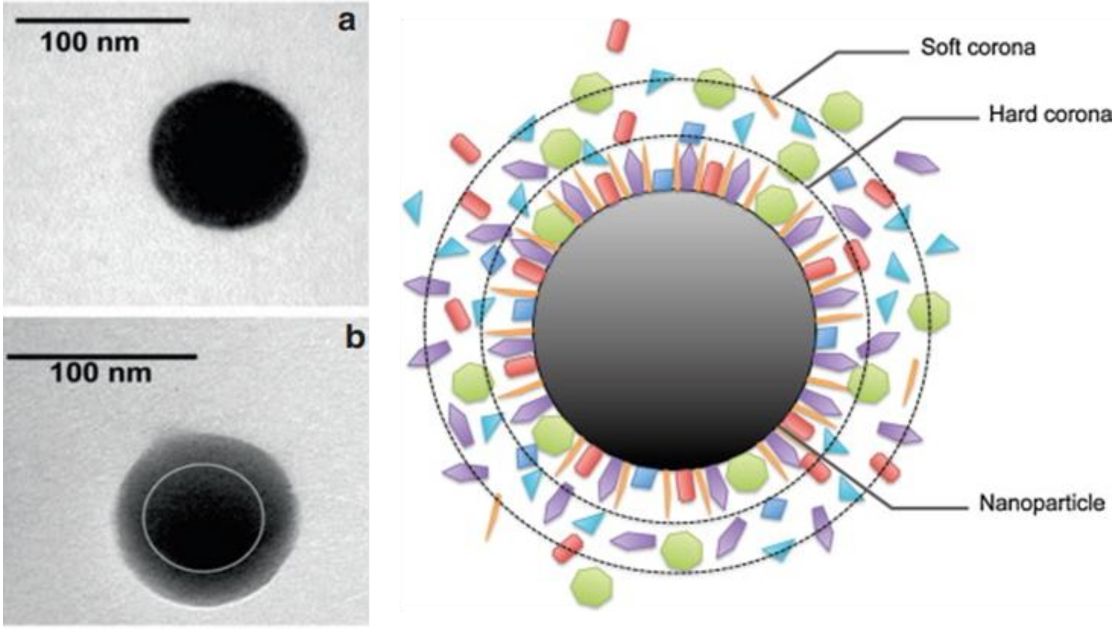

**Figure 49 Structure et composition de la couronne de protéine (Protein Corona) formée autour d'une nanoparticule.**

Par ailleurs, le taux de cisaillement correspond au changement de vitesse du sang lorsque les différentes couches de liquides dans le vaisseau interagissent entre elles. Notre approche par microfluidique utilise un taux de cisaillement du sang similaire à celui des artérioles ($500\ s^{-1}$). Ce taux est variable dans la microcirculation (Koutsiaris *et al.*, 2013) et il serait intéressant de modifier les paramètres en microfluidique, pour étudier le ciblage moléculaire en fonction du taux de cisaillement au niveau de la microcirculation. Par ailleurs, beaucoup d'avancées ont été faites dans le domaine de la microfluidique pour l'ingénierie de systèmes vasculaires *in vitro* (Hu *et al.*, 2019). D'autres études de microfluidique pourrait alors être envisagées afin de se rapprocher au plus proche des conditions de formation de microthrombi (Muthard and Diamond, 2013).

Les microthrombi formés dans notre expérience sont particulièrement riches en plaquettes et en fibrine. Plusieurs publications se sont intéressées à la composition des microthrombi et ont démontré que les signaux microemboliques étaient induit par des thrombi riches en plaquettes et fibrine, après rupture de plaque athérosclérotique (Goertler *et al.*, 2002; Junghans and Siebler, 2003). Cependant nous avons vu précédemment que les thrombi et microthrombi présents dans l'AVC n'ont pas une composition unique. Leur structure peut varier en fonction de l'étiologie, et font l'objet de nombreuses recherche en médecine dite « personnalisée » où le traitement est adapté en fonction des caractéristiques des caillots de chaque patient (Sporns *et al.*, 2019). C'est pourquoi il serait intéressant de déterminer si les PHYSIOMIC présentent une affinité similaire pour les caillots riches en érythrocytes et en leucocytes. Cela est par exemple possible *in vitro,* par induction de thrombose avec du chlorure de fer (Ciciliano *et al.*, 2015).

Ainsi, les PHySIOMIC semble montrer une affinité pour les thrombi et microthrombi *in vitro*. En utilisant les mêmes particules micrométriques nous avons réussi à visualiser, *in vivo*, le ciblage des microthrombi par microscopie biphotonique. Dans un modèle murin d'AVC thromboembolique, qui induit la formation d'une multitude de microthrombi dans le cortex cérébral, nous avons créer une fenêtre crânienne au-dessus de la microvascularisation, où se place l'objectif du microscope (Figure 50). L'injection d'un flurochrome par voie intraveineuse (l'indocyanine) met en évidence l'arborisation vasculaire par fluorescence. Les microparticules injectées émettent en fluorescence dans d'autres longueur d'ondes et nous ont permis d'observer le ciblage des microthrombi. Par la suite, notre étude s'est portée sur l'utilisation des PHySIOMIC spécifiquement pour l'imagerie moléculaire de la microthrombose.

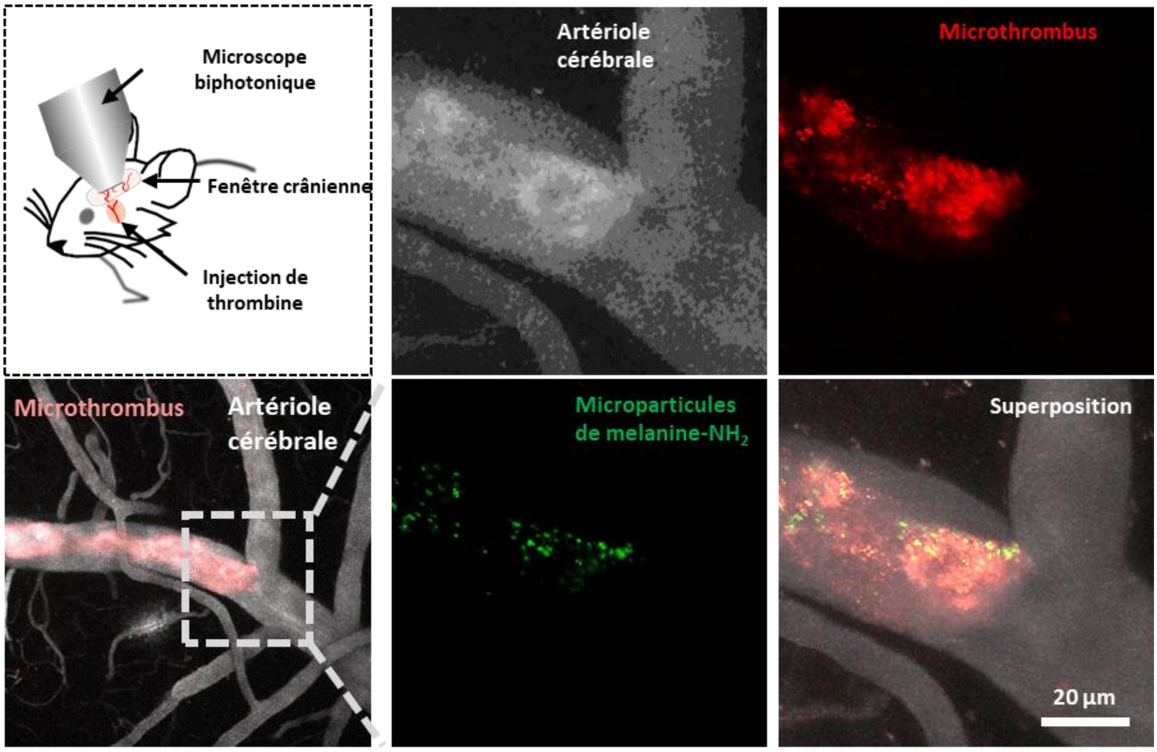

**Figure 50 Ciblage de la microthrombose en microscopie biphotonique.**

Dans un modèle murin d'AVC, les microthrombi sont observés en fluorescnece par microscopie biphotonique, à travers une fenêtre crânienne.

## 2. IRM moléculaire avec les PHySIOMIC

Plusieurs agents de contraste sont disponibles pour imager la thrombose en IRM. Mais aucun des agents de contraste disponible ou en développement ne montre à la fois une relaxivité suffisante pour être visible, même à faible concentrations, et un ciblage de la microthrombose.

Nos résultats ont permis de révéler la microthrombose formée dans un modèle thromboembolique murin, après injection par voie intraveineuse des PHySIOMIC, à la phase aigüe. L'injection de SPIO dans le même modèle ne montre pas de changement de signal de façon significatif après l'injection et démontre la nécessité d'utiliser des particules de tailles micrométriques pour l'observation de la microthrombose en imagerie moléculaire.

Dans un second temps, l'analyse de l'hyposignal induit par l'injection de PHySIOMIC et du signal de lésion observé 24 heures après l'occlusion de l'artère cérébrale moyenne montre une correlation entre ces deux évènements. L'analyse de l'étendue de la microthrombose au temps aigüe pourrait donc prédire la taille de la lésion ischémique dans ce modèle d'AVC. Ce résultat souligne l'intérêt de l'utilisation des PHySIOMIC pour la compréhension au niveau préclinique des mécanismes intervenant dans la formation de la lésion, et par conséquent, pour l'évaluation de molécules thérapeutiques ciblant la microthrombose.

Les hyposignaux corticaux formés suite à l'injection des PHySIOMIC dans le modèle thromboembolique disparaissent après 24 heures. L'injection répétées des microparticules serait possible à condition que celles-ci soient espacées de 24 heures, et pourrait permettre le suivi longitudinal des animaux.

Nous avons ensuite injecté les PHySIOMIC dans un autre modèle d'AVC, induit par application de chlorure d'aluminium au niveau de l'artère cérébrale moyenne. Les résultats n'ont pas montré d'hyposignaux dans le cortex ipsilatérale, confirmant ainsi l'absence de microthrombose dans ce modèle, malgré l'occlusion de l'artère cérébrale moyenne par un thrombus.

L'induction d'un AVC ischémique par insertion d'un filament le long de la carotide interne est un modèle très utilisé chez les rongeurs. Il permet la restauration du flux sanguin par retrait du filament, et mime ainsi les thérapies endovasculaires. Dans ce modèle, la part de la lésion dû à la formation de microthrombose secondaire au retrait du filament, est estimée à 70% (Pham *et al.*, 2010). Dans ce modèle, 2 heures après une occlusion par insertion du filament pendant 60 minutes, nous avons injecté les PHySIOMIC (Figure 51). Contrairement aux résultats attendus, les images IRM post injection ne montrent pas d'hyposignal pouvant correspondre à une microthrombose secondaire (Figure 51, D). Des études complémentaires sont prévues pour déterminer si l'absence de signal est dû à l'absence de microthrombose secondaire dans nos conditions expérimentales, ou à l'absence de ciblage des microparticules.

Une étude de Tang et collaborateurs montre une augmentation de la thrombogénicité au niveau des artérioles cérébrales après une brève ischémie transitoire, pouvant avoir une incidence sur le rôle de la microthrombose dans la pathogenèse de l'AIT et à l'augmentation du risque d'apparition d'AVC silencieux après (Tang *et al.*, 2014). L'injection de PHySIOMIC dans un modèle murin d'AIT (Quenault *et al.*, 2017), n'a pas révéler de microthrombose secondaire. Il est envisageable d'étendre cette étude en augmentant le temps d'injection après induction de l'AIT, pour vérifier la présence de microthrombose dans ce modèle (Figure 51, E).

Comme décrit précedemment, la microthrombose est un phénomène observé dans différentes pathologies. Dans un modèle animal par injection intra-striatale de staurosporine, une protéine induisant l'apoptose par inhibition des protéines kinases, nous avons observé l'apparition d'hyposignaux après injection des PHySIOMIC (Figure 51, F). Ainsi, l'utilisation des PHySIOMIC pourrait s'étendre aux autres phénomènes intracérébraux microvasculaires entrainant une microthrombose (El Amki et al., 2018).

La présence d'un seul thrombus localisé au niveau d'une artériole entraîne la création d'une microlésion, associée au développement de démences (Arvanitakis *et al.*, 2011). Nous pouvons envisager l'utilisation d'un modèle d'occlusion d'une artériole par injection de rose benguale puis excitation avec un laser pour occlure les microvaisseaux (Shih *et al.*, 2013). Ce modèle validerait l'efficacité des PHYSIOMIC pour la visualisation d'un microthrombi unique.

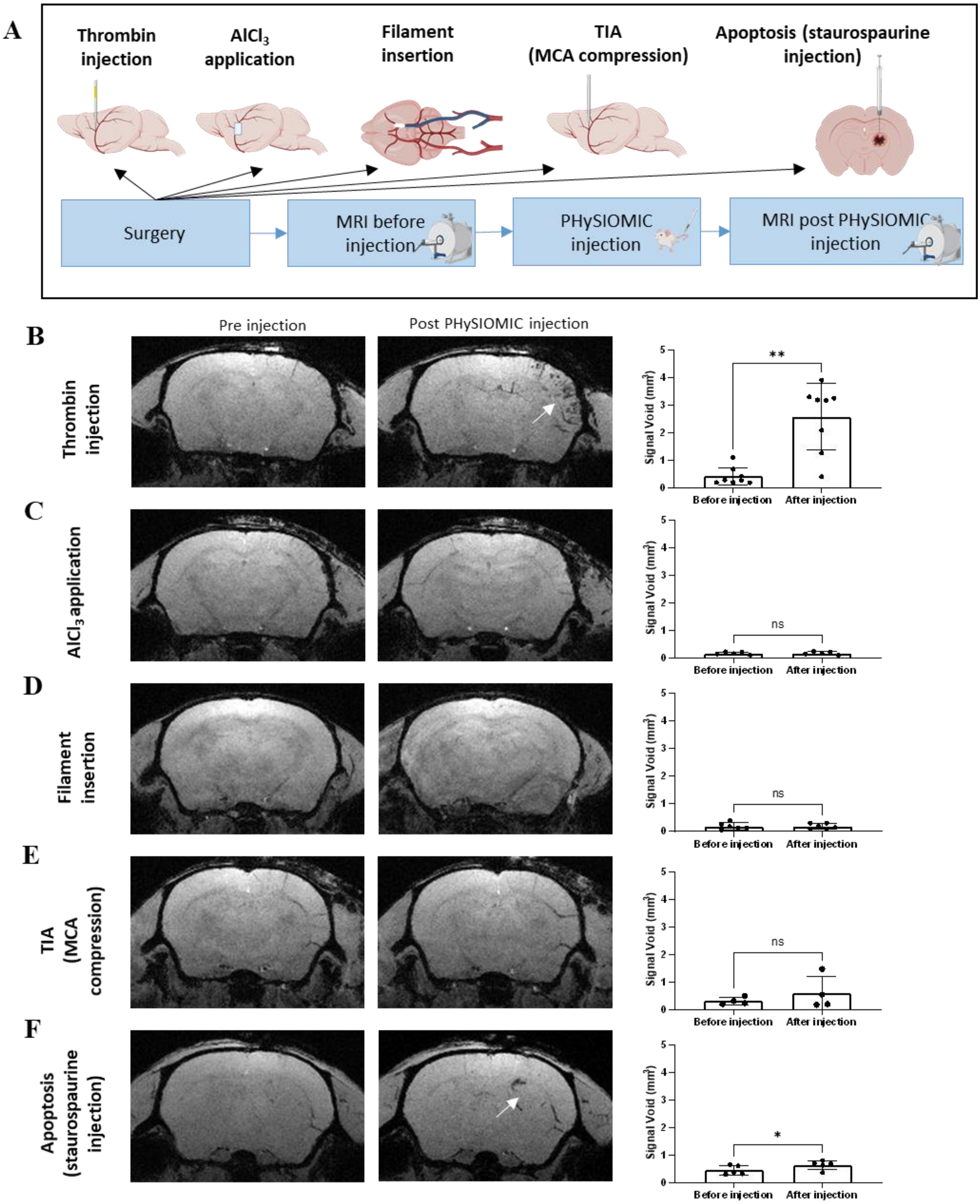

**Figure 51 Imagerie moléculaire de la microthrombose après injection des PHySIOMIC dans plusieurs modèles murin d'AVC et d'apoptose.**
L'injection des PHySIOMIC induit la formation d'hyposignaux dans le modèle avec injection de thrombine (B) et de staurosporine intrastriatale(F), mais pas dans les modèles par application de chlorure de fer sur l'ACM (C), par insertion d'un filament (D) et dans le modèle d'AIT (E).

Notre étude ne couvre pas les évenements hémorragiques induisant une microthrombose. L'ischémie cérébrale retardée est très décrite dans les hémorragies sous-arachnoïdiennes (HSA), et 20 à 30 % des patients avec HSA en souffrent dans les premiers 3 à 14 jours suivant l'hémorragie (Monsour *et al.*, 2022). Par ailleurs, les événements de lésions cérébrales secondaires au trauma crânien comprennent les réponses inflammatoires et l'activation de la coagulation entraînant la formation de microthrombi. L'analyse par imagerie moléculaire de la microthrombose pourrait donc s'élargir aux modèles animaux hémorragiques et traumatiques cérébraux.

## 3. Suivi de la microthrombose pour évaluer l'efficacité des traitements

Le modèle thromboembolique utilisé dans notre étude crée des thrombi et microthrombi riches en fibrine, et donc sensibles à la thrombolyse par injection de rtPA (Orset *et al.*, 2007). L'injection de PHySIOMIC dans ce modèle avant le traitement par thrombolyse des souris, a permis le suivi de la microthrombose. Nous avons observé une très grande diminution de cet hyposignal, après traitement par rtPA, par rapport au groupe contrôle. En comparant ce résultat avec le score angiographique IRM, nous pouvons en déduire que la diminution du signal observé correspond à l'augmentation du score angiographique, et à la reperfusion des microvaisseaux et artérioles du cortex ischémique.

Ce modèle est notamment utilisé pour le développement de nouveaux traitements, le développement de nouveaux outils de diagnostic et, plus généralement, dans les études précliniques sur les mécanismes moléculaires impliqués dans l'AVC ischémique (Chavignon *et al.*, 2022; Correa-Paz *et al.*, 2022; Peña-Martínez *et al.*, 2022). C'est le cas notamment d'un article (Autres travaux, 3), qui montre l'efficacité d'un nouveau traitement ciblant le facteur von Willebrand dans l'AVC ischémique. Au cours de ce projet, nous avons réalisé que la répartition de la microthrombose est hétérogène dans ce modèle et que les PHySIOMIC permettent de révéler en aigu la quantité de microthrombi avant et après traitement. Les PHySIOMIC et leur utilisation pour le suivi des microthrombi pourraient donc s'avérer très utile pour révéler une part de l'hétérogénéité du modèle et ainsi normaliser les études précliniques. Cela pourrait permettre d'affiner considérablement les études précliniques testant les nouveaux thrombolytiques sur ce modèle.

## 4. Futurs traitements et perspectives

Le traitement par thrombolyse consiste à amener le rtPA jusqu'aux caillots pour les dégrader. Son efficacité est rapidement limitée par les inhibiteurs du tPA comme PAI-1, et l'α-antiplasmine : protéine inhibitrice de la plasmine, et donc de la fibrinolyse, ce qui implique d'augmenter la concentration du rtPA pour atteindre sa cible. Or, cette forte concentration est responsable de troubles hémorragiques secondaires au traitement, en modifiant l'hémostase de la circulation cérébrale. Ces limitations ont poussé le développement de particules (liposomes, macromolécules, particules de polymères) qui, par un ciblage spécifique des thrombi, permettent de diminuer la dose de rtPA injecté (Disharoon *et al.*, 2019). Le rtPA peut être encapsulés ou encore fonctionnalisé à la surface de ces particules.

Dans un article présenté dans les autres travaux (Autres travaux, 1), le rtPA est adsorbé à la surface de particules submicrométriques, composées de polysaccharides de dextran, avec à la surface un autre polysaccharide, le fucoïdane, protéine qui présente une haute affinité pour la P-sélectine (molécule d'adhésion des cellules endothéliales) et vont cibler spécifiquement les thrombi (Zenych *et al.*, 2021, Figure 52).

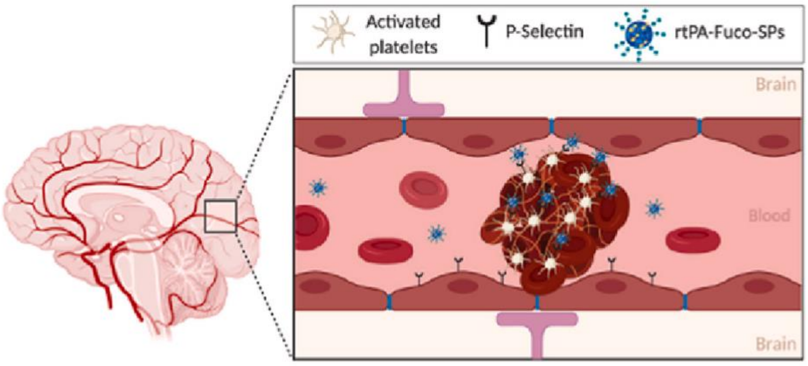

**Figure 52 Utilisation de nanoparticules après adsorption de rtPA, et fonctionnalisées avec du fucoïdane, pour le traitement de la thrombose.**

D'après Zenych et al., 2021

L'utilisation de rtPA encapsulé dans des microparticules *in vitro* et en préclinique s'est ainsi relevé être plus efficace que le traitement standard par fibrinolyse avec le rtPA, tout en diminuant les hémorragies secondaires à l'ischémie (Colasuonno *et al.*, 2018). Dans une étude de Zhou et collaborateurs, un agent théragnostique composé de rtPA encapsulé dans des nanoparticules composé d'un polymère, le poly(acide lactique-co-glycolique), et d'oxydes de fer a été synthétisé. Ces nanoparticules sont fonctionnalisées avec du chitosane, qui cible les récepteurs GPIIb/IIIa des plaquettes, pour relarguer le tPA encapsulés directement aux thrombi (Zhou *et al.*, 2014).

La thrombolyse en clinique se fait par injection intraveineuse (parfois intra-artériel) d'un bolus de rtPA suivit d'une infusion qui dure 60 min. Cette infusion est nécessaire à cause de la demi-vie très courte du rtPA dans la circulation sanguine. L'association du rtPA à des nanoparticules ou microparticules offre l'avantage d'une demi-vie plus longue, ne nécessitant pas d'infusion, et le ciblage direct des caillots, ce qui réduit le temps de traitement pour obtenir la dissolution de ceux-ci (Absar *et al.*, 2015).

La PDA, d'abord utilisée comme revêtement de surface de matériaux, puis pour la synthèse de nanoparticules, a montré des capacités d'encapsulation et de fonctionnalisation remarquables, grâce à la présence de nombreux groupes amines à sa surface. Zong et collaborateurs ont ainsi utilisé la PDA pour enveloppé des liposomes afin qu'ils ne soient pas endommagés dans la circulation et délivrent de manière plus efficace un agent anti-cancéreux à sa cible (Zong *et al.*, 2016).

La mise en relation de tous ces éléments laisse entrevoir les bénéfices que pourrait apporter l'encapsulation ou la conjugaison de microparticules de PDA avec le rtPA, pour la fibrinolyse. Les recherches seront d'ailleurs poursuivies dans ce sens, et le développement d'un agent théragnostic en fonctionnalisant les PHySIOMIC avec du rtPA est le sujet d'une étudiante en première année de thèse le laboratoire PhIND, qui s'inscrit dans la continuité du projet présenté dans ce manuscrit de thèse.

Beaucoup d'études faites dans notre laboratoire ont prouvé l'efficacité de l'utilisation de MPIO, conjugués à des anticorps anti-VCAM-1, une molécule d'adhésion des cellules endothéliales, exprimées en cas d'inflammation (Gauberti *et al.*, 2013; Montagne *et al.*, 2012; Quenault *et al.*, 2017). L'association de microparticules de PDA et d'oxydes de fer pour la détection de l'inflammation a d'ailleurs menée à la publication récente d'un article (Autres travaux, 2). Dans cet article, la fonctionnalisation des particules « M3P » avec l'anticorps anti-VCAM-1 cible les réponses immunitaires dans différentes pathologies (Martinez de Lizarrondo *et al.*, 2022), tout en étant biocompatible (Figure 53).

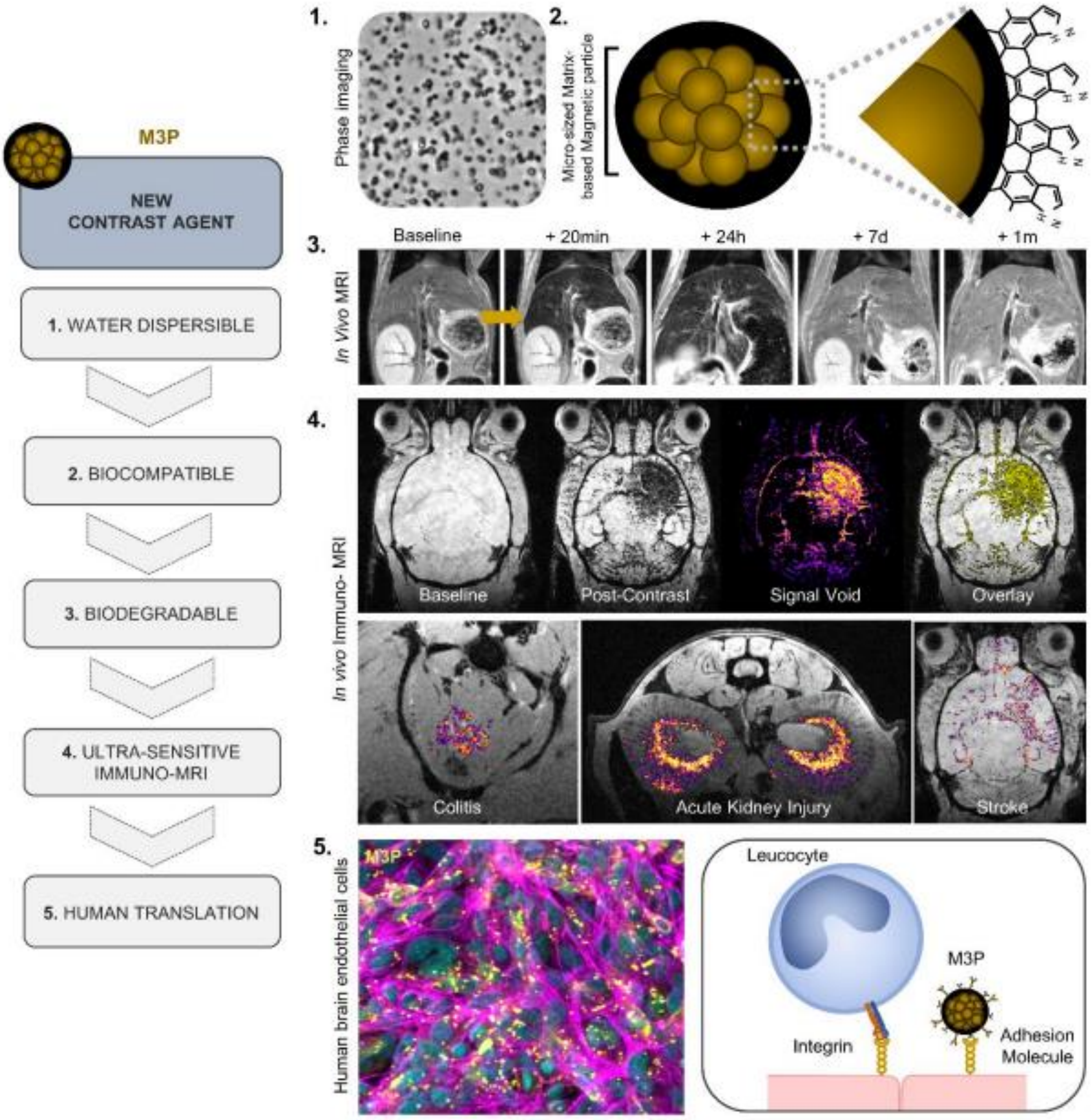

**Figure 53 La synthèse de microparticules d'oxydes de fer biodégradables fonctionnalisées avec un anticorps anti-VCAM-1, permet révéler l'inflammation à l'IRM.**
D'après Martinez de Lizarrondo et al., 2022

Les nombreux atouts de tels complexes de PDA et d'oxydes de fer en font également d'excellents candidats dans une nouvelle modalité d'imagerie : l'imagerie par particules magnétiques (MPI ou Magnetic Particle Imaging). Cette technique est non-invasive et extrêmement sensible aux inhomogénéités de champs induits par les oxydes de fer (Figure 54). L'avantage principale de cette technique est qu'elle est quantitative. Il est parfaitement envisageable d'utiliser les PHySIOMIC pour l'imagerie moléculaire des microthrombi observé en MPI, fournissant ainsi un suivi quantitatif de la microthrombose pendant la thrombolyse par exemple.

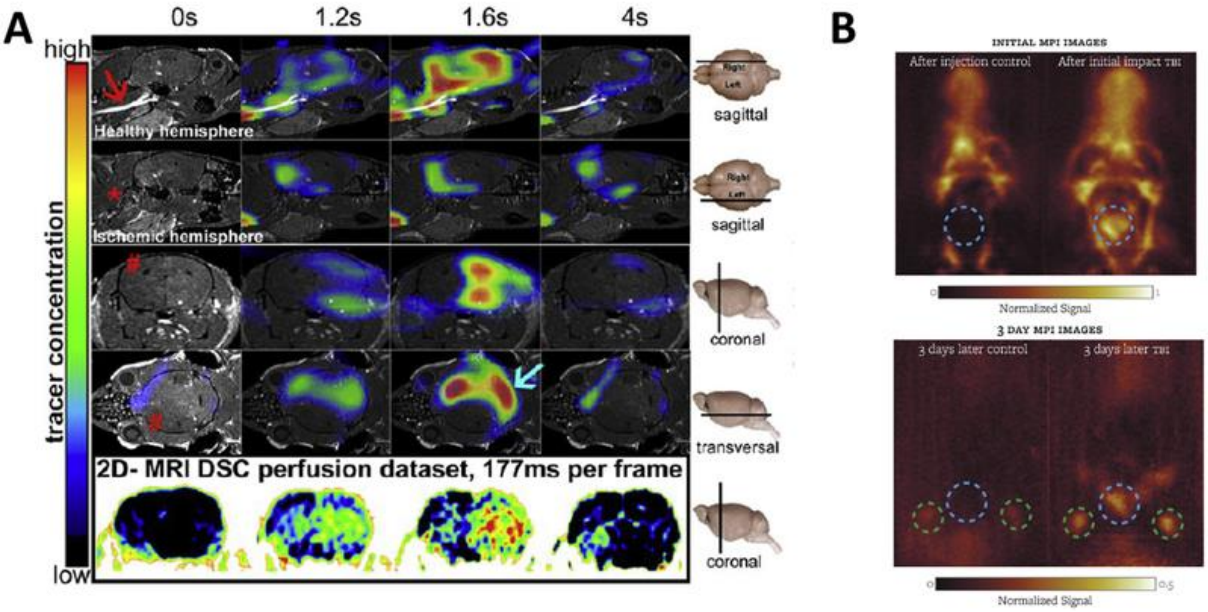

**Figure 54 Utilisation de la MPI dans un modèle murin d'ischémie cérébral.**

Nous avons démontré dans l'étude de biodistribution, que le signal induit par les PHySIOMIC capturées au niveau du foie et de la rate disparaît un mois après l'injection. L'observation en microcopie électronique a montré également que les particules étaient dégradées au sein des cellules de Kupffer. D'autres études pour assurer la biocompatibilité des PHySIOMIC sont en cours, comme la mesure de la quantité de fer dans les organes (foie, rate, rein, poumons) par spectroscopie de résonance paramagnétique électronique electron paramagnetic resonance (Lartigue *et al.*, 2013).

Par ailleurs, il est important de garder en considération pour le passage en clinique, que les microparticules ne doivent pas présenter d'effets thrombogéniques, qui pourrait aggraver la lésion ischémique. Pour investiguer cet effet, nous avons comparé les tailles de lésions formées 24 heures après l'occlusion de l'artère cérébrale moyenne, chez des souris ayant reçu des PHySIOMIC et des souris contrôles (Figure 55). Nos résultats ne montrent pas de différence significative de taille de lésion dans ces deux groupes. Le nombre d'échantillons étant faible dans cette étude, il faudrait augmenter le nombre d'animaux pour s'assurer que les PHySIOMIC n'entraînent pas une augmentation de la taille de lésion. Par ailleurs, il faudrait prendre en compte d'autres paramètres que la taille de lésion, tels que le taux de reperfusion spontanée et l'évaluation de déficits cognitifs, pour confirmer ces résultats.

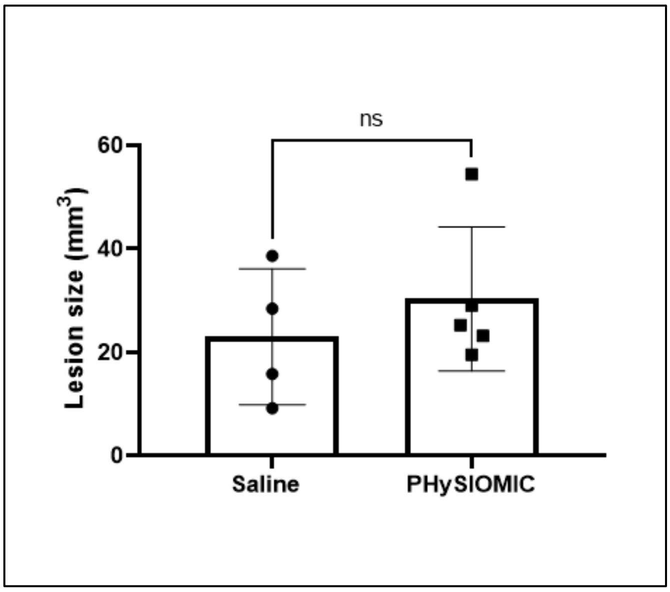

**Figure 55 Evaluation de la thrombogénicité des PHySIOMIC.**
Les mesures de la taille de lésion obtenues en séquence pondérée en T2, 24h après l'occlusion) ne montrent pas de différence significative entre les souris qui ont reçu une injection de PHySIOMIC, et les souris contrôles.

Le passage en clinique nécessite donc des études complémentaires et, parmi celles-ci, des études démontrant à la fois l'innocuité et l'efficacité des PHySIOMIC dans d'autres modèles d'ischémie chez des animaux plus gros, comme le cochon. Récemment, il a été développé une nouvelle approche endovasculaire pour induire la formation d'une ischémie chez le cochon (Golubczyk *et al.*, 2020). Cette approche utilise l'injection au niveau de l'artère cérébrale moyenne de thrombine, similaire au modèle thromboembolique utilisé pour nos études, par voie endovasculaire. Nous pouvons donc envisager l'utilisation de ce modèle pour démontrer l'efficacité des PHySIOMIC dans la détection de la microthrombose chez le gros animal, pour ainsi avancer vers l'utilisation de ce nouvel agent de contraste chez des patients victimes d'AVC ischémique afin de mieux caractériser la présence ou non de microthrombi.

# CONCLUSION

Nous avons démontré dans ces travaux de thèse, la synthèse de particules de taille micrométriques, par encapsulation de nanoparticules d'oxydes de fer (SPIO) dans une matrice de PDA (appelées PHySIOMIC), pour le ciblage en imagerie moléculaire de la microthrombose dans l'AVC ischémique.

La première étape de l'évaluation du ciblage de la microthrombose *in vitro*, montre que les PHySIOMIC injectées, marquées en fluorescence, sont retrouvées fixées au microthrombi dans la chambre microfluidique. Nous avons par cette étude également montré que le mécanisme de fixation est complexe et probablement induit par les terminaisons amines présentes à la surface des microparticules, probablement via la CP formées sur celles-ci en présence de sang humain.

Dans un second temps, l'évaluation *in vivo*, dans un modèle murin thromboembolique, a montré l'efficacité des PHySIOMIC pour l'imagerie moléculaire de la microthrombose en l'IRM, sur une séquence pondérée en T2*. Elle a également mis en évidence la relation entre la microthrombose et la lésion ischémique formée dans ce modèle animal, ainsi que la diminution de la microthrombose après l'application d'un traitement fibrinolytique.

Enfin un intérêt particulier s'est porté sur l'élimination des PHySIOMIC dans l'organisme. Nous avons confirmé la capture des microparticules par les cellules du SRE et leur dégradation au sein des lysosomes des cellules de Kupffer du foie. Et montrer l'intérêt et le potentiel de l'utilisationdes PHySIOMIC en clinique, pour détecter les microthrombi en IRM.

# AUTRES TRAVAUX

Les différentes collaborations réalisées lors de mon doctorat ont participées à la publication de trois articles de recherche cités ci-dessous :

1) Fucoidan-functionalized polysaccharide submicroparticles loaded with alteplase for efficient targeted thrombolytic therapy.

Dans cette article, ma participation s'est faite dans la partie *in vivo* des expérimentations. J'ai réalisés les modèles animaux d'AVC pour tester les nanoparticules fonctionnalisées. J'ai également contribué à la réailsation de l'imagerie IRM et aux analyses des images obtenues.

2) Tracking the immune response by MRI using biodegradable and ultrasensitive microprobes

Je suis co-première autrice dans cet article. Les expérimentations dans cet article ont été réalisées en parrallèle des expérimentations réalisées pour l'article présenté dans les résultats, Notemment pour la caractérisation des microparticules. J'ai réalisé une expérimentation de dégradation des particules et analyses par marquage histologique de Perls, ainsi que la figure associée présentée dans les figures supplémentaires de l'article.

3) VWF-targeted thrombolysis to overcome rh-tPA resistance in experimental thrombotic stroke models

Dans cet article dans lequel je suis cinquième autrice, j'ai contribué aux premières expérimentations-tests *in vivo*. Mon rôle a été de réaliser les modèles d'AVC pour injecter le traitement fournit par nos collaborateurs, et contribuer à l'imagerie.

# 1. Fucoidan-functionalized polysaccharide submicroparticles loaded with alteplase for efficient targeted thrombolytic therapy

Biomaterials 277 (2021) 121102

Contents lists available at ScienceDirect

Biomaterials

journal homepage: www.elsevier.com/locate/biomaterials

# Fucoidan-functionalized polysaccharide submicroparticles loaded with alteplase for efficient targeted thrombolytic therapy

Alina Zenych [a], Charlène Jacqmarcq [b,1], Rachida Aid [a,c,1], Louise Fournier [a],
Laura M. Forero Ramirez [a], Frédéric Chaubet [a], Thomas Bonnard [b], Denis Vivien [b,d,1],
Didier Letourneur [a,1], Cédric Chauvierre [a,*]

[a] *Université de Paris, Université Sorbonne Paris Nord, UMR S1148, INSERM, F-75018, Paris, France*
[b] *INSERM U1237 Physiopathology and Imaging of Neurological Disorders (PhIND), Institut Blood and Brain @ Caen Normandie (BB@C), GIP Cyceron, 14074, Caen, France*
[c] *Université de Paris, FRIM, UMS 034, INSERM, F-75018, Paris, France*
[d] *Department of Clinical Research, Caen Normandie University Hospital (CHU), 14074, Caen, France*

ARTICLE INFO

*Keywords:*
Nanomedicine
Drug delivery
Targeted thrombolysis
Polysaccharides
Fucoidan
*P*-Selectin

ABSTRACT

Intravenous administration of fibrinolytic drugs is the standard treatment of acute thrombotic diseases. However, current fibrinolytics exhibit limited clinical efficacy because of their short plasma half-lives and might trigger hemorrhagic transformations. Therefore, it is mandatory to develop innovative nanomedicine-based solutions for more efficient and safer thrombolysis with biocompatible and biodegradable thrombus-targeted nanocarrier. Herein, fucoidan-functionalized hydrogel polysaccharide submicroparticles with high biocompatibility are elaborated by the inverse miniemulsion/crosslinking method. They are loaded with the gold standard fibrinolytic – alteplase – to direct site-specific fibrinolysis due to nanomolar interactions between fucoidan and *P*-selectin overexpressed on activated platelets and endothelial cells in the thrombus area. The thrombus targeting properties of these particles are validated in a microfluidic assay containing recombinant *P*-selectin and activated platelets under arterial and venous blood shear rates as well as *in vivo*. The experiments on the murine model of acute thromboembolic ischemic stroke support this product's therapeutic efficacy, revealing a faster recanalization rate in the middle cerebral artery than with free alteplase, which reduces post-ischemic cerebral infarct lesions and blood-brain barrier permeability. Altogether, this proof-of-concept study demonstrates the potential of a biomaterial-based targeted nanomedicine for the precise treatment of acute thrombotic events, such as ischemic stroke.

## 1. Introduction

Acute thrombotic pathologies such as myocardial infarction, ischemic stroke, and venous thromboembolism remain a major global healthcare challenge contributing to a significant number of deaths and disabilities [1]. Current thrombolytic therapy, the intravenous injection of Plasminogen Activators (PA), is administrated to lyse a clot-induced vascular occlusion and restore the blood flow in the vessel. The recombinant tissue plasminogen activator (rtPA) is the most commonly applied clot-busting drug in clinics and the only one approved to treat acute ischemic stroke [2]. rtPA is a fibrin-specific serine protease that activates the endogenous proenzyme plasminogen and converts it to the active form plasmin, thus, degrading the thrombus fibrin network. However, systemic delivery of rtPA is limited by the rapid drug elimination (half-life 4–6 min), physiological deactivation by its antidotes such as Plasminogen Activator Inhibitors (PAI-1 and PAI-2), and deleterious side-effects such as intracranial hemorrhages [3]. This restricts its use to a narrow therapeutic window (4.5 h of stroke symptom onset when injected alone and 6 h when combined with mechanical thrombectomy), beyond which the deleterious effects of rtPA overcome its benefits. Moreover, the rate of acute recanalization after intravenous administration of rtPA is low: only ~30% of patients experienced full or partial recanalization [4].

Therapeutic strategies that intend to address the challenges of

---

* Corresponding author.
*E-mail address:* cedric.chauvierre@inserm.fr (C. Chauvierre).

[1] Equal contribution.

https://doi.org/10.1016/j.biomaterials.2021.121102
Received 9 February 2021; Received in revised form 22 June 2021; Accepted 25 August 2021

thrombolytic therapy and boost survival rates remain of great clinical interest. Certainly, novel thrombolytic molecules are being researched to increase reperfusion, improve safety, and protect the brain neurovascular unit [5,6]. Apart from that, nanomedical approaches for the targeted delivery of thrombolytic agents have been intensively proposed [7]. Korin et al. reported the microaggregates of poly (lactic-co-glycolic acid) (PLGA) nanoparticles (NPs) dissociated into rtPA-bearing nanocompounds when exposed to abnormally high hemodynamic shear stress, typical for the vascular occlusions, that performed effective thrombolysis in several preclinical models [8]. Colasuonno et al. formulated rtPA-loaded discoidal porous nanoconstructs from a mixture of PLGA and polyethylene glycol (PEG) with high thrombolytic potential presumably attributed to the erythrocyte-mimicking shape of the NPs and their deformability, leading to efficient circulation profiles and accumulation on the clot [9]. While these nanosystems with passive targeting succeeded in a promising thrombolytic efficacy in preclinical studies, more recent and advanced examples are formulated with actively targeted nanocarriers.

Active targeting permits drug accumulation specifically at the thrombus site and has the potential to enhance the enzyme penetration into deeply localized thrombi. Apart from the magnetic nanoparticle targeting under an external magnetic field [10–12] active blood clot targeting is currently achieved by directing the functionalized NPs towards fibrin or activated platelets (mostly integrin GPIIb/IIIa and less adhesion receptor *P*-selectin) with antibodies and/or peptides. Notably, Zhou et al. developed a theranostic system for thrombus molecular imaging and targeted therapy that could bind GPIIb/IIIa owing to a film of cyclic arginine-glycine-aspartic acid (cRGD) peptide grafted onto the chitosan, which covered the surface of rtPA-encapsulated $Fe_3O_4$-based PLGA NPs [13]. Nevertheless, both antibodies and peptides have their limitations for targeted drug delivery. The immunogenicity, purity, and sufficient circulation time are the main concerns of the application of the antibodies [14], while peptides might suffer from weak binding affinity, immunogenicity, a high costs of peptide synthesis, and metabolic instability with fast renal clearance due to their small sizes [15].

An effective alternative could be the nanoparticle functionalization with fucoidan [16], a naturally-occurring algae-derived sulfated polysaccharide that exhibits a strong and specific tropism for the *P*-selectin overexpression in cardiovascular pathologies [17,18]. Fucoidan emerged as an affordable, high-quality targeting ligand to *P*-selectin that was prior validated by our group on various polysaccharide-based nano- & microsystems for molecular diagnostics and targeted therapy [19–23]. Following the obtention of the label "raw materials for pharmaceutical uses" in 2015 in France, it became a part of the large-scale European Union project NanoAthero as a contrast agent for Single-Photon Emission Computed Tomography (SPECT) imaging in human atherothrombosis, coordinated by our laboratory [24]. The first in the world Phase I clinical trial on intravenous delivery of fucoidan radiolabeled by Technetium-99m reported its safety and favorable biodistribution [25], while Phase IIa for the imaging of deep vein thrombosis and pulmonary embolism is ongoing.

It is critical to ensure an excellent safety profile of the designed nanocarrier for targeted thrombolysis in future clinical translation by selecting biocompatible and fully biodegradable materials with the U.S. Food and Drug Administration (FDA)-approval [26]. Contrary to the attractiveness of synthetic polymers such as PLGA, the NPs made of polysaccharides are explored to a lesser degree for thrombolytic therapy. Yet, they benefit from the general advantages of natural polymers: biocompatibility, low cost, and hydrophilicity. Polysaccharide hydrogels, which are crosslinked three-dimensional polymer networks, absorb large quantities of water and can effectively load macromolecules with high encapsulation efficiency [27], including plasminogen activators. Few publications reported the nanoformulations of thrombolytic agents with chitosan, a cationic chitin-derived polysaccharide that can form polyelectrolyte complexes with negatively charged molecules [28]. For instance, superior thrombolytic potential *in vivo* was demonstrated on self-assembled chitosan NPs crosslinked with sodium tripolyphosphate and loaded with urokinase [29]. Liao et al. formulated the lumbrokinase-bearing NPs from quaternized derivative of chitosan - N,N,N-Trimethyl Chitosan covalently grafted with cRGD peptide to target GPIIb/IIIa receptors that could accelerate thrombolysis [30].

Dextran, an exocellular bacterial water-soluble polysaccharide, is extensively employed in clinics, particularly in its low molecular weight (40 and 70 kDa), for plasma volume expansion, thrombosis prophylaxis, peripheral blood flow enhancement, artificial tears, *etc*. [31] Dextran coating of magnetic NPs is applied to ensure their environmental stability and prolong the blood circulation time [32,33]. However, there is no reported exclusively dextran nanocarrier with hydrogel structure for thrombolytic application to our knowledge. Meeting the requirements of biocompatibility, biodegradability, non-immunogenicity, dextran stands out as an attractive polymer to design an alteplase delivery system.

Herein, we fabricated novel fucoidan-functionalized dextran submicroparticles (SPs) by a green chemistry method using fully biodegradable and biocompatible compounds, all of them approved by the FDA. After physico-chemical and biosafety characterization of these hydrogel-like SPs, rtPA was loaded onto the SPs with a high encapsulation capacity, and its release in saline and *in vitro* amidolytic and fibrinolytic activities were tested. Through the *in vitro* microfluidic experiments under continuous arterial or venous flow, we provided evidence that fucoidan-functionalized SPs (Fuco-SPs) have a high and specific affinity to *P*-selectin and accumulate on activated platelet aggregates. Also, these particles bind to the thrombi *in vivo*. Finally, rtPA-associated Fuco-SPs proved superior *in vivo* thrombolytic efficacy in a mouse stroke thrombin model with a faster vessel recanalization that minimized cerebral tissue damage: the post-ischemic lesion and blood-brain barrier (BBB) permeability.

## 2. Materials and methods

*Materials:* Dextran 40 kDa and TRITC-dextran 40 kDa were provided by TdB Consultancy (Uppsala, Sweden). Fucoidan (Mn = 18 kDa/Mw = 104 kDa, 14.1 wt % sulfates by elemental analysis) was a gift from Algues & Mer (Ouessant, France). Sodium trimetaphosphate (STMP), methylene blue hydrate, and Human Serum Albumin (HSA) were purchased from Sigma-Aldrich (Saint-Quentin-Fallavier, France). Polyglycerol polyricinoleate (PGPR) was obtained from Palsgaard France S.A.S. (Lyon, France). Vegetable – sunflower – oil (Lesieur - Huile Coeur de Tournesol, Lesieur S.A.S, Asnières-sur-Seine, France) was purchased from a local supermarket (Monoprix, Paris, France). The SPs were encapsulated with commercially available rtPA (Actilyse®, Boehringer Ingelheim) that was reconstituted at 1 mg/ml, aliquoted, and stored at −80 °C. Chromatography paper was obtained from GE Healthcare (Chicago, Illinois, United States). Fibrillar type I collagen from equine tendon Horm® was purchased from Takeda (Linz, Austria). 96-Well Cell Culture Plates (Costar) were obtained from Corning Incorporated. PPACK (Phe-Pro-Arg-Chloromethylketone) 75 μM tubes were purchased from Cryopep (Montpellier, France). Flow chambers (Vena8 Fluoro+) were provided by Cellix Ltd (Dublin, Ireland).

*Submicroparticle synthesis:* Polysaccharide submicroparticles (SPs) were obtained via a water-in-oil (w/o) emulsification combined with a crosslinking process [19,20]. Polysaccharide solution (300 mg/ml, 6 M NaCl) was prepared as a mixture of dextran 40 and 5% TRITC-dextran 40 (for fluorescent SPs). To synthesize functionalized SPs with fucoidan (Fuco-SPs), 10% w/w of fucoidan was added. Table S1, Supplementary Data describes the synthesis parameters of SPs.

First, the organic phase of 15 mL of sunflower oil and 6% w/v PGPR in Falcon® 50 mL was prepared and cooled down for 20 min at −20 °C. In the meantime, 1200 mg of the polysaccharide solution was incubated with 120 μL of 10 M NaOH under magnetic stirring for 10 min. 240 μL of STMP solution (30% w/v in water) was added into the aqueous phase under magnetic stirring and mixed for 20 s on ice. Next, emulsification was achieved by the dropwise injection of 600 μL of the aqueous phase into the organic phase and dispersed with a stand-disperser (Polytron PT 3100, dispersing aggregate PT-DA 07/2 EC-B101, Kinematica, Luzernerstrasse, Switzerland) at 30,000 rpm for 4 min on ice. The obtained w/o emulsion was transferred into 50 °C for the crosslinking reaction of polysaccharides with STMP for 20 min. The crosslinked suspension was washed in 30 mL PBS 10X for 40 min under high magnetic stirring at 750 rpm. The mixture was then centrifuged (BR4i, JOUAN SA, Saint Herblain, France) for 10 min at 3000 g in Falcon tubes. The organic phase was recovered and ultracentrifuged (Optima MAX-XP, Ultracentrifuge, Beckman Coulter, Brea, California, United States) in PBS for 45 min at 15,000 g. The obtained pellet was washed by ultracentrifugation 2 times in 0.04% Sodium Dodecyl Sulfate (SDS) solution and then 3 times in ultrapure water to purify the SPs. The resulting SPs were suspended in water or 0.9% NaCl with 0.02% Tween 20 (Sigma) and stored at 4 °C.

*Physico-chemical characterization:* The submicroparticle (SP) formulations were studied for particle morphology, size and zeta potential distributions, mass concentration, and elemental composition.

Particle morphology was visualized by Transmission Electron Microscopy (TEM) (Philips FEI Tecnai 12, Amsterdam, Netherlands), negatively stained with 1% (w/v) uranyl acetate for 5 min, and Environmental Scanning Electron Microscopy (ESEM) (Philips XL30 ESEM-FEG, Amsterdam, Netherlands) with the following parameters: HV 5 kV, HFW 25.4 μm, magnification 5 000 x, WD 9.4 mm, mode SE, pressure 3.00e-6 Torr.

Hydrodynamic size and Zeta potential (ζ-potential) were measured by Dynamic Light Scattering (DLS) and Electrophoretic Light Scattering (ELS), respectively (Zetasizer Nano ZS, Malvern Instruments SARL, Orsay, France). Samples were diluted in distilled water or saline for size and in 1 mM KCl for ζ-potential determination. All runs were performed at 25 °C in triplicate.

Mass concentration was determined by freeze-drying. An elemental analyzer-mass spectrophotometer was used for the quantification of the sulfur (presence of fucoidan). To prove the crosslinking with STMP, the total reflection X-ray fluorescence spectroscopy (TXRF) technique was applied to quantify the phosphorus content on the SPs (S2 PICOFOX Bruker, Massachusetts, United States).

*Sulfate and fucoidan quantification:* The sulfate content of fucoidan was determined by a semi-quantitative solid-phase colorimetric assay [34]. Briefly, 5 μL of Fuco-SPs in suspension at a concentration of 2 mg/ml were dropped on a piece of Whatman Chromatography paper grade 1. This was repeated 5 times on the same point, allowing the paper to dry at 50 °C in between. The paper was first soaked into a methanol/acetone (6:4) solution for 3 min and then into a methanol/acetone/water (6:4:15) solution with 50 mM HCl and 0.1% w/w methylene blue for 10 min. Finally, the paper was extensively washed with acetic acid/methanol/acetone/water (5:6:4:75) until no coloration was detected in the washing solution. The paper was then transferred to the Eppendorf, containing 0.5 mL methanol with 2% w/v SDS, and incubated for 15 min at 50 °C. 0.2 mL of the extracted dye was placed in a 96-well plate, and its concentration was determined by reading absorbance at 663 nm on an Infinite® 200 PRO microplate reader (TECAN Group Ltd, Mannedorf, Switzerland). Standard curves were obtained from fucoidan in solution with known concentrations.

*Cell culture and cytotoxicity assay:* To evaluate the cytotoxicity of the SPs, Fluorometric Cell Viability Assay (Resazurin) was used on confluent Human Umbilical Vein Endothelial Cells (HUVECs). The cells were cultured in DMEM supplemented with 10% (v/v) fetal bovine serum, 4 mmol of L-glutamine, 100 units/ml of penicillin, and 100 μg/ml of streptomycin and kept in an incubator at 37 °C in a humidified atmosphere of 5% $CO_2$. Cells were seeded into 96-well plates to adhere, 10,000 cells per well. Following 24 h of incubation to reach ~80% confluency, the medium in the wells was changed to the one containing the SPs at concentrations ranging from 0.1 to 1.5 mg/ml and cultured for another 24 h. The SPs were prior sterilized under the UV light for 15 min. Next, the medium was replaced with 100 μL 10% Resazurin solution, and the plates were covered in foil and incubated for 2 h. Culture media were used as a negative control. The Resazurin's fluorescent signals were monitored using 540 nm excitation and 590 nm emission wavelengths on Infinite® 200 PRO microplate reader (TECAN Group Ltd, Mannedorf, Switzerland). The obtained fluorescence (Fl) values were blank corrected, and the relative cell viability was expressed as $Fl_{SPs}/Fl_{control} \times 100\%$, where $Fl_{control}$ was obtained in the absence of the SPs. The experiment was performed in hexaplicate.

To examine the potential cell cytoskeleton organization mediated by Fuco-SPs, HUVECs cells were cultured in 8-well Lab-Tek II Chamber Slide w/Cover (Lab-Tek®, Thermo Fischer Scientific, Massachusetts, United States) with 10,000 cells per well. The wells' medium was changed 24 h after to the one containing TRITC-Fuco-SPs at 1.5 mg/ml and was incubated for another 24 h. Cells cultured in the medium without the SPs were set as control. Next, cells were fixed with 4% paraformaldehyde for 30 min at room temperature (RT). After rinsing with PBS, cells were labeled and permeabilized with the 200 μl mixture of FITC-Phalloidin (1:200, Sigma-Aldrich, USA)/DAPI (1:100, Thermo Fisher Scientific, Massachusetts, United States)/0.01% v/v Tween 20 in PBS and incubated under low agitation for 1 h at RT. The cells were afterward washed 3 times with PBS. The support of the chamber slides was removed, and the slides were mounted with a few drops of the aqueous mounting medium and kept at 4 °C until visualization with the confocal microscope (Zeiss LSM 780, Iena, Germany).

*Hemocompatibility test*: Hemolysis assay was adapted from the publication [20] and performed on washed isolated murine erythrocytes. Murine blood was collected in sodium citrate 3.8% (w/v) and centrifuged at 800 g for 5 min to isolate red blood cells. The supernatant was removed, and the pellet of erythrocytes was resuspended at 20% (v/v) in distilled water (positive control, 100% hemolysis), normal saline (negative control, no hemolysis), and the Fuco-SPs at concentrations from 0.1 to 1.5 mg/ml in Eppendorf. The tubes were incubated on a rotator at 37 °C for 1.5 h and then centrifuged at 3000 g for 5 min. The absorbance (A) of the supernatants was measured on Infinite® 200 PRO microplate reader (TECAN Group Ltd, Mannedorf, Switzerland) at 590 nm. Each sample was run in triplicate. The percentage of hemolysis was determined by the formula: Hemolysis degree (%) = 100% x $(A_{sample} - A_{negative\ control})/(A_{positive\ control} - A_{negative\ control})$.

*Loading rtPA on the SPs:* rtPA was immobilized onto the SPs by adsorption. 100 μl of SPs (5 mg/ml) was mixed with 100 μl of rtPA (1 mg/ml) in ultrapure water and then incubated for 1 h at RT. Free unabsorbed rtPA was removed by 3 cycles of ultracentrifugation (15 min, 15,000 g). The SPs with adsorbed rtPA (rtPA-SPs) were resuspended in water and used for the drug loading efficiency quantification.

*Drug encapsulation efficiency:* The amount of rtPA loaded on the SPs was measured using the Pierce BCA protein assay kit (Life Technologies SAS, Courtaboeuf, France). Briefly, 200 μl of working reagent was added to 25 μL of each sample in 96 well-plate. The absorbance at 562 nm was read on the Infinite® 200 PRO microplate reader (TECAN Group Ltd, Mannedorf, Switzerland) after 30 min of incubation at 37 °C and cooling to RT for 10 min. The concentration of the drug was extrapolated by a calibration curve prepared with different concentrations of rtPA.

The encapsulation efficacy (EE) was calculated as EE (%) = 100% x B/A, whereas B is the amount of rtPA loaded onto the SPs and A is the total quantity of rtPA put in contact with the SPs.

*In vitro rtPA release:* The release of rtPA from the Fuco-SPs was assessed by flow cytometry [35]. FITC-rtPA (Abcam, Cambridge, United Kingdom) at 1 mg/ml was placed in contact with TRITC Fuco-SPs at 5 mg/ml for 1 h at RT. The suspensions were added to tubes pre-filled with 400 μL of saline and placed under gentle agitation at 37 °C. At each time point of 0, 15, 30, 45, 60, and 90 min, the tubes were analyzed with a BD FACS Aria™ III flow cytometer (Becton Dickinson, New Jersey, United States). The TRITC-Dextran, excited by a 543 nm laser, was detected at 569 nm, while the FITC-rtPA, excited at 480 nm, was detected on a 530/30 nm PMT. Flow cytometry analyses were performed in triplicates with Diva software (Becton Dickinson). The protein release curve was obtained by normalizing the values of Mean Fluorescence Intensity (MFI) of the FITC-rtPA still associated with TRITC-Fuco-SPs.

*In vitro amidolytic activity of rtPA-loaded SPs:* Amidolytic activity of rtPA loaded SPs was assessed with the fluorogenic substrate PefaFluor® tPA (Cryopep, Montpellier, France). 2.5 μL of samples (20 μg/ml) was put in contact with 97.5 μL of 100 mM HEPES buffer (pH 8.0, 154 mM NaCl, 0.1% HAS) in the 96-well plate. After the addition of 10 μL PefaFluor® at 1 mM, a kinetic profile was obtained by measuring the fluorescence level at 440 nm every 2 min for 90 min at 37 °C with Infinite® 200 PRO microplate reader (TECAN Group Ltd, Mannedorf, Switzerland). Free rtPA was used at the same concentration based on the Pierce BCA protein assay. Increase of fluorescence corresponded to the fluorogenic peptide substrate hydrolysis by rtPA. Enzymatic activity was determined from the resulting kinetic profile and compared to the one of free rtPA.

*In vitro fibrinolytic activity of rtPA-loaded SPs:* To assess the fibrinolytic activity of rtPA-loaded SPs, a fibrin lysis clot experiment was performed. 5 mL of TRIS Buffer with 3% w/v low melting agarose (Carl Roth GmbH þ Co. KG, Karlsruhe, Germany) were heated to 65 °C. 5 mL of fibrinogen (from human plasma, Sigma Aldrich) solution in TRIS buffer (5 mg/ml) was slowly heated to 37 °C. Once the agarose solution reached 65 °C, it was cooled to 37 °C, and 2.5 U of thrombin (from human plasma, Sigma Aldrich) was added. Next, a fibrinogen solution was slowly added into the agarose/thrombin mixture under gentle agitation to avoid the formation of bubbles. The reaction mixture was poured into a 9 cm Petri dish and cooled at 4 °C for 30 min until the fibrin clot became visible. On the solidified agarose gel, round wells were formed using a 3 mm punch as sample reservoirs. 5 μL of each SPs sample (45 μg/ml) was dropped into the wells and incubated overnight at 37 °C in a humid environment. The degree of fibrin lysis was quantified with ImageJ by comparing the size of the fibrinolysis circle of the samples and free rtPA at the equivalent concentration based on the Pierce BCA protein assay.

*Flow microchamber experiments:* An *in vitro* flow adhesion assay was performed to evaluate the affinity of the Fuco-SPs with their molecular target. Micro-channels of Vena8 Fluoro$^+$ chambers (width: 0.04 cm, height: 0.01 cm, and length: 2.8 cm; Cellix Ltd, Dublin, Ireland) were coated overnight with recombinant human *P*-selectin, L-selectin or E-selectin (R&D systems France, Lille, France) at 100 μg/ml and left overnight at 4 °C. To confirm the concentration-dependent binding of Fuco-SPs to *P*-selectin, some channels were coated with *P*-selectin at a range of concentrations (5, 25, 50, and 100 μg/ml). Channels were then washed with NaCl 0.9% and further incubated with HSA at 10 μg/ml for 2 h.

A suspension of fluorescently labeled Control-SPs or Fuco-SPs (1 mg/ml) in saline was passed through the channels for 5 min at arterial and venous flow conditions (shear stress 67.5 dyne/cm$^2$ and 6.75 dyne/cm$^2$) using an ExiGo™ pump (Cellix Ltd, Dublin, Ireland). For the competitive binding experiment, fucoidan solution (10 mg/ml) was injected 5 min prior to the Fuco-SPs at the same rate. Then, all the channels were washed with NaCl 0.9% for 1 min. The binding of the adhered SPs was visualized in real-time under fluorescence microscopy (Axio Observer, Carl Zeiss Microimaging GmbH, Iena, Germany). For the quantitative analysis, the number of fluorescent SP clusters on each channel was measured using the "Analyze particles" tool in the image analysis software ImageJ (NIH, Bethesda, U.S.) with a 4-pixel threshold to eliminate the background noise.

To further investigate the binding efficiency of unloaded and loaded SPs to activated platelets, the microchannels of Vena8 Fluoro$^+$ were coated with fibrillar type I collagen Horm® (50 μg/ml) overnight at 4 °C and rinsed with NaCl 0.9% before use. Human whole blood (EFS, Bichat Hospital, Paris, France), collected in the PPACK tubes and labeled with 5 μM DIOC6 (Life Technologies SAS, Saint-Aubin, France), was perfused at arterial shear stress for 5 min to induce platelet activation and aggregation. Platelet aggregation through contact with collagen was visualized in real-time with phase-contrast microscopy (Axio Observer, Carl Zeiss Microscopy, Oberkochen, Germany). After rinsing with NaCl 0.9%, fluorescent Control-SPs or Fuco-SPs (unloaded or loaded with rtPA) at 1 mg/ml were injected into the channels in saline for 5 min. Their accumulation onto activated aggregates was monitored in real-time. Channels were then washed for 1 min with NaCl 0.9%. Finally, the MFI of the fluorescent SPs bound to the platelets on each channel was analyzed with ImageJ. Intensity settings were kept the same for both types of SPs.

*Tissue distribution of Fuco-SPs in vivo:* Animal studies were performed on C57BL/6 male mice (EJ, Le Genest, St-Berthevin, France) aged 5–8 weeks (~25 g weight) in respect of the principles of laboratory about animal experimentation and with the approval of the animal care and use committee of the Claude Bernard Institute (APAFIS #8724, Paris, France). Mice were anesthetized under the application of 2% isoflurane (Aerrane, Baxter). 200 μL of Fuco-SPs (5 mg/ml) were injected through the retro-orbital route (n = 3). To histologically analyze the particle accumulation, mice were sacrificed 30 min following their administration. The liver, spleen, lungs, and kidneys were excised, washed in saline, and fixed in paraformaldehyde 4%. The tissues were then frozen and cryosectioned at 10 μm thickness. The samples were stained with alcian blue & nuclear fast red staining protocol. Strongly negative structures, including the Fuco-SPs, are stained blue, nuclei are stained pink to red, and cytoplasms appear pale pink. The slides with tissue slices were scanned with the Nanozoomer (Hamamatsu, Hamamatsu City, Japan) and viewed with the NDP.view2 software.

*Animals and thromboembolic stroke model in vivo:* Animal experiments were carried out on male Swiss wild-type mice (8–9 weeks old; 35–45 g; CURB, Caen, France). All experiments were performed following the French (Decree 87/848) and the European Communities Council (2010/63/EU) guidelines and were approved by the institutional review board (French ministry of Research). All the experiments were validated by the local ethical committee of Normandy (CENOMEXA) registered under the reference number APAFIS#13172. Anesthesia was induced by the application of 5% isoflurane (Aerrane, Baxter) and maintained by 2% isoflurane in a mixture of $O_2/N_2O$ (30%/70%).

Mice were placed in a stereotaxic device, then a small craniotomy was performed, the dura was excised, and the middle cerebral artery (MCA) was exposed. To induce the occlusion of the MCA, the coagulation cascade was triggered by the pneumatical injection of 1 μL murine α-thrombin (1 IU; Stago BNL) with a glass micropipette, as previously described [36]. Successful MCA occlusion was confirmed by the Laser Doppler flowmeter (Oxford Optronix). For the treatment, the animals were intravenously injected through a tail vein catheter (200 μL, 10% bolus, 90% infusion over 40 min) with either saline, Actilyse® rtPA 10 mg/kg, or rtPA-Fuco-SPs (loaded rtPA at 10 mg/kg, SPs at 71 mg/kg) 20 min after thrombus formation ($n \geq 5$). Brain perfusion was monitored by Laser Speckle Contrast Imager (MOOR FLPI-2, Moor Instruments) throughout the treatment. Region of interest (ROI) was selected on the ipsilateral to occlusion and contralateral hemispheres to monitor the relative cerebral blood flow in the affected region $Fl_t$ (%) = 100% x $Fl_{ipsi}/Fl_{contra}$. The post-stroke reperfusion was expressed as a Growth Rate (GR) of the blood flow increase in the ipsilateral ROI to contralateral one at a time point, and it was quantified as GR (%) = 100% x $(Fl_{t2} - Fl_{t1})/Fl_{t1}$.

*Magnetic resonance imaging acquisition and analysis:* Mice were anesthetized with 5% isoflurane and maintained with 1.5–2% isoflurane in a mixture of $O_2/N_2O$ (30%/70%) during the acquisitions. Experiments were carried out on a Pharmascan 7 T (Bruker Biospin, Wissembourg, France). Three-dimensional T2-weighted images were acquired using a Multi-Slice Multi-Echo sequence (TE/TR 39.9 ms/3500 ms, 2 averages) 24 h after the stroke. Lesion volumes were quantified on these images using ImageJ software (slice thickness 0.5 mm). Magnetic resonance angiography was performed using a 2D-TOF sequence (TE/TR 4.24 ms/12 ms, 1 average) 24 h after ischemia, and the recanalization status of the MCA was determined blindly from the analysis of the merged MCA angiograms with maximum intensity. The angiographic score is based on the TICI (Thrombolysis in Cerebral Infarction) grade flow scoring (from Score 0: no perfusion to Score 3: full recanalization). For the *in vivo* detection of the BBB permeability, three-dimensional T1 FLASH sequences (TE/TR 4.37 ms/15.12 ms; 3 averages) were used, 15 min after the intravenous injection of 200 μL gadolinium chelate (DOTAREM) in saline (0.25 mg/ml). BBB leakage was measured 4 days after the stroke induction, and its volume was quantified using ImageJ.

*Thrombus targeting by Fuco-SPs in a murine model of venous thrombosis:* Animal studies were done following principles of laboratory animal care and with the approval of the animal care and use committee of the Claude Bernard Institute (APAFIS #8724, Paris, France). $FeCl_3$-induced *in vivo* thrombosis model on mesenteric vein was carried out on C57BL/6 male mice (EJ, Le Genest, St-Berthevin, France) aged 5–8 weeks. Mice were anesthetized with an intraperitoneal injection of ketamine (100 mg/kg) and xylazine (10 mg/kg). After midline abdominal incision, the mesentery was exposed, and vessels were visualized by an intravital microscope (Leica MacroFluo, Leica Microsystems SAS, Nanterre Cedex, France) using Orca Flash 4.0 scientific CMOS camera (Hamamatsu Photonics France SARL, Massy, France). For green fluorescent labeling of mitochondria of platelets and leucocytes, DIOC6 (Life Technologies SAS, Saint-Aubin, France) at 25 μM was retro-orbitally injected. The mesentery vein was covered with a 1 mm Whatman chromatography paper that was prior soaked in a 10% w/v iron chloride (Sigma-Aldrich) solution for 1 min, and then washed with saline. The formation of non-occlusive thrombi was monitored in real-time by fluorescence microscopy by an accumulation of fluorescently labeled platelets. TRITC-fluorescent labeled Control-SPs or Fuco-SPs were retro-orbitally injected 10 min after thrombus initiation with the volume of 150 μL (5 mice per group).

For histological evaluation, mice were sacrificed with pentobarbital overdose 5 min after administration of SPs. The affected part of the mesenteric vein was cut, washed in 0.9% NaCl, fixed in paraformaldehyde 4% (w/v), and frozen. The vein samples were cryosectioned at 10 μm thickness. The cell nuclei of a venous vascular wall were labeled with DAPI (Thermo Fisher Scientific, Massachusetts, United States) contained in a mounting medium (Vecto laboratories). The samples were observed by fluorescence microscopy. For the quantitative analysis, normalized MFI of the TRITC signal from SPs was expressed, defined as total TRITC fluorescence intensity divided by the size of the thrombus area on 2 slides from each mouse with the ImageJ (NIH, Bethesda, U.S.).

*Statistical analysis:* Quantitative data were expressed as mean ± standard error of the mean (SEM) ($n \geq 3$). Statistical tests were carried out with GraphPad Prism 9 (GraphPad Software, Inc, La Jolla, U.S.) with a 95% confidence level. Kolmogorov-Smirnov normality test was utilized to examine if variables are normally distributed. Normally distributed data were analyzed then with unpaired *t*-test or one-way analysis of variance (ANOVA) with post hoc Turkey's test. The Mann-Whitney *U* test was applied otherwise. The p-values of $^{*}p < 0.05$; $^{**}p < 0.01$; $^{***}p < 0.001$ were considered statistically significant.

## 3. Results

### 1. *Submicroparticle synthesis and characterization*

Novel polysaccharide SPs were elaborated by a simple two-step synthesis process (Fig. 1A). First, a stable w/o miniemulsion of the aqueous phase with hydrophilic polysaccharides and vegetable (sunflower) oil was prepared. Chemical crosslinking of polysaccharides with the crosslinking agent STMP under alkaline conditions (Fig. 1B & Figure S1, Supplementary Data) produced a suspension of uniform SPs. We refer to the hydrogel particles only from dextran as Control-SPs, and

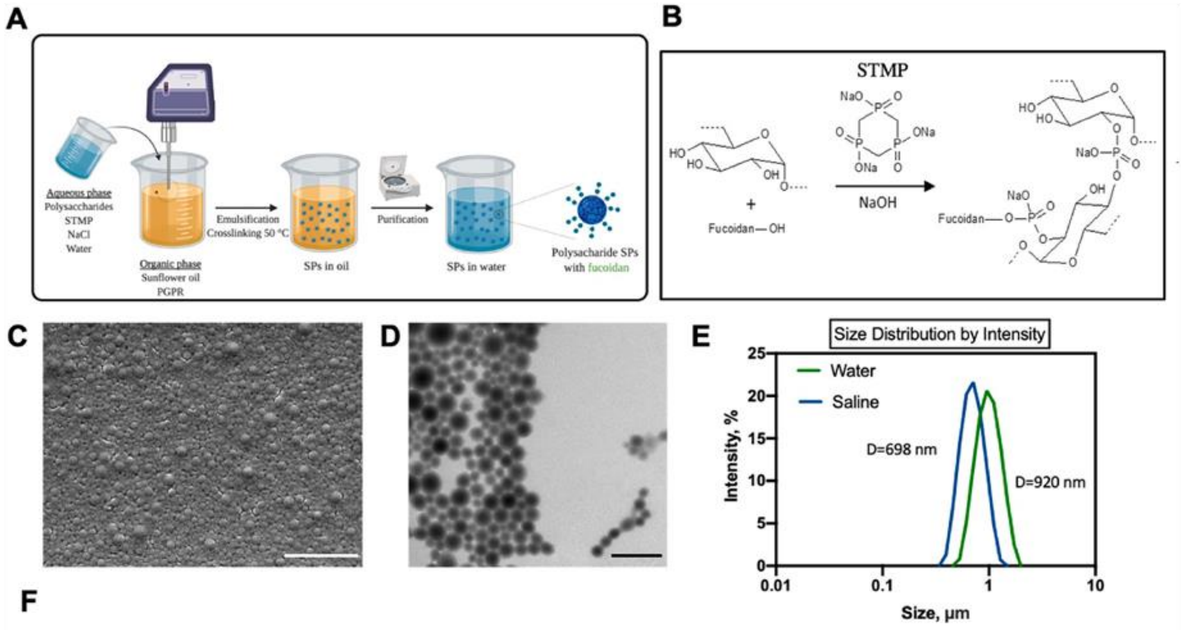

F

| Sample | | Size, nm | PDI | Zeta potential, mV | Phosphorus content, mg/l | Fucoidan content (Sulfate), %, w/w | Fucoidan content (Sulfur) %, w/w |
|---|---|---|---|---|---|---|---|
| Control-SPs | D0 | 674.87 ± 59.35 | 0.24 ± 0.05 | -24.83 ± 0.09 | 33.2 ± 0.1 | - | - |
| | D30 | 662.26 ± 46.04 | 0.18 ± 0.04 | -25.24 ± 0.15 | | | |
| Fuco-SPs | D0 | 708.48 ± 40.00 | 0.21 ± 0.10 | -27.07 ± 0.39 | 30.6 ± 0.1 | 9.30 ± 1.07 | 8.60 ± 0.01 |
| | D30 | 669.35 ± 61.93 | 0.23 ± 0.07 | -27.90 ± 0.20 | | | |

**Fig. 1.** Synthesis and physico-chemical characterization of the SPs. A. Overall schematic of the synthesis process of the SPs – miniemulsion/crosslinking. B. Simplified chemical structures of dextran and fucoidan and crosslinking with STMP in alkaline conditions. SEM (C) (scale bar = 5 μm) and TEM (D) (scale bar = 3 μm) images of the Fuco-SPs. E. Swelling in the water of the Fuco-SPs due to the hydrogel nature of the particles. The size of one sample when resuspended in water (green) and in saline (blue). F. Size, zeta potential, and chemical composition of the SPs; D0 – at the day of synthesis, D30 – one month after the synthesis.

from a mixture of dextran and fucoidan as Fuco-SPs in this manuscript.

To ensure desirable safety of the future drug delivery platform, a thoughtful approach to material selection was effectuated. Low molecular weight dextran 40 kDa of clinical-grade was utilized without any chemical modification. Having a large number of hydroxyl groups, dextran is a suitable compound for subsequent chemical crosslinking with STMP [31], an FDA-approved food additive [37] that is preferred over conventional crosslinker glutaraldehyde known for cytotoxicity [38]. Fucoidan, a marine polysaccharide approved as a pharmaceutical compound [39] that exhibits a nanomolar affinity to *P*-selectin [40], served as a targeting ligand to thrombi. Hence, both natural polysaccharides applied in this study are affordable, biodegradable, biocompatible compounds, non-immunogenic, and approved for clinical applications.

Instead of commonly used organic solvents, sunflower oil was applied as an emulsion continuous phase. The choice of the stabilizing agent plays an important role in reducing the interfacial tension and Laplace pressure when fabricating a stable emulsion and future nanocarrier. In this work, we selected a potent oil-soluble nonionic surfactant for stabilizing w/o emulsions – PGPR, which is also recognized by the FDA as a safe compound and is frequently used as an emulsifier in the food production industry [41]. In addition, to counteract the Ostwald ripening of water droplets, 6 M NaCl was added to the aqueous phase as an osmotic agent to adjust the osmotic gradient and to stabilize the w/o emulsion further. Overall, multiple parameters were optimized to obtain a stable and homogenous miniemulsion and subsequent nano-delivery system. It was found that the size of the templating droplet and the ultimate hydrogel SPs being directly proportional to the polysaccharide molecular weight and inversely proportional to the amount of surfactant and crosslinking agent as well as homogenization speed (data not shown).

ESEM and TEM images revealed a well-defined spherical morphology and uniform size distribution of SPs (Fig. 1C and D). As hydrogel-based particles, they could swell in an aqueous medium while maintaining their network structure (Fig. 1E).

Functionalized Fuco-SPs contained 1.21 ± 0.01 wt% sulfates, which corresponded to a fucoidan content of 8.60 ± 0.01% by elemental analysis of sulfur, and 9.30 ± 1.07% of fucoidan by quantification of the sulfate content by a semi-quantitative colorimetric assay. In such a way, two different techniques estimated ~9% fucoidan composition in the SPs. The physico-chemical properties of these nanoformulations are displayed in Fig. 1F. The SPs exhibited the hydrodynamic size 674.87 ± 59.35 nm (Control-SPs) and 708.48 ± 40.00 nm (Fuco-SPs), determined by DLS. It is important to highlight that a relatively large size of the SPs might limit the accumulation of associated rtPA within the brain parenchyma and reduce the risk of hemorrhagic events. The negative $\zeta$-potential of the SPs —24.83 ± 0.09 mV for Control-SPs and —27.07 ± 0.39 mV for Fuco-SPs ensured colloidal stability as a result of the anionic nature of the fucoidan and the formation of the anionic phosphate functional groups, produced during the crosslinking reaction with STMP. The phosphorus content of the SPs is indicated in Fig. 1F.

The size and zeta potential of both SPs remained relatively stable for at least 30 days at 4 °C (Fig. 1F). Besides, effective storage of the SPs can be ensured by freeze-drying with 5% (w/v) sucrose as a cryoprotectant and subsequent resuspension in an aqueous medium. The overall yield of the synthesis was 11.1 ± 0.6%, resulting in the production 13.4 ± 0.7 mg of SPs per batch.

### 3.2. Biocompatibility of the SPs

The injectable hydrogel SPs were produced according to the green chemistry principles through the formulation method without using hazardous substances and organic solvents and were expected to be biocompatible.

An initial *in vitro* evaluation of biocompatibility of the developed SPs examined cyto- and hemocompatibility. The cytocompatibility of the SPs was assessed with a resazurin cell viability assay on endothelial cells. Following 24 h exposure, Control-SPs and Fuco-SPs did not affect cellular viability and metabolic activity of HUVECs at concentrations ranging from 0.1 to 1.5 mg/ml, exhibiting an excellent cytocompatible profile (cell survival >90%, up to the highest tested concentrations of SPs) (Fig. 2A). The upper limit for the tested concentration 1.5 mg/ml of the SPs was selected to surpass the tested concentrations for the majority of the nanosystems *in vitro* (typically, maximum 400 μg/ml) [42] and the concentration of the SPs employed for further *in vivo* experiments in this work (71 mg SPs per 1 kg body weight or 1.1 mg SPs per 1 mL of blood). There was no significant difference between the Control-SPs and Fuco-SPs, as both did not provoke cytotoxicity.

Since the SPs in this study were designed for intravenous administration and were expected to have direct contact with blood, the Fuco-SPs were examined for their blood-compatible behavior by a hemolysis test on isolated murine red blood cells *in vitro* (Fig. 2B). Even at the highest concentration of 1.5 mg/ml, the SPs presented a hemolytic index 1.51 ± 0.02%, below 2%, and considered nonhemolytic according to ISO 10993 - 4 standard [43,44].

Morphology of the cells, co-cultured with Fuco-SPs, was visualized with confocal microscopy. No obvious morphological differences were revealed for HUVECs with Fuco-SPs and negative control, as depicted in Fig. 2C. FITC-Phalloidin staining was used to visualize a cytoplasm and DAPI for nuclei.

Collectively, these results suggest that the polysaccharide SPs have favorable biocompatibility for their application *in vivo*.

### 3.3. Binding of SPs to P-selectin in vitro

Knowing that fucoidan was homogeneously distributed in the structure of the hydrogel Fuco-SPs and constituted ~9% w/w of the composition, we investigated whether its quantity on the surface was sufficient for specific adhesion to its molecular target. While most of the publications assess targeting strategy *in vitro* in static conditions by flow cytometry or confocal microscopy [20,45,46], our group developed a robust and tunable dynamic microfluidic method that mimics arterial or venous blood flow conditions to study the targeting efficacy for recombinant *P*-selectin or/and human activated platelet aggregates expressing *P*-selectin. It was previously validated on fucoidan-coated nano-/microcarriers (Figure S2, Supplementary Data) [21–23].

First, fluorescent Fuco-SPs and Control-SPs were injected in the microchannels coated with recombinant *P*-selectin under arterial or venous shear rates (67.50 dyne/cm$^2$ vs. 6.75 dyne/cm$^2$), and their adhesion was visualized and quantified in real-time under fluorescence microscopy. According to obtained results, fluorescent Fuco-SPs depicted a significantly higher adhesion to *P*-selectin coating than Control-SPs both in arterial (374.25 ± 115.33 adhered Fuco-SPs vs. 30.25 ± 13.84 adhered Control-SPs, $^*p < 0.05$) and venous (228.25 ± 36.67 adhered Fuco-SPs vs. 34.50 ± 18.16 adhered Control-SPs, $^{**}p < 0.01$) flow conditions (Fig. 3A, E). There was no significant difference between the fluorescent signal of Fuco-SPs accumulation for arterial and venous flow conditions ($p = 0.27$). Fuco-SPs accumulation after injection onto *P*-selectin coating was in a linear dose-dependent manner as regards to the *P*-selectin concentration, $R^2 = 0.99$ (Fig. 3B). An experiment of competitive interaction illustrates that fucoidan solution pre-injection at 10 mg/ml considerably reduced the attachment of the Fuco-SPs onto the microchannels with *P*-selectin (374.25 ± 115.33 vs. 19.75 ± 10.06, $^*p < 0.05$) (Fig. 3C).

To establish the specificity of the Fuco-SPs binding to *P*-selectin, the targeting assay was extended to other members of the selectin family: E- and L-selectin [47]. The percentage of the Fuco-SPs adhered to the E- and L-selectin was normalized over the mean number of the attached Fuco-SPs to a *P*-selectin coating at the equivalent concentration. Indeed, only 12.73 ± 3.66% of the SPs adhered to E-selectin and 0.26 ± 0.19% to L-selectin coating (Fig. 3D). Thus, our results indicate that Fuco-SPs bind specifically to *P*-selectin but not to E- and L-selectins, and these results

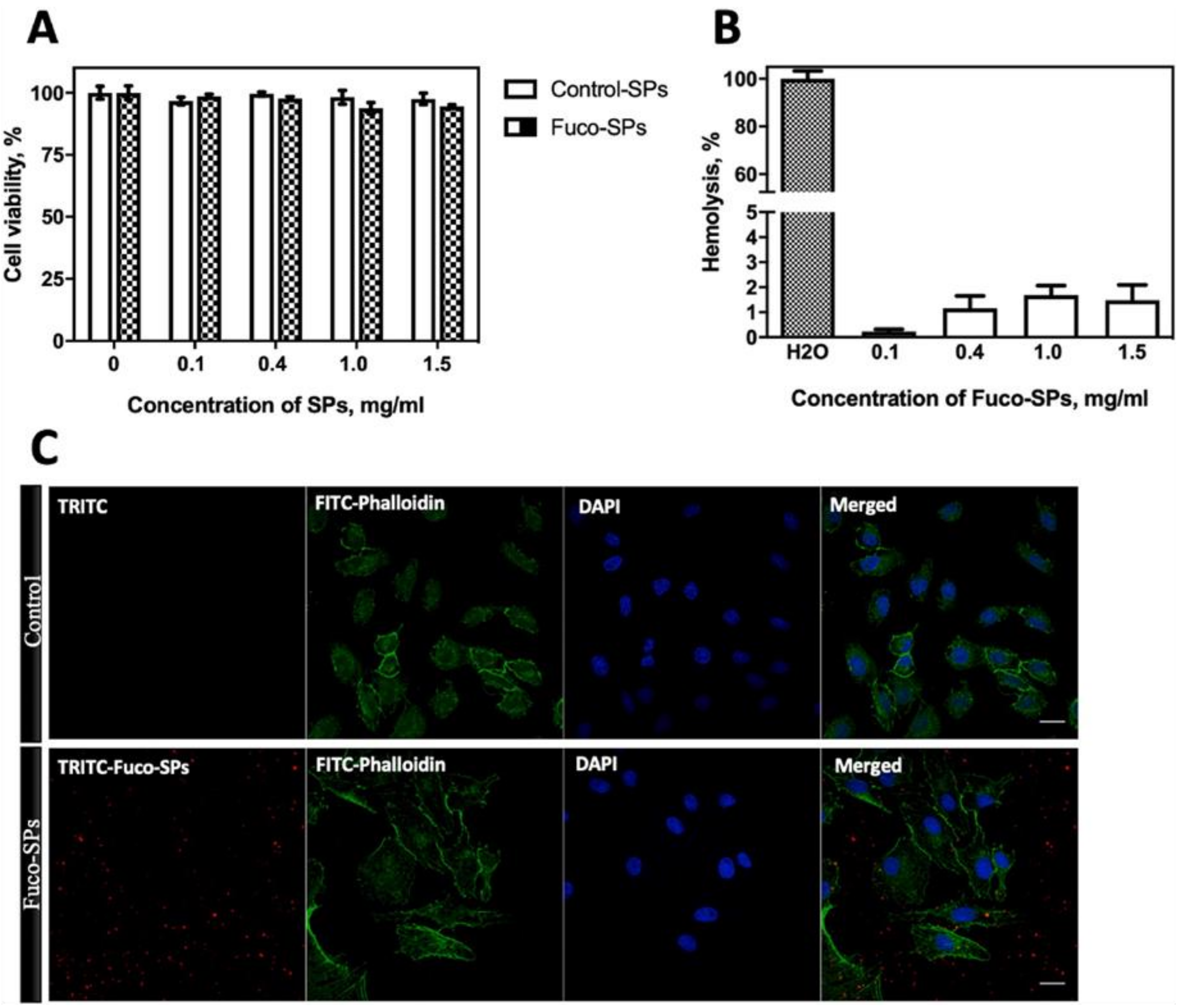

**Fig. 2.** Biocompatibility of the SPs. Cytocompatibility (A) and hemocompatibility (B). Confocal microscopy of HUVECs cultured without (control) and with Fuco-SPs (C) (scale bar = 30 μm).

are in accordance with a previous work of our group published by Bo Li et al. of fucoidan-functionalized polymer microcapsules [21].

Overall, these findings are encouraging evidence of the sensitivity and selectivity of the Fuco-SPs, confirming fucoidan potential as a natural ligand of *P*-selectin.

### *3.4. rtPA loading onto the SPs and its release in saline. In vitro thrombolytic activity o rtPA-loaded SPs*

Due to rtPA low bioavailability and requirement of high dose administration, coupling this enzyme to the biocompatible nanocarrier could overcome the drawbacks associated with a drug high dosage. Herein, an efficient rtPA encapsulation was achieved through the physical adsorption method due to electrostatic interaction: the protein, which is an amphoteric molecule, was put in contact with negatively charged polysaccharide SPs in the water at pH below rtPA isoelectric point IP = 7.7 [48,49] when rtPA presented a positive charge. The hydrogel nature of the SPs allowed reaching a high encapsulation efficiency of the rtPA of 64.78 ± 2.16% and 81.04 ± 1.86% for Control-SPs and Fuco-SPs, respectively. The confocal microscopy images of FITC-rtPA loaded onto TRITC-labeled Fuco-SPs revealed the uniform distribution of the rtPA within a porous structure of the hydrogel SPs, as evidenced by a green fluorescence from FITC-rtPA colocalized with the red fluorescence from the particles (Figure S3A, Supplementary Data).

The release kinetics of rtPA from fucoidan-functionalized SPs was analyzed *in vitro* by flow cytometry [35] in saline at 37 °C under gentle agitation by quantifying the MFI of the FITC-labeled rtPA associated with TRITC-fluorescent Fuco-SPs. Figure S3B, Supplementary Data indicated a gradual and continuous sustained release of the lytic agent from the SPs during the observation period: 46.41 ± 1.34% of the encapsulated protein was released during the first 15 min, and 76.98 ± 1.74% after 90 min. This release profile is classical for the hydrogels [50].

The thrombolytic activity of the rtPA-loaded SPs *in vitro* was analyzed as a combination of amidolytic and fibrinolytic activities (Fig. 4A, B, C). Amidolytic or enzymatic activity featured the ability of the proteolytic enzyme to hydrolyze the rtPA substrate. Interestingly, the amidolytic activities of rtPA on Control-SPs and Fuco-SPs were comparable to that of free rtPA (Fig. 4A and B). The fibrinolytic experiment *in vitro* of the rtPA-loaded SPs was performed in a fibrin plate assay (Figure S4A, Supplementary Data). The results indicated full retention of fibrinolytic activity (Fig. 4C; Figure S4B, Supplementary Data). rtPA loaded onto the SPs appeared to diffuse into the fibrin-agarose matrix and induce fibrinolysis in contact with fibrin. No significant difference was detected between both types of SPs, enabling us to utilize them in the following experiments.

Overall, the rtPA association with the SPs did not affect the drug amidolytic activity and fibrinolytic potential in our design. This result is in accordance with most studies on nanogels suggesting that drug encapsulation via a passive diffusion into the preformed nanogels does not affect the secondary structure of the adsorbed protein and its biological activity [51].

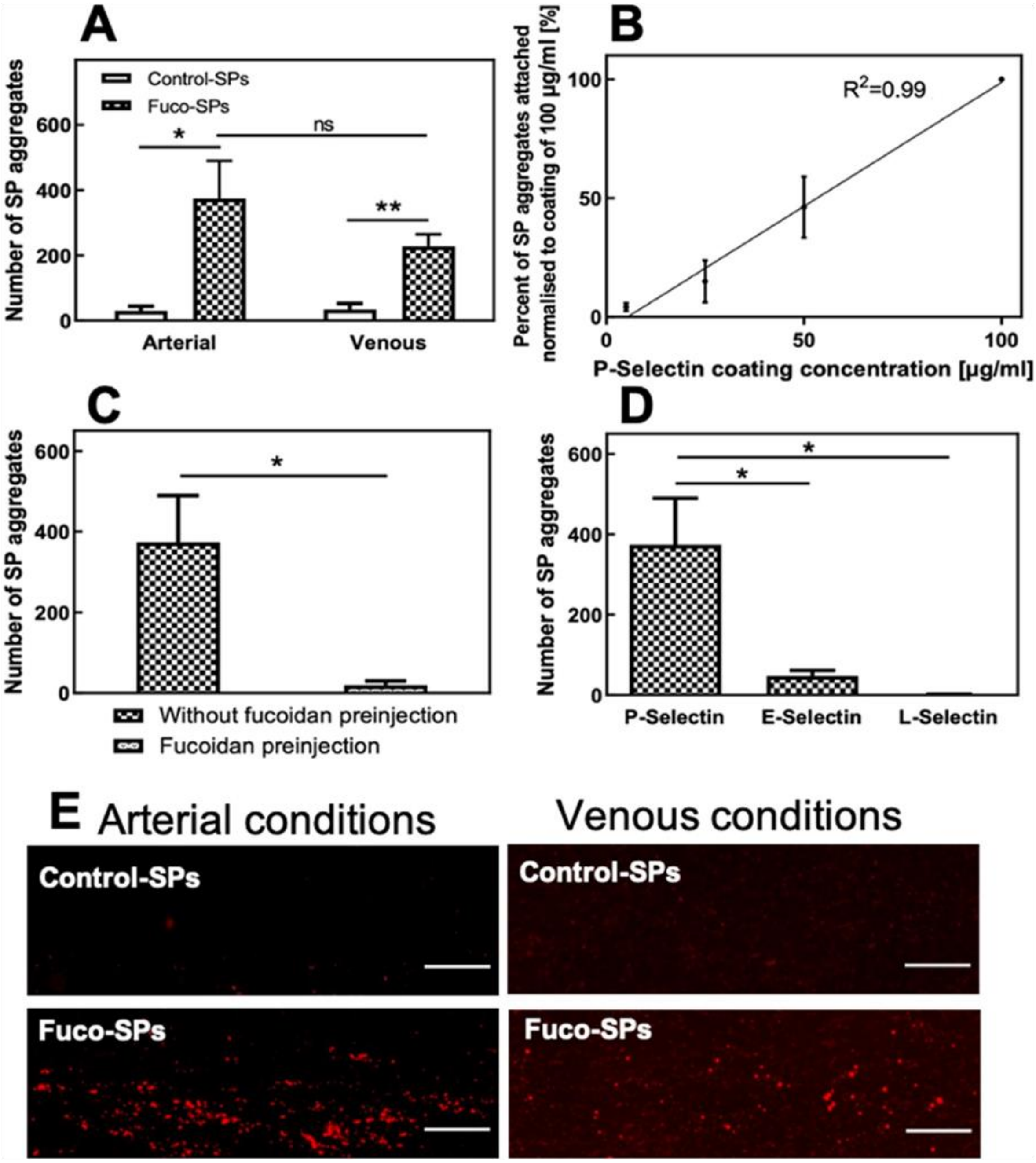

**Fig. 3.** Evaluation of the SPs interactions with selectins. A. Adhesion of the Control-SPs or Fuco-SPs on the coating of the recombinant *P*-selectin in the microfluidic assay under arterial and venous flow conditions (n = 4). B. Concentration-dependent binding of the Fuco-SPs onto the coating of the *P*-selectin at a range of concentrations. C. Fucoidan pre-injection inhibited Fuco-SPs adhesion onto the *P*-selectin. D. Comparison of the Fuco-SPs binding to other selectins: E— and L-Selectin. E. Fluorescent microscope view of Control-SPs or Fuco-SPs adhesion over a *P*-selectin coating of 100 µg/ml under arterial and venous shear rates (scale bar = 20 µm).

### *3.5. Unloaded and rtPA-loaded Fuco-SPs adhere to activated platelet aggregates in vitro under arterial flow*

Since aggregation of activated platelets and platelet-mediated coagulation pathways are hallmark events in thrombosis, activated platelets are a suitable cellular target for nanocarrier binding to thrombi [52]. Before the *in vivo* tests, we complemented the targeting evaluation on selectins with the second set of microfluidic experiments to validate Fuco-SPs capability to actively anchor onto the surface of activated platelets, expressing *P*-selectin. Thus, human whole blood was passed into collagen-coated microchannels to induce platelet activation and aggregation. Fuco-SPs or Control-SPs were then perfused at arterial shear stress and the accumulation of the fluorescence from the adhered SPs was detected on the surface of activated platelet aggregates. A quantitative analysis of the MFI revealed that Fuco-SPs adhered significantly more onto activated platelets than Control-SPs (2678.34 ± 237.40 for Fuco-SPs vs. 392.44 ± 137.15 for Control-SPs, ***p < 0.001, Fig. 5A–B Left). Notably, adsorption of rtPA did not impair the Fuco-SPs clot-binding ability (1880.80 ± 429.37 for rtPA-Fuco-SPs vs. 77.56 ± 40.25 for rtPA-Control-SPs, **p < 0.01, Fig. 5B Right). There was no significant difference between unloaded and rtPA-loaded Fuco-SPs adhering to the activated platelets (p = 0.11).

In conclusion, these *in vitro* experiments provided crucial evidence of molecular interaction and high affinity between the *P*-selectin on the activated platelets and fucoidan-functionalized SPs, which was maintained after loading the thrombolytic agent. This finding presumes that

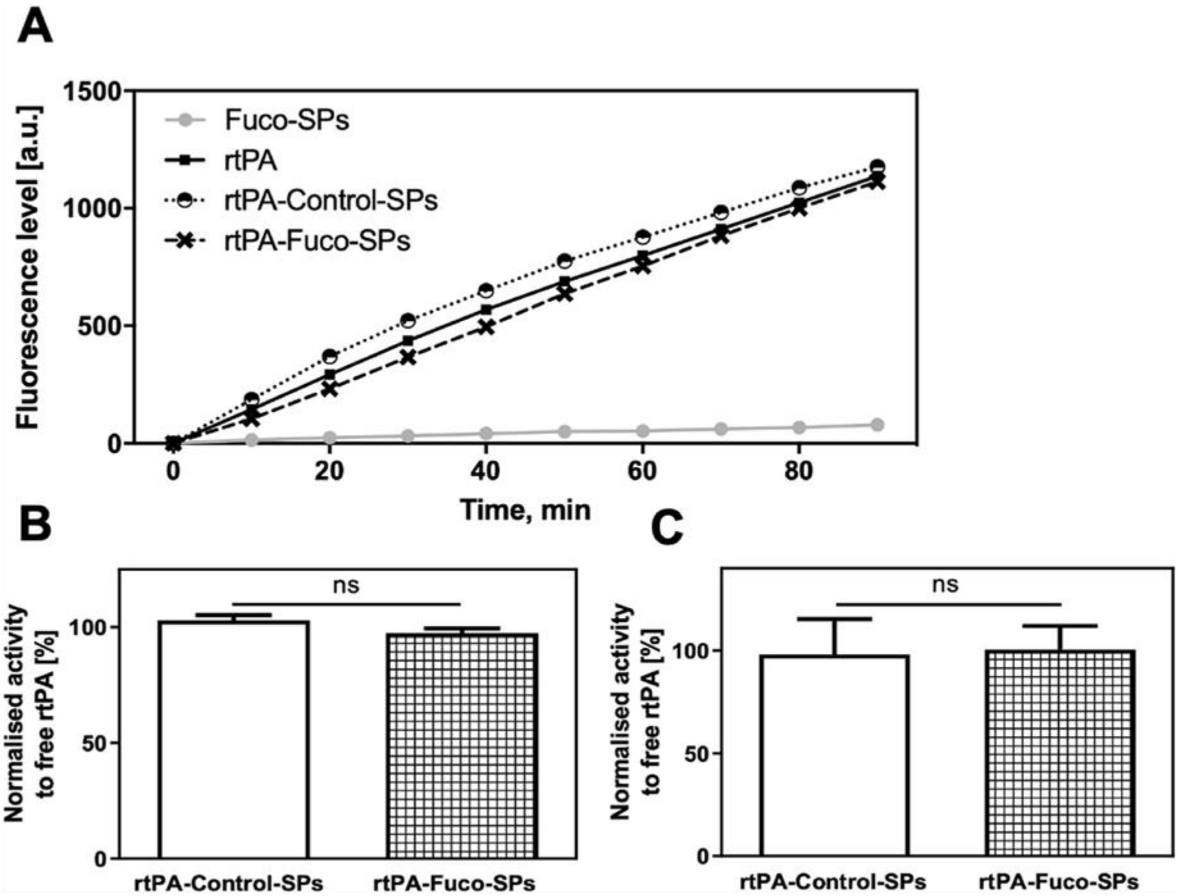

**Fig. 4.** Thrombolytic efficacy *in vitro* of the rtPA-loaded SPs. A - B. Amidolytic activity measured by the PefaFluor® fluorogenic assay. A. The curves correspond to the mean value of fluorescence release and are correlated with the enzymatic velocity over 90 min. B. Corresponding quantitative analysis normalized to free rtPA at the same concentration at 90 min (n = 3). C. Fibrinolytic activities of the SPs determined by a fibrin-plate agarose assay. The quantitative analysis normalized to free rtPA at the same concentration (n = 3).

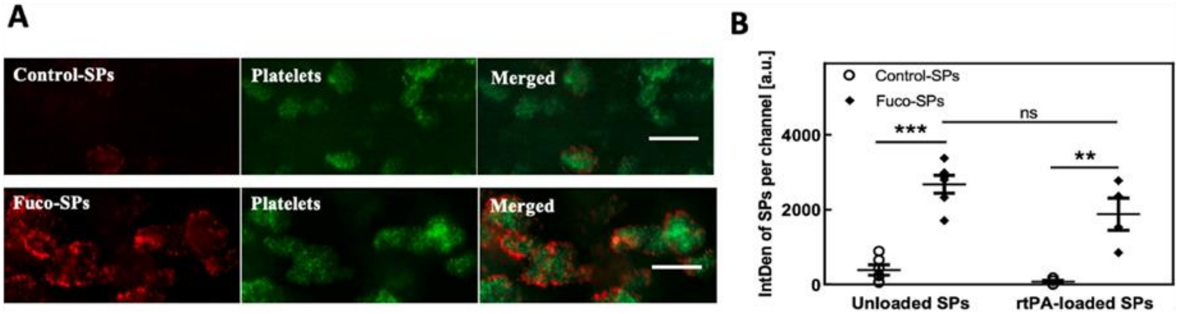

**Fig. 5.** Adhesion of the SPs over activated platelet aggregates. A. Visualization by fluorescent microscopy of the attached unloaded SPs on the microchannels after the formation of the platelet aggregates (scale bar = 20 μm). B. Corresponding quantification of the integral density of the unloaded (n = 6) and rtPA-loaded (n = 4) Control-SPs and Fuco-SPs in ImageJ.

the administration of the rtPA-Fuco-SPs could enable a specific delivery of the rtPA-immobilized SPs to the platelet-rich thrombus with higher drug accumulation.

### 3.6. *Tissue distribution in vivo of fucoidan-functionalized SPs*

After their intravenous injection, the distribution *in vivo* of Fuco-SPs was examined by histological analysis of the excised tissues with alcian blue staining of negatively charged particles in the healthy mouse. The presence of Fuco-SPs in four main organs of excretion (liver, spleen, lungs, and kidneys) was assessed on several sections for each organ. Our results revealed that the polysaccharide Fuco-SPs distributed primarily into the spleen post-administration, indicating the splenic clearance. The particles accumulated in the liver to a lower extent, while their presence in the kidneys and lungs remained minor. These differences are presented in Figure S5, Supplementary Data. Our data are in agreement with other deformable polymer hydrogel-like particles in their submicron and micron size range [53].

### 3.7. *In vivo thrombolytic efficacy*

Whereas demonstrating the *in vitro* activity of the rtPA immobilized on the drug delivery system is important, the *in vivo* therapeutic effect is paramount. A murine thromboembolic stroke model was established by *in situ* injection of 1 IU of thrombin into the MCA by provoking a coagulation cascade and formation of both fibrin- and platelet-rich clots in the lumen of the artery [54,55]. Fig. 6A highlights the *in vivo* experiments design, and Fig. 6B the potential mode of action of the Fuco-SPs in the thrombus. The treatment options – control saline, rtPA 10 mg/kg, or rtPA-Fuco-SPs at 10 mg/kg rtPA – were intravenously injected 20 min after ischemic onset under rtPA clinical mode of administration: 10% bolus followed by 90% infusion. It is important to note that 10 mg/kg is a relevant dose in mice in place of 0.9 mg/kg in humans because of a lower sensitivity of human rtPA in murine plasma [56]. No morbidity or mortality was observed in the mice during therapeutic experiments, suggesting that rtPA-Fuco-SPs do not provoke acute toxicity under the current conditions.

Cerebral blood flow was monitored throughout the treatment via laser Doppler speckle contrast imaging, a high resolution and high-speed technique that instantly visualizes microcirculatory tissue blood perfusion. The reduction of the blood flow in the ipsilateral cerebral hemisphere due to the stroke was restored by 33.97 ± 5.15% after 40 min treatment with rtPA-Fuco-SPs; by contrast, in the rtPA and saline group for which the perfusion was improved only by 15.16 ± 6.49% and 10.33 ± 4.62%, respectively, in this experiment (Fig. 6E). The representative laser Doppler speckle multispectral imaging in the ipsilateral and the contralateral hemispheres at 0 min and 40 min are expressed in Fig. 6D. Accelerated Video S1A, B, C recorded the perfusion in real-time for all conditions. These data were confirmed by the angiographic analysis performed 24 h later and assessed by a blinded observer based on TICI grade flow scoring measured by magnetic resonance angiography (MRA). Indeed, similar to some untreated stroke patients, some blood clots were gradually lysed post-stroke in this murine model: at 24 h after thrombotic occlusion, 40% of mice exhibited a total recanalization (score 3) of the MCA when injected with saline, while treatment of 40% of animals resulted in partial perfusion (score 2), and 20% achieved only minimal flow (score 1) (Fig. 6H; Figure S6A, Supplementary Data). However, after the treatment with rtPA-Fuco-SPs, most of the cases were entirely recanalized (score 3). For the rtPA treated group, no animal achieved a score 1 of minimal perfusion, and 67% of cases showed a partial score 2 level of recanalization.

We then utilized magnetic resonance imaging as a powerful technique to quantify the volume of brain damage at 24 h after stroke onset. Using T2-weighted MRI sequences, we observed that the size of the ischemic brain lesions for the control saline group was 14.80 ± 3.34 $mm^3$ whereas for the rtPA-loaded fucoidan-targeted SPs it was 4.63 ± 1.59 $mm^3$ (Fig. 6F and G). rtPA-conjugated Fuco-SPs reduced the ischemic zone almost 2-fold of the free rtPA, despite the fact that these data were non-significant due to the limited number of the animals as to the well-known effect of free rtPA in this murine model [55]. Out of all treated animals with rtPA-Fuco-SPs, 66.6% of the animals displayed small lesion sizes (<3 $mm^3$), and 33.3% had medium lesion sizes (<11

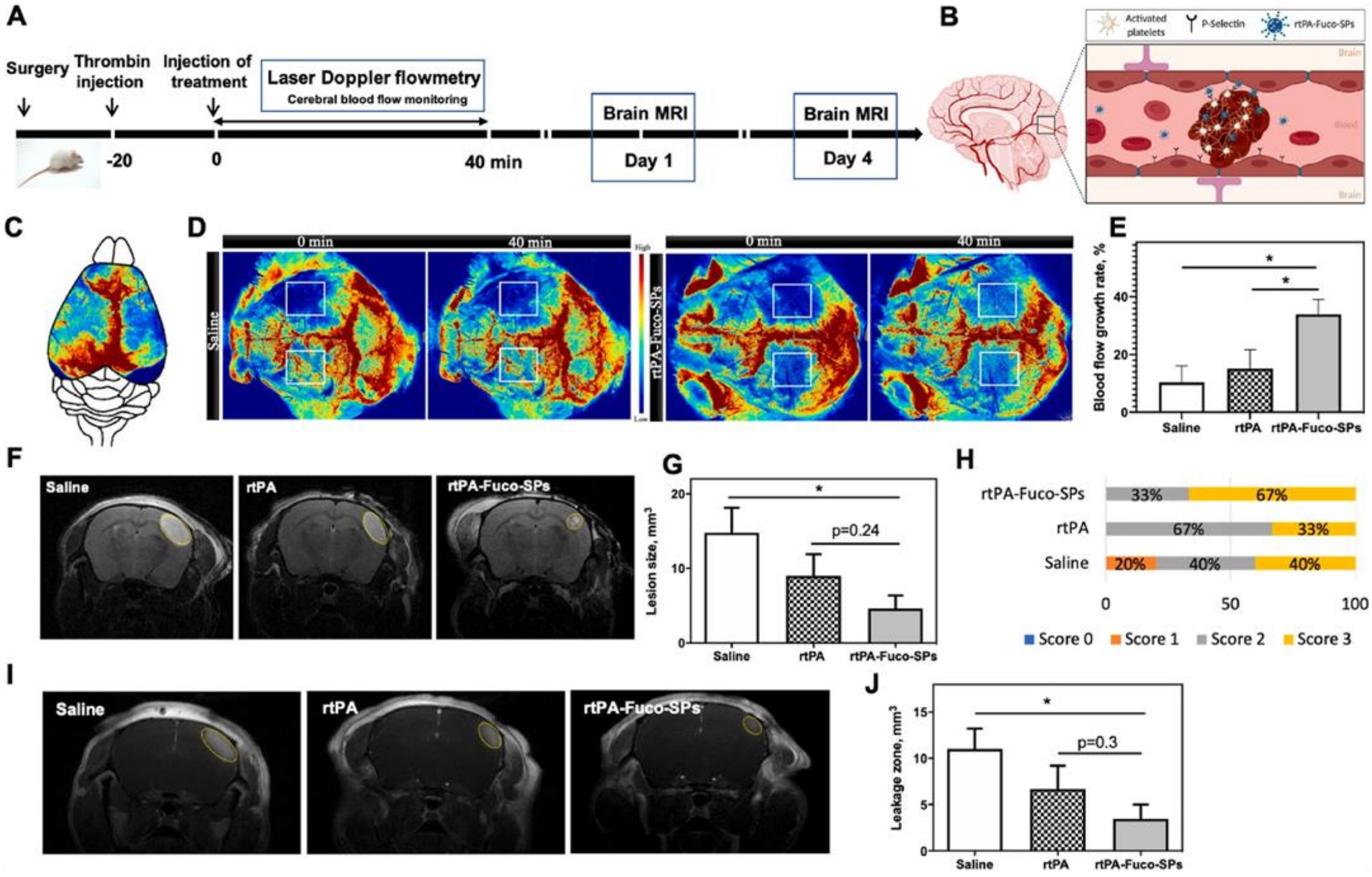

**Fig. 6.** Thrombolytic efficacy *in vivo* in the murine ischemic stroke model. A. Schematic of the design of the *in vivo* experiment. B. Proposed therapeutic mode of action of the rtPA-loaded Fuco-SPs after the ischemic stroke: the Fuco-SPs accumulate on the surface of the activated platelets due to *P*-selectin affinity of fucoidan and perform local thrombolysis with alteplase. C – E. Cerebral blood flow reperfusion monitored by the laser speckle contrast imaging during the 40-min treatment (n ≥ 5). Schematic image of the perfusion in the microcirculatory brain tissue (C). The representative multispectral photos in the ROI of ipsilateral (upper) and contralateral (lower) hemispheres at 0 min and 40 min for saline and rtPA-Fuco-SPs groups (D). The growth rate of the cerebral reperfusion in the ipsilateral hemisphere after 40 min treatment injection (E). F. MRI images of the infarct lesion 24 h post-stroke with the corresponding quantification of its volume (G), (n ≥ 5). H. Angiographic scores of the MCA reperfusion at day 1 after stroke induction by MRI. I. MRI images of the BBB permeability at day 4 post-stroke with the corresponding quantification of its volume (J), (n ≥ 5).

mm$^3$). In the rtPA group, only 33.3% of the animals displayed a small infarct zone. In the saline treatment group, we recorded 60% of the animals with severe ($<20$ mm$^3$) and critical ($>20$ mm$^3$) lesions and no animals with small lesions (Figure S6B, Supplementary Data).

To monitor the BBB integrity disrupted by ischemic stroke [57], extravasation of gadolinium injected intravenously was detected and quantified on T1-weighted MRI images at day 4 after stroke (Fig. 6I and J). Gadolinium extravasation from the blood into the brain parenchyma was unmistakably located at the ischemia-affected region where the BBB was compromised. rtPA-Fuco-SPs treatment group demonstrated a significant BBB preservation over control groups of free rtPA and saline with only a subtle BBB breakdown of $3.45 \pm 1.40$ mm$^3$.

In order to confirm the accumulation of Fuco-SPs within the thrombus area *in vivo*, we injected fluorescent-labeled SPs at the therapeutic concentration as in the stroke model into the $FeCl_3$ model of venous thrombosis in mice. Upon histological examination of the thrombus-affected area of the mesenteric vein, Fuco-SPs were clearly identified on the green-fluorescent labeled thrombus (Fig. 7A). By a quantitative analysis of the MFI normalized by the size of the thrombus, it was evidenced a highly increased TRITC signal from fucoidan-functionalized SPs group comparing with Control-SPs ($9.48 \pm 2.19$ for Fuco-SPs vs. $1.48 \pm 0.35$ for Control-SPs, $^{**}p < 0.01$, Fig. 7B).

Overall, the apparent superiority of rtPA-Fuco-SPs to reduce the brain tissue injury area in comparison with saline and rtPA at the same dose, combined with a favorable safety profile of the SPs, makes them a promising nanomedicine-based approach for the treatment of acute arterial thrombosis.

## 4. Discussion

The revolutionary treatment with alteplase to dissolve thrombi and restore blood flow is a standard of care in acute thrombotic events, but it is certainly not risk-free. Nanomedicine exploits a profound understanding of the molecular mechanisms involved in thrombus formation and offers outside-the-box strategies to effectively target and dissolve the blood clots in the body with fewer systemic and neurological complications [58].

In this study, rtPA was associated with hydrogel-like polysaccharide SPs, synthesized by a simple miniemulsion/crosslinking process. The soft structure of chemically crosslinked hydrogels resembles those of extracellular matrices and may prevent tissue irritation, providing a convenient and versatile platform for storage and site-specific delivery of a drug to the thrombi [59]. Our approach's novelty is exclusively polysaccharide nature of the particles – from dextran and fucoidan without any prior chemical modification, as well as green chemistry synthesis technique. Intriguingly, several articles claim that dextran [60] and fucoidan [61,62] themselves exert some antithrombotic action that makes them an excellent starting material for the nanocarrier. Hydrophilic polysaccharide surfaces lead to longer circulating NPs since they avert the formation of a protein corona and early macrophage internalization [63]. Moreover, natural polysaccharides are advantageous to synthetic polymers in terms of safety, abundance in nature, and low cost. Overall, we considered the issues imperative for high biosafety and potential future clinical translation of Fuco-SPs by (I) the choice of biocompatible and biodegradable materials, all with FDA-approval; (II) a relatively simple and efficient production by a mild synthesis method without the utilization of the hazardous substances and organic solvents; (III) targeting agent of natural origin – fucoidan – that is being validated in clinical trials for thrombosis.

After fabrication and extensive physico-chemical characterization of the SPs, we confirmed their cyto- and hemocompatibility at concentrations up to 1.5 mg/ml (Figs. 2A and 3B). The main pathway of the polysaccharide Fuco-SPs tissue distribution *in vivo* upon intravenous injection was the spleen (Figure S5, Supplementary Data). Future studies should include the tests of thrombogenicity and immunogenicity *in vivo*.

The Fuco-SPs were associated with a thrombolytic agent by physical adsorption, allowing a high encapsulation efficiency of the rtPA of $81.04 \pm 1.86\%$ due to their hydrogel-based structure. Classically, alteplase is loaded onto the NPs using the covalent amide bond formation via EDC/NHS reaction between the primary amines on the rtPA molecule and the nanocarriers containing carboxyl groups. As a mild drug encapsulation method, adsorption is preferred to covalent bioconjugation to load fragile molecules such as proteins to avoid changes in the protein structure and function that might result in its partial denaturation and loss of biological activity [64]. The fibrinolytic diffused through the matrix of the porous SPs (Figure S3A, Supplementary Data), fully preserving its enzymatic and fibrinolytic potential *in vitro* (Fig. 4). Friedrich et al. demonstrated that the adsorptive bound rtPA liberated faster from the particles and spread more readily into the fibrin matrix than covalently bound rtPA [65], which may be beneficial in targeted thrombolysis. Although a rising number of recent articles apply a controlled release of the thrombolytics via endogenous and exogenous stimuli, we chose not to incorporate sophisticated nanodesigns and demonstrated a gradual and continuous rtPA release from the SPs without an external trigger (Figure S3B, Supplementary Data) so as to facilitate future regulatory approvals.

The clot targeting strategy of the SPs was achieved by the introduction of the fucoidan to the polysaccharide solution at 9% w/w. Functionalization with fucoidan permitted the high-affinity binding of Fuco-SPs to its molecular target *P*-selectin in a dynamic microfluidic method that mimics arterial or venous blood flow conditions in a dose-dependent manner (Fig. 3A, B, E). Importantly, this type of interaction is selective, as SPs did not adhere a lot to other selectins: E- and L-selectin *in vitro* (Fig. 3D). When the microchannels were covered with activated platelet aggregates, both unloaded and rtPA-loaded Fuco-SPs were capable of binding these micro-clots (Fig. 5). Once tested in the *in vivo*

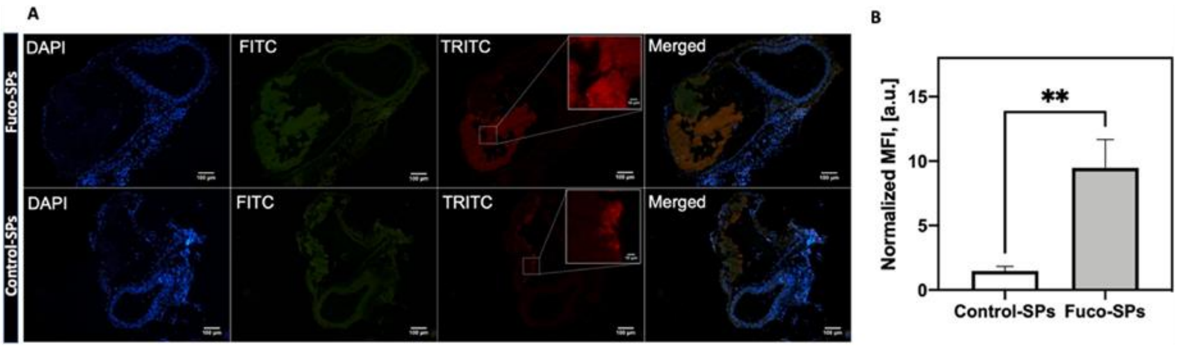

Fig. 7. *In vivo* targeting in the $FeCl_3$ murine model of thrombosis. A. Histological analysis of thrombi in the mesenteric vein by fluorescent microscopy. The venous vascular wall is visualized with DAPI staining; thrombus is stained in green due to DIOC6 labeling of platelets; Fuco-SPs and Control-SPs are fluorescently labeled with TRITC. Inserts are a magnification of dashed Regions of Interest of the TRITC signal. B. Corresponding quantification of MFI from the adhered TRITC-SPs in the thrombi (n = 5).

model of venous thrombosis, Fuco-SPs were identified on the $FeCl_3$-induced thrombi by histological examination, contrary to Control-SPs (Fig. 7). Our data validate an inimitable and efficient thrombus targeting approach of the Fuco-SPs, using a clinical algae-derived compound. Yet, a surge in strategies involving dual or even more surface targeting moieties is being witnessed in academic works. For instance, the combinatory targeting of GPIIb/IIIa receptors and *P*-selectin on activated platelets with two peptide ligands on the lipid nanovesicles enhanced thrombus binding capacities in a synergic manner [66]. Another notable example is the biomimetic functionalization of NPs with platelet membrane coating that enabled thrombus directing via multiple platelet receptors [67]. These combinations of NP modifications represent a promising strategy for developing next-generation blood clot-targeting NP platforms for therapy and/or diagnostics.

The experiments on the murine thrombin-induced thromboembolic stroke model supported the therapeutic effect of the rtPA-Fuco-SPs *in vivo* (Fig. 6). The findings of the submicroparticle-associated rtPA treatment group outperformed those of free rtPA at the same concentration, as we observed a more rapid clot dissolution and MCA reperfusion, which minimized the brain injury and resulted in subsequently smaller infarct area post-stroke by MRI. Several groups previously reported the reduction of the infarct zone in preclinical models by nanomedicinal product. For example, the magnetic iron oxide ($Fe_3O_4$)-microrods [10] and polyacrylic acid-stabilized magnetic NPs [12] conjugated with rtPA diminished the brain infarct lesion in the $FeCl_3$ murine model of ischemic stroke of MCA. These designs, however, require an external magnet for targeting and to complement chemical lysis with rtPA with mechanical one of the magnetic rotations. Without any clinically approved medical device to impose a high magnetic force on the NPs in deep blood vessels, it would probably be desirable for nanocarrier formulation to avoid external assistance. Mei et al. stated that only the synergistic effect of rtPA-loaded polymer micelles and a reactive oxygen species (ROS)-eliminating antioxidant suppressed an infarct volume and improved neurological deficit after brain ischemia in the mouse model of photo-thrombotic MCA occlusion [68]. In our case, the therapeutic benefit of rtPA-Fuco-SPs could be ascribed to faster MCA reperfusion and, hence, prevention of the major brain injury due to higher rtPA accumulation on the thrombus site as to active targeting and specific *P*-selectin interactions of the Fuco-SPs.

Moreover, the animals in the rtPA-Fuco-SPs group suffered a lower level of BBB disruption by the ischemic stroke that was quantified on T1-weighted MRI images with gadolinium. It is vital to underline that although in this article we utilized fucoidan on the SPs purely for the *P*-selectin targeting purpose, new avenues of research are deciphering its neuroprotective role, particularly after cerebral ischemic events [69]. Altogether, this first proof-of-concept *in vivo* results of Fuco-SPs show an astonishing potential of the nanomedicine-based approach for the targeted treatment of acute thrombosis. We speculate that the submicron size of the particles, along with their active thrombus-targeting moiety, should maintain rtPA-loaded nanocarrier within the intravascular compartment to exert its thrombolytic activity. It should prevent the leakage of rtPA into the brain parenchyma, reducing the risks of NMDA receptors-mediated neurotoxicity and hemorrhages [70]. Further studies could compare a single or a double bolus route of administration of rtPA-Fuco-SPs due to the rtPA preservation by SPs, and, thus, a more comfortable treatment option for patients. Besides, these particles could also vehicle other therapeutic and/or molecular imaging agents in the vascular compartment to target *P*-selectin overexpressed pathologies, such as cardiovascular diseases [71] or some cancers [72,73]. Considering the detrimental role of *P*-selectin in chronic or acute inflammatory pathologies [10], it might be relevant to explore the immunomodulatory and anti-inflammatory effects of fucoidan in the Fuco-SPs, in addition to its binding *P*-selectin, bearing in mind that natural variability of fucoidans (the source, species, molecular weight, composition, and structure of the polysaccharides) influences their biological activity and potential therapeutic application.

Nevertheless, as none of the available *in vivo* rodent experimental models of acute thrombosis accurately recapitulates all the aspects of human disease progression and heterogeneity, it is recommended to validate any translational concept in multiple models to ensure its therapeutic efficacy and safety. Notably, in 2019, Xu et al. proposed a biomimetic strategy of platelet membrane-camouflaged PLGA NPs with rtPA that was studied in several *in vivo* models: pulmonary embolism, $FeCl_3$-induced arterial thrombosis, and ischemic stroke model [67].

Due to technical challenges and strict regulatory requirements, the clinical translation of the nanopharmaceutical products happens slowly. The rtPA-Fuco-SPs representing an actively targeted nanodelivery system reach a balance of safety, simplicity, and functionality concerning the projected clinical application. While they were designed and fabricated in the academic laboratory at the range of ~10 mg per batch, the industrial scale-up of the process with high reproducibility under GMP conditions and intended quality standards is essential to establish in order to obtain the necessary amounts for further screening and, ultimately, clinical use. For instance, high-precision microfluidic and micropatterning methods for the fabrication of monodisperse NPs with uniform physicochemical characteristics and low batch-to-batch variability are becoming prevalent and are compatible with GMP standards [74]. Finally, an adequate sterilization method should be validated to prevent nanoparticle damage and alteration in the product's parameters.

## 5. Conclusions

In the present study, we designed and fabricated fucoidan-functionalized 100% polysaccharide submicroparticles from biocompatible and FDA approved components as a *P*-selectin targeting drug delivery system for thrombolytic therapy. The physico-chemical properties and a biocompatibility analysis of these SPs were thoroughly evaluated, and alteplase was effectively immobilized onto the SPs with full retention of its enzymatic and fibrinolytic potential *in vitro* and sustained drug-release kinetics. We established *in vitro* by dynamic flow microchamber assays that the fucoidan-functionalized nanosystem specifically adhered to the recombinant *P*-selectin in a dose-dependent manner, but not to E- and L-Selectins, and to human activated platelets. In $FeCl_3$ model of thrombosis, Fuco-SPs accumulated in the thrombus. Finally, our findings revealed in the murine model of ischemic stroke that rtPA conjugation to the Fuco-SPs could enhance the thrombolytic activity of the clinical agent *in vivo*. The blood flow perfusion was restored more rapidly, which resulted in smaller post-ischemic cerebral infarct lesions and higher BBB protection. In summary, an alteplase-associated hydrogel-based nano-delivery system with fucoidan demonstrates a solid argument for improved thrombolytic therapy in terms of safety and efficacy in the preclinical studies.

## Credit author statement

Alina ZENYCH: Conceptualization; Investigation; Data curation; Formal analysis; Writing - Original & Revised Draft; Visualization. Charl`ene JACQMARCQ: Investigation. Rachida AID: Investigation; Validation. Louise FOURNIER: Investigation. Laura M. FORERO RAMIREZ: Methodology. Fr´ed´eric CHAUBET: Methodology; Visualization. Thomas BONNARD: Methodology; Investigation; Validation; Writing – review & editing. Denis VIVIEN: Resources; Project administration; Writing – review & editing. Didier LETOURNEUR: Resources; Project administration. C´edric CHAUVIERRE: Conceptualization; Validation; Resources; Writing – review & editing; Supervision; Project administration; Funding acquisition. All the authors approved the final revised version of the manuscript.

## Declaration of competing interest

The authors declare that they have no known competing financial interests or personal relationships that could have appeared to influence the work reported in this paper.

## Acknowledgments

The authors would like to acknowledge Marie-Françoise Bricot from the Institut de Chimie des Substances Naturelles of the Université Paris-Saclay for performing a microanalysis of the fucoidan and the Fuco-SPs. We also thank the ImagoSeine core facility of the Institut Jacques Monod, a member of IBiSA and France-Bio-Imaging (ANR-10-INBS-04) infrastructures for the TEM. The authors are grateful for Christine ChoqueuX, who performed the Environmental SEM at Université de Technologie de Compiègne, Compiègne, France. We kindly thank Pr. Antonino Nicoletti for his advice on designing an *in vitro* release study and Dr. Kevin Guedj for assistance with flow cytometry. We also thank Dr. Yoann Lalatonne for the technical support with the TXRF technique and Dr. Samira Benadda with confocal microscopy. The illustrations were designed with BioRender software (biorender.com). Funding: The authors thank INSERM, Université de Paris, and Université Sorbonne Paris Nord for financial support. This work also received funding from the EU project FP7-NMP-2012-LARGE-6-309820 "NanoAthero" and ANR-13-LAB1-0005-01"FucoChem". Alina Zenych is grateful for the Ph. D. fellowship from the INSPIRE program of the European Union's Horizon 2020 research and innovation program (Marie Sklodowska-Curie grant # 665850).

## Appendix A. Supplementary data

Supplementary data to this article can be found online at https://doi.org/10.1016/j.biomaterials.2021.121102.

## References

1 E.J. Benjamin, P. Muntner, A. Alonso, M.S. Bittencourt, C.W. Callaway, A. P. Carson, A.M. Chamberlain, A.R. Chang, S. Cheng, S.R. Das, F.N. Delling, L. Djousse, M.S.V. Elkind, J.F. Ferguson, M. Fornage, L.C. Jordan, S.S. Khan, B. M. Kissela, K.L. Knutson, T.W. Kwan, D.T. Lackland, T.T. Lewis, J.H. Lichtman, C. T. Longenecker, M.S. Loop, P.L. Lutsey, S.S. Martin, K. Matsushita, A.E. Moran, M. E. Mussolino, M. O'Flaherty, A. Pandey, A.M. Perak, W.D. Rosamond, G.A. Roth, U. K.A. Sampson, G.M. Satou, E.B. Schroeder, S.H. Shah, N.L. Spartano, A. Stokes, D. L. Tirschwell, C.W. Tsao, M.P. Turakhia, L.B. VanWagner, J.T. Wilkins, S.S. Wong, S.S. Virani, Heart disease and stroke statistics—2019 update: a report from the American heart association, Circulation (2019), https://doi.org/10.1161/CIR.0000000000000659.

[2] W.J. Powers, A.A. Rabinstein, T. Ackerson, O.M. Adeoye, N.C. Bambakidis, K. Becker, J. Biller, M. Brown, B.M. Demaerschalk, B. Hoh, E.C. Jauch, C. S. Kidwell, T.M. Leslie-Mazwi, B. Ovbiagele, P.A. Scott, K.N. Sheth, A. M. Southerland, D.V. Summers, D.L. Tirschwell, Guidelines for the early management of patients with acute ischemic stroke: 2019 update to the 2018 guidelines for the early management of acute ischemic stroke: a guideline for healthcare professionals from the American heart association/American stroke, Stroke 50 (2019) e344, https://doi.org/10.1161/STR.0000000000000211. –e418.

3 J. Mican, M. Toul, D. Bednar, J. Damborsky, Structural biology and protein engineering of thrombolytics, Comput. Struct. Biotechnol. J. 17 (2019) 917–938, https://doi.org/10.1016/j.csbj.2019.06.023.

4 R. Bhatia, M.D. Hill, N. Shobha, B. Menon, S. Bal, P. Kochar, T. Watson, M. Goyal, A.M. Demchuk, Low rates of acute recanalization with intravenous recombinant tissue plasminogen activator in ischemic stroke: real-world experience and a call for action, Stroke 41 (2010) 2254–2258, https://doi.org/10.1161/STROKEAHA.110.592535.

[5] A.M. Thiebaut, M. Gauberti, C. Ali, S. Martinez De Lizarrondo, D. Vivien, M. Yepes, B.D. Roussel, The role of plasminogen activators in stroke treatment: fibrinolysis and beyond, Lancet Neurol. 17 (2018) 1121–1132, https://doi.org/10.1016/S1474-4422(18)30323-5.

6 A. Pal Khasa, Y. Pal Khasa, The evolution of recombinant thrombolytics: current status and future directions, Bioengineered 8 (2017) 331–358, https://doi.org/10.1080/21655979.2016.1229718.

7 S. Liu, X. Feng, R. Jin, G. Li, Tissue plasminogen activator-based nanothrombolysis for ischemic stroke, Expet Opin. Drug Deliv. 15 (2018) 173–184, https://doi.org/10.1080/17425247.2018.1384464.

8 N. Korin, M. Kanapathipillai, B.D. Matthews, M. Crescente, A. Brill, T. Mammoto, K. Ghosh, S. Jurek, S.A. Bencherif, D. Bhatta, A.U. Coskun, C.L. Feldman, D. D. Wagner, D.E. Ingber, Shear-activated nanotherapeutics for drug targeting to obstructed blood vessels, Science 337 (2012) 738–742, https://doi.org/10.1126/science.1217815, 80.

9 M. Colasuonno, A.L. Palange, R. Aid, M. Ferreira, H. Mollica, R. Palomba, M. Emdin, M. Del Sette, C. Chauvierre, D. Letourneur, P. Decuzzi, Erythrocyte-Inspired discoidal polymeric nanoconstructs carrying tissue plasminogen activator for the enhanced lysis of blood clots, ACS Nano 12 (2018) 12224–12237, https://doi.org/10.1021/acsnano.8b06021.

10 J. Hu, S. Huang, L. Zhu, W. Huang, Y. Zhao, K. Jin, Q. Zhuge, Tissue plasminogen activator-porous magnetic microrods for targeted thrombolytic therapy after ischemic stroke, ACS Appl. Mater. Interfaces 10 (2018) 32988–32997, https://doi.org/10.1021/acsami.8b09423.

11 H.-W. Yang, M.-Y. Hua, K.-J. Lin, S.-P. Wey, R.-Y. Tsai, S.-Y. Wu, Y.-C. Lu, H.-L. Liu, T. Wu, Y.-H. Ma, Bioconjugation of recombinant tissue plasminogen activator to magnetic nanocarriers for targeted thrombolysis, Int. J. Nanomed. 7 (2012) 5159–5173, https://doi.org/10.2147/IJN.S32939.

12 L. Huang, J. Wang, S. Huang, F. Siaw-Debrah, M. Nyanzu, Q. Zhuge, Polyacrylic acid-coated nanoparticles loaded with recombinant tissue plasminogen activator for the treatment of mice with ischemic stroke, Biochem. Biophys. Res. Commun. 516 (2019) 565–570, https://doi.org/10.1016/j.bbrc.2019.06.079.

13 J. Zhou, D. Guo, Y. Zhang, W. Wu, H. Ran, Z. Wang, Construction and evaluation of Fe3O4-based PLGA nanoparticles carrying rtPA used in the detection of thrombosis and in targeted thrombolysis, ACS Appl. Mater. Interfaces 6 (2014) 5566–5576, https://doi.org/10.1021/am406008k.

14 A. Friedman, S. Claypool, R. Liu, The smart targeting of nanoparticles, Curr. Pharmaceut. Des. 19 (2013) 6315–6329, https://doi.org/10.2174/13816128113199990375.

15 W. jin Jeong, J. Bu, L.J. Kubiatowicz, S.S. Chen, Y.S. Kim, S. Hong, Peptide–nanoparticle conjugates: a next generation of diagnostic and therapeutic platforms? Nano Converg 5 (2018) 1–18, https://doi.org/10.1186/s40580-018-0170-1.

16 L. Chollet, P. Saboural, C. Chauvierre, J.-N. Villemin, D. Letourneur, F. Chaubet, Fucoidans in Nanomedicine, Mar. Drugs. 14 (2016) 1–24, https://doi.org/10.3390/md14080145.

17 L. Bachelet, I. Bertholon, D. Lavigne, R. Vassy, M. Jandrot-Perrus, F. Chaubet, D. Letourneur, Affinity of low molecular weight fucoidan for P-selectin triggers its binding to activated human platelets, Biochim. Biophys. Acta Gen. Subj. 1790 (2009) 141–146, https://doi.org/10.1016/j.bbagen.2008.10.008.

18 P. Saboural, F. Chaubet, F. Rouzet, F. Al-Shoukr, R. Ben Azzouna, N. Bouchemal, L. Picton, L. Louedec, M. Maire, L. Rolland, G. Potier, D. Le Guludec, D. Letourneur, C. Chauvierre, Purification of a low molecular weight fucoidan for SPECT molecular imaging of myocardial infarction, Mar. Drugs 12 (2014) 4851–4867, https://doi.org/10.3390/md12094851.

19 T. Bonnard, J.-M. Serfaty, C. Journ´e, B. Ho Tin Noe, D. Arnaud, L. Louedec, M. Derkaoui, D. Letourneur, C. Chauvierre, C. Le Visage, Leukocyte mimetic polysaccharide microparticles tracked in vivo on activated endothelium and in abdominal aortic aneurysm, Acta Biomater. 10 (2014) 3535–3545, https://doi.org/10.1016/j.actbio.2014.04.015.

20 T. Bonnard, G. Yang, A. Petiet, V. Ollivier, O. Haddad, D. Arnaud, L. Louedec, L. Bachelet-Violette, S.M. Derkaoui, D. Letourneur, C. Chauvierre, C. Le Visage, Abdominal aortic aneurysms targeted by functionalized polysaccharide microparticles: a new tool for SPECT imaging, Theranostics 4 (2014) 592–603, https://doi.org/10.7150/thno.7757.

21 B. Li, M. Juenet, R. Aid-Launais, M. Maire, V. Ollivier, D. Letourneur, C. Chauvierre, Development of polymer microcapsules functionalized with fucoidan to target P-selectin overexpressed in cardiovascular diseases, Adv. Healthc. Mater. 6 (2017) 1–11, https://doi.org/10.1002/adhm.201601200.

22 B. Li, R. Aid-Launais, M.-N. Labour, A. Zenych, M. Juenet, C. Choqueux, V. Ollivier, O. Couture, D. Letourneur, C. Chauvierre, Functionalized polymer microbubbles as new molecular ultrasound contrast agent to target P-selectin in thrombus, Biomaterials 194 (2019) 139–150, https://doi.org/10.1016/j.biomaterials.2018.12.023.

23 M. Juenet, R. Aid-Launais, B. Li, A. Berger, J. Aerts, V. Ollivier, A. Nicoletti, D. Letourneur, C. Chauvierre, Thrombolytic therapy based on fucoidan-functionalized polymer nanoparticles targeting P-selectin, Biomaterials 156 (2018) 204–216, https://doi.org/10.1016/j.biomaterials.2017.11.047.

24 C. Chauvierre, D. Letourneur, The European project NanoAthero to fight cardiovascular diseases using nanotechnologies, Nanomedicine 10 (2015) 3391–3400, https://doi.org/10.2217/nnm.15.170.

25 K.H. Zheng, Y. Kaiser, E. Poel, H. Verberne, J. Aerts, F. Rouzet, E. Stroes, D. Letourneur, C. Chauvierre, 99Mtc-Fucoidan as diagnostic agent for P-selectin imaging: first-in-human evaluation (phase I), Atherosclerosis 287 (2019) e143, https://doi.org/10.1016/j.atherosclerosis.2019.06.425.

26 I. Cicha, C. Chauvierre, I. Texier, C. Cabella, J.M. Metselaar, J. Szebeni, L. D´ezsi, C. Alexiou, F. Rouzet, G. Storm, E. Stroes, D. Bruce, N. MacRitchie, P. Maffia, D. Letourneur, From design to the clinic: practical guidelines for translating cardiovascular nanomedicine, Cardiovasc. Res. 114 (2018) 1714–1727, https://doi.org/10.1093/cvr/cvy219.

27 K. Ganguly, K. Chaturvedi, U.A. More, M.N. Nadagouda, T.M. Aminabhavi, Polysaccharide-based micro/nanohydrogels for delivering macromolecular therapeutics, J. Contr. Release 193 (2014) 162–173, https://doi.org/10.1016/j.jconrel.2014.05.014.

28 J. Zhang, W. Xia, P. Liu, Q. Cheng, T. Tahirou, W. Gu, B. Li, Chitosan modification and pharmaceutical/biomedical applications, Mar. Drugs 8 (2010) 1962–1987, https://doi.org/10.3390/md8071962.

29 H.J. Jin, H. Zhang, M.L. Sun, B.G. Zhang, J.W. Zhang, Urokinase-coated chitosan nanoparticles for thrombolytic therapy: preparation and pharmacodynamics in vivo, J. Thromb. Thrombolysis 36 (2013) 458–468, https://doi.org/10.1007/s11239-013-0951-7.

30 J. Liao, X. Ren, B. Yang, H. Li, Y. Zhang, Z. Yin, Targeted thrombolysis by using c-RGD-modified N,N,N-Trimethyl Chitosan nanoparticles loaded with lumbrokinase, Drug Dev. Ind. Pharm. 45 (2019) 88–95, https://doi.org/10.1080/03639045.2018.1522324.

31 S.R. Van Tomme, W.E. Hennink, Biodegradable dextran hydrogels for protein delivery applications, Expet Rev. Med. Dev. 4 (2007) 147–164, https://doi.org/10.1586/17434440.4.2.147.

32 J.R. McCarthy, I.Y. Sazonova, S.S. Erdem, T. Hara, B.D. Thompson, P. Patel, I.Botnaru, C.P. Lin, G.L. Reed, R. Weissleder, F.A. Jaffer, Multifunctional nanoagent for thrombus-targeted fibrinolytic therapy, Nanomedicine 7 (2012) 1017–1028, https://doi.org/10.2217/nnm.11.179.

33 S. Heid, H. Unterweger, R. Tietze, R.P. Friedrich, B. Weigel, I. Cicha, D. Eberbeck, A.R. Boccaccini, C. Alexiou, S. Lyer, Synthesis and characterization of tissue plasminogen activator-functionalized superparamagnetic iron oxide nanoparticles for targeted fibrin clot dissolution, Int. J. Mol. Sci. 18 (2017), https://doi.org/10.3390/ijms18091837.

34 J.M. Lee, Z.-U. Shin, G.T. Mavlonov, I.Y. Abdurakhmonov, T.-H. Yi, Solid-phase colorimetric method for the quantification of fucoidan, Appl. Biochem. Biotechnol. 168 (2012) 1019–1024, https://doi.org/10.1007/s12010-012-9837-y.

35 S. Petersen, A. Fahr, H. Bunjes, Flow cytometry as a new approach to investigate drug transfer between lipid particles, Mol. Pharm. 7 (2010) 350–363, https://doi.org/10.1021/mp900130s.

36 C. Orset, R. Macrez, A.R. Young, D. Panthou, E. Angles-cano, E. Maubert, V. Agin, D. Vivien, Mouse model of in situ thromboembolic stroke and reperfusion, Stroke 38 (2007) 2771–2778, https://doi.org/10.1161/STROKEAHA.107.487520.

37 T.E. Furia, CRC Handbook of Food Additives, second ed., CRC Press, 1973.

38 W.E. Hennink, C.F. van Nostrum, Novel crosslinking methods to design hydrogels, Adv. Drug Deliv. Rev. 54 (2002) 13–36, https://doi.org/10.1016/S0169-409X(01)00240-X.

39 C. Chauvierre, R. Aid-Launais, J. Aerts, M. Maire, L. Chollet, L. Rolland, R. Bonafé, S. Rossi, S. Bussi, C. Cabella, D. Laszlo, T. Fülöp, J. Szebeni, Y. Chahid, K.H. Zheng, E.S.G. Stroes, D. Le Guludec, F. Rouzet, D. Letourneur, Pharmaceutical development and safety evaluation of a GMP-grade fucoidan for molecular diagnosis of cardiovascular diseases, Mar. Drugs 17 (2019) 1–17, https://doi.org/10.3390/md17120699.

40 F. Rouzet, L. Bachelet-Violette, J.-M. Alsac, M. Suzuki, A. Meulemans, L. Louedec, A. Petiet, M. Jandrot-Perrus, F. Chaubet, J.-B. Michel, D. Le Guludec, D. Letourneur, Radiolabeled fucoidan as a P-selectin targeting agent for in vivo imaging of platelet-rich thrombus and endothelial activation, J. Nucl. Med. 52 (2011) 1433–1440, https://doi.org/10.2967/jnumed.110.085852.

41 F. Wolf, K. Koehler, H.P. Schuchmann, Stabilization of water droplets in oil with PGPR for use in oral and dermal applications, J. Food Process. Eng. 36 (2013) 276–283, https://doi.org/10.1111/j.1745-4530.2012.00688.x.

42 J. Matuszak, J. Baumgartner, J. Zaloga, M. Juenet, A.E. da Silva, D. Franke, G. Almer, I. Texier, D. Faivre, J.M. Metselaar, F.P. Navarro, C. Chauvierre, R. Prassl, L. Dézsi, R. Urbanics, C. Alexiou, H. Mangge, J. Szebeni, D. Letourneur, I. Cicha, Nanoparticles for intravascular applications: physicochemical characterization and cytotoxicity testing, Nanomedicine 11 (2016) 597–616, https://doi.org/10.2217/nnm.15.216.

43 M. Weber, H. Steinle, S. Golombek, L. Hann, C. Schlensak, H.P. Wendel, M. Avci-Adali, Blood-contacting biomaterials: in vitro evaluation of the hemocompatibility, Front. Bioeng. Biotechnol. 6 (2018) 99, https://doi.org/10.3389/fbioe.2018.00099.

44 ISO 10993-4:2017, Biol. Eval. Med. Devices — Part 4 Sel. Tests Interact. With Blood, 2017. https://www.iso.org/standard/63448.html.

45 B. Vaidya, G.P. Agrawal, S.P. Vyas, Platelets directed liposomes for the delivery of streptokinase: development and characterization, Eur. J. Pharmaceut. Sci. 44 (2011) 589–594, https://doi.org/10.1016/j.ejps.2011.10.004.

46 N. Zhang, C. Li, D. Zhou, C. Ding, Y. Jin, Q. Tian, X. Meng, K. Pu, Y. Zhu, Cyclic RGD functionalized liposomes encapsulating urokinase for thrombolysis, Acta Biomater. (2018), https://doi.org/10.1016/j.actbio.2018.01.038.

47 K. Ley, The role of selectins in inflammation and disease, Trends Mol. Med. 9 (2003) 263–268, https://doi.org/10.1016/S1471-4914(03)00071-6.

48 J.-H. Kim, J.-Y. Yoon, Protein adsorption on polymer particles, Encycl. Surf. Colloid Sci. (2002) 4373–4381, https://doi.org/10.1002/jbm.820210202.

49 I. Politis, L. Wang, J.D. Turner, B.K. Tsang, Changes in tissue-type plasminogen activator-like and plasminogen activator inhibitor activities in granulosa and theca layers during ovarian follicle development in the domestic Hen1, Biol. Reprod. 42 (1990) 747–754, https://doi.org/10.1095/biolreprod42.5.747.

50 V. Wintgens, C. Lorthioir, P. Dubot, B. Sébille, C. Amiel, Cyclodextrin/dextran based hydrogels prepared by cross-linking with sodium trimetaphosphate, Carbohydr. Polym. 132 (2015) 80–88, https://doi.org/10.1016/j.carbpol.2015.06.038.

51 L. Arnfast, C.G. Madsen, L. Jorgensen, S. Baldursdottir, Design and processing of nanogels as delivery systems for peptides and proteins, Ther. Deliv. 5 (2014) 691–708, https://doi.org/10.4155/tde.14.38.

52 Z.M. Ruggeri, Platelets in atherothrombosis, Nat. Med. 8 (2002) 1227–1234, https://doi.org/10.4065/81.1.59.

53 T.J. Merkel, K. Chen, S.W. Jones, A.A. Pandya, S. Tian, M.E. Napier, W.E. Zamboni, J.M. Desimone, The effect of particle size on the biodistribution of low-modulus hydrogel PRINT particles, J. Contr. Release 162 (2012) 37–44, https://doi.org/10.1016/j.jconrel.2012.06.009.

[54] C. Orset, B. Haelewyn, S.M. Allan, S. Ansar, F. Campos, T.H. Cho, A. Durand, M. El Amki, M. Fatar, I. Garcia-Yébenes, M. Gauberti, S. Grudzenski, I. Lizasoain, E. Lo, R. Macrez, I. Margaill, S. Maysami, S. Meairs, N. Nighoghossian, J. Orbe, J. A. Paramo, J.J. Parienti, N.J. Rothwell, M. Rubio, C. Waeber, A.R. Young, E. Touzé, D. Vivien, Efficacy of alteplase in a mouse model of acute ischemic stroke: a retrospective pooled analysis, Stroke 47 (2016) 1312–1318, https://doi.org/10.1161/STROKEAHA.116.012238.

55 S.M. De Lizarrondo, C. Gakuba, B.A. Herbig, Y. Repessé, C. Ali, C.V. Denis, P. J. Lenting, E. Touzé, S.L. Diamond, D. Vivien, M. Gauberti, Potent thrombolytic effect of N-acetylcysteine on arterial thrombi, Circulation 136 (2017) 646–660, https://doi.org/10.1161/CIRCULATIONAHA.117.027290.

56 H.R. Lijnen, B. Van Hoef, V. Beelen, D. Collen, Characterization of the murine plasma fibrinolytic system, Eur. J. Biochem. 224 (1994) 863–871, https://doi.org/10.1111/j.1432-1033.1994.00863.x.

57 R. Brouns, P.P. De Deyn, The complexity of neurobiological processes in acute ischemic stroke, Clin. Neurol. Neurosurg. 111 (2009) 483–495, https://doi.org/10.1016/j.clineuro.2009.04.001.

58 A. Zenych, L. Fournier, C. Chauvierre, Nanomedicine progress in thrombolytic therapy, Biomaterials 258 (2020) 120297, https://doi.org/10.1016/j.biomaterials.2020.120297.

59 K.S. Masters, D.N. Shah, L.A. Leinwand, K.S. Anseth, Crosslinked hyaluronan scaffolds as a biologically active carrier for valvular interstitial cells, Biomaterials 26 (2005) 2517–2525, https://doi.org/10.1016/j.biomaterials.2004.07.018.

60 C.I. Jones, D.A. Payne, P.D. Hayes, A.R. Naylor, P.R.F. Bell, M.M. Thompson, A. H. Goodall, The antithrombotic effect of dextran-40 in man is due to enhanced fibrinolysis in vivo, J. Vasc. Surg. 48 (2008) 715–722, https://doi.org/10.1016/j.jvs.2008.04.008.

61 E.M. Balboa, E. Conde, A. Moure, E. Falqué, H. Domínguez, In vitro antioxidant properties of crude extracts and compounds from brown algae, Food Chem. 138 (2013) 1764–1785, https://doi.org/10.1016/j.foodchem.2012.11.026.

62 Y. Choi, S.K. Min, R. Usoltseva, A. Silchenko, T. Zvyagintseva, S. Ermakova, J. K. Kim, Thrombolytic fucoidans inhibit the tPA-PAI1 complex, indicating activation of plasma tissue-type plasminogen activator is a mechanism of fucoidan-mediated thrombolysis in a mouse thrombosis model, Thromb. Res. 161 (2018) 22–25, https://doi.org/10.1016/j.thromres.2017.11.015.

63 K. Knop, R. Hoogenboom, D. Fischer, U.S. Schubert, Poly(ethylene glycol) in drug delivery: pros and cons as well as potential alternatives, Angew. Chem. Int. Ed. 49 (2010) 6288–6308, https://doi.org/10.1002/anie.200902672.

64 M. Di Marco, K.A. Razak, A.A. Aziz, C. Devaux, E. Borghi, L. Levy, C. Sadun, Overview of the main methods used to combine proteins with nanosystems : absorption, bioconjugation, and encapsulation, Int. J. Nanomed. 5 (2010) 37–49.

65 R.P. Friedrich, J. Zaloga, E. Schreiber, I.Y. Tóth, E. Tombácz, S. Lyer, C. Alexiou, Tissue plasminogen activator binding to superparamagnetic iron oxide nanoparticle-covalent versus adsorptive approach, Nanoscale Res. Lett. 11 (2016) 1–11, https://doi.org/10.1186/s11671-016-1521-7.

66 C.L. Pawlowski, W. Li, M. Sun, K. Ravichandran, D. Hickman, C. Kos, G. Kaur, A. Sen Gupta, Platelet microparticle-inspired clot-responsive nanomedicine for targeted fibrinolysis, Biomaterials 128 (2017) 94–108, https://doi.org/10.1016/j.biomaterials.2017.03.012.

67 J. Xu, Y. Zhang, J. Xu, G. Liu, C. Di, X. Zhao, X. Li, Y. Li, N. Pang, C. Yang, Y. Li, B. Li, Z. Lu, M. Wang, K. Dai, R. Yan, S. Li, G. Nie, Engineered nanoplatelets for targeted delivery of plasminogen activators to reverse thrombus in multiple mouse thrombosis models, Adv. Mater. 32 (2019) 1905145, https://doi.org/10.1002/adma.201905145.

68 T. Mei, A. Kim, L.B. Vong, A. Marushima, S. Puentes, Y. Matsumaru, A. Matsumura, Y. Nagasaki, Encapsulation of tissue plasminogen activator in pH-sensitive self-assembled antioxidant nanoparticles for ischemic stroke treatment-Synergistic effect of thrombolysis and antioxidant, Biomaterials 215 (2019) 1–12, https://doi.org/10.1016/j.biomaterials.2019.05.020.

69 H. Kim, J.H. Ahn, M. Song, D.W. Kim, T.K. Lee, J.C. Lee, Y.M. Kim, J.D. Kim, J. H. Cho, I.K. Hwang, B.C. Yan, M.H. Won, J.H. Park, Pretreated fucoidan confers neuroprotection against transient global cerebral ischemic injury in the gerbil hippocampal CA1 area via reducing of glial cell activation and oxidative stress, Biomed. Pharmacother. 109 (2019) 1718–1727, https://doi.org/10.1016/j.biopha.2018.11.015.

70 D. Vivien, M. Gauberti, A. Montagne, G. Defer, E. Touzé, Impact of tissue plasminogen activator on the neurovascular unit: from clinical data to experimental evidence, J. Cerebr. Blood Flow Metabol. 31 (2011) 2119–2134, https://doi.org/10.1038/jcbfm.2011.127.

71 S. Yokoyama, H. Ikeda, N. Haramaki, H. Yasukawa, T. Murohara, T. Imaizumi, Platelet P-selectin plays an important role in arterial thrombogenesis by forming large stable platelet-leukocyte aggregates, J. Am. Coll. Cardiol. 45 (2005) 1280–1286, https://doi.org/10.1016/j.jacc.2004.12.071.

72 S.R. Barthel, J.D. Gavino, L. Descheny, C.J. Dimitroff, Targeting selectins and selectin ligands in inflammation and cancer, Expert Opin. Ther. Targets 11 (2007) 1473–1491, https://doi.org/10.1517/14728222.11.11.1473.

73 Y. Shamay, M. Elkabets, H. Li, J. Shah, S. Brook, F. Wang, K. Adler, E. Baut, M. Scaltriti, P. V Jena, E.E. Gardner, J.T. Poirier, C.M. Rudin, J. Baselga, A. Haimovitz-Friedman, D.A. Heller, P-selectin is a nanotherapeutic delivery target in the tumor microenvironment, Sci. Transl. Med. 8 (2016) 345ra87, https://doi.org/10.1126/scitranslmed.aaf7374.

[74] J.P.A. Ioannidis, B.Y.S. Kim, A. Trounson, How to design preclinical studies in nanomedicine and cell therapy to maximize the prospects of clinical translation, Nat. Biomed. Eng. 2 (2018) 797–809, https://doi.org/10.1038/s41551-018-0314-y.

# Supplementary Data

## Fucoidan-Functionalized Polysaccharide Submicroparticles Loaded with Alteplase for Efficient Targeted Thrombolytic Therapy

Alina Zenych[1], Charlène Jacqmarcq[2,#], Rachida Aid[1,3,#], Louise Fournier[1], Laura M. Forero Ramirez[1], Frédéric Chaubet[1], Thomas Bonnard[2], Denis Vivien[2,4,#], Didier Letourneur[1,#], and Cédric Chauvierre[1,*]

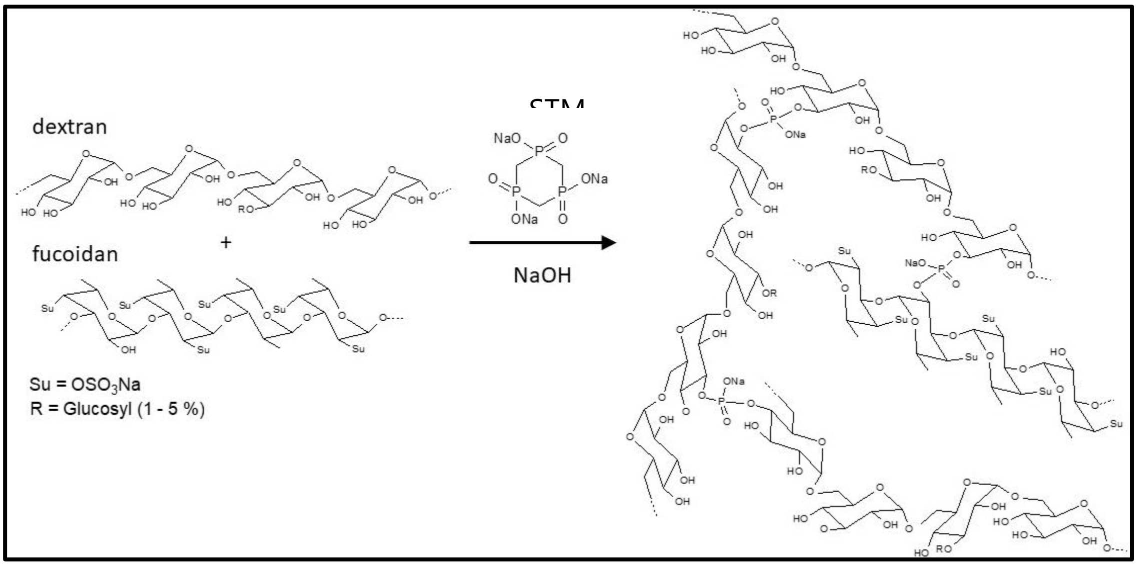

**Figure S1. Schematic of crosslinking of the polysaccharides (dextran and fucoidan) with STMP.**

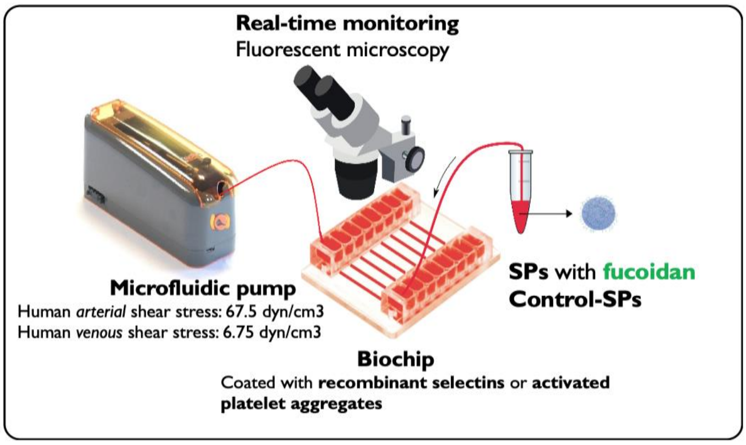

**Figure S2. Schematic illustration of the *in vitro* targeting assay.**

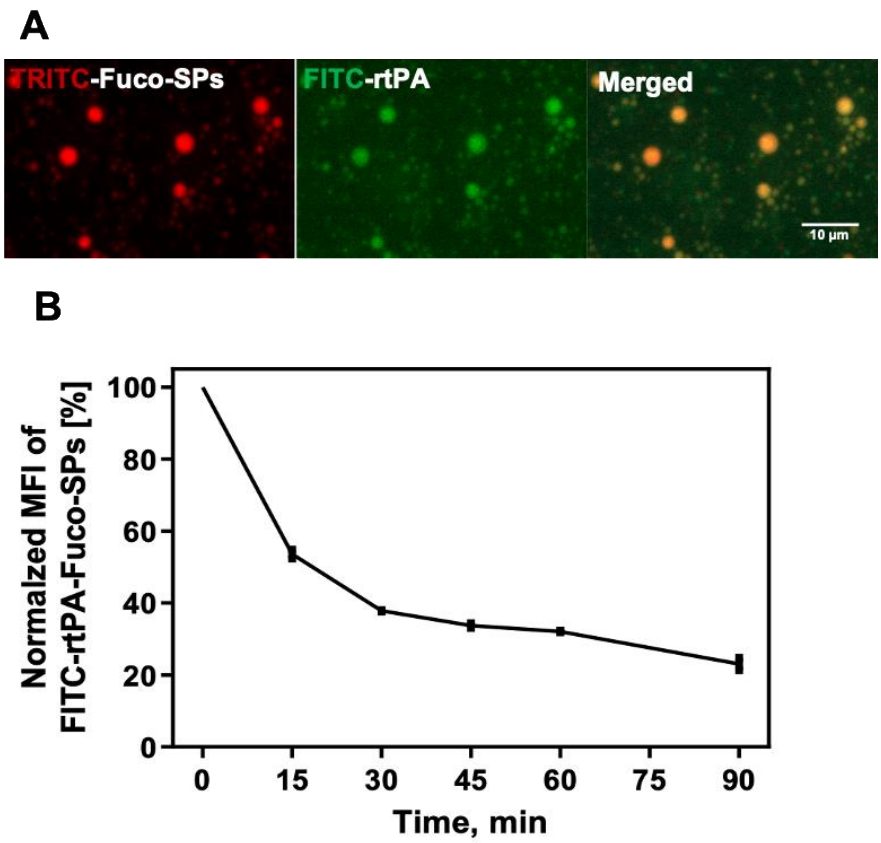

**Figure S3. Loading and release of rtPA from Fuco-SPs. A.** FITC-rtPA loading onto the TRITC-Fuco-SPs visualized by confocal microscopy. **B.** *In vitro* rtPA release from rtPA-encapsulated Fuco-SPs by flow cytometry.

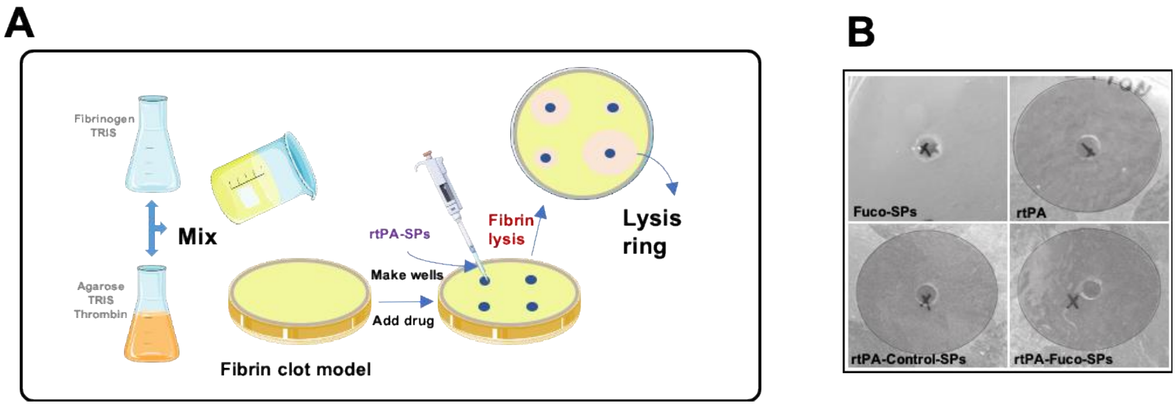

**Figure S4. Fibrinolytic activity of the rtPA-loaded SPs *in vitro*. A.** Schematic illustration of the *in vitro* fibrinolytic test. **B.** Lysed circles as the fibrinolytic potential of the SPs *in vitro* by a fibrin-plate agarose assay at the equal concentration of the rtPA.

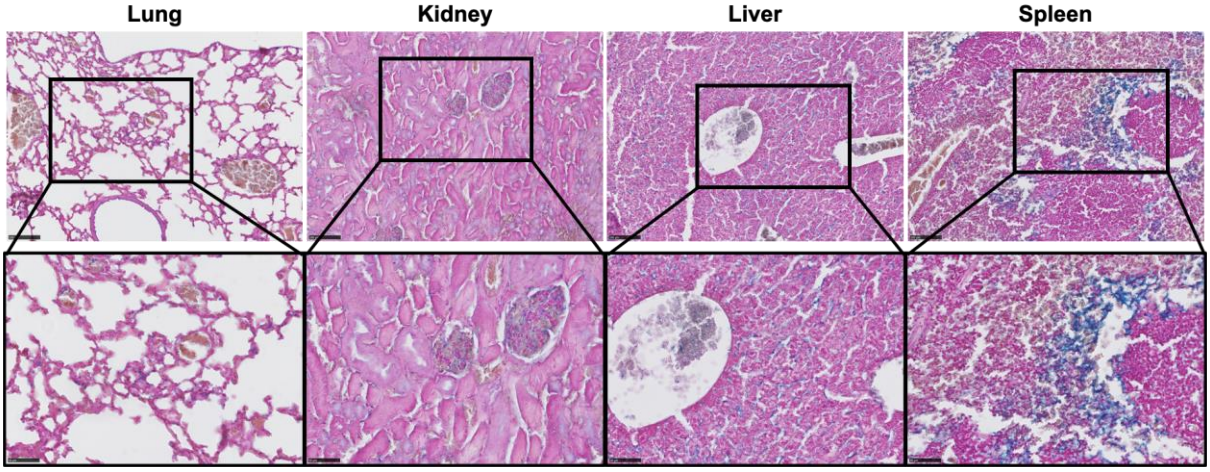

**Figure S5. Histological analysis of Fuco-SPs in four organs of excretion.** The cytoplasm appears pale pink, nuclei are red, and the Fuco-SPs are stained blue. Few particles were detected in the lungs, kidneys, and liver, whereas they were mainly accumulated in the spleen. The scale bar in the upper row = 100 μm, in the lower row (magnified image) = 50 μm.

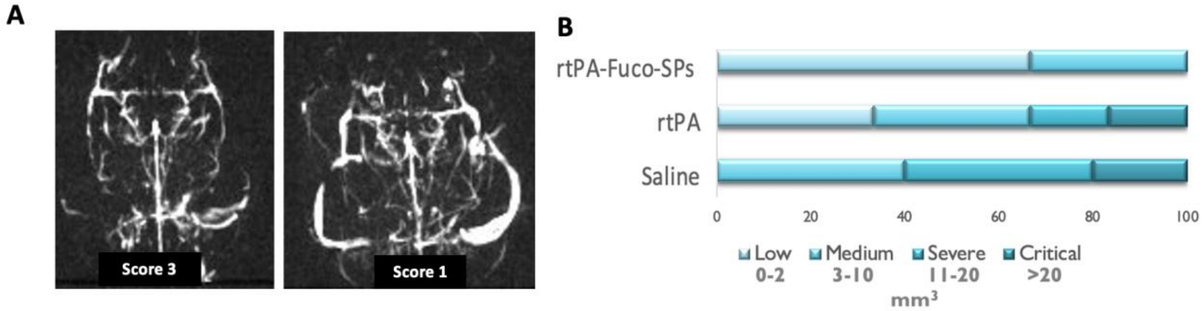

**Figure S6. Therapeutic efficacy of the rtPA-Fuco-SPs *in vivo*. A.** Merged image of the MRA scores (Score 3: full recanalization, score 1: low perfusion). **B.** Distribution of the cases by the infarct zone sizes by MRI 24 h post-stroke.

**Video S1.** Cerebral blood flow reperfusion monitored by the laser speckle contrast imaging during the 40-min treatment regimen with saline (**A**), rtPA (**B**), and rtPA-Fuco-SPs (**C**) in the ROI of ipsilateral (2) and contralateral (1) hemispheres.

**Table S1**. The synthesis parameters for the polysaccharide SPs.

| Synthesis method | Polysaccharide [c], mg/ml | STMP, [c], mg/ml | NaOH [c], M | Phase ratio, (Aq/ Org/) | Surfactant | Homogenization | Crosslinking |
|---|---|---|---|---|---|---|---|
| W/O emulsion / crosslinking | 300 | 56.11 | 1.15 | 4% w/v | PGPR, 6% | 30,000 rpm, 4 min, 4 °C | 20 min, 50 ºC |

Abbreviation: W/O, water-in-oil; Aq, aqueous; Org organic.

# 2. Tracking the immune response by MRI using biodegradable and ultrasensitive microprobes

SCIENCE ADVANCES | RESEARCH ARTICLE

CELL BIOLOGY

# Tracking the immune response by MRI using biodegradable and ultrasensitive microprobes

Sara Martinez de Lizarrondo[1]†, Charlene Jacqmarcq[1]†, Mikael Naveau[2], Manuel Navarro-Oviedo[1], Swannie Pedron[1], Alexandre Adam[3], Barbara Freis[3], Stephane Allouche[4], Didier Goux[5], Sarah Razafindrakoto[6], Florence Gazeau[6], Damien Mertz[3], Denis Vivien[1,7], Thomas Bonnard[1]†, Maxime Gauberti[1,8]*†

**Molecular magnetic resonance imaging (MRI) holds great promise for diagnosis and therapeutic monitoring in a wide range of diseases. However, the low intrinsic sensitivity of MRI to detect exogenous contrast agents and the lack of biodegradable microprobes have prevented its clinical development. Here, we synthetized a contrast agent for molecular MRI based on a previously unknown mechanism of self-assembly of catechol-coated magnetite nanocrystals into microsized matrix-based particles. The resulting biodegradable microprobes (M3P for microsized matrix-based magnetic particles) carry up to 40,000 times higher amounts of superparamagnetic material than classically used nanoparticles while preserving favorable biocompatibility and excellent water dispersibility. After conjugation to monoclonal antibodies, targeted M3P display high sensitivity and specificity to detect inflammation in vivo in the brain, kidneys, and intestinal mucosa. The high payload of superparamagnetic material, excellent toxicity profile, short circulation half-life, and widespread reactivity of the M3P particles provides a promising platform for clinical translation of immuno-MRI.**

## INTRODUCTION

Magnetic resonance imaging (MRI) is a promising modality for molecular imaging but remains limited by low sensitivity (*1*). The usual concentration of relevant targets for molecular imaging is around $10^{-9}$ to $10^{-12}$ M in human tissues, whereas MRI detects clinically approved gadolinium chelate at concentrations over $10^{-6}$ M (*2*, *3*). Magnetic resonance spectroscopy and deuterium metabolic imaging allow quantitative mapping of the in vivo dynamics of cellular metabolism but are not available for all molecular targets (*4*). Amplification strategies aiming at binding a large amount of contrast material to the molecular target are thus necessary. To date, nanosized contrast agents such as ultrasmall particles of iron oxide (USPIO) with a diameter ranging from 10 to 50 nm have been the primary focus of molecular MRI studies (*5*). USPIO can be conjugated to targeting moieties such as peptides or antibodies and have a favorable safety profile in humans. However, the low sensitivity (due to the small amount of iron payload per particle), poor specificity (due to passive extravasation through permeated endothelial barriers), and long delay between administration and imaging (up to 24 hours after intravenous injection) have precluded the use of USPIO as targeted molecular imaging agents (*6*).

More recently, microparticles of iron oxide (MPIO) with diameters close to 1 μm have been used as a new family of contrast agent for molecular MRI (*7*). MPIO display a higher sensitivity than USPIO thanks to higher iron content (*8*). We and others demonstrated the applicability of targeted MPIO for molecular MRI in several experimental models, including cardiovascular (*9*, *10*) and neurovascular disorders (*11*), autoimmune diseases (*12*, *13*), and cancer (*14*). Notably, MPIO are rapidly eliminated from the circulation by the reticuloendothelial system, thereby limiting their ability to reach their target (*15*). Therefore, there are strict constrains on the inner structure and coating of MPIO to allow their accumulation at concentrations high enough to be detected by MRI. Unfortunately, the MPIO used in preclinical studies are made of a polystyrene matrix and are not clinically compatible (*6*). Covalent assembly of USPIO with peptidase-degradable bonds has been described as an alternative to MPIO, but the resulting product has a low sensitivity (*16*). Thus, there is still no contrast agent combining the high sensitivity of currently available MPIO with the biocompatibility and biodegradability of USPIO. This limitation prevents the clinical translation of molecular MRI.

Here, we describe the production and characterization of a new class of contrast agent based on a previously unknown mechanism of self-assembly of dopamine-coated magnetite nanocrystals (MNcs) into microsized matrix-based magnetic particles (M3P). Using only three common reagents (iron chloride, dopamine, and ammonia), we produced M3P with mean diameters tunable from 300 to 700 nm and polydispersity index <0.2. Thanks to a biocompatible, hydrophilic, and reactive polydopamine (PDA) matrix (*17*, *18*), M3P can be efficiently functionalized with targeting moieties such as monoclonal antibodies (immuno-MRI). By targeting vascular cell adhesion molecule–1 (VCAM-1) (*19*) and mucosal addressin cell adhesion molecule–1 (MAdCAM-1) (*20*), two proteins expressed by activated endothelial cells and involved in leucocyte trafficking, M3P allows tracking the immune response in a noninvasive manner. We demonstrate the applicability of this new platform for ultrasensitive

---

[1] Normandie Université, UNICAEN, INSERM, PhIND (Physiopathology and Imaging of Neurological Disorders), Institut Blood and Brain @ Caen-Normandie, Cyceron, 14000 Caen, France. [2] Normandie Université, UMS 3408 Cyceron, CNRS, University of Caen Normandy, GIP CYCERON, Caen, France. [3] Institut de Physique et de Chimie des Matériaux de Strasbourg (IPCMS), UMR-7504 CNRS–Université de Strasbourg, 23 rue du Loess, 67034 Strasbourg, France. [4] CHU Caen, Department of Biochemistry, CHU de Caen Côte de Nacre, Caen, France. [5] Centre de Microscopie Appliquée à la Biologie (CMAbio), UniCaen, Normandie University, SF4206 Icore, 14000 Caen, France. [6] MSC, Université de Paris CNRS, UMR7057, 45 rue des Saints Pères 75006, Paris, France. [7] CHU Caen, Clinical Research Department, CHU de Caen Côte de Nacre, Caen, France. [8] CHU Caen, Department of Diagnostic Imaging and Interventional Radiology, CHU de Caen Côte de Nacre, Caen, France.
*Corresponding author. Email: gauberti@cyceron.fr
†These authors contributed equally to this work.

molecular imaging of inflammation in the brain, kidneys, and intestinal mucosa.

## RESULTS

### Synthesis of M3P

Our first objective was to produce a microsized magnetic particle that is fully biodegradable and can be functionalized for molecular MRI. Previous studies demonstrated that in alkaline buffers, dopamine oxidation induces the formation of submicrometric particles of PDA (*21*). We hypothesized that nanocrystals coated with dopamine would be incorporated as building blocks during the formation of PDA particles. Thus, we synthetized MNc by a classical coprecipitation method using a 2:1 $FeCl_3$:$FeCl_2$ ratio (Fig. 1A and fig. S1). After several washing steps, purified nanocrystals (MNc) were incubated with dopamine under continuous sonication to obtain dopamine-coated MNc (MNc@Dopamine). Dynamic light scattering data on MNc@Dopamine are presented in fig. S2. The resulting suspension was stirred using a mechanical disperser at room temperature, and ammonia was added to start dopamine polymerization. This led to the self-assembly of catechol-coated MNc into large multimeric particles (M3P; Fig. 1B). The mean hydrodynamic diameters of the M3P can be tuned from 300 to 700 nm (as measured by dynamic light scattering) by adjusting the concentration of ammonia during particle formation. Polydispersity indexes were all inferior to 0.2 (Fig. 1, C and D), and zeta potentials at pH 7.4 ranged from −30 to −42 mV. Dynamic light scattering data on large 700-nm M3P are presented in fig. S3. M3P were highly dispersible in water, without noticeable aggregate, as assessed by optical phase microscopy at different scales (movies S1 and S2). The particles produced were large enough to be rapidly separated from an aqueous solution using a bench magnet (fig. S4).

### Physical characterization of M3P

The large 700-nm M3P, carrying the largest amount of contrast material, were further characterized by optical and electronic microscopy (Fig. 2, A to C). These particles have pseudo-spherical shapes and are made of numerous MNcs embedded in a matrix with comparatively low electronic density, consistent with a PDA matrix. The respective amounts of the organic fraction (PDA) and the inorganic fraction (magnetite) composing the M3P were quantified by thermogravimetric analysis (TGA), revealing that 67.3% of the particle mass is inorganic (fig. S5). X-ray powder diffraction patterns of the particles exhibited the characteristic peaks of a spinel crystalline structure with a mean crystallite size of 11.0 nm, with lattice parameters between magnetite and maghemite phases (fig. S6). Magnetization curves at 5 and 300 K are presented in fig. S7. At 5 K, a hysteresis cycle can be observed when, at 300 K, the particles present a superparamagnetic behavior. Saturation magnetization was 65.3 electromagnetic unit/g as assessed by superconducting quantum interference device magnetometry. Smaller M3P presented similar characteristics (figs. S5 and S6). At 37°C and 1.41 T (60 MHz), the relaxivity r1 value of 700-nm M3P was low (2.1 $mM^{-1} s^{-1}$), whereas the r2 value was high (188.2 $mM^{-1} s^{-1}$), as assessed by a magnetic resonance spectrometer.

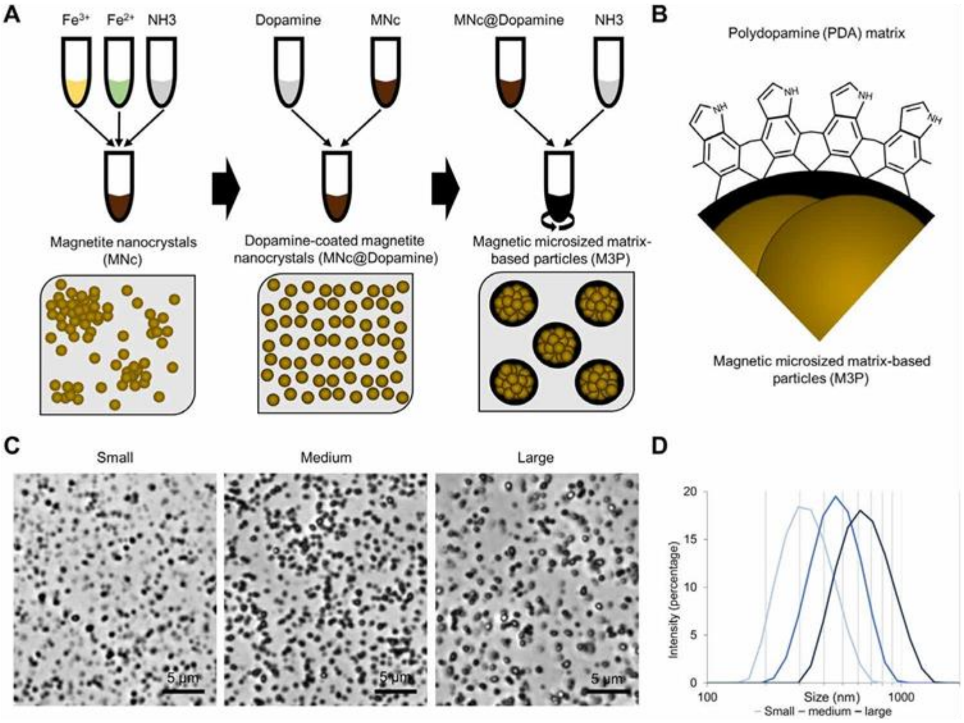

**Fig. 1. Synthesis of M3P.** (**A**) Schematic representation of the main step of M3P synthesis. First, MNc were produced by coprecipitation of ferric ($Fe^{3+}$) and ferrous chloride ($Fe^{2+}$) in the presence of ammonia ($NH_3$). Second, MNc were stabilized by a coating with dopamine (MNc@Dopamine). Third, PDA matrix was initiated by the addition of different doses of ammonia under mechanical stirring, leading to the formation of M3P. (**B**) Schematic representation of the surface and inner structure of M3P. (**C**) Representative phase microscopy images of production of M3P of different sizes obtained by using different concentrations of ammonia during synthesis. (**D**) Size distribution of M3P as assessed by dynamic light scattering (representative of three independent experiments in three independent batches).

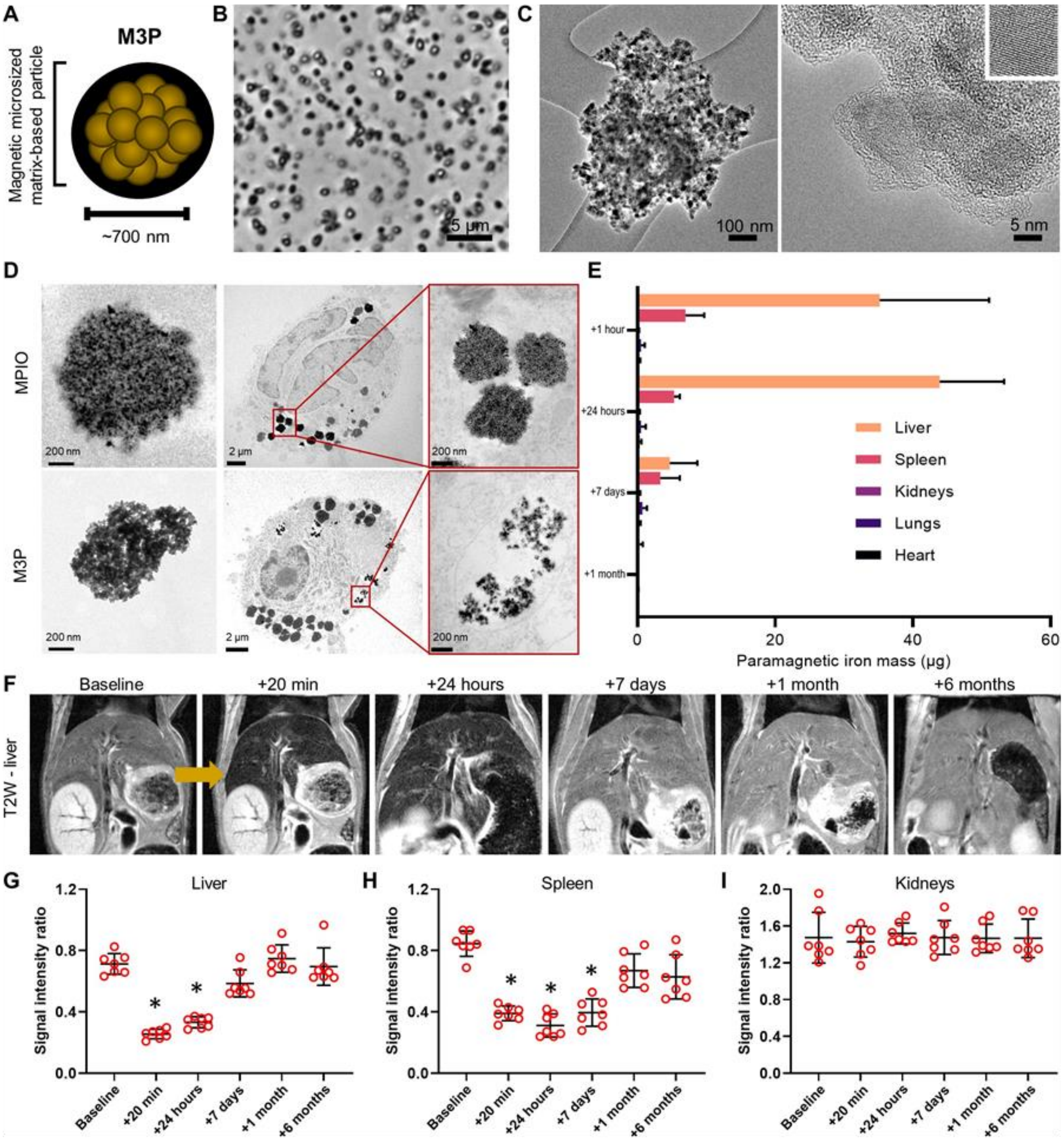

**Fig. 2. Large M3P are degraded in vitro and in vivo.** (**A**) Schematic representation of large M3P. (**B**) Representative phase microscopy image of one batch of large M3P. (**C**) Representative high-resolution transmission electron microscopy (TEM) of a large M3P. The small insert on the upper right depicts the crystalline structure of one clustered MNc. (**D**) Representative TEM images of commercial MPIO (top) and M3P (down) before (left) and 96 hours (middle and right) after incubation with macrophages. (**E**) Mass of paramagnetic iron in the liver, spleen, kidneys, lungs, and heart at different time points after intravenous injection of large M3P (4 mg/kg), as assessed by electronic paramagnetic resonance. (**F**) Representative longitudinal T2-weighted images of the liver at baseline and at different time points after intravenous injection of large M3P (4 mg/kg). (**G**) Evolution of the signal intensity on T2-weighted imaging in the liver (*n* = 7 per group). Ratio was calculated by taking the signal of the paravertebral muscles as reference. (**H**) Evolution of the signal intensity on T2-weighted imaging in the spleen (*n* = 7 per group). (**I**) Evolution of the signal intensity on T2-weighted imaging in the right kidney (*n* = 7 per group). $^{*}P < 0.05$ versus baseline.

Using a preclinical MRI, at room temperature and 7 T (300 MHz), the relaxivity values for r1, r2, and r2* were 0.35, 139.9, and 301.7 $mM^{-1}\ s^{-1}$, respectively (fig. S8). All these parameters are within the range of previously reported values in the literature for superparamagnetic particles with similar crystallite sizes, supporting that clustering MNc using PDA preserves their favorable superparamagnetic properties.

## Biodegradability of M3P

Biodegradability of 700-nm M3P was investigated both in vitro and in vivo. First, the particles were incubated in phosphate-buffered saline (PBS), artificial lysosomal fluid (ALF), citrate buffer, or citrate buffer with hydrogen peroxide. These buffers mimic the lysosomal environment where large particles accumulate after intravenous injection. Degradation was monitored by direct visual inspection and ultraviolet-visible (UV-vis) spectroscopy for 1 week at 37°C under mild agitation (fig. S9). We studied the degradation of M3P of different sizes and MNc@Dopamine (i.e., without PDA). Visual aspect and UV-vis spectroscopy of MNc@Dopamine and M3P in PBS did not change substantially during the monitoring. In ALF and citrate buffers, the brown color of the MNc@Dopamine solution turned with time into the expected yellow color of free Fe(III) ions. The same phenomenon occurred for M3P solutions, but an additional dark precipitate remained present at every time point. This precipitate appeared dark brown on bright-field microscopy and was not attracted by a magnet (fig. S10). This appearance was compatible with free PDA remaining after MNc degradation. In line with this hypothesis, this precipitate progressively solubilized in samples containing hydrogen peroxide, which generates hydroxyl radicals that are able to degrade PDA. UV-vis spectroscopy further supported these findings by showing progressive degradation of M3P in ALF and citrate, with persistence of a chemical species absorbing in the near-infrared region (650 nm), compatible with PDA (fig. S8, B to D). In citrate with hydrogen peroxide buffer, the absorbance of the solution initially containing M3P progressively diminished in the near-infrared region until reaching zero after 7 days of incubation. At day 7, the UV-vis curve was almost undistinguishable between solutions initially containing dopamine-coated iron oxide nanocrystals or M3P, supporting complete degradation of PDA in this buffer mimicking conditions of oxidative stress by endogenous reactive oxygen species.

Second, the degradation of 700-nm M3P was investigated in cell culture of macrophages, the cell type in which large particles accumulate after intravenous injection in vivo. Macrophages were obtained by activation of a human monocytic cell line (THP-1) and were incubated with either M3P or nonbiodegradable commercial MPIO (Dynabeads MyOne) made of iron oxide nanocrystals embedded in a polystyrene matrix. After 96 hours, the cells and particles were observed by transmission electronic microscopy (Fig. 2D). Both types of particles were internalized at this time point. Whereas commercial MPIO remained morphologically intact, M3P fragmented into smaller particles, demonstrating that the PDA matrix is rapidly degraded and releases iron oxide nanocrystals once internalized in macrophages.

In vivo, the biodistribution of M3P was investigated in mice at different time points after intravenous injection (from 1 hour to 6 months) by electron paramagnetic resonance (EPR) that quantifies superparamagnetic components in ex vivo tissue (Fig. 2E and fig. S11), in vivo MRI (Fig. 2, F to I, and fig. S12), and histochemistry with Prussian blue staining (fig. S13). All the methods concur in showing that M3P first accumulate in the liver and spleen (reticuloendothelial system) and that their superparamagnetic components are subsequently degraded or excreted. No residual particles were detected more than 7 days after intravenous injection. There was no significant accumulation of M3P in the kidneys, lungs, or heart at any time points (fig. S13). Neither microvascular plugging nor pathological change in liver volume was observed (fig. S14).

### Biocompatibility of M3P

The biocompatibility of 700-nm M3P was investigated both in vitro and in vivo. No significant cytotoxicity on endothelial cells [human umbilical cord endothelial cells (HUVECs)] was detected at doses up to 320 μg/ml for 3 hours (figs. S15 and S16). After 24 hours of incubation, the viability of endothelial cells was slightly reduced in the high-dose groups. Hemolysis (fig. S17), coagulation (fig. S18), and fibrinolysis (figs. S19 and S20) were all unaffected by 700-nm M3P using either human or murine blood. After intravenous injection of 700-nm M3P (4 mg/kg; equivalent iron), body weight remained within normal ranges (fig. S21) and neither liver enzyme (fig. S22), inflammatory cytokines (fig. S23), nor histological findings (fig. S24) were of toxicological significance.

### Conjugation of M3P to monoclonal antibodies for targeted imaging

Having demonstrated favorable biocompatibility and biodegradability profiles, we investigated the feasibility of using 700-nm M3P as a platform for immuno-MRI. To this aim, we coated M3P with antibodies in phosphate buffer at pH 8.5 since alkaline buffer favors reactive quinone over catechol groups on the PDA coating. We performed a dose-response experiment by varying the concentration of antibodies [immunoglobulin G (IgG)] in the solution during coupling to obtain antibody/particle ratio between 0 and 400 μg/mg (Fig. 3A). Then, we measured the concentration of bound antibodies on M3P by flow cytometry and the concentration of unbound antibodies in the solution by SDS–polyacrylamide gel electrophoresis (SDS-PAGE) and UV-vis (Fig. 3, B to D). We selected the dose of 160 μg of antibodies for 1 mg of M3P for further experiments since the yield of coupling decreased at higher doses (Fig. 3, D and E). Using this ratio, we coated M3P with monoclonal antibodies targeting mouse VCAM-1, MAdCAM-1, or control IgG (M3P@aVCAM-1, M3P@aMAdCAM-1, and M3P@IgG, respectively). Using fluorescent secondary antibodies, the conjugated M3P can be detected by immunofluorescence by revealing the primary antibodies on their surface (fig. S25), confirming the success of the coating step.

Then, we investigated the binding of targeted M3P in vitro. To this aim, anti-human M3P@aVCAM-1 or control M3P@IgG was incubated with either quiescent or activated human cerebral endothelial cells (hCMECD/3). The number of bound particles was evaluated by immunofluorescence microscopy. M3P@aVCAM-1 bound significantly more to activated endothelial cells than control M3P@IgG (Fig. 3, F to H). Moreover, M3P@aVCAM-1 bound significantly more to activated than quiescent endothelial cells, in line with a higher expression of VCAM-1 after tumor necrosis factor (TNF) stimulation by the formers as assessed by flow cytometry (fig. S26). These results demonstrate that M3P coated with anti–VCAM-1 monoclonal antibodies are able to bind selectively activated human endothelial cells (Fig. 3I).

### M3P@aVCAM-1 reveals neuroinflammation at high sensitivity

To determine the feasibility of molecular MRI using targeted M3P in vivo, we used an experimental model of neuroinflammation in mice, induced by intrastriatal injection of *Escherichia coli* lipopolysaccharide (LPS). Twenty-four hours after injection of LPS (1.0 μg), brain MRI was performed both before and 3 min after iterative injections of M3P@aVCAM-1 corresponding to doses from 1.33 to 4 mg/kg of iron (Fig. 4, A and B, and movie S3). On precontrast images, no significant difference between the right and left hemispheres was observed in these mice on neither T2- nor T2*-weighted images. After intravenous injection of M3P@aVCAM-1, numerous signal voids were observed predominantly in the right striatum (Fig. 4A). Iterative injection demonstrated that higher doses led to more signal voids. The contralateral signal voids were expected in

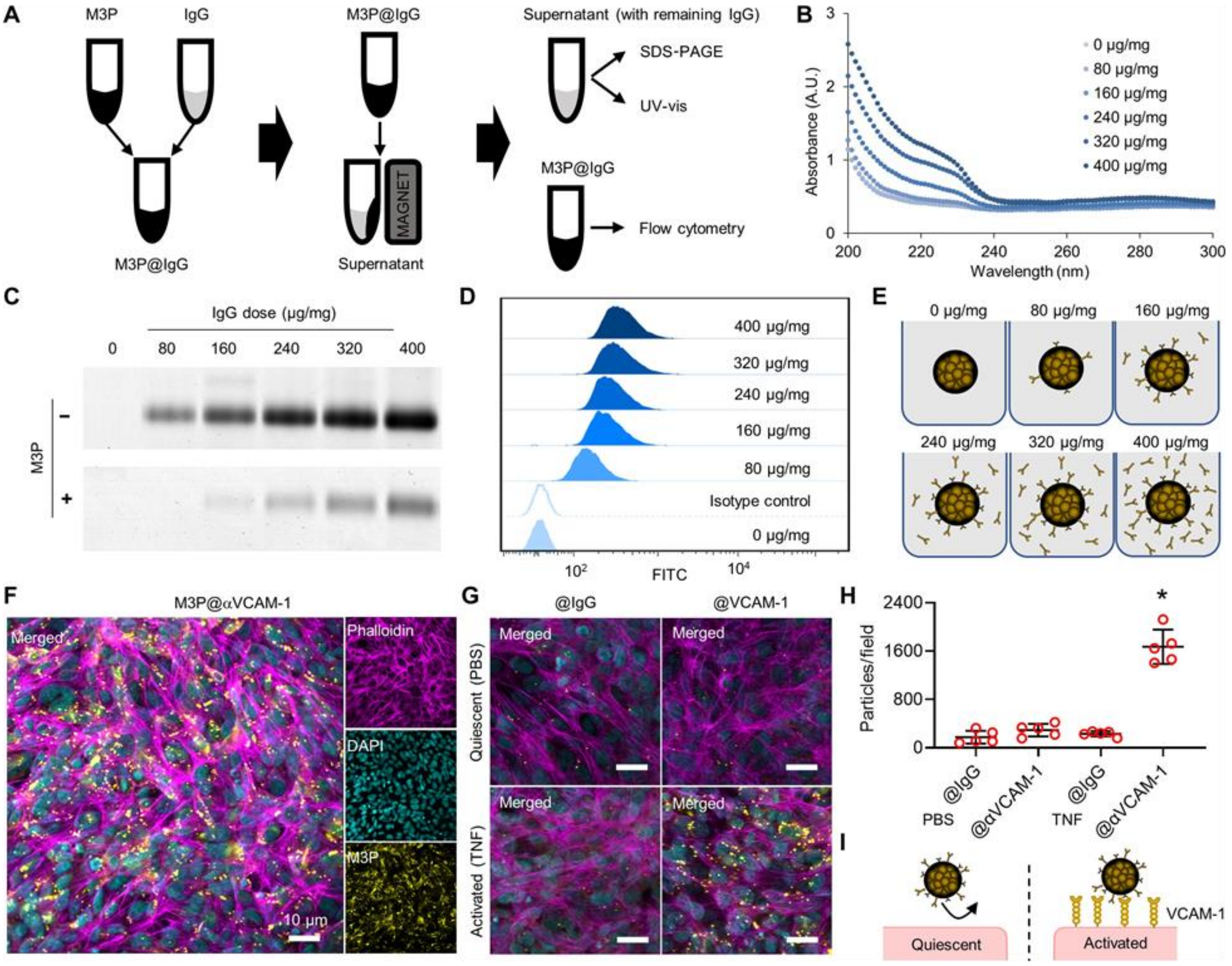

**Fig. 3. Complexation of immunoglobulins to M3P.** (**A**) Schematic representation of the methods for complexation and characterization of M3P. (**B**) UV-vis spectroscopy of the supernatant of M3P@IgG after complexation to different doses of IgG (from 80 to 400 μg/mg). A.U., arbitrary units. (**C**) SDS-PAGE of the supernatant of M3P@IgG after complexation to different doses of IgG. (**D**) Flow cytometry of M3P@IgG after complexation to different doses of IgG (rat) using anti-rat or control (anti-goat) secondary antibodies. (**E**) Schematic representation of M3P@IgG and its supernatant according to the dose of IgG used during complexation. (**F**) Representative immunofluorescence images of anti-human M3P@aVCAM-1 after incubation with activated human cerebral endothelial cells (hCMECD/3). (**G**) Representative immunofluorescence images of anti-human M3P@aVCAM-1 or control M3P@IgG after incubation with quiescent (treated with PBS) or activated (treated with TNF) hCMECD/3. (**H**) Corresponding quantification of the number of particles per field ($n = 5$ per group). $^*P < 0.05$ versus all other groups. (**I**) Schematic representation of the main findings revealing selective binding of M3P@aVCAM-1 on activated human endothelial cells. DAPI, 4′,6-diamidino-2-phenylindole.

this model since it has already demonstrated that ipsilateral injection of pro-inflammatory cytokines in the striatum also induces contralateral inflammation, albeit at a milder level (22). We selected the dose of 4 mg/kg for further experiments to achieve high sensitivity while keeping within clinically tolerated doses of iron. Notably, M3P@aVCAM-1 was detectable at clinically relevant spatial resolution in this model and at this dose (fig. S27).

Thereafter, to investigate whether the signal voids of M3P@aVCAM-1 correlate with the severity of neuroinflammation, we administered different doses of LPS (0, 0.25, 0.5, or 1.0 μg) in the right striatum of naive mice. Twenty-four hours thereafter, we injected M3P@aVCAM-1 (4 mg/kg) intravenously and performed postcontrast T2*-weighted MRI of the brain. Consistent with a higher expression of VCAM-1, more signal voids were observed in the right hemisphere of the mice that received the highest doses of LPS (Fig. 4, C and D). Almost no signal void was observed in the brain of control mice, in line with a low basal expression of VCAM-1. Moreover, by comparing post- to preinjection images, we were able to generate three-dimensional (3D) maps of VCAM-1 expression in the brain in vivo and at high spatial resolution (movie S4).

### M3P@aVCAM-1 combines high sensitivity with high specificity

To investigate the specificity of our method, we compared M3P@aVCAM-1 to control M3P@IgG. Whereas M3P@aVCAM-1 induced numerous signal voids in the right striatum 24 hours after intrastriatal injection of LPS (1 μg), no signal void was visible in mice that received M3P@IgG (Fig. 4, E to G). Histological analyses confirmed the MRI findings by revealing significantly more M3P@aVCAM-1 than M3P@IgG in the right hemisphere of LPS-treated mice (fig. S28). By varying the ratio of IgG and aVCAM-1 on the surface of particles (0, 50, or 100% aVCAM-1/IgG ratio), we observed that the higher the concentration of

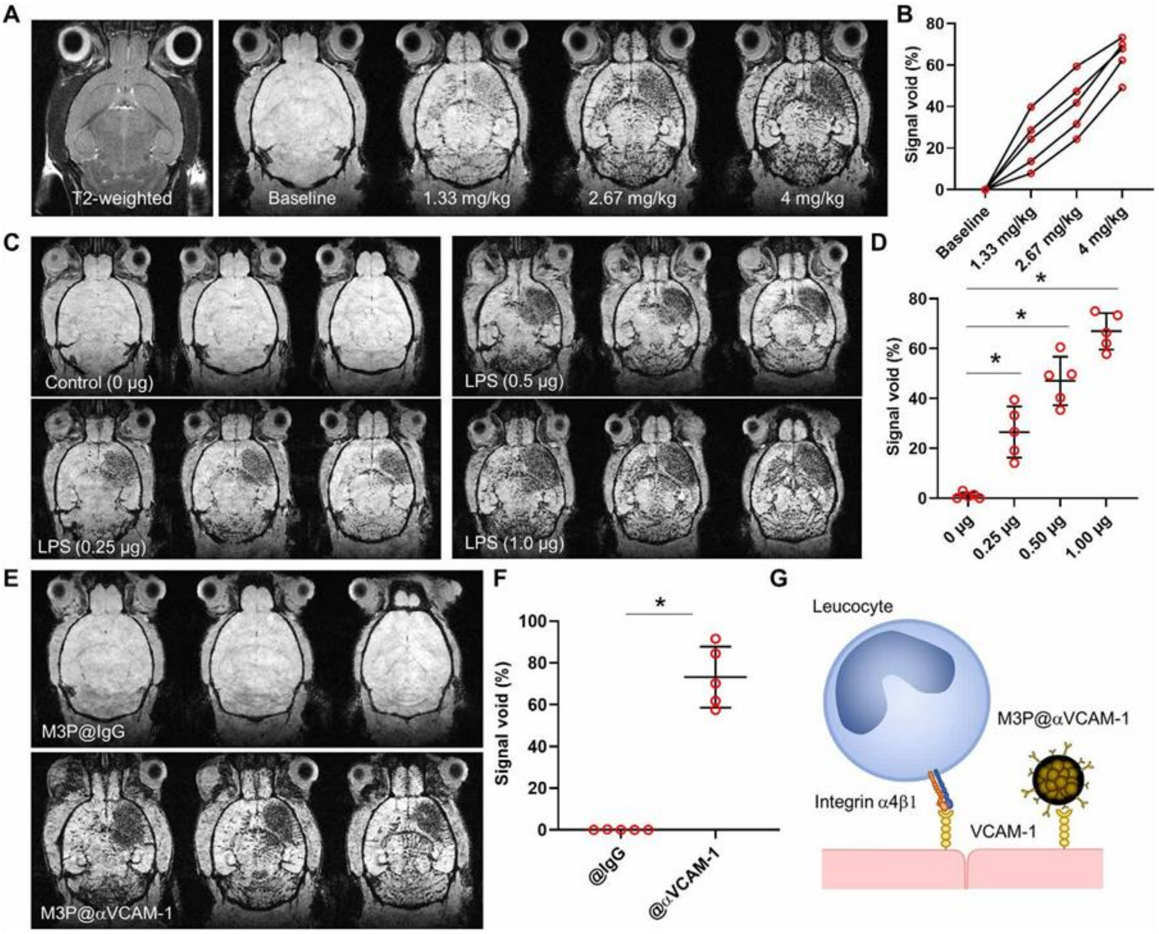

**Fig. 4. Ultrasensitive molecular imaging of VCAM-1 in the inflamed brain.** (**A**) Representative T2-weighted image and T2*-weighted images at baseline and 10 min after successive intravenous injection of M3P targeted against VCAM-1 using monoclonal antibodies (M3P@aVCAM-1) up to 4 mg/kg (equivalent iron) 24 hours after injection of 1 µg of LPS in the right striatum. (**B**) Corresponding quantification of M3P@aVCAM-1 induced signal void in the right striatum (*n* = 5). (**C**) Representative T2*-weighted images (three slices per animal) after intravenous injection of M3P@aVCAM-1 (4 mg/kg) 24 hours after injection of different doses of LPS in the right striatum (from 0 to 1.0 µg). (**D**) Corresponding quantification of M3P@aVCAM-1 induced signal void in the right striatum (*n* = 5 per group). (**E**) Representative T2*-weighted images (three slices per animal) after intravenous injection of M3P@IgG or M3P@aVCAM-1 (4 mg/kg) 24 hours after injection of 1 µg of LPS in the right striatum. (**F**) Corresponding quantification of signal void in the right striatum (*n* = 5 per group). (**G**) Schematic representation of the findings that M3P@aVCAM-1 binds VCAM-1 on the surface of endothelial cells, thereby mimicking activated leucocytes. *$P < 0.05$.

targeted antibodies, the higher the binding of M3P@aVCAM-1 in the inflamed striatum (fig. S29). Moreover, when the mice were pretreated with aVCAM-1 monoclonal antibodies to saturate M3P@aVCAM-1 binding sites, no significant binding of M3P@aVCAM-1 was observed, confirming the specificity of the contrast agent (fig. S30).

Using high temporal resolution imaging, we also investigated the kinetic of M3P@aVCAM-1 binding on activated endothelial cells in the LPS model. As shown on fig. S31, the targeted particles rapidly accumulate in the right striatum, with near-maximal contrast reached less than 60 s after intravenous injection (movie S5). Control M3P@IgG only induced a short transient drop of T2*-weighted signal in the right striatum, consistent with a free flow through the microcirculation and a lack of binding. Both particles were rapidly cleared from the circulation with an estimated primary half-life of 50 to 70 s (fig. S31). At later time points (up to 14 days), T2*-weighted imaging revealed that progressive unbinding of the particles from the right striatum with near-complete disappearance of M3P@aVCAM-1 induced signal voids 24 hours after injection (fig. S32). Histological analyses revealed that unbound M3P@IgG accumulated macrophages in the liver (fig. S33). We also wanted to investigate whether the particles remained stable after incubation in whole blood (fig. S34). After 5 min of incubation, we did not detect large aggregates on blood smears from citrated whole blood, supporting that M3P@IgG is stable enough to remain dispersed during their circulating time after intravenous injection (5 min is equal to about five plasmatic half-lives of M3P). In contrast, we observed aggregates after 60 min of incubation. Considering their short plasmatic half-lives, these results support that conjugated M3P are stable enough in whole blood to avoid the formation of large aggregates before reaching their endothelial target. Together, these experiments demonstrate that M3P@aVCAM-1 is both sensitive and specific to reveal VCAM-1 overexpression in the brain vasculature.

### M3P improves the sensitivity of molecular imaging compared to classically used USPIO

To illustrate the gain in sensitivity provided by clustering superparamagnetic nanocrystals into microsized particles, we compared the sensitivity of unclustered USPIO and small (300 nm) and large (700 nm) M3P conjugated to anti–VCAM-1 monoclonal antibodies to reveal endothelial activation in vivo (Fig. 5A). In the LPS model of neuroinflammation, mice received 4 mg/kg of either particle. MRI was performed 20 min thereafter to allow clearance of the smallest particles. Quantitative analysis revealed significantly more signal void in the mice that received the largest particles (Fig. 5B). Almost no signal void was observed in mice that received control large M3P@IgG. These results support the improved sensitivity of large microsized particles compared to unclustered USPIO for molecular imaging of endothelial targets (Fig. 5C).

### M3P conjugated to antibodies targeting activated endothelial cells reveal inflammation in clinically relevant experimental models

Then, we performed molecular imaging of endothelial activation in more clinically relevant experimental models. The first is in a model of ischemic stroke induced by permanent middle cerebral artery occlusion (pMCAo). In this model, aseptic inflammation develops in the subacute phase (from 24 hours to 7 days after pMCAo), which is thought to play a key role in stroke pathophysiology (*23*). At 24 hours after pMCAo, intravenous injection of M3P@aVCAM-1 induced numerous signal voids in the right hemisphere in the periphery of the ischemic lesion (Fig. 6, A and B). In contrast, no significant signal void was observed after injection of control M3P@IgG. These data demonstrate that M3P@aVCAM-1 can unmask the neuroinflammatory reaction taking place in the subacute phase of ischemic stroke.

The second is in a model of acute kidney injury induced by rhabdomyolysis. An intramuscular injection of glycerol is performed in the two limbs to induce rhabdomyolysis, thereby releasing myoglobin from the muscles into the bloodstream and leading to subsequent acute kidney injury related to hypovolemia and direct toxicity of myoglobin on renal tubules. M3P@aVCAM-1 revealed endothelial inflammation mainly in the kidney medulla, in line with anatomical repartition of renal tubules (Fig. 6, C and D). Again, M3P@IgG did not induce any significant signal void.

The last is in a model of inflammatory bowel disease. Mice were treated for 5 days with dextran sulfate sodium (DSS) in the drinking water. DSS induces intestinal inflammation by disrupting the intestinal epithelial monolayer lining, leading to the entry of luminal bacteria and associated antigens into the mucosa, triggering an immune response. We performed molecular imaging of the descending colon both before and after injection of M3P@aMAdCAM-1, targeted to an adhesion molecule overexpressed by activated endothelial cells in mucosal tissues. As shown on Fig. 6 (E and F), intravenous injection of M3P@aMAdCAM-1 induced numerous signal void

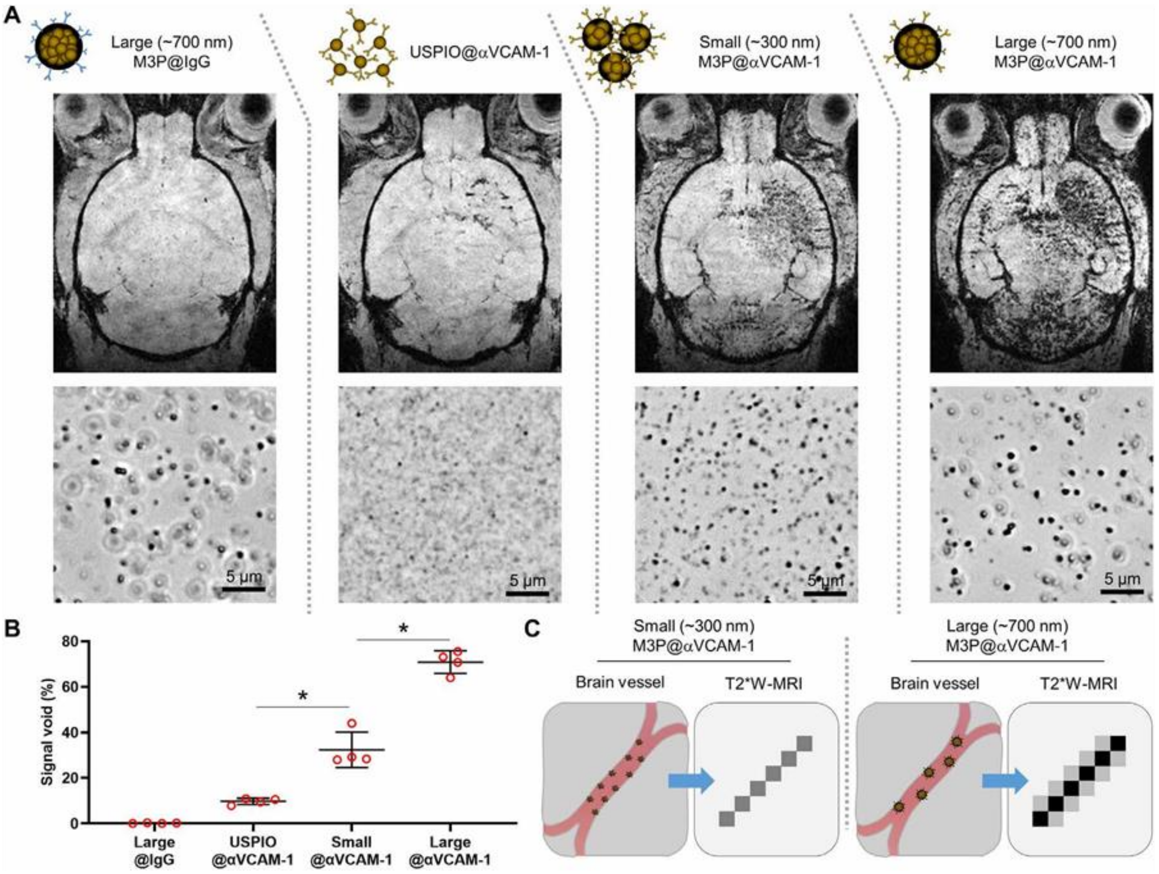

**Fig. 5. Clustering M3P into submicrometric particles improves sensitivity of molecular MRI of VCAM-1.** (**A**) Top: Schematic representation of the particles. Middle: Representative T2*-weighted images after intravenous injection of the corresponding particles (4 mg/kg) 24 hours after injection of 1 µg of LPS in the right striatum. Bottom: Representative phase microscopy images of the particles after conjugation to control IgG or anti-VCAM-1 antibodies. (**B**) Corresponding quantification (*n* = 4 per group). (**C**) Schematic representation of the findings that large M3P (700 nm) provides better sensitivity than small M3P (300 nm). $^*P < 0.05$.

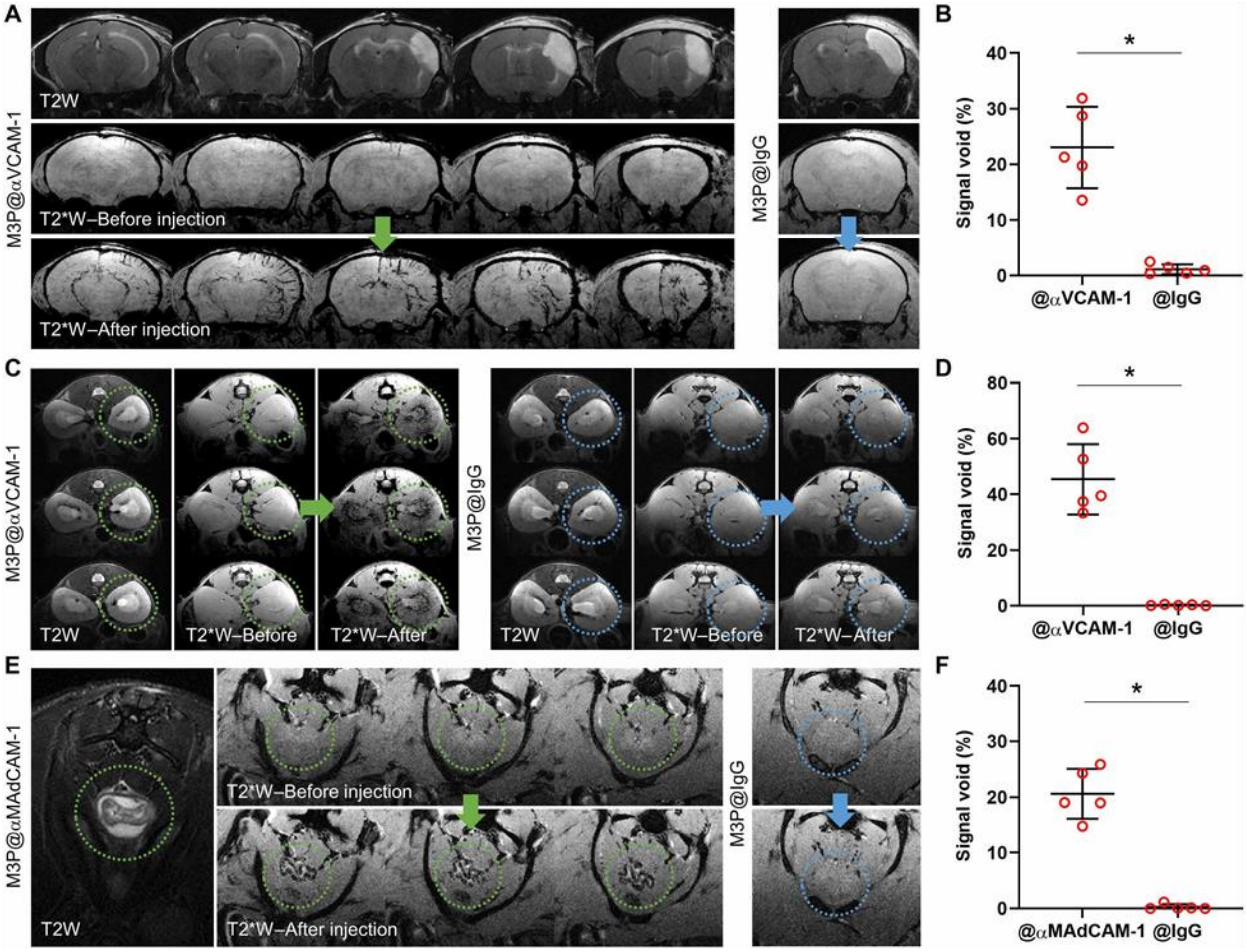

**Fig. 6. Molecular imaging of endothelial activation in clinically relevant experimental models.** (**A**) Representative T2-weighted and T2*-weighted images before and after intravenous injection of M3P@aVCAM-1 (left) or M3P@IgG (right) (4 mg/kg) 24 hours after ischemic stroke induction by electrocoagulation of the right middle cerebral artery. (**B**) Corresponding quantification of signal void in the right hemisphere (*n* = 5 per group). (**C**) Representative T2-weighted and T2*-weighted images before and after intravenous injection of M3P@aVCAM-1 (left) or M3P@IgG (right) (4 mg/kg) 48 hours after acute kidney injury (rhabdomyolysis) induced by intramuscular injection of 50% glycerol. Yellow and blue dotted circles indicate the localization of the right kidney. (**D**) Corresponding quantification of signal void in the kidney medulla (*n* = 5 per group). (**E**) Representative T2-weighted and T2*-weighted images before and after intravenous injection of M3P@aMAdCAM-1 (left) or M3P@IgG (right) (4 mg/kg) in an acute colitis model induced by 5-day treatment with 2.0% of dextran sodium sulfate in the drinking water. Yellow and blue dotted circles indicate the localization of the descending colon. (**F**) Corresponding quantification of signal void in the descending colon (*n* = 5 per group). $^*P < 0.05$.

in the inflamed mucosa of DSS-treated mice, whereas M3P@IgG did not.

Together, these results demonstrate that immuno-MRI using targeted M3P can reveal inflammation in clinically relevant experimental models, as shown in three different organs (brain, kidney, and intestines) and with two different targets (VCAM-1 and MAdCAM-1).

## DISCUSSION

In the present study, we synthetized M3P, a new contrast agent for molecular MRI made of MNc embedded in a PDA matrix. The synthesis is based on the finding that MNc@Dopamine self-assemble into microsized particles in the presence of ammonia. M3P size can be tuned from 300 to 700 nm by varying the concentration of ammonia during synthesis. We demonstrated that these particles are water dispersible, biocompatible, and biodegradable and display favorable superparamagnetic properties. These M3P can be targeted through complexation to monoclonal antibodies (and theoretically to any molecules with free amine or thiol groups), representing a promising tool for immuno-MRI. In particular, we demonstrated that M3P coated with anti–VCAM-1 and anti–MAdCAM-1 antibodies are highly sensitive and specific to reveal inflammation by MRI in clinically relevant experimental models (summarized in fig. S35). We also demonstrated that this strategy is effective to target human activated endothelial cells, paving the way for clinical translation.

The use of PDA as a matrix presents several key features for molecular imaging. First, as a major component of naturally occurring neuromelanin, PDA is biocompatible and biodegradable in vivo, although the precise pathways for its biodegradation remain unknown (*24*). Second, a variety of ligand can be conjugated at high density with PDA via Michael addition or Schiff base reactions (*25*). The ability to conjugate a large amount of targeting moieties on the surface of M3P is required to maximize binding to the target and reach a high sensitivity (as illustrated in fig. S27). We cannot exclude however that a fraction of the antibodies on the M3P surface might be absorbed rather than covalently linked. Third, PDA is hydrophilic and negatively charged at physiological pH, providing a negative zeta potential for the coated particles and preventing their aggregation in solution. Last, dopamine interacts strongly with the surface of MNc through the phenolic hydroxyl groups (*26*). Thus, the PDA matrix in M3P is relatively resistant to ultrasonication (*27*), allowing dispersing aggregated particles without fragmenting the particles or detaching the conjugated ligands.

An important finding is the significantly improved sensitivity of molecular MRI using large particles compared to smaller ones. This result challenges the current focus of molecular imaging studies on nanosized contrast agents (<100 nm) (*28*). Considering that the shape of the particles remains the same, the amount of iron carried by a single particle increases proportionally to its radius at the power of 3. In our study, since the diameter of large M3P (700 nm) is 35 times larger than classically used USPIO (20 nm), the amount of contrast material carried per particle is >40,000 times larger. Even if it is conceivable that smaller particles can accumulate more efficiently on the endothelial surface thanks to a longer circulation time, our data show that the use of large M3P is much more effective. Previous studies also reported an improved margination on the vessel wall of large particles compared to smaller ones (*29*) and better performances of large particles for molecular MRI of endothelial targets (*30*). These results support the use of micrometric or submicrometric particles rather than nanoparticles for molecular imaging of endothelial activation, especially when the sensitivity of the imaging modality is limited. Understandably, there is an upper limit of the size of rigid particles to allow free circulation through capillary vessels. Notably, the use of nanosized crystallites inside the M3P remains mandatory to preserve the superparamagnetic behavior and avoid particle aggregation.

Beyond improved sensitivity, this larger size also prevents passive extravasation and accumulation of the contrast carrying particles and, therefore, improves the specificity of the signal. This comes at the cost of a strictly intravascular biodistribution, limiting imaging to vascular targets, and a short half-life due to rapid uptake by the reticuloendothelial system (*13*, *31*). Accordingly, the plasmatic half-life of targeted 700-nm M3P is very short, with near-complete plasma clearance achieved a couple of minutes after intravenous injection. This is similar to what has been observed previously using microsized magnetic particles both in terms of circulation half-life and biodistribution pattern (*30*). This pharmacokinetic profile allows performing postcontrast MRI almost immediately after intravenous injection, which would be useful in clinical practice to ease patient workflow.

Although the increase in sensitivity to detect endothelial activation allowed by large contrast-carrying particles is valuable to image the immune response, it has also some limitations. First, some level of endothelial activation and adhesion molecule expression can be observed in quiescent tissues, albeit at much lower intensity than in inflamed tissues. Therefore, it is important to consider the degree of signal changes after M3P injection to accurately identify inflammatory versus quiescent tissue. It is also important to acknowledge that molecular imaging of endothelial activation using targeted M3P gives only a semiquantitative information on the extent of inflammation. Second, in the context of focal injury, the inflammatory reaction can be so intense that highly sensitive imaging can detect endothelial activation far from the injury site (*32*). In such conditions, targeted M3P-enhanced imaging will lack spatial selectivity to precisely identify the site of injury. Moreover, because of the constraints inherent in clinical imaging, including lower magnetic field, lower spatial resolution, and possibly lower iron dose, it is expected that the sensitivity of M3P-enhanced imaging will be lower in humans. It is however reinsuring that M3P@αVCAM-1 is easily detected at clinically relevant spatial resolution at 24 hours after intrastriatal LPS injection in mice.

Overall, M3P present favorable characteristics for clinical translation. The synthesis is easy to perform at room temperature and atmospheric pressure and should be amenable to large-scale production, and the required reagents are cheap and widely available. The sensitivity for molecular MRI of endothelial activation is high enough to detect inflammation in clinically relevant model and at clinically relevant spatial resolution. The iron dose used in the present study (4 mg/kg) was slightly higher than the dose reported in clinical studies that used nanosized particles of iron oxide for neuroimaging (2.6 mg/kg) (*33*). Notably, in the context of the treatment of iron deficiency, much higher doses of USPIO (up to 1.5 g in a single injection) are well tolerated in humans (*34*). Since MRI is a routinely performed imaging technique and our contrast agent can be detected using standard sequences and magnets, M3P could be rapidly and widely adopted in clinical practice. A minor modification of currently performed imaging protocols could allow the inclusion of a post-contrast T2*-weighted sequence, therefore allowing M3P detection. To enable clinical translation, several potential limitations of M3P remain to be addressed including evaluation of the risk of anaphylaxis that has been reported for iron oxide nanoparticles, the putative short- and long-term effects of rapid liver and spleen accumulation after intravenous injection, the risk of particle aggregation once in the blood and subsequent small vessel embolization, and the risk of immunological reactions. The risks associated with intravenous injection of micrometric and submicrometric particles also remain unknown since, to our knowledge, there are no clinically approved biomaterials in this size range for intravenous use. Among the most straightforward applications of this technology are early diagnosis of autoimmune diseases, prediction of treatment response to immune checkpoint inhibitors in cancer, and noninvasive monitoring of immunomodulatory therapies. While additional translational hurdles will need to be considered for future clinical development, M3P provides a promising platform for the clinical translation of immuno-MRI.

## MATERIALS AND METHODS

### Study design

The main objective of this study was to synthesize a microsized magnetic particle that is fully biodegradable and to demonstrate the feasibility of molecular imaging of inflammation in vivo using this particle. We determined sample sizes in the in vivo MRI experiments based on our previous experience. We commonly used four to five mice per group to measure the signal changes induced by contrast agent administration compared to control condition (mice with inflammation versus mice without inflammation, targeted M3P versus control M3P, etc.). This sample size was large enough to detect differences in these all-or-nothing experimental paradigms. No animal was excluded from the analysis. All animals were randomized to the different experimental groups, ensuring equivalent representation of each animal cage in each experimental group. Twenty-three batches of M3P were produced for this study, and consistent results were obtained with all batches. All the animals from the same experiments received M3P from the same batches to avoid putative batch differences. All image analyses were performed blinded to the experimental data using the anonymization procedure of the MRI software.

## Reagents for M3P production

The following reagents were purchased from Sigma-Aldrich: ferric chloride hexahydrate, ferrous chloride tetrahydrate, ammonia solution (32%), dopamine hydrochloride, sodium phosphate monobasic, sodium phosphate dibasic, and mannitol. Antibodies for conjugation to M3P were rat anti-mouse VCAM-1 [clone A(429), BD Biosciences], mouse anti-human VCAM-1 (clone 1.G11B1, Thermo Fisher Scientific), and rat anti-mouse MAdCAM-1 (clone MECA367, BD Biosciences), and corresponding isotype polyclonal IgG were purchased from Sigma-Aldrich.

## Synthesis of MNcs

MNc were produced by a coprecipitation method in an alkaline buffer. In a typical synthesis, 540 mg of $FeCl_3.6H_2O$ and 198.8 mg of $FeCl_2.4H_2O$ were dissolved in 5.7 ml of distilled water by vortexing, yielding a homogenous yellow solution. Under continuous agitation at room temperature, 6.3 ml of a 13% ammonia solution was progressively added at a rate of 0.2 ml/min. The solution turned from yellow to brown and, ultimately, to a deep black color, corresponding to the formation of magnetite. The precipitate was washed five times with distilled water by magnetic separation and resuspended in 10 ml of distilled water.

## Synthesis of dopamine-coated MNcs

Eight milliliters of the solution of MNc was resuspended in 40 ml of a solution containing dopamine hydrochloride (2.5 mg/ml). The resulting solution was sonicated for 15 min at 70% amplitude and 26 kHz using a UP200ST sonicator (Hielscher). The color of the solution slightly changed from black to dark brown. Then, the solution was centrifuged at 3000*g* for 5 min to remove large remaining nanocrystals aggregates. Thirty milliliters of the supernatant containing MNc@Dopamine and free dopamine hydrochloride were transferred to a new vial.

## Synthesis of M3P

The solution containing MNc@Dopamine and free dopamine hydrochloride was placed under vigorous steering using an Ultra-Turrax T-25 disperser at 20,500 rpm. To produce large M3P (700 nm), 67 □ of a 13% ammonia solution was first added to the solution, which was left to react for 60 min. Then, 203 □of a 13% ammonia solution was added, and the incubation was continued for 30 min to allow further PDA. To produce medium-sized M3P (500 nm), 270 □of a 13% ammonia solution was added in one time and the solution was left to react for 60 min. To produce small-sized M3P (300 nm), 2160 □ of a 13% ammonia solution was added in one time and the solution was left to react for 60 min. Then, the solution was centrifuged at 1000*g* for 3 min to remove the largest aggregates, the pellet was discarded, and 24 ml of the supernatant was transferred to a new vial. The M3P were then washed five times with distilled water and lastly resuspended in 8 ml of distilled water and stored at 4°C until further use.

## Determination of iron concentration

Iron content of M3P suspension was measured with the FerroZine method. Particles were degraded overnight at room temperature in 1 M HCl, releasing ferric ($Fe^{3+}$) and ferrous ($Fe^{2+}$) ions in solution. Samples were incubated 30 min with 0.65% (w/v) ascorbic acid to reduce ferric ions in ferrous ions. Sample pH was adjusted with 12% (w/v) ammonium acetate. 3-(2-Pyridyl)-5,6-diphenyl-1,2,4-triazine-*p*,*p*′-disulfonic acid monosodium salt hydrate was added (1 mM; FerroZine Iron Reagent, Sigma-Aldrich), and absorbance was measured at 562 nm with a spectrophotometer (ELx808 Absorbance reader, BioTek) indicating the amount of complexes formed with ferrous ions. Iron content was determined against standard curves obtained from iron chloride dilutions.

## Determination of the hydrodynamic diameter of the particles

Dynamic light scattering was used to determine the average hydrodynamic diameter, the polydispersity index and the diameter distribution by volume of the M3P particles with a Nano ZS apparatus (Malvern Instruments, Worcestershire, UK) equipped with a 633-nm laser at a fixed scattering angle of 173°. The temperature of the cell was kept constant at 25°C, and all dilutions were performed in pure water. Measurements were performed in triplicate.

## Zeta potential measurement

Zeta potential analyses were realized, after 1/100 dilution in 1 mM NaCl, using a Nano ZS apparatus equipped with DTS 1070 cell. All measurements were performed in triplicate at 25°C, with a dielectric constant of 78.5, a refractive index of 1.33, a viscosity of 0.8872 centipoise, and a cell voltage of 150 V. The zeta potential was calculated from the electrophoretic mobility using the Smoluchowski equation.

## Thermogravimetric analysis

TGA was achieved on a TA SDT 600 instrument to measure the mass fractions of the organic and inorganic parts of the M3P. For the runs, the samples were heated from 25° to 800°C at a rate of 5°C/min under air.

## X-ray diffraction

The x-ray diffractograms of the M3P were obtained at ambient temperature with a Bruker D8 Advance diffractometer (Bruker, Billerica, MA, USA) equipped with a monochromatic copper radiation source (Ka = 0.154 056 nm) and a LYNXEYE detector in the 20° to 70° (2□) range with a scan step of 0.03°. High-purity silicon powder ($a$ = 0.543 082 nm) was used as an internal standard. Profile fitting refinements were realized via the FullProf program using Le Bail's method with the modified Thompson-Cox-Hasting pseudo-Voigt profile model.

## Superconducting quantum interference device

Hysteresis cycles at 5 K and 300 K of the M3P were performed with a superconducting quantum interference device (Quantum Design MPMS3). For that, 50 □of M3P suspensions at ca. 7 mg of Fe/ml was dried and evaporated in a capsule. This procedure was done again until the dried M3P cover the capsule bottom part.

## Measurements of the relaxivities by $^1H$ nuclear magnetic resonance spectroscopy

The longitudinal T1 and transverse T2 relaxation times of the samples were measured by using a Bruker Minispec 60 (Karlsruhe, Germany) apparatus working at 37°C, at a field of 1.41 T corresponding to a Larmor frequency of 60 MHz. The corresponding longitudinal (R1) and transverse (R2) relaxivities were calculated according to the following expression involving the contrast agent: $R = R0 + r \times [Fe]$, where [Fe] is the iron concentration of the samples, $R$ is the relaxation rate ($1/T$) (in the presence of the particles), R0 is the relaxation rate of the aqueous solution (in the absence of the particles), and $r$ is the fitted relaxivity value.

### Measurements of the relaxivities by 1H 7-T MRI

Large 700-nm M3P was dispersed in agarose gels (2%) in tris-acetate-EDTA buffer at different concentrations. The samples were then imaged using a BioSpec 7-T TEP-MRI, and the following sequences were performed: T1 mapping using flow-sensitive alternating inversion recovery–rapid acquisition with relaxation enhancement (RARE) sequence with repetition time (TR) = 3000 ms and inversion time ranging from 6.5 to 2000 ms, T2 mapping using multislice multiecho (MSME) sequence with TR = 4000 ms and echo time (TE) ranging from 3.65 to 51.11 ms, and T2* mapping using multigradient echo sequence with TR = 4000 ms and TE ranging from 2 to 17.47 ms. The corresponding R1, R2, and R2* relaxivities were calculated as described above.

### In vitro degradation in buffers

Stability and biodegradability of small, medium, and large M3P, as well as MNc@Dopamine, were studied in vitro in different relevant biological buffer solutions: ALF, acidic solution [20 mM citrate buffer (pH 4.0)], and citrate + $H_2O_2$ [20 mM citrate buffer (pH 4.0) + 30 mM $H_2O_2$] buffer. PBS was used as a control buffer. ALF was prepared as previously reported by Milosevic *et al.* (*35*) Briefly, sodium chloride (3.210 g), sodium chloride (0.097 g), sodium hydroxide (6.000 g), citric acid (20.800 g), calcium chloride (0.097 g), sodium phosphate heptahydrate (0.179 g), sodium sulfate (0.039 g), magnesium chloride hexahydrate (0.106 g), glycerin (0.059 g), sodium citrate dehydrate (0.077 g), sodium tartrate dehydrate (0.090 g), sodium lactate (0.085 g), sodium pyruvate (0.086 g), and formaldehyde (1000 ml added fresh before use) were dissolved in 200 ml of purified water to obtain a 5× stock solution, which was later diluted with purified water and particles during incubation. To assess particle stability and/or dissolution in PBS, ALF, citric, and citrate + $H_2O_2$ buffers, all four particles types were incubated in those buffers [at Fe (20 µg/ml)], and consequently, UV-vis spectra were measured and images of the dispersion were taken at the beginning (baseline), 3 hours, 24 hours, 72 hours, and 7 days (the end of the incubation).

### In vitro degradation in THP-1 macrophages

THP-1 cells (American Type Culture Collection) were cultivated in RPMI 1640 medium (Sigma-Aldrich) supplemented with 10% fetal calf serum and 2% penicillin-streptomycin, at 37°C with 5% $CO_2$. Cells were plated in a 24-well plate over glass microslides at 500,000 cells per well and differentiated into macrophages with phorbol 12-myristate 13-acetate (2 µM, Sigma-Aldrich). At 24 hours, cells in suspension were removed and 700-nm M3P or nondegradable MPIO (Dynabeads MyOne Carboxylic Acid, Thermo Fisher Scientific) were added at a final iron content of 15 µg/ml. At 96 hours, THP-1 macrophages were processed for transmission electron microscopy (TEM).

### Transmission electron microscopy

For observation of M3P or MPIO in suspension, a droplet of particles was after deposited on a hydrophilized 400-mesh grid. High-resolution TEM was performed on an aberration-corrected JEOL ARM 200-F microscope operating at 80 kV (Laboratoire Matériaux et Phénomènes Quantiques, UMR7162, Université de Paris/CNRS, France). For observation of THP-1 cells, the cells were cultured and incubated with particles on microscope coverslips. Cells were fixed with 2.5% glutaraldehyde in 0.1 M cacodylate buffer (pH 7.4) overnight at 4°C, rinsed in 0.1 M cacodylate buffer (pH 7.4), postfixed 1 hour with 1% osmium tetroxide in 0.1 M cacodylate buffer (pH 7.4) at 4°C, and rinsed in 0.1 M cacodylate buffer (pH 7.4). The cells were then dehydrated in progressive bath of ethanol (70 to 100%) and embedded in resin EMbed 812. After 20 hours of polymerization at 60°C, the coverslip were then separated from the cell's resin bloc and polymerization continued for 28 hours. Ultrathin sections were collected and contrasted with uranyl acetate and lead citrate. Sections were observed with TEM JEOL 1011, and images were taken with Camera MegaView 3 and AnalySIS FIVE software.

### Clot lysis

The effect of M3P during clot formation and lysis was studied by monitoring the change in turbidity in human or mouse plasma using a microplate reader (FLUOstar Optima, BMG Labtech). Calcium chloride (final concentration, 25 mM) was added to citrated plasma diluted 1:2 in Hepes buffer [10 mM Hepes, 150 mM NaCl, and 0.4% bovine serum albumin (BSA) (pH 7.4)] to promote coagulation. Samples were incubated at 37°C with M3P at different doses, and absorbance (405 nm) was monitored for 12 hours every 30 s at 37°C. When appropriate, recombinant tissue-type plasminogen activator (alteplase, Boehringer Ingelheim) was also added to promote clot lysis. Results are expressed as the time to achieve 75% maximal absorbance [clotting time (CT)], and the 50% lysis time was calculated as the time from initiation of clot formation to the time at which maximal absorbance falls to 50%. All experiments were performed in triplicate.

### Rotational thromboelastography

For thromboelastography assays, human fresh blood was drawn into 0.109 M trisodium citrate. Within 30 min, 300 µl of blood was added in EXTEM-S reagent vial (EXTEM) in the presence of increasing concentrations of large M3P [0 (control), 20, 40, and 80 µg/ml] diluted in saline and clotting was monitored. CT (in seconds), amplitude at 10 min (A10), clot formation time (CFT; in seconds), maximal clot firmness (in millimeters), and a angle (in degrees) were measured to characterize and quantify the coagulation activation, clot firmness, and clot stability using rotational thromboelastography (TEM). Blood of healthy donors (Etablissement Français du Sang, Ile de France) was collected and tested with the appropriate ethics prior approval as stated in the EFS/INSERM U1237 agreement #PLER-UPR/2018/017, ensuring that all donors gave a written informed consent and providing anonymized samples.

### Erythrocyte hemolysis assay

The erythrocyte toxicity of the M3P was conducted as described by Mazzarino *et al.* (*36*) with minor modifications on human and mouse blood. Briefly, 1 ml of blood was obtained by venous (human) or intracardial puncture (mice) in 1/10 citrate buffer. Erythrocytes were purified by centrifugation at 2000*g* for 5 min and washed three times in 10 ml of saline. Then, 50 µl of purified and washed erythrocytes was added to 950 µl of saline containing different concentrations of M3P (final concentration, 0, 20, 40, and 80 µg/ml) and incubated in 37°C under mild agitation. Then, erythrocytes were removed by centrifugation at 2000*g* for 5 min. Then, the absorbance of the resulting supernatant was measured by UV-vis and by spectrometer at 540 nm. Saline control solution (0.9% NaCl) and distilled water were used as negative (0% lysis) and positive (100% lysis) controls, respectively. The hemolysis rate at 540 nm was calculated as follows: hemolysis rate (%) = $(A_s - A_{c-}/A_{c+} - A_{c-}) \times 100$, where $A_s$, $A_{c-}$, and $A_{c+}$ represent the absorbance of the sample, negative control, and positive control, respectively (*37*). The experiments were performed in triplicate using either human or mouse erythrocytes.

### In vitro cell death screening studies

In vitro studies using primary cultures of HUVECs (Merck KGaA, C-12203) were used to assess acute and chronic toxicity of M3P. To allow for the more efficient screening, we combined two independent tests into one cell death screening assay developed by Filipova *et al.* (*38*) with minor modifications: first, the cell proliferation and viability test based on WST-1 (4-[3-(4-iodophenyl)-2-(4-nitro-phenyl)-2H-5-tetrazolium]-1,3-benzene sulfonate, monosodium salt) assay (Roche) and, second, the cell membrane integrity and cell necrosis by lactate dehydrogenase (LDH; Cytotoxic Detection Kit, Roche) assay. Both assays were performed in sequence on the cells in the same well. Briefly, HUVECs were obtained from Merck and were cultured in precoated 0.2% gelatin in 25-cm$^2$ flasks in endothelial cell growth medium (EGM-2; Lonza) containing 2% fetal bovine serum (FBS) and supplements (Lonza BulletKit, CC-3202) at 37°C in a humidified 5% $CO_2$ atmosphere. After reaching ~85% confluence, cells were harvested in trypsin/EDTA phenol red for endothelial cells (Gibco) and centrifuged at 300*g* for 5 min, and 10 × 10$^3$ cells were seeded in 200 μl of fresh EGM-2 media per well in 96-well plates (Thermo Fisher Scientific). After 48 hours, HUVECs were treated in five replicates with increasing concentrations of large M3P (in saline solution) from 0 to 320 μg/ml diluted in saline solution (dose-response), positive control (1% Triton X-100), and negative control (freshly added medium). Plate was incubated for 0, 3, and 24 hours (time-response experiment). Then, 50 μl of supernatants was transferred into a new 96-well plate. The LDH assay was performed following the manufacturer's instructions by measuring absorbance at 490 and 660 nm. Thereafter, same wells containing 150 μl of media were treated with 15 μl of WST-1 reagent and were incubated for 1 hour at 37°C. Subsequently, 100 μl of the media with developed color was transferred to a new 96-well plate, and absorbance was measured at 450 and 660 nm. The net absorbance corresponding to the LDH and WST-1 (after elimination of M3P contribution to absorbance) was calculated following the corrective formulas of Filipova *et al*. (*38*). Both values of cell viability and integrity are expressed as a percentage of the negative control values. Besides, impact of cell viability after M3P addition at increasing doses was performed by a follow-up of histological images. In this experiment, 3 × 10$^6$ HUVEC cells were seeded in 2 ml of fresh EGM-2 media per well in six-well plates (Thermo Fisher Scientific). After 48 hours, HUVECs were treated in two replicates with increasing concentrations of large M3P from 0, 80, 160, to 320 μg/ml diluted in purified water. Images were taken at baseline, 20 min, 3 hours, 6 hours, and 24 hours (before and after washing). Negative control was freshly added medium. For all experiments, cells were used at third to fourth passage.

### Optimization of antibodies binding to M3P surface

To calculate the best concentration of antibodies at the surface of M3P, we performed a dose-response experiment using rat IgG. To that aim, 560 μg of large M3P was washed one time with purified water and resuspended in 1 ml of 10 mM phosphate buffer (pH 8.5). Then, dose escalation of 0 to 225 μg of rat IgG (0, 45, 90, 135, 180, and 225 μg) was incubated with M3P at room temperature for 24 hours. In parallel, the resulting solutions were washed in 1/300 ammonia solution (from a 13% ammonia solution) and sonicated for 1 min at 20% amplitude and 26 kHz using a UP200ST sonicator to break any aggregates. The supernatants were kept to measure the concentration of unbound antibodies by UV-vis and Coomassie SDS-PAGE. In parallel, the coated M3P were then washed twice with a 0.3 M mannitol solution and incubated with secondary anti-rat fluorescein isothiocyanate (FITC) secondary antibodies (or anti-rabbit FITC for isotype mimicking control condition in borate buffer for 30 min at room temperature in the dark). After incubation, M3P solutions were washed twice and resuspended in PBS and 2% BSA buffer for acquisition in the flow cytometer. M3P were acquired on a FACSVerse cytometer (BD Biosciences). The results were analyzed using FlowJo version 7.6.5 (BD Biosciences).

### Coating of M3P with antibodies

In a typical coating procedure, 2.5 mg of M3P was washed one time with purified water and resuspended in 5 ml of 10 mM phosphate buffer (pH 8.5). Then, 400 μg of monoclonal antibodies (or another appropriate amount) was incubated with M3P at room temperature for 24 hours. The resulting solution was sonicated for 5 min at 20% amplitude and 26 kHz using a UP200ST sonicator to break any aggregates. The coated M3P were then washed three times with a 0.3 M mannitol solution and lastly resuspended in 5 ml of a 0.3 M mannitol solution and stored at 4°C until further use.

### Production of USPIO@aVCAM-1

We first produced MNc@Dopamine as described above. Then, the excess dopamine was removed by dialysis against purified water (10-kDa cutoff). Thereafter, the purified nanoparticles were incubated with anti–VCAM-1 antibodies in a phosphate buffer [10 mM (pH 8.5)] to obtain USPIO@aVCAM-1 by direct bioconjugation (using the same antibody/iron ratio as during the conjugation of M3P, i.e., 160 μg/mg). The excess antibody was removed by several cycles of magnetic purification, and last, USPIO@aVCAM-1 was resuspended in an isotonic mannitol buffer and briefly sonicated to break any aggregates. Using this methodology, USPIO@aVCAM-1 and the two M3P@aVCAM-1 formulation (small and large) were made of the same nanocrystals of iron oxide, were conjugated using the same antibody/iron ratio, and were injected at the same dose (4 mg/kg), thereby allowing to investigate specifically the effect of particle size on imaging sensitivity.

### In vitro binding of M3P@aVCAM-1 to TNF-activated human brain endothelial cells

Chamber experiments were performed to assess the binding affinity of anti–VCAM-1 antibody conjugated to M3P to human activated brain endothelial cells. To that aim, the hCMEC/D3 was cultured as described previously (*39*). Endothelial cells were cultured in precoated rat collagen-I 25-cm$^2$ flasks in EGM-2 (Lonza) containing 2% FBS and supplements (Lonza BulletKit, CC-3202) at 37°C in a humidified 5% $CO_2$ atmosphere. The media were renewed every 2 days until confluence was reached at ~85%, after which the cells were harvested in trypsin/EDTA phenol red for endothelial cells (Gibco), centrifuged at 300*g* for 5 min, and seeded in 300 μl of fresh EGM-2 media per well in Ibidi μ-Slide 8 well ibiTreat (#CC80826) at 5 × 10$^4$ cells/ml.

After 24 hours, hCMEC/D3 cells were changed to endothelial cell serum-free media (Gibco) and exposed to human TNF (50 ng/ml; activated condition; #300-01A, PeproTech) or PBS (for the control/quiescent condition) for >16 hours to induce endothelial VCAM-1 expression. After that, control and stimulated cells were washed with fresh EGM-2 media and incubated in duplicates with either M3P@aVCAM-1 or M3P@IgG (40 □g/ml) for 30 min at room temperature with constant mixing. Unbound particles were removed by extensive washing with PBS. Thereafter, cells were fixed with 4% paraformaldehyde (PFA) for 10 min, washed three times with PBS, and permeabilized with 0.1% Triton X-100-PBS solution for 15 min at room temperature. To visualize bound M3P (either VCAM-1 or IgG), anti-mouse specific secondary antibodies conjugated for Cy3 were purchased from Jackson ImmunoResearch Laboratories. To visualize the actin protein, iFluor488-phalloidin (#176753 Cytopainter, Abcam), a bicyclic heptapeptide that specifically binds to F-actin protein, was used. Slides were coverslipped with Fluoromount-G containing 4′,6-diamidino-2-phenylindole (DAPI) for nuclei staining (Thermo Fisher Scientific). Confocal images were acquired on an SP8 confocal microscope (40× objective; Leica Microsystems) and captured at 1024 × 1024 high-quality resolution with a *Z* step of 0.10 □m The image data were analyzed, processed, and reconstructed with ImageJ 1.5 software (National Institutes of Health). M3P@aVCAM-1 and M3P@IgG binding to cells was assessed in five fields of view per TNF and PBS dose and quantified using ImageJ. To confirm the overexpression of VCAM-1 in brain endothelial cells after TNF stimulation, hCMEC/D3 was stimulated with TNF for 24 hours (or PBS for quiescent conditions), washed with PBS, and detached using trypsin-EDTA. Quiescent (PBS) and activated (TNF) cells were centrifuged (300*g* for 5 min) and resuspended at $1 \times 10^5$ cells in 100 □of PBS. Primary antibodies to anti-mouse VCAM-1 coupled to FITC (Invitrogen) and isotype controls were incubated in both groups in PBS + BSA 2% at a final concentration of 10 □g/ml for 30 min at room temperature under the dark. Cells were washed twice in PBS + BSA buffer. Flow cytometry experiments were performed on a FACSVerse flow cytometer (BD Biosciences) equipped with its accompanying software (FACSuite, BD Biosciences) on 20,000 events after gating the population by forward scatter and side scatter and performing FITC density plots.

## Animals

All experiments were performed on 8- to 16-week-old male Swiss mice (Janvier, France). Animals were maintained under specific pathogen–free conditions at the Centre Universitaire de Ressources Biologiques (CURB, Basse-Normandie, France), and all had free access to food and tap water. Experiments were approved by the local ethical committee of Normandy (CENOMEXA, APAFIS#22318). A catheter was inserted into the tail vein of mice for intravenous administration of the contrast agent.

## Inflammatory cytokines and transaminases dosage

Blood samples were collected from the inferior vena cava on either 3.2% (w/v) sodium citrate or heparinized tubes. Plasma was isolated by centrifugation (2× 1500*g* for 15 min) and kept at −20°C until use. Inflammatory cytokines were quantified in citrated plasma samples with a multiplex sandwich immunoassay using a pro-inflammatory panel kit for mouse (MSD multi-spot assay system, V-PLEX). Concentrations of TNF-a, interleukin-1□ (IL-1□), IL-2, IL-6, interferon-□, and CXCL1 were determined in picograms per milliliter with an electrochemiluminescent substrate by backfitting the signal to calibration curves with Discovery Workbench software (v 4.3). Alanine and aspartate aminotransferase activities were determined using an AU5800 chemistry analyzer (Beckman Coulter) on heparinized plasma with blank determination and quality controls (three different levels) performed as described by validated quality procedures. These assays are based on transamination of alanine in pyruvate and aspartate into oxaloacetate coupled to a second reaction where these alpha-keto acids are reduced in the presence of Nicotinamide adenine dinucleotide; the reaction was followed at 340 nm.

## Biodistribution study

Mice were anesthetized with isoflurane (1.5 to 2.0%) and maintained at 37°C, and M3P were injected intravenously (4 mg/kg). At 1 hour, 24 hours, 7 days, 1 month, and 6 months after injection, 0.5 to 1 ml of blood was collected from the inferior vena cava on 3.2% (w/v) sodium citrate, mice were perfused with saline, and tissues of interest were collected: liver, spleen, kidneys, lung, and heart. Plasma was isolated from blood samples by centrifugation (2× 1500*g* for 15 min) and kept at −20°C for pro-inflammatory cytokine and transaminase dosages. Tissues were weighted and divided for various analyses. A piece of liver, one kidney, half of the lung, half of the heart, and half of the spleen were weighted and frozen at −80°C for EPR analysis. The rest of the tissues were fixed in 4% phosphate-buffered PFA for histology studies. The study was designed with one group per time point with additional groups of mice treated for 24 hours with intraperitoneal injection of LPS (5 mg/kg) and mice injected with vehicle control ($n = 5$ mice per group).

## Electron paramagnetic resonance

EPR was performed with a Bruker ELEXSYS 500 EPR spectrometer operating at X band (9 GHz). The first derivative of the power absorption $dW(B)/dB$ was recorded as a function of the applied field $B$ in the range 0 to 6000 G, with a modulation field at a frequency of 100 kHz and amplitude of 10 G.

The area of the EPR absorption curve [calculated by a double integration of the spectrum $dW(B)/dB$] was proportional to the amount of nondegraded superparamagnetic M3P in the sample. An absolute calibration was performed using suspensions of initial M3P in 2-□l sample at different iron concentrations. For quantification of superparamagnetic components in ex vivo tissue, excised pieces of organs were first weighed and let dry for 3 days in an oven at 80°C. The dried organ samples were weighed again and introduced into a quartz tube. The net mass of dehydrated organs in the quartz tube was then weighed, and EPR spectra were recorded.

## Intrastriatal LPS injection

Swiss mice received an intrastriatal injection of LPS from *E. coli* (1.5 □gper mouse; 0111:B4; Sigma-Aldrich, L'isle d'Abeau, France) that was performed after placing male Swiss mice in a stereotaxic frame (coordinates: 0.5 mm anterior, 2.0 mm lateral, −3 mm ventral to the bregma) under isoflurane anesthesia (2.0%). Solutions were injected by the use of a glass micropipette.

## Permanent middle cerebral artery occlusion

Male Swiss mice were placed in a stereotaxic frame under isoflurane anesthesia (2.0%); the skin between the right ear and the right eye was incised, and the temporal muscle was carefully retracted. Then, the middle cerebral artery was exposed through a small craniotomy and permanently occluded by electrocoagulation.

### Rhabdomyolysis-induced acute kidney injury

To induce rhabdomyolysis, the animals were injected intramuscularly, on each thigh caudal muscle, with 50% glycerol (7.5 ml/kg) [99.5% (m/v); VWR International S.A.S., France] or saline as a control.

### DSS model of acute colitis

DSS-treated mice received 2.0% (w/v) DSS (40,000 molecular weight; Alfa Aesar, Thermo Fisher Scientific, France) in drinking water for 5 days to induce an acute episode of colitis. Drink and food were provided ad libitum. DSS, food consumption, and body weight were measured daily.

### Whole-body MRI

Experiments were performed using a BioSpec 7-T TEP-MRI system with a volume coil resonator (Bruker, Germany). Mice were anesthetized with isoflurane (1.5 to 2.0%) and maintained at 37°C by the integrated heat animal holder, and the breathing rate was monitored during the imaging procedure. Whole-body scans including T2-weighted (RARE sequence, with TR/TE = 3000 ms/50 ms) and T2$^*$-weighted sequences [fast-low angle shot (FLASH) sequence, with TR/TE = 50 ms/3.5 ms] were performed before, 20 min, 24 hours, 7 days, 1 month, and 6 months after the intravenous injection of 700-nm M3P (4 mg/kg). Signal intensity ratios were measured by drawing the region of interest in the liver, spleen, kidney, and paravertebral muscles. Ratios were computed as the signal intensity of the organ of interest divided by the signal intensity of the paravertebral muscle ($n = 7$).

### In vivo immuno-MRI

Experiments were carried out on a Pharmascan 7-T/12-cm system using surface coils (Bruker, Germany). Mice were anesthetized with isoflurane (1.5 to 2.0%) and maintained at 37°C by the integrated heat animal holder, and the breathing rate was monitored during the imaging procedure. To image the brain, T2-weighted images were acquired using an MSME sequence (spatial resolution of 70 μm by 70 μm by 500 μm) with TE/TR 51 ms/2500 ms and a flip angle of 90°. T2$^*$-weighted images were acquired using a 3D FLASH gradient echo imaging (spatial resolution of 78 μm by 78 μm by 150 μm) with TE/TR 8.6 ms/50 ms, and a flip angle of 20° was performed to reveal M3P and USPIO (acquisition time, 17 min). High-resolution T2$^*$-weighted images presented in this study are minimum intensity projections of three consecutive slices (yielding a $Z$ resolution of 450 μm). Fast acquisition of the brain for biodistribution study was performed using a FLASH sequence with only one slice and TR/TE 20 ms/7 ms with a flip angle of 8°. To image the kidneys, T2-weighted images were acquired using a turbo RARE sequence (spatial resolution of 78 μm by 78 μm by 500 μm) with TR/TE 2500 ms/40 ms and RARE factor of 8. T2$^*$-weighted images were acquired using a FLASH sequence with TR/TE 250 ms/5 ms and a flip angle of 30°. To image the colon, T2$^*$-weighted images were acquired using a 2D FLASH sequence (spatial resolution of 67 μm by 67 μm by 350 μm) without gating with TE/TR 5.4 ms/300 ms and a flip angle of 35°. T2-weighted images were acquired using a 2D RARE sequence (spatial resolution of 67 μm by 67 μm by 750 μm) with TE/TR 36 ms/2500 ms and a flip angle of 90°. When appropriate, mice randomly received M3P or appropriate control. When appropriate, T2$^*$-weighted images were acquired both before and after injection of contrast agent. Although injections of contrast agent were usually performed outside the magnet, the positions of the mice during pre- and postcontrast acquisitions did not change (the mice were placed exactly at the same position and were not removed from the animal holder).

### Competition experiments

When appropriate, mice received an intravenous injection of anti–VCAM-1 antibody [2.5 mg/kg, clone A(429)] or control isotype IgG 15 min before M3P@αVCAM-1 to saturate the binding sites of the contrast agent.

### Histology

Mice were perfused transcardially with heparinized saline and 4% phosphate-buffered PFA, and the different organs were harvested. Then, the organs were washed three times in 20% sucrose in veronal buffer and embedded in a Cryomatrix (Tissue-Tek OCT) before cryostat sectioning. For iron oxide detection, tissue sections (thickness, 10 μm) were subjected to Prussian blue iron kit (Perl's staining, Leica Biosystems). Briefly, tissue sections were rehydrated in distilled water for 15 min and covered with a mix of potassium hexacyanoferrate and hydrochloric acid (50/50%) for 20 min. The sections were washed in distilled water and counterstained using nuclear fast red. They were then dehydrated in a gradient bath of ethanol (70, 95, and 100%) and mounted with synthetic resin (EUKITT, Dutscher). For morphology evaluation, we used a ready-to-use kit for hematoxylin and eosin staining (BioGnost). Briefly, frozen sections were successively rehydrated in deionized water, stained using hematoxylin reagent, rinsed in deionized water, and counterstained with a nuclear bluing reagent. Then, the sections were dehydrated in a gradient bath of ethanol (70, 95, and 100%) and mounted with synthetic resin. Images were digitally captured using a VS120 Virtual Slide Microscope (Olympus) and visualized with QuPath (v0.2.3).

### Immunofluorescence

Mice were intracardially perfused with heparinized saline and 4% phosphate-buffered PFA, and the brain and liver were harvested. The organs were cryoprotected in 20% PBS sucrose for 24 hours and embedded in a Cryomatrix (Tissue-Tek OCT) before cryostat sectioning. Cryostat-cut sections (thickness, 10 μm) were collected on polylysine slides and stored at –80°C before processing. Sections were coincubated overnight with rat anti-mouse CD68 (1:800; Abcam, 53444), goat anti-mouse collagen IV (1:1000; SouthernBiotech, 1340), and rat anti-mouse VCAM-1 (1:500; BD Bioscience, 550547). Primary antibodies were revealed by using Fab′2 fragments of donkey anti-rabbit linked to Cy3, anti-rat linked to Cy3, and anti-goat IgG linked to FITC (1:600; Jackson ImmunoResearch, West Grove, USA). Washed sections were coverslipped with antifade medium containing DAPI. Epifluorescence images (~10 images per section) were digitally captured using a Leica DM6000 epifluorescence microscope coupled CoolSNAP camera, visualized with Leica MM AF 2.2.0 software (Molecular Devices, USA), and further processed using ImageJ 1.51k software.

### Statistical analysis

Results are presented as means ± SD. Statistical analyses were performed using Mann-Whitney $U$ test. When more than two groups were compared, statistical analyses were performed using Kruskal-Wallis (for multiple comparisons) followed by Mann-Whitney post hoc $U$ test. When comparing two groups, a $P < 0.05$ was considered significant (two-sided).

## SUPPLEMENTARY MATERIALS

Supplementary material for this article is available at https://science.org/doi/10.1126/sciadv.abm3596

## REFERENCES AND NOTES

1. J. Lohrke, T. Frenzel, J. Endrikat, F. C. Alves, T. M. Grist, M. Law, J. M. Lee, T. Leiner, K.-C. Li, K. Nikolaou, M. R. Prince, H. H. Schild, J. C. Weinreb, K. Yoshikawa, H. Pietsch, 25 years of contrast-enhanced MRI: Developments, current challenges and future perspectives. *Adv. Ther.* **33**, 1-28 (2016).
2. P. Caravan, Strategies for increasing the sensitivity of gadolinium based MRI contrast agents. *Chem. Soc. Rev.* **35**, 512-523 (2006).
3. M. L. James, S. S. Gambhir, A molecular imaging primer: Modalities, imaging agents, and applications. *Physiol. Rev.* **92**, 897-965 (2012).
4. L. J. Rich, P. Bagga, N. E. Wilson, M. D. Schnall, J. A. Detre, M. Haris, R. Reddy, $^1$H magnetic resonance spectroscopy of $^2$H-to-$^1$H exchange quantifies the dynamics of cellular metabolism in vivo. *Nat. Biomed. Eng.* **4**, 335-342 (2020).
5. S. Laurent, D. Forge, M. Port, A. Roch, C. Robic, L. Vander Elst, R. N. Muller, Magnetic iron oxide nanoparticles: Synthesis, stabilization, vectorization, physicochemical characterizations, and biological applications. *Chem. Rev.* **108**, 2064-2110 (2008).
6. M. Gauberti, A. Montagne, A. Quenault, D. Vivien, Molecular magnetic resonance imaging of brain-immune interactions. *Front. Cell. Neurosci.* **8**, 389 (2014).
7. M. A. McAteer, N. R. Sibson, C. von Zur Muhlen, J. E. Schneider, A. S. Lowe, N. Warrick, K. M. Channon, D. C. Anthony, R. P. Choudhury, In vivo magnetic resonance imaging of acute brain inflammation using microparticles of iron oxide. *Nat. Med.* **13**, 1253-1258 (2007).
8. M. Gauberti, A. P. Fournier, F. Docagne, D. Vivien, S. Martinez de Lizarrondo, Molecular magnetic resonance imaging of endothelial activation in the central nervous system. *Theranostics* **8**, 1195-1212 (2018).
9. C. von Zur Muhlen, D. von Elverfeldt, J. A. Moeller, R. P. Choudhury, D. Paul, C. E. Hagemeyer, M. Olschewski, A. Becker, I. Neudorfer, N. Bassler, M. Schwarz, C. Bode, K. Peter, Magnetic resonance imaging contrast agent targeted toward activated platelets allows in vivo detection of thrombosis and monitoring of thrombolysis. *Circulation* **118**, 258-267 (2008).
10. C. von Zur Muhlen, N. R. Sibson, K. Peter, S. J. Campbell, P. Wilainam, G. E. Grau, C. Bode, R. P. Choudhury, D. C. Anthony, A contrast agent recognizing activated platelets reveals murine cerebral malaria pathology undetectable by conventional MRI. *J. Clin. Invest.* **118**, 1198-1207 (2008).
11. A. Quenault, S. Martinez de Lizarrondo, O. Etard, M. Gauberti, C. Orset, B. Haelewyn, H. C. Segal, P. M. Rothwell, D. Vivien, E. Touzé, C. Ali, Molecular magnetic resonance imaging discloses endothelial activation after transient ischaemic attack. *Brain* **140**, 146-157 (2017).
12. A. P. Fournier, A. Quenault, S. Martinez de Lizarrondo, M. Gauberti, G. Defer, D. Vivien, F. Docagne, R. Macrez, Prediction of disease activity in models of multiple sclerosis by molecular magnetic resonance imaging of P-selectin. *Proc. Natl. Acad. Sci. U.S.A.* **114**, 6116-6121 (2017).
13. A. P. Fournier, S. Martinez de Lizarrondo, A. Rateau, A. Gerard-Brisou, M. J. Waldner, M. F. Neurath, D. Vivien, F. Docagne, M. Gauberti, Ultrasensitive molecular imaging of intestinal mucosal inflammation using leukocyte-mimicking particles targeted to MAdCAM-1 in mice. *Sci. Transl. Med.* **12**, eaaz4047 (2020).
14. S. Serres, M. S. Soto, A. Hamilton, M. A. McAteer, W. S. Carbonell, M. D. Robson, O. Ansorge, A. Khrapitchev, C. Bristow, L. Balathasan, T. Weissensteiner, D. C. Anthony, R. P. Choudhury, R. J. Muschel, N. R. Sibson, Molecular MRI enables early and sensitive detection of brain metastases. *Proc. Natl. Acad. Sci. U.S.A.* **109**, 6674-6679 (2012).
15. J. Belliere, S. Martinez de Lizarrondo, R. P. Choudhury, A. Quenault, A. Le Béhot, C. Delage, D. Chauveau, J. P. Schanstra, J. L. Bascands, D. Vivien, M. Gauberti, Unmasking silent endothelial activation in the cardiovascular system using molecular magnetic resonance imaging. *Theranostics* **5**, 1187-1202 (2015).
16. F. Perez-Balderas, S. I. van Kasteren, A. A. A. Aljabali, K. Wals, S. Serres, A. Jefferson, M. Sarmiento Soto, A. A. Khrapitchev, J. R. Larkin, C. Bristow, S. S. Lee, G. Bort, F. De Simone, S. J. Campbell, R. P. Choudhury, D. C. Anthony, N. R. Sibson, B. G. Davis, Covalent assembly of nanoparticles as a peptidase-degradable platform for molecular MRI. *Nat. Commun.* **8**, 14254 (2017).
17. H. Lee, S. M. Dellatore, W. M. Miller, P. B. Messersmith, Mussel-inspired surface chemistry for multifunctional coatings. *Science* **318**, 426-430 (2007).
18. D. Wu, J. Zhou, M. N. Creyer, W. Yim, Z. Chen, P. B. Messersmith, J. V. Jokerst, Phenolic-enabled nanotechnology: Versatile particle engineering for biomedicine. *Chem. Soc. Rev.* **50**, 4432-4483 (2021).
19. J. Teixidó, A. Hidalgo, S. Fagerholm, Editorial: Leukocyte trafficking in homeostasis and disease. *Front. Immunol.* **10**, 2560 (2019).
20. S. Zundler, E. Becker, L. L. Schulze, M. F. Neurath, Immune cell trafficking and retention in inflammatory bowel disease: Mechanistic insights and therapeutic advances. *Gut* **68**, 1688-1700 (2019).
21. K. Ai, Y. Liu, C. Ruan, L. Lu, G. M. Lu, Sp2 C-dominant N-doped carbon sub-micrometer spheres with a tunable size: A versatile platform for highly efficient oxygen-reduction catalysts. *Adv. Mater.* **25**, 998-1003 (2013).
22. A. Montagne, M. Gauberti, R. Macrez, A. Jullienne, A. Briens, J. S. Raynaud, G. Louin, A. Buisson, B. Haelewyn, F. Docagne, G. Defer, D. Vivien, E. Maubert, Ultra-sensitive molecular MRI of cerebrovascular cell activation enables early detection of chronic central nervous system disorders. *Neuroimage* **63**, 760-770 (2012).
23. C. Iadecola, M. S. Buckwalter, J. Anrather, Immune responses to stroke: Mechanisms, modulation, and therapeutic potential. *J. Clin. Invest.* **130**, 2777-2788 (2020).
24. H. Fedorow, F. Tribl, G. Halliday, M. Gerlach, P. Riederer, K. L. Double, Neuromelanin in human dopamine neurons: Comparison with peripheral melanins and relevance to Parkinson's disease. *Prog. Neurobiol.* **75**, 109-124 (2005).
25. H. Lee, J. Rho, P. B. Messersmith, Facile conjugation of biomolecules onto surfaces via mussel adhesive protein inspired coatings. *Adv. Mater.* **21**, 431-434 (2009).
26. E. Amstad, T. Gillich, I. Bilecka, M. Textor, E. Reimhult, Ultrastable iron oxide nanoparticle colloidal suspensions using dispersants with catechol-derived anchor groups. *Nano Lett.* **9**, 4042-4048 (2009).
27. W. Yang, C. Liu, Y. Chen, Stability of polydopamine coatings on gold substrates inspected by surface plasmon resonance imaging. *Langmuir* **34**, 3565-3571 (2018).
28. E. Terreno, D. D. Castelli, A. Viale, S. Aime, Challenges for molecular magnetic resonance imaging. *Chem. Rev.* **110**, 3019-3042 (2010).
29. M. Cooley, A. Sarode, M. Hoore, D. A. Fedosov, S. Mitragotri, A. Sen Gupta, Influence of particle size and shape on their margination and wall-adhesion: Implications in drug delivery vehicle design across nano-to-micro scale. *Nanoscale* **10**, 15350-15364 (2018).
30. N. Zarghami, A. A. Khrapitchev, F. Perez-Balderas, M. S. Soto, J. R. Larkin, L. Bau, N. R. Sibson, Optimization of molecularly targeted MRI in the brain: Empirical comparison of sequences and particles. *Int. J. Nanomedicine* **13**, 4345-4359 (2018).
31. E. Blanco, H. Shen, M. Ferrari, Principles of nanoparticle design for overcoming biological barriers to drug delivery. *Nat. Biotechnol.* **33**, 941-951 (2015).
32. D. L. Carden, D. N. Granger, Pathophysiology of ischaemia-reperfusion injury. *J. Pathol.* **190**, 255-266 (2000).
33. T. Tourdias, S. Roggerone, M. Filippi, M. Kanagaki, M. Rovaris, D. H. Miller, K. G. Petry, B. Brochet, J. P. Pruvo, E. W. Radüe, V. Dousset, Assessment of disease activity in multiple sclerosis phenotypes with combined gadolinium- and superparamagnetic iron oxide-enhanced MR imaging. *Radiology* **264**, 225-233 (2012).
34. N. F. Adkinson, W. E. Strauss, I. C. Macdougall, K. E. Bernard, M. Auerbach, R. F. Kaper, G. M. Chertow, J. S. Krop, Comparative safety of intravenous ferumoxytol versus ferric carboxymaltose in iron deficiency anemia: A randomized trial. *Am. J. Hematol.* **93**, 683-690 (2018).
35. A. MilosevicAc, J. Bourquin, D. Burnand, P. Lemal, F. Crippa, C. A. Monnier, L. Rodriguez-Lorenzo, A. Petri-Fink, B. Rothen-Rutishauser, Artificial lysosomal platform to study nanoparticle long-term stability. *Chimia (Aarau)* **73**, 55-58 (2019).
36. L. Mazzarino, G. Loch-Neckel, L. Dos Santos Bubniak, F. Ourique, I. Otsuka, S. Halila, R. Curi Pedrosa, M. C. Santos-Silva, E. Lemos-Senna, E. Curti Muniz, R. Borsali, Nanoparticles made from xyloglucan-block-polycaprolactone copolymers: Safety assessment for drug delivery. *Toxicol. Sci.* **147**, 104-115 (2015).
37. J. Zhang, X. G. Chen, Y. Y. Li, C. S. Liu, Self-assembled nanoparticles based on hydrophobically modified chitosan as carriers for doxorubicin. *Nanomedicine* **3**, 258-265 (2007).
38. M. Filipova, O. K. Elhelu, S. H. De Paoli, Z. Fremuntova, T. Mosko, D. Cmarko, J. Simak, K. Holada, An effective "three-in-one" screening assay for testing drug and nanoparticle toxicity in human endothelial cells. *PLOS ONE* **13**, e0206557 (2018).
39. B. Weksler, I. A. Romero, P. O. Couraud, The hCMEC/D3 cell line as a model of the human blood brain barrier. *Fluids Barriers CNS* **10**, 16 (2013).

**Acknowledgments:** We acknowledge C. Péchoux (INRAE, UMR 1313, Plateforme MIMA2, Jouy en Josas, France) for electron microscopy preparation and observations. We thank S. Bégin-Colin for help in analyzing the magnetic properties of M3P. The hCMEC/D3 cell line was donated by Institut Cochin, Université Paris Descartes, France. **Funding:** This work was supported by the European Union's Horizon 2020 research and innovation program under grant agreement no. 685795 (to F.G. and S.R.); IdEx Université de Paris, Agence Nationale de la Recherche ANR-18-IDEX-0001 (to F.G.); Agence Nationale de la Recherche "MAD-GUT" ANR-19-CE19-0018 (to M.G.); Agence Nationale de la Recherche "FLAMRING" ANR-20-CE19-0032-01 (to S.M.d.L.); the French National Research Program for Environmental and Occupational Health of ANSES (2018/1/007) and Region Île de France under the convention SESAME 2019—IVETh (no. EX047011) (to F.G.); and "Fondation Bettencourt Schueller" for a CCA-Inserm-Bettencourt position (to M.G.). **Author contributions:** Conceptualization: S.M.d.L., C.J., T.B., and M.G. Investigation: S.M.d.L., C.J., M.N., M.N.-O., S.P., A.A., B.F., S.A., D.G., S.R., F.G., D.M., T.B., and M.G. Funding acquisition: S.M.d.L., F.G., D.V., T.B., and M.G. Project administration: D.V. and M.G. Supervision: S.M.d.L., D.V., T.B., and M.G. Writing (original draft): S.M.d.L. and M.G. Writing (review and editing): S.M.d.L., C.J., M.N., M.N.-O., S.P., A.A., B.F., S.A., D.G., S.R., F.G., D.V., D.M., T.B., and M.G. **Competing interests:** The authors declare the following competing interests: S.M.d.L., C.J., D.V., T.B., and M.G. have filed patent application

EP N° 21 306 073.4 (30 July 2021) for the use of M3P as contrast agent. The other authors declare that they have no competing interests. **Data and materials availability:** All data needed to evaluate the conclusions in the paper are present in the paper and/or the Supplementary Materials.

Submitted 12 September 2021
Accepted 26 May 2022
Published 13 July 2022
10.1126/sciadv.abm3596

Science Advances

# Tracking the immune response by MRI using biodegradable and ultrasensitive microprobes

Sara Martinez de LizarrondoCharlene JacqmarcqMikael NaveauManuel Navarro-OviedoSwannie PedronAlexandre AdamBarbara FreisStephane AlloucheDidier GouxSarah RazafindrakotoFlorence GazeauDamien MertzDenis VivienThomas BonnardMaxime Gauberti

*Sci. Adv.*, 8 (28), eabm3596. • DOI: 10.1126/sciadv.abm3596

---

# 3. VWF-targeted thrombolysis to overcome rh-tPA resistance in experimental thrombotic stroke models

American Society of Hematology
2021 L Street NW, Suite 900,
Washington, DC 20036
Phone: 202-776-0544 | Fax 202-776-0545
editorial@hematology.org

# VWF-targeted thrombolysis to overcome rh-tPA resistance in experimental thrombotic stroke models

Tracking no: BLD-2022-016342R1

Marc V.A. van Moorsel (TargED Biopharmaceuticals, Netherlands) Steven de Maat (TargED Biopharmaceuticals, Netherlands) Kristof Vercruysse (TargED Biopharmaceuticals, Netherlands) Esther M. van Leeuwen (University Medical Center Utrecht and Utrecht University, Netherlands) Charlene Jacqmarcq (Department of Clinical Research, Caen Normandie University Hospital, Caen, France, France) Thomas Bonnard (Department of Clinical Research, Caen Normandie University Hospital, Caen, France, France) Denis Vivien (INSERM U1237, France) H. van der Worp (University Medical Center Utrecht and Utrecht University, Netherlands) Rick Dijkhuizen (University Medical Center Utrecht and Utrecht University,, Netherlands) Coen Maas (TargED Biopharmaceuticals, Netherlands)

**Abstract:**

Recombinant human tissue plasminogen activator (rh-tPA) is an important thrombolytic agent for treatment of acute ischemic stroke (AIS). It requires fibrin binding for plasminogen activation. In contrast, Microlyse, a novel thrombolytic agent, requires von Willebrand factor (VWF) binding for plasminogen activation. We compared rh-tPA with Microlyse, administered 20 minutes after inducing thrombosis, in two randomized blinded AIS mouse models. Thrombosis was induced in the middle cerebral artery (MCA) with different experimental triggers. Where thrombin infusion generates fibrin-rich thrombi, topical $FeCl_3$-application generates platelet-rich thrombi. In the fibrin-rich model, both rh-tPA and Microlyse increased cortical reperfusion (determined by laser-speckle imaging) 10 minutes after therapy administration (35.8±17.1%; p=0.001; 39.3±13.1%; p<0.0001; 15.6±7.5%, respectively vs vehicle). In addition, both thrombolytic agents reduced cerebral lesion volume (determined by magnetic resonance imaging; MRI) after 24 hours (18.9±11.2$mm^3$; p=0.033; 16.1±13.9$mm^3$; p=0.018; 26.6±5.6$mm^3$, respectively vs vehicle). In the platelet-rich model, rh-tPA nor Microlyse increased cortical reperfusion 10 minutes after therapy (7.6±8.8%; p=0.216; 16.3±13.9%; p=0.151; 10.1±7.9%, respectively vs vehicle). However, Microlyse, but not rh-tPA, reduced cerebral lesion volumes (13.9±11.4$mm^3$; p<0.001; 23.6±11.1$mm^3$; p=0.188; 30.3±10.9$mm^3$, respectively vs vehicle). These findings support broad applicability of Microlyse in ischemic stroke irrespective of the thrombus composition.

**Conflict of interest:** COI declared - see note

**COI notes:** C.M. has been a speaker for Shire/Takeda on topics unrelated to this work. C.M., M.v.M, K.V and S.d.M are founders of TargED BV, a biotech spinout company of University Medical Center Utrecht (to develop Microlyse based upon the WO2019185723 A1 patent). C.M. and S.d.M participate in revenue sharing as inventors through the commercialization arm of the University Medical Center Utrecht. D.V. is scientific advisor to Strok@lliance (Caen, France). H.B.v.d.W. serves as a consultant to Bayer.

**Preprint server:** No;

**Author contributions and disclosures:** M.v.M., S.d.M., K.V., D.V., R.M.D., and C.M. conceived/designed the study. E.v.L., C.J. and T.B. performed experiments.

**Non-author contributions and disclosures:** No;

**Agreement to Share Publication-Related Data and Data Sharing Statement:** Emails to the corresponding author

**Clinical trial registration information (if any):**

**Journal:** Blood

**Type of submission:** Brief report

# **Title:** VWF-targeted thrombolysis to overcome rh-tPA resistance in experimental thrombotic stroke models

**Authors:** Marc V.A. van Moorsel[1,2,*], Steven de Maat[1,2,*], Kristof Vercruysse[2], Esther M. van Leeuwen[3], Charlène Jacqmarcq[4,5], Thomas Bonnard[4,5], Denis Vivien[4,5], H. Bart van der Worp[6], Rick M. Dijkhuizen[3], Coen Maas[1,2,*]

1 *Central Diagnostic Laboratory Research, University Medical Center Utrecht and Utrecht University, Utrecht, the Netherlands*

2 *TargED Biopharmaceuticals, Utrecht, the Netherlands*

* *contributed equally*

3 *Biomedical MR Imaging and Spectroscopy Group, Center for Image Sciences, University Medical Center Utrecht and Utrecht University, Utrecht, the Netherlands.*

4 *Normandie University, UNICAEN, INSERM U1237, Physiopathology and Imaging of Neurological Disorders (PhIND), Cyceron, Institut Blood and Brain @ Caen-Normandie (BB@C), 14000 Caen, France*

5 *Department of Clinical Research, Caen Normandie University Hospital, Caen, France*

6 *Department of Neurology and Neurosurgery, Brain Center, University Medical Center Utrecht and Utrecht University, Utrecht, the Netherlands*

**Correspondence:** Coen Maas, PhD, UMC Utrecht. E-mail: cmaas4@umcutrecht.nl. Tel.: +31.6.43.82.96.81

**Abstract word count:** 191

**Text word count:** 1.199

**Appendix word count:** 875

**Figure count:** 2

**Reference count:** 27

## KEY POINTS

Microlyse is non-inferior to rh-tPA when AIS is driven by fibrin-rich thrombi, but superior in AIS driven by platelet-rich thrombi

VWF-targeted plasminogen activation overcomes the intrinsic resistance of platelet-rich thrombi against rh-tPA mediated thrombolysis

## ABSTRACT

Recombinant human tissue plasminogen activator (rh-tPA) is an important thrombolytic agent for treatment of acute ischemic stroke (AIS). It requires fibrin binding for plasminogen activation. In contrast, Microlyse, a novel thrombolytic agent, requires von Willebrand factor (VWF) binding for plasminogen activation. We compared rh-tPA with Microlyse, administered 20 minutes after inducing thrombosis, in two randomized blinded AIS mouse models. Thrombosis was induced in the middle cerebral artery (MCA) with different experimental triggers. Where thrombin infusion generates fibrin-rich thrombi, topical $FeCl_3$-application generates platelet-rich thrombi. In the fibrin-rich model, both rh-tPA and Microlyse increased cortical reperfusion (determined by laser-speckle imaging) 10 minutes after therapy administration (35.8±17.1%; p=0.001; 39.3±13.1%; p<0.0001; 15.6±7.5%, respectively vs vehicle). In addition, both thrombolytic agents reduced cerebral lesion volume (determined by magnetic resonance imaging; MRI) after 24 hours (18.9±11.2mm$^3$; p=0.033; 16.1±13.9mm$^3$; p=0.018; 26.6±5.6mm$^3$, respectively vs vehicle). In the platelet-rich model, rh-tPA nor Microlyse increased cortical reperfusion 10 minutes after therapy (7.6±8.8%; p=0.216; 16.3±13.9%; p=0.151; 10.1±7.9%, respectively vs vehicle). However, Microlyse, but not rh-tPA, reduced cerebral lesion volumes (13.9±11.4mm$^3$; p<0.001; 23.6±11.1mm$^3$; p=0.188; 30.3±10.9mm$^3$, respectively vs vehicle). These findings support broad applicability of Microlyse in ischemic stroke irrespective of the thrombus composition.

## 1. INTRODUCTION

Intravenous administration of recombinant human tissue Plasminogen Activator (rh-tPA; *Alteplase*) is the only approved thrombolytic treatment for acute ischemic stroke (AIS). Nonetheless, its efficacy, based on survival in the absence of disability, is estimated less than 35% with a persistent risk for intracranial bleeding of 7%.[1–6] tPA is a endogenous protease that requires binding to fibrin to activate plasminogen into plasmin, which then actively degrades fibrin. Plasmin can also cleave von Willebrand Factor (VWF)[7], but none of the known plasminogen activators can activate plasminogen in a VWF-dependent manner.

The limited efficacy of rh-tPA to prevent ischemic injury is also known as “rh-tPA resistance”.[8–10] This phenomenon could be explained by new insights in clot architecture that challenge the assumption that fibrin is always available for rh-tPA binding in thrombi that cause AIS. First, experimental models for thrombosis following vascular injury *in vivo* have shown that fibrin forms in the thrombus core, near the site of injury, whereas the shell, reaching into the vessel lumen, is fibrin-poor.[11,12] In this context, fibrin is not accessible to intravascular thrombolytic agents. Second, histopathological examination of thrombectomized human thrombi (by definition excluding microvascular thrombi) showed large variability in the fibrin content.[8,13,14] Combined, these findings suggest that targeting non-fibrin components may hold value in the treatment of AIS.[8] VWF is a critical component in thrombus formation.[6] Indeed, degrading VWF by administration of ADAMTS13, at either supra-physiological levels[15] or via a gain-of-function mutant[16], reduced cerebral lesion volumes in preclinical AIS models. However, ADAMTS13 cannot degrade fibrin[17], limiting its applicability to VWF-dependent thrombi.[15]

In current clinical practice, the clot composition is unknown prior to treatment. Consequently, the availability of fibrin that determines rh-tPA efficacy is not guaranteed. In an attempt to improve the efficacy of thrombolytic therapy, we recently developed Microlyse. Microlyse is a single polypeptide consisting of a VWF-targeting nanobody and the catalytic domain of urokinase plasminogen activator (uPA). Upon binding VWF, Microlyse initiates localized plasminogen activation.[18] We demonstrated its efficacy in a preclinical model for thrombotic thrombocytopenic purpura (TTP), without increasing bleeding risk. TTP is a thrombotic microangiopathy with a dominant role for VWF and a minor, if any, role for fibrin. As plasmin can degrade both fibrin as well as VWF, we here set out to compare the efficacy of Microlyse and rh-tPA in both a fibrin- and a platelet-rich mouse model of AIS. Based on the ability to reduce ischemic lesion volumes, it was previously shown that the fibrin-rich model is rh-tPA sensitive, whereas the platelet-rich model is rh-tPA resistant but ADAMTS13 sensitive (i.e. VWF-dependent).[15,19]

## 2. METHODS

The experimental design is shown in Figures 1A-2A, and an expanded description of the Methods is supplied in the supplemental Data.

Thrombosis was induced at the M2 segment of the right MCA of OF1 mice under anesthesia. Experiments were performed in a randomized and blinded manner. Fibrin-rich thrombosis[19] (n=12-13 mice per group) was induced by the luminal injection of 1 UI murine thrombin (*Diagnostica Stago, France*).[20] Platelet-rich thrombosis (n=15-16 mice per group) was induced by the topical application of

$FeCl_3$ (20%, 4 minutes).[10,21] Laser doppler flowmetry was started to confirm full MCA segment occlusion. At T=10min, baseline cortical perfusion was determined via laser-speckle imaging (*FLPI-2, Moor Instrument, Axminster, United Kingdom*). Between T=20min and T=60min, vehicle, 0.8mg/kg Microlyse or 10mg/kg rh-tPA was administered by bolus injection (10% of total dose) and infusion via the tail vein (90% of total dose). Doses were selected based on dose-range efficacy studies in a VWF-driven model for thrombotic microangiopathy.[18] For rh-tPA, the highest effective dose without hemorrhagic transformation in mice was selected.[22] At T=70min, cortical perfusion was remeasured. Reperfusion data indicate the difference in perfusion before and after therapy. At T=24hrs, mice were anesthetized and subjected to MRI examination as described[23] to measure cerebral lesion volume (T2-weighted imaging), to detect cerebral hemorrhage (T2*-weighted imaging) and to assess MCA recanalization (time-of-flight angiography). Lesion volume, expressed in $mm^3$, was measured from the cortical areas displaying hyperintensity on twenty 2D-images. Cerebral hemorrhage per animal, identified as hypointensity, was scored present versus absent. MCA recanalization was scored in a blinded manner as full recanalization (full MCA was visible), partial recanalization (MCA was poorly visible, or sections were missing) or no recanalization (distal part invisible). Data are presented as mean±SD and treatment groups were compared with vehicle using Wilcoxon-Mann Whitney test. Differences were considered significant when $p<0.05$.

## 3. RESULTS & DISCUSSION

In the fibrin-rich AIS model, spontaneous reperfusion (T=70min) in vehicle-treated mice was 15.6±7.5% (Fig. 1B). Reperfusion levels were higher after rh-tPA or Microlyse administration (35.8±17.1%; $p=0.001$; 39.3±13.1%; $p<0.0001$, respectively) (Fig. 1B, C). After 24 hours, all mice showed full MCA recanalization. In addition, lesion volumes were smaller after administration of rh-tPA or Microlyse (18.9±11.2 $mm^3$; $p=0.033$; 16.1±13.9 $mm^3$; $p=0.018$; 26.6±5.6 $mm^3$, respectively vs vehicle) (Fig. 1D, E). Intracerebral hemorrhage was detected in one mouse (rh-tPA group).

In the platelet-rich AIS model, spontaneous reperfusion (T=70min) in vehicle-treated mice was 10.1±7.9% (Fig. 2B). Comparable reperfusion was measured after rh-tPA or Microlyse administration (7.6±8.8%; $p=0.216$; 16.3±13.9%; $p=0.151$, respectively) (Fig. 2B, C). After 24 hours, 25% of the vehicle-treated mice showed MCA recanalization, suggesting that this model results in more severe thrombotic occlusion than is seen in the fibrin-rich model. By comparison, MCA recanalization was observed in 62% of Microlyse-treated mice and 92% of rh-tPA-treated mice ($p<0.001$; $p=0.073$, respectively vs vehicle). However, lesion volumes were only smaller after administration of Microlyse, but not after rh-tPA administration ($13.9\pm11.4$ mm$^3$; $p<0.001$; $23.6\pm11.1$ mm$^3$; $p=0.188$; $30.3\pm10.9$ mm$^3$, respectively vs vehicle) (Fig. 2D, E). No intracerebral hemorrhage was detected with either treatment in this model. The observed variation in reperfusion and lesion volumes, as well as the observation that individual mice receiving vehicle have better outcomes than mice receiving thrombolytic therapy, is in line with previous studies in the field.[10,15,16,20]

The presence and accessibility of fibrin is a critical determinant in the efficacy of rh-tPA in mouse models for stroke.[13,19] In contrast, the efficacy of Microlyse is critically dependent on VWF-binding.[18] Indeed, rh-tPA increased reperfusion (T=70min) and reduced cerebral lesion volumes (T=24hr) in a fibrin-rich AIS model. The same holds true for Microlyse, supporting histopathological findings that VWF is present in all thrombi (average 30%; minimally 5%)[8], even when these are fibrin-rich. In sharp contrast, in a platelet-rich AIS model, neither agent increased early reperfusion (T=70min). This either suggests that thrombus formation is still ongoing between the moment of therapy administration and the time of perfusion measurements (T=70min), or alternatively, that these thrombi are more robust than those induced via thrombin. At T=24hrs after AIS induction, we observed two seemingly contradictive results. First, although Microlyse did not improve reperfusion at T=70min, it reduced lesion volumes (T=24hrs) nonetheless. This suggest that it acts in the time frame in between both measurements.[24] Second, rh-tPA showed better MCA recanalization (T=24hrs) than Microlyse (92% vs 62%, respectively) but was not associated with a reduced lesion volume. This either suggest that Microlyse triggers (partial) MCA recanalization earlier than rh-tPA, or that Microlyse, but not rh-tPA, removes secondary distal microthrombi. Future studies will have to examine the performance of Microlyse in dose-escalation effects and thrombolysis-related bleeding in models of hemorrhagic transformation.[25–27] Altogether, Microlyse's ability to degrade both tPA-sensitive and tPA-resistant thrombi supports its further development as promising thrombolytic treatment for acute ischemic stroke.

## ACKNOWLEDGMENTS

C.M. gratefully acknowledges Stichting Life Sciences Health –TKI (Health~Holland) for the LSH PPP Allowance grant 2020 (#TKI2023). S.d.M gratefully acknowledges the TTW section of the Netherlands Organization for Scientific Research (NWO, 2019/TTW/00704802). The authors would like to thank Strok@lliance (Caen, France), and in specific Dr. Annelise Letourneur and Dr. Nicolas Violle, for performing the *in vivo* experiments and analysis.

## AUTHORSHIP CONTRIBUTIONS

*M.v.M., S.d.M., K.V., D.V., R.M.D., and C.M. conceived/designed the study. E.v.L., C.J. and T.B. performed (pilot) experiments. M.v.M., S.d.M., H.B.v.d.W., R.M.D. and C.M wrote the paper.*

## DISCLOSURE OF CONFLICT OF INTEREST

C.M. has been a speaker for Shire/Takeda on topics unrelated to this work. C.M., M.v.M, K.V and S.d.M are founders of TargED Biopharmaceuticals BV, a biotech spinout company of University Medical Center Utrecht (to develop Microlyse based upon the WO2019185723 A1 patent). C.M. and S.d.M participate in revenue sharing as inventors through the commercialization arm of the University Medical Center Utrecht. D.V. is scientific advisor to Strok@lliance (Caen, France). H.B.v.d.W. serves as a consultant to Bayer and TargED Biopharmaceuticals BV.

## REFERENCES

1. Alper BS, Malone-Moses M, Prasad K. Intervention for Acute Stroke. *JAMA*. 2015;314(6):625-626. doi:10.1001/JAMA.2015.7848
2. Radecki RP. Factors Driving Expanded Use of Tissue Plasminogen Activator for Acute Ischemic Stroke - ACEP Now. https://www.acepnow.com/article/factors-driving-expanded-use-tissue-plasminogen-activator-acute-ischemic-stroke/
3. Mandrola JM. The Case Against Thrombolytic Therapy in Stroke. https://www.medscape.com/viewarticle/895159
4. Pilcher CA. Stroke: The times they are a-changin'. http://pilchermd.com/2018/05/26/stroke-the-times-they-are-a-changin/
5. Ciccone A, Valvassori L, Nichelatti M, et al. Endovascular treatment for acute ischemic stroke. *N Engl J Med*. 2013;368(10):904-913. doi:10.1056/NEJMOA1213701
6. Nayak MK, Flora GD, Chauhan AK. Constitutively active ADAMTS13: An emerging thrombolytic agent for acute ischemic stroke. *J Thromb Haemost*. Published online 2022. doi:10.1111/JTH.15649
7. Berkowitz SD, Dent J, Roberts J, et al. Epitope mapping of the von Willebrand factor subunit distinguishes fragments present in normal and type IIA von Willebrand disease from those generated by plasmin. *The Journal of Clinical Investigation*. 1987;79(2):524-531. doi:10.1172/JCI112843
8. Brinjikji W, Mereuta OM, Dai D, et al. Mechanisms of fibrinolysis resistance and potential targets for thrombolysis in acute ischaemic stroke: lessons from retrieved stroke emboli. *Stroke and Vascular Neurology*. 2021;6(4):1032. doi:10.1136/SVN-2021-001032
9. Jang IK, Gold HK, Ziskind AA, et al. Differential sensitivity of erythrocyte-rich and platelet-rich arterial thrombi to lysis with recombinant tissue-type plasminogen activator. A possible

explanation for resistance to coronary thrombolysis. *Circulation*. 1989;79(4):920-928. doi:10.1161/01.CIR.79.4.920

10. Sun YY, Kuo YM, Chen HR, Short-Miller JC, Smucker MR, Kuan CY. A murine photothrombotic stroke model with an increased fibrin content and improved responses to tPA-lytic treatment. *Blood Adv*. 2020;4(7):1222-1231. doi:10.1182/BLOODADVANCES.2019000782

11. Chernysh IN, Nagaswami C, Kosolapova S, et al. The distinctive structure and composition of arterial and venous thrombi and pulmonary emboli. *Scientific Reports*. 2020;10(1). doi:10.1038/S41598-020-59526-X

12. Tomaiuolo M, Matzko CN, Poventud-Fuentes I, Weisel JW, Brass LF, Stalker TJ. Interrelationships between structure and function during the hemostatic response to injury. *Proc Natl Acad Sci U S A*. 2019;116(6):2243-2252. doi:10.1073/PNAS.1813642116/VIDEO-2

13. Staessens S, Denorme F, François O, et al. Structural analysis of ischemic stroke thrombi: histological indications for therapy resistance. *Haematologica*. 2020;105(2):498-507. doi:10.3324/HAEMATOL.2019.219881

14. Meglio L di, Desilles JP, Ollivier V, et al. Acute ischemic stroke thrombi have an outer shell that impairs fibrinolysis. *Neurology*. 2019;93(18):E1686-E1698. doi:10.1212/WNL.0000000000008395

15. Denorme F, Langhauser F, Desender L, et al. ADAMTS13-mediated thrombolysis of t-PA-resistant occlusions in ischemic stroke in mice. *Blood*. 2016;127(19):2337-2345. doi:10.1182/BLOOD-2015-08-662650

16. South K, Saleh O, Lemarchand E, et al. Robust Thrombolytic and Anti-Inflammatory Action of a Constitutively Active ADAMTS13 Variant in Murine Stroke Models. *Blood*. Published online June 2021. doi:10.1182/BLOOD.2021012787

17. Zheng XL. ADAMTS13 and von Willebrand factor in thrombotic thrombocytopenic purpura. *Annu Rev Med*. 2015;66:211-225. doi:10.1146/ANNUREV-MED-061813-013241

18. de Maat S, Clark C, Barendrecht AD, et al. Microlyse; a thrombolytic agent that targets VWF for clearance of microvascular thrombosis. *Blood*. Published online June 2021. doi:10.1182/BLOOD.2021011776

19. Lizarrondo SM de, Gakuba C, Herbig BA, et al. Potent Thrombolytic Effect of N-Acetylcysteine on Arterial Thrombi. *Circulation*. 2017;136(7):646-660. doi:10.1161/CIRCULATIONAHA.117.027290

20. Orset C, Macrez R, Young AR, et al. Mouse model of in situ thromboembolic stroke and reperfusion. *Stroke*. 2007;38(10):2771-2778. doi:10.1161/STROKEAHA.107.487520

21. Karatas H, Erdener SE, Gursoy-Ozdemir Y, et al. Thrombotic distal middle cerebral artery occlusion produced by topical FeCl(3) application: a novel model suitable for intravital

microscopy and thrombolysis studies. *J Cereb Blood Flow Metab*. 2011;31(6):1452-1460. doi:10.1038/JCBFM.2011.8

22. Amki M el, Lerouet D, Coqueran B, et al. Experimental modeling of recombinant tissue plasminogen activator effects after ischemic stroke. *Exp Neurol*. 2012;238(2):138-144. doi:10.1016/J.EXPNEUROL.2012.08.005

23. Planas AM. Noninvasive Brain Imaging in Small Animal Stroke Models: MRI and PET. *Neuromethods*. 2010;47:139-165. doi:10.1007/978-1-60761-750-1_11

24. Eckly A, Hechler B, Freund M, et al. Mechanisms underlying FeCl3-induced arterial thrombosis. *J Thromb Haemost*. 2011;9(4):779-789. doi:10.1111/J.1538-7836.2011.04218.X

25. Orset C, Arkelius K, Anfray A, Warfvinge K, Vivien D, Ansar S. Combination treatment with U0126 and rt-PA prevents adverse effects of the delayed rt-PA treatment after acute ischemic stroke. *Sci Rep*. 2021;11(1). doi:10.1038/S41598-021-91469-9

26. García-Yébenes I, Sobrado M, Zarruk JG, et al. A mouse model of hemorrhagic transformation by delayed tissue plasminogen activator administration after in situ thromboembolic stroke. *Stroke*. 2011;42(1):196-203. doi:10.1161/STROKEAHA.110.600452

27. Grisotto C, Taïlé J, Planesse C, et al. High-Fat Diet Aggravates Cerebral Infarct, Hemorrhagic Transformation and Neuroinflammation in a Mouse Stroke Model. *Int J Mol Sci*. 2021;22(9). doi:10.3390/IJMS22094571

## FIGURE LEGENDS

**Figure 1. Fibrin-rich thrombosis model (thrombin-induced; rh-tPA sensitive).** (A) AIS was induced by intravascular injection of thrombin into the MCA. Clot formation was considered to be stable when blood flow in the MCA was zero for 10 minutes. Cortical perfusion over the entire dorsal brain area was measured via Speckle Imaging between T=10min and T=70min. Treatment was given at T=20min as 10% bolus and 90% infusion over 40 minutes. MRI was performed after 24 hours to assess lesion volumes (T2-weighted), possible hemorrhage (T2*-weighted) and MCA recanalization (MR angiography). (B) Bar graph (mean+SD) displaying the percentage of reperfusion of the ischemic core, calculated as difference between levels of perfusion 10 minutes after treatment (T=70min) and 10 minutes before treatment (T=10min). From individual mice indicated as red circles (reflecting median values), images are presented hereafter. (C) Representative laser speckle flow images (from subjects indicated at red circles in panel B) before and after treatment from a single mouse per group. Reperfusion is visible when the blue hemisphere (bottom half of each image) before treatment is turning green/yellow/red after treatment. Mean cerebral blood flow levels in the ischemic core (expressed as % of the unaffected hemisphere) are shown below the images. (D) Bar graph (mean+SD) displaying lesion volumes, calculated from T2-

weighted MR images. From individual mice indicated as red circles (reflecting median values), images are presented hereafter. (E) Representative T2-weighted images of coronal mouse brain slices displaying the hyperintense lesion area in a single mouse per group (indicated as red circles in panel D). Lesion volume values are shown below the images. Asterisks indicate significance levels as measured by Mann-Whitney tests: $^*p<0.05$ ; $^{**}p<0.01$ ; $^{***}p<0.001$.

**Figure 2. Platelet-rich thrombosis model ($FeCl_3$ induced; rh-tPA resistant).** (A) AIS was induced by topical application of $FeCl_3$ on the MCA. (B) Bar graph (mean+SD) displaying the percentage of reperfusion of the ischemic core, calculated as difference between levels of perfusion 10 minutes after treatment (T=70min) and 10 minutes before treatment (T=10min). From individual mice indicated as red circles, images are presented hereafter. (C) Representative laser speckle flow images (from subjects indicated at red circles in panel B) before and after treatment from a single mouse per group. Reperfusion appears absent as the blue/green hemisphere (bottom half of each image) before treatment remains blue/green after treatment. Mean cerebral blood flow levels in the ischemic core (expressed as % of the unaffected hemisphere) are shown below the images. (D) Bar graph (mean+SD) displaying lesion volumes, calculated from T2-weighted MR-images. From individual mice indicated as red circles (reflecting median values), images are presented hereafter. (E) Representative T2-weighted images of coronal mouse brain slices displaying the hyperintense lesion area in a single mouse with median lesion volume per group (indicated as red circles in panel D). Lesion volume values are shown below the images. Asterisks indicate significance levels as measured by Mann-Whitney tests: $^*p<0.05$ ; $^{**}p<0.01$ ; $^{***}p<0.001$.

# Figure 1

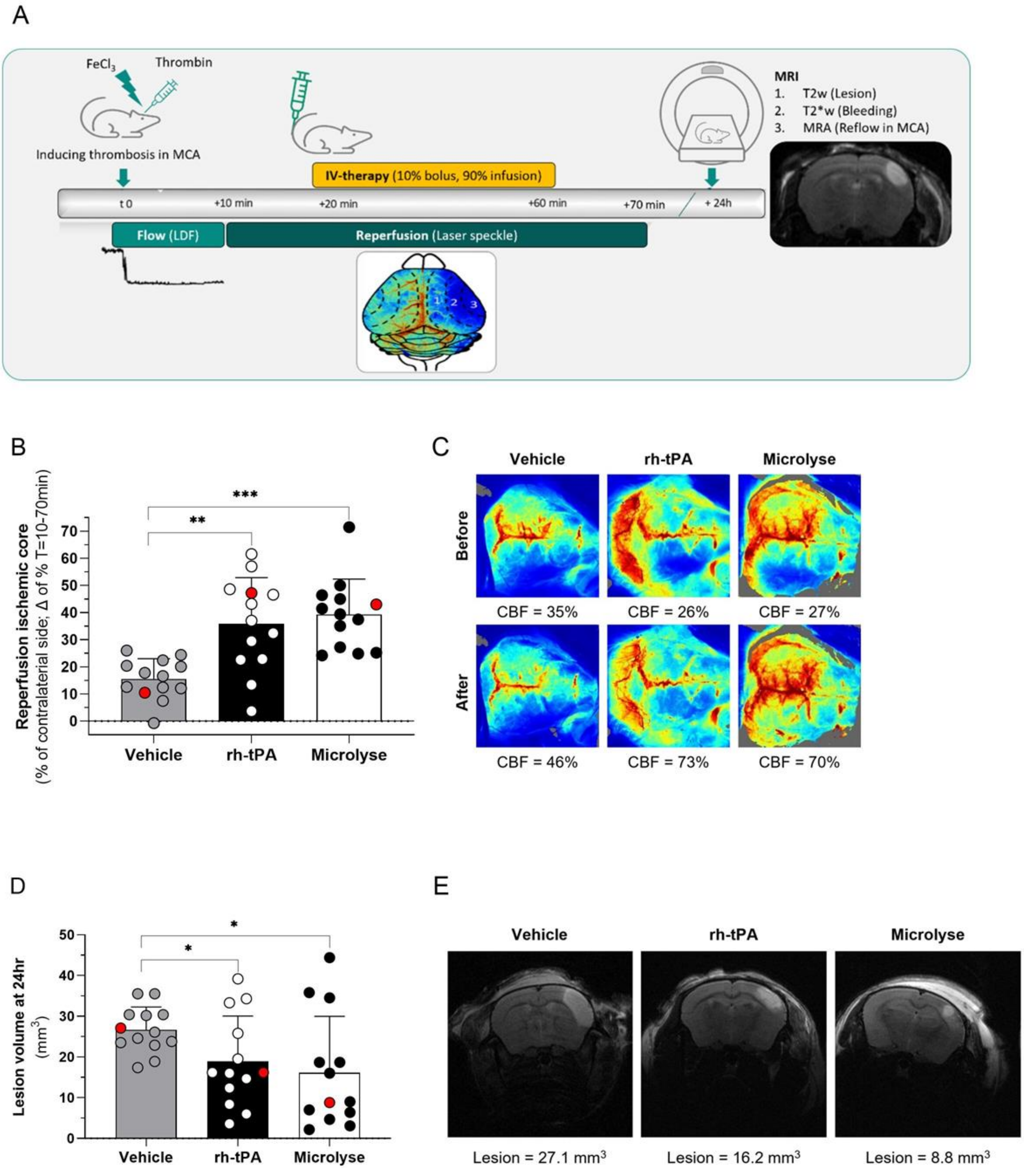
A
FeCl$_3$
Thrombin
Inducing thrombosis in MCA
IV-therapy (10% bolus, 90% infusion)
MRI
1. T2w (Lesion)
2. T2*w (Bleeding)
3. MRA (Reflow in MCA)
t 0
+10 min
+20 min
+60 min
+70 min
+ 24h
Flow (LDF)
Reperfusion (Laser speckle)
1
2
3
B
Reperfusion ischemic core
(% of contralaterial side; Δ of % T=10-70min)
70
60
50
40
30
20
10
0
***
**
Vehicle
rh-tPA
Microlyse
C
Vehicle
rh-tPA
Microlyse
Before
After
CBF = 35%
CBF = 26%
CBF = 27%
CBF = 46%
CBF = 73%
CBF = 70%
D
Lesion volume at 24hr
(mm$^3$)
50
40
30
20
10
0
*
*
Vehicle
rh-tPA
Microlyse
E
Vehicle
rh-tPA
Microlyse
Lesion = 27.1 mm$^3$
Lesion = 16.2 mm$^3$
Lesion = 8.8 mm$^3$

# Figure 2

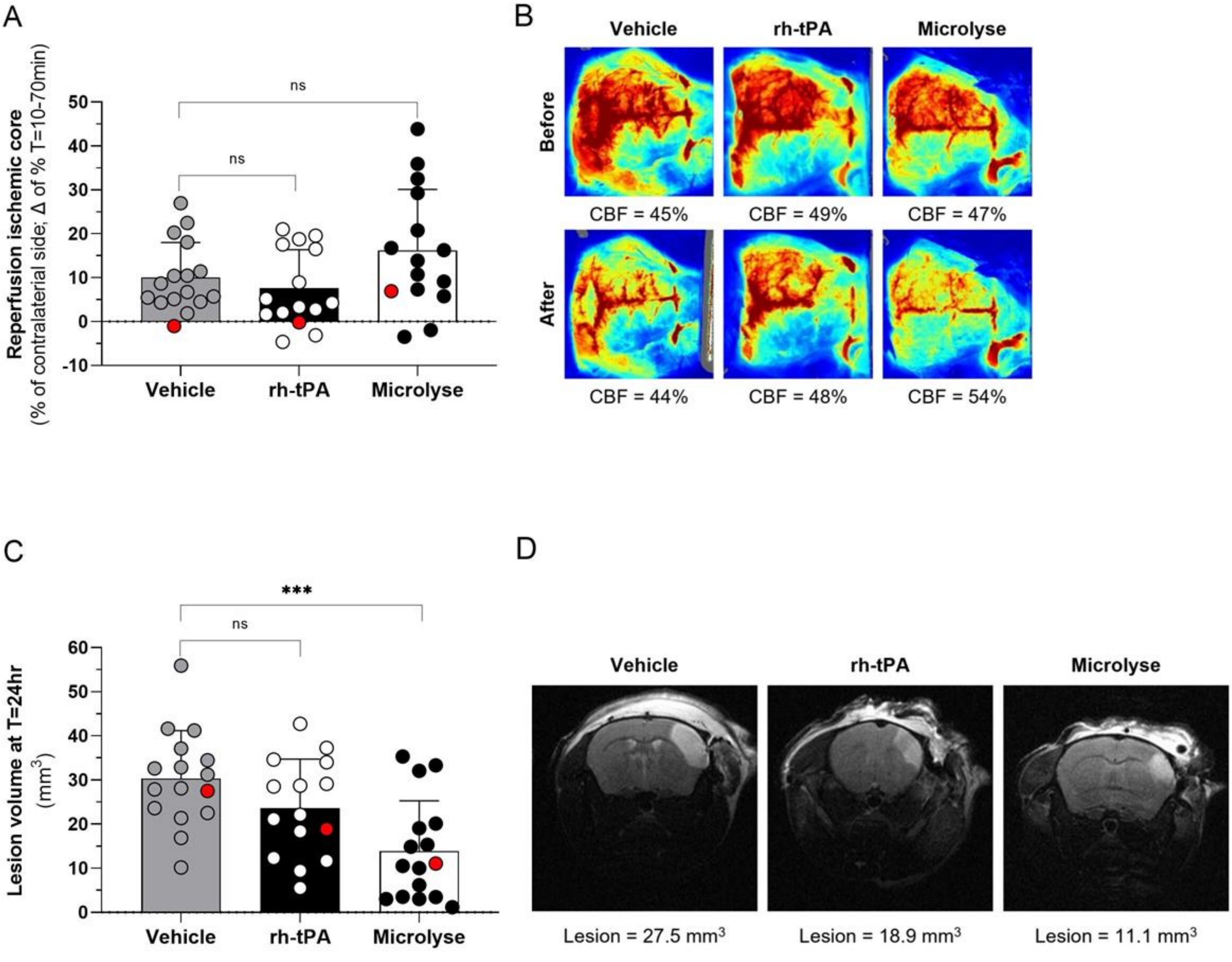
A
Reperfusion ischemic core
(% of contralateral side; Δ of % T=10-70min)
50
40
30
20
10
0
-10
ns
ns
Vehicle
rh-tPA
Microlyse
B
Vehicle
rh-tPA
Microlyse
Before
CBF = 45%
CBF = 49%
CBF = 47%
After
CBF = 44%
CBF = 48%
CBF = 54%
C
Lesion volume at T=24hr
(mm$^3$)
60
50
40
30
20
10
0
***
ns
Vehicle
rh-tPA
Microlyse
D
Vehicle
rh-tPA
Microlyse
Lesion = 27.5 mm$^3$
Lesion = 18.9 mm$^3$
Lesion = 11.1 mm$^3$

## SUPPLEMENTAL

## EXPANDED METHODS

### 1. *Mice and materials*

Experiments were performed by Strok@lliance (*Caen, France*) with 12-week-old male OF1 mice (*Charles River, Saint-Germain-sur-l'Arbresle, France*) with ethical approval of the Ministry of Higher Education and Research (n° APAFIS#21066-2019061410324646v2 and n° APAFIS#29981). Microlyse[1] was provided by UMC Utrecht (*Utrecht, The Netherlands*). This fusion protein binds to the CT/CK domain of human and murine VWF and contains the protease domain of murine urokinase-type plasminogen activator. rh-tPA (Actilyse) was purchased from Boehringer Ingelheim (*Germany*) and was reconstituted according to the manufacturer's instructions. Sterile NaCl 0.9% served as solvent and vehicle control.

### 2. *Randomization and blinding procedure*

Mice were allocated to experimental groups on the day of the surgery based on both body weight and a block randomization method to avoid order bias and surgery station bias. Groups were coded A, B and C, according to treatment allocation. Research assistants who executed experimental procedures and image analyses were blinded for group and treatment assignments.

### 3. *Thrombotic occlusion of the MCA*

Mice were anesthetized with 5.0% isoflurane for induction and 2.0% as maintenance in a 70/30% $N_2O/O_2$ mixture. Body temperature was maintained at 37.5°C during the entire procedure with a homeothermic pad connected to a rectal probe. Mice were placed in a stereotactic frame; the scalp was incised, and the temporalis muscle dissociated. Craniotomy was performed over the M1/M2 bifurcation, after which the dura mater was removed. At T=0 min, thrombosis was induced at the M2 segment of the right middle cerebral artery (MCA). The first model (n=12-13 per group) included the luminal injection of 1 UI murine thrombin (*Diagnostica Stago, France*)[16]. The model was selected as it results in fibrin-rich thrombi, which are rh-tPA-sensitive[2], but by definition ADAMTS13-resistant. The second model (n=15-16 per group) included the topical application of a Whatman™ filter paper soaked in freshly prepared $FeCl_3$ (20%, 4 minutes).[17] The model was selected as it results in platelet-rich thrombi[9] which are rh-tPA-resistant[2], but ADAMTS13-sensitive (Fig. 1A).[13] Via laser-doppler flow measurements on the MCA distally from the occlusion, we considered vessel occlusion to be stable when flow was zero for 10 minutes. At T=20 min, vehicle, 0.8mg/kg Microlyse or 10mg/kg rh-tPA were intravenously administered via the tail vein by bolus-injection (10% of total dose) and infusion for 40 minutes (90% of total dose). The selected dose of rh-tPA is proven the highest effective dose without haemorrhagic transformation as side effect in mice.[3] Perfusion of the cortex was measured between 10 minutes before-(T=10min) and after (T=70min) therapy via laser-speckle imaging (*FLPI-2, Moor Instrument,* *Axminster, United Kingdom*). At T=70 min, anesthesia was discontinued and mice received subcutaneous buprenorphine injection (0.05 mg/kg, Buprecare, *Axience, Pantin, France*) for peri-operative pain relief and were allowed to recover. At T=24hrs, mice were re-anesthetized with isoflurane as previously described and were subjected to MRI examination.

### 4. *Exclusion criteria*

Mice were excluded in case of death during the experimental procedure (n=2 in fibrin-rich AIS; n=2 in platelet-rich AIS, respectively), technical problems (n=3 fibrin-rich AIS; n=3 platelet-rich AIS), lesion outside MCA territory (n=2 fibrin-rich AIS; n=1 platelet-rich AIS) and unsuccessful induction of thrombosis defined as CBF >60% in ischemic core at T=20min (n=2 fibrin-rich AIS; n=12 platelet-rich AIS).

### 5. *Reperfusion measurement (T=10-70min)*

Transcranial CBF measurements were performed over the full dorsal aspect of the cerebral cortex via laser Speckle using MoorFLIP Review 5.0 software (Moor Instruments). Perfusion was expressed as percentage of the value in the contralateral (unaffected) cortex. The level of reperfusion was determined from the difference between perfusion before (T=10min) and after IV-therapy (T=70min).

### 6. *MRI measurements (T=24hr) to assess infarct volume, bleeding and recanalization of the MCA*

With a preclinical MRI system (7T-Pharmascan MRI system, Bruker BioSpin MRI GmbH, *Ettlinger, Germany*) we executed the following MRI protocols over 20 minutes[4]: 1) T2-weighted imaging to measure the cerebral lesion; 2) T2*-weighted imaging to detect deoxyhaemoglobin deposits in the cerebral parenchyma that indicate cerebral hemorrhage and 3) Time-of-flight angiography (TOF-MRA) for assessment of flow through the MCA. T2-weighted imaging included T2 Rapid Imaging with Refocused Echoes (RARE) sequence (T2_TurboRARE_T2W). Parameters were set as follow: RT/ET 40/3500ms, Echo Spacing: 13.33ms, Rare factor 8°, Field of View = 17.92 × 17.92 × 10 mm, Matrix = 256 × 256, 20 coronal slices of 0.5 mm thickness, leading to a resolution of 0.07 × 0.07 × 0.5 mm. T2* weighted imaging included Fast-Low Angle Shot (FLASH) sequence (T2s_rapide_FcFLASh). Parameters were set as follow: RT/ET 500/8.65ms, Flip Angle = 40°, Field of View: 17.92 × 17.92 × 10 mm, Matrix = 256 × 356; 20 coronal slices of 0.5 mm thickness, leading to a resolution of 0.07 x 0.07 x 0.5 mm. TOF-MRA imaging included the following parameters: RT/ET 14/2.6ms, Flip Angle = 20°, Field of View = 17.92 x 17.92 x 10 mm, Matrix = 256 x 256; 72 coronal slices, leading to a resolution of 0.07 x 0.07 x 0.139 mm.

Lesions appeared as hyperintensity areas on images. Lesion volume was expressed in $mm^3$ by analysing twenty 2D-images. Cerebral haemorrhage was scored present versus absent. Recanalization was scored as full recanalization (when MCA was visible over the full length), partial recanalization (when MCA was poorly visible, or sections were missing) or no recanalization (when distal part MCA was invisible). All images were analysed using ImageJ v1.48 (NIH, Bethesda, USA).

### 7. *Statistical analysis*

Reperfusion level (%), lesion volumes ($mm^3$) and MCA recanalization (present versus absent) of treatment groups were compared with vehicle using Wilcoxon-Mann Whitney tests (unpaired, nonparametric). Differences were considered significant when $p<0.05$.

## REFERENCES APPENDIX A

1. de Maat S, Clark C, Barendrecht AD, et al. Microlyse; a thrombolytic agent that targets VWF for clearance of microvascular thrombosis. *Blood*. Published online November 12, 2021. doi:10.1182/BLOOD.2021011776

2. De Lizarrondo SM, Gakuba C, Herbig BA, et al. Potent Thrombolytic Effect of N-Acetylcysteine on Arterial Thrombi. *Circulation*. 2017;136(7):646-660. doi:10.1161/CIRCULATIONAHA.117.027290

3. El Amki M, Lerouet D, Coqueran B, et al. Experimental modeling of recombinant tissue plasminogen activator effects after ischemic stroke. *Exp Neurol*. 2012;238(2):138-144. doi:10.1016/J.EXPNEUROL.2012.08.005

4. Planas AM. Noninvasive Brain Imaging in Small Animal Stroke Models: MRI and PET. *Neuromethods*. 2010;47:139-165. doi:10.1007/978-1-60761-750-1_11

# BIBLIOGRAPHIE

Aaslid, R., Markwalder, T.M., Nornes, H., 1982. Noninvasive transcranial Doppler ultrasound recording of flow velocity in basal cerebral arteries. J Neurosurg 57, 769–774. https://doi.org/10.3171/jns.1982.57.6.0769

Absar, S., Gupta, N., Nahar, K., Ahsan, F., 2015. Engineering of plasminogen activators for targeting to thrombus and heightening thrombolytic efficacy. Journal of Thrombosis and Haemostasis 13, 1545–1556. https://doi.org/10.1111/jth.13033

Adams, H.P., 2011. 21 - Clinical Scales to Assess Patients with Stroke, in: Mohr, J.P., Wolf, P.A., Grotta, J.C., Moskowitz, M.A., Mayberg, M.R., von Kummer, R. (Eds.), Stroke (Fifth Edition). W.B. Saunders, Saint Louis, pp. 307–333. https://doi.org/10.1016/B978-1-4160-5478-8.10021-1

Adams, H.P., Bendixen, B.H., Kappelle, L.J., Biller, J., Love, B.B., Gordon, D.L., Marsh, E.E., 1993. Classification of subtype of acute ischemic stroke. Definitions for use in a multicenter clinical trial. TOAST. Trial of Org 10172 in Acute Stroke Treatment. Stroke 24, 35–41. https://doi.org/10.1161/01.str.24.1.35

Albers, G.W., Marks, M.P., Kemp, S., Christensen, S., Tsai, J.P., Ortega-Gutierrez, S., McTaggart, R.A., Torbey, M.T., Kim-Tenser, M., Leslie-Mazwi, T., Sarraj, A., Kasner, S.E., Ansari, S.A., Yeatts, S.D., Hamilton, S., Mlynash, M., Heit, J.J., Zaharchuk, G., Kim, S., Carrozzella, J., Palesch, Y.Y., Demchuk, A.M., Bammer, R., Lavori, P.W., Broderick, J.P., Lansberg, M.G., DEFUSE 3 Investigators, 2018. Thrombectomy for Stroke at 6 to 16 Hours with Selection by Perfusion Imaging. N Engl J Med 378, 708–718. https://doi.org/10.1056/NEJMoa1713973

Alvares, R.D.A., Szulc, D.A., Cheng, H.-L.M., 2017. A scale to measure MRI contrast agent sensitivity. Sci Rep 7, 15493. https://doi.org/10.1038/s41598-017-15732-8

Alves, H.C., Treurniet, K.M., Jansen, I.G.H., Yoo, A.J., Dutra, B.G., Zhang, G., Yo, L., van Es, A.C.G.M., Emmer, B.J., van den Berg, R., van den Wijngaard, I.R., Lycklama à Nijeholt, G.J., Vos, J.-A., Roos, Y.B.W.E.M., Schonewille, W., Marquering, H.A., Majoie, C.B.L.M., null, null, 2019. Thrombus Migration Paradox in Patients With Acute Ischemic Stroke. Stroke 50, 3156–3163. https://doi.org/10.1161/STROKEAHA.119.026107

Ames, A., Wright, R.L., Kowada, M., Thurston, J.M., Majno, G., 1968. Cerebral ischemia. II. The no-reflow phenomenon. Am. J. Pathol. 52, 437–453.

Ansar, S., Chatzikonstantinou, E., Wistuba-Schier, A., Mirau-Weber, S., Fatar, M., Hennerici, M.G., Meairs, S., 2014. Characterization of a New Model of Thromboembolic Stroke in C57 black/6J mice. Transl Stroke Res 5, 526–533. https://doi.org/10.1007/s12975-013-0315-9

Arkelius, K., Vivien, D., Orset, C., Ansar, S., 2020. Validation of a stroke model in rat compatible with rt-PA-induced thrombolysis: new hope for successful translation to the clinic. Sci Rep 10. https://doi.org/10.1038/s41598-020-69081-0

Arvanitakis, Z., Leurgans, S.E., Barnes, L.L., Bennett, D.A., Schneider, J.A., 2011. Microinfarct pathology, dementia, and cognitive systems. Stroke 42, 722–727. https://doi.org/10.1161/STROKEAHA.110.595082

Association of outcome with early stroke treatment: pooled analysis of ATLANTIS, ECASS, and NINDS rt-PA stroke trials, 2004. . The Lancet 363, 768–774. https://doi.org/10.1016/S0140-6736(04)15692-4

Awad, I., Modic, M., Little, J.R., Furlan, A.J., Weinstein, M., 1986. Focal parenchymal lesions in transient ischemic attacks: correlation of computed tomography and magnetic resonance imaging. Stroke 17, 399–403. https://doi.org/10.1161/01.STR.17.3.399

Barber, P.A., Demchuk, A.M., Hudon, M.E., Pexman, J.H.W., Hill, M.D., Buchan, A.M., 2001. Hyperdense Sylvian Fissure MCA "Dot" Sign. Stroke 32, 84–88. https://doi.org/10.1161/01.STR.32.1.84

Bekkers, S.C.A.M., Yazdani, S.K., Virmani, R., Waltenberger, J., 2010. Microvascular Obstruction: Underlying Pathophysiology and Clinical Diagnosis. Journal of the American College of Cardiology 55, 1649–1660. https://doi.org/10.1016/j.jacc.2009.12.037

Benjamin, E.J., Blaha, M.J., Chiuve, S.E., Cushman, M., Das, S.R., Deo, R., de Ferranti, S.D., Floyd, J., Fornage, M., Gillespie, C., Isasi, C.R., Jiménez, M.C., Jordan, L.C., Judd, S.E., Lackland, D., Lichtman, J.H., Lisabeth, L., Liu, S., Longenecker, C.T., Mackey, R.H., Matsushita, K., Mozaffarian, D., Mussolino, M.E., Nasir, K., Neumar, R.W., Palaniappan, L., Pandey, D.K., Thiagarajan, R.R., Reeves, M.J., Ritchey, M., Rodriguez, C.J., Roth, G.A., Rosamond, W.D., Sasson, C., Towfighi, A., Tsao, C.W., Turner, M.B., Virani, S.S., Voeks, J.H., Willey, J.Z., Wilkins, J.T., Wu, J.H., Alger, H.M., Wong, S.S., Muntner, P., American Heart Association Statistics Committee and Stroke Statistics Subcommittee, 2017. Heart Disease and Stroke Statistics-2017 Update: A Report From the American Heart Association. Circulation 135, e146–e603. https://doi.org/10.1161/CIR.0000000000000485

Berkhemer, O.A., Fransen, P.S.S., Beumer, D., van den Berg, L.A., Lingsma, H.F., Yoo, A.J., Schonewille, W.J., Vos, J.A., Nederkoorn, P.J., Wermer, M.J.H., van Walderveen, M.A.A., Staals, J., Hofmeijer, J., van Oostayen, J.A., Lycklama à Nijeholt, G.J., Boiten, J., Brouwer, P.A., Emmer, B.J., de Bruijn, S.F., van Dijk, L.C., Kappelle, L.J., Lo, R.H., van Dijk, E.J., de Vries, J., de Kort, P.L.M., van Rooij, W.J.J., van den Berg, J.S.P., van Hasselt, B.A.A.M., Aerden, L.A.M., Dallinga, R.J., Visser, M.C., Bot, J.C.J., Vroomen, P.C., Eshghi, O., Schreuder, T.H.C.M.L., Heijboer, R.J.J., Keizer, K., Tielbeek, A.V., den Hertog, H.M., Gerrits, D.G., van den Berg-Vos, R.M., Karas, G.B., Steyerberg, E.W., Flach, H.Z., Marquering, H.A., Sprengers, M.E.S., Jenniskens, S.F.M., Beenen, L.F.M., van den Berg, R., Koudstaal, P.J., van Zwam, W.H., Roos, Y.B.W.E.M., van der Lugt, A., van Oostenbrugge, R.J., Majoie, C.B.L.M., Dippel, D.W.J., 2015. A Randomized Trial of Intraarterial Treatment for Acute Ischemic Stroke. New England Journal of Medicine 372, 11–20. https://doi.org/10.1056/NEJMoa1411587

Boehme, A.K., Esenwa, C., Elkind, M.S.V., 2017. Stroke Risk Factors, Genetics, and Prevention. Circulation Research 120, 472–495. https://doi.org/10.1161/CIRCRESAHA.116.308398

Bonnard, T., Jayapadman, A., Putri, J.A., Cui, J., Ju, Y., Carmichael, C., Angelovich, T.A., Cody, S.H., French, S., Pascaud, K., Pearce, H.A., Jagdale, S., Caruso, F., Hagemeyer, C.E., 2018. Low-Fouling and Biodegradable Protein-Based Particles for Thrombus Imaging. ACS Nano 12, 6988–6996. https://doi.org/10.1021/acsnano.8b02588

Borissoff, J.I., Spronk, H.M.H., ten Cate, H., 2011. The hemostatic system as a modulator of atherosclerosis. N Engl J Med 364, 1746–1760. https://doi.org/10.1056/NEJMra1011670

Bourrinet, P., Bengele, H.H., Bonnemain, B., Dencausse, A., Idee, J.-M., Jacobs, P.M., Lewis, J.M., 2006. Preclinical safety and pharmacokinetic profile of ferumoxtran-10, an ultrasmall superparamagnetic iron oxide magnetic resonance contrast agent. Invest Radiol 41, 313–324. https://doi.org/10.1097/01.rli.0000197669.80475.dd

Broocks, G., Meyer, L., Kabiri, R., Kniep, H.C., McDonough, R., Bechstein, M., van Horn, N., Lindner, T., Sedlacik, J., Cheng, B., Thomalla, G., Schön, G., Fiehler, J., Hanning, U., Schönfeld, M.H., 2021. Impact of intravenous alteplase on sub-angiographic emboli in high-resolution diffusion-weighted imaging following successful thrombectomy. Eur Radiol 31, 8228–8235. https://doi.org/10.1007/s00330-021-07980-0

Brouns, R., De Deyn, P.P., 2009. The complexity of neurobiological processes in acute ischemic stroke. Clin Neurol Neurosurg 111, 483–495. https://doi.org/10.1016/j.clineuro.2009.04.001

Burgin, W.S., Malkoff, M., Felberg, R.A., Demchuk, A.M., Christou, I., Grotta, J.C., Alexandrov, A.V., 2000. Transcranial doppler ultrasound criteria for recanalization after thrombolysis for middle cerebral artery stroke. Stroke 31, 1128–1132. https://doi.org/10.1161/01.str.31.5.1128

Campbell, B.C.V., Mitchell, P.J., Yan, B., Parsons, M.W., Christensen, S., Churilov, L., Dowling, R.J., Dewey, H., Brooks, M., Miteff, F., Levi, C., Krause, M., Harrington, T.J., Faulder, K.C., Steinfort, B.S., Kleinig, T., Scroop, R., Chryssidis, S., Barber, A., Hope, A., Moriarty, M., McGuinness, B., Wong, A.A., Coulthard, A., Wijeratne, T., Lee, A., Jannes, J., Leyden, J., Phan, T.G., Chong, W., Holt, M.E., Chandra, R.V., Bladin, C.F., Badve, M., Rice, H., de Villiers, L., Ma, H., Desmond, P.M., Donnan, G.A., Davis, S.M., EXTEND-IA investigators, 2014. A multicenter, randomized, controlled study to investigate EXtending the time for Thrombolysis in Emergency Neurological Deficits with Intra-Arterial therapy (EXTEND-IA). Int J Stroke 9, 126–132. https://doi.org/10.1111/ijs.12206

Cedervall, T., Lynch, I., Lindman, S., Berggård, T., Thulin, E., Nilsson, H., Dawson, K.A., Linse, S., 2007. Understanding the nanoparticle–protein corona using methods to quantify exchange rates and affinities of proteins for nanoparticles. Proc Natl Acad Sci U S A 104, 2050–2055. https://doi.org/10.1073/pnas.0608582104

Chavignon, A., Hingot, V., Orset, C., Vivien, D., Couture, O., 2022. 3D transcranial ultrasound localization microscopy for discrimination between ischemic and hemorrhagic stroke in early phase. Sci Rep 12, 14607. https://doi.org/10.1038/s41598-022-18025-x

Chettibi, M., Benghezel, S., Bertal, S., Nedjar, R., Bouraghda, M.A., Bouafia, M.T.C., 2015. No reflow : quels facteurs prédictifs ? Annales de Cardiologie et d’Angéiologie, Numéro spécial GRCI 2015. 22e Réunion Nationale 64, 472–480. https://doi.org/10.1016/j.ancard.2015.09.059

Chung, J., Park, S.H., Kim, N., Kim, W., Park, J.H., Ko, Y., Yang, M.H., Jang, M.S., Han, M., Jung, C., Kim, J.H., Oh, C.W., Bae, H., 2014. Trial of ORG 10172 in Acute Stroke Treatment (TOAST) Classification and Vascular Territory of Ischemic Stroke Lesions Diagnosed by Diffusion-Weighted Imaging. Journal of the American Heart Association 3, e001119. https://doi.org/10.1161/JAHA.114.001119

Ciciliano, J.C., Sakurai, Y., Myers, D.R., Fay, M.E., Hechler, B., Meeks, S., Li, R., Dixon, J.B., Lyon, L.A., Gachet, C., Lam, W.A., 2015. Resolving the multifaceted mechanisms of the ferric chloride thrombosis model using an interdisciplinary microfluidic approach. Blood 126, 817–824. https://doi.org/10.1182/blood-2015-02-628594

Colasuonno, M., Palange, A.L., Aid, R., Ferreira, M., Mollica, H., Palomba, R., Emdin, M., Del Sette, M., Chauvierre, C., Letourneur, D., Decuzzi, P., 2018. Erythrocyte-Inspired Discoidal Polymeric Nanoconstructs Carrying Tissue Plasminogen Activator for the Enhanced Lysis of Blood Clots. ACS Nano 12, 12224–12237. https://doi.org/10.1021/acsnano.8b06021

Collaboration, A.T. (ATT), Baigent, C., Blackwell, L., Collins, R., Emberson, J., Godwin, J., Peto, R., Buring, J., Hennekens, C., Kearney, P., Meade, T., Patrono, C., Roncaglioni, M.C., Zanchetti, A., 2009. Aspirin in the primary and secondary prevention of vascular disease: collaborative meta-analysis of individual participant data from randomised trials. Lancet 373, 1849–1860.

Collaborative overview of randomised trials of antiplatelet therapy--I: Prevention of death, myocardial infarction, and stroke by prolonged antiplatelet therapy in various categories of patients. Antiplatelet Trialists’ Collaboration, 1994. . BMJ 308, 81–106.

Corbo, C., Molinaro, R., Parodi, A., Toledano Furman, N.E., Salvatore, F., Tasciotti, E., 2016. The impact of nanoparticle protein corona on cytotoxicity, immunotoxicity and target drug delivery. Nanomedicine (Lond) 11, 81–100. https://doi.org/10.2217/nnm.15.188

Correa-Paz, C., Navarro Poupard, M.F., Polo, E., Rodríguez-Pérez, M., Migliavacca, M., Iglesias-Rey, R., Ouro, A., Maqueda, E., Hervella, P., Sobrino, T., Castillo, J., Del Pino, P., Pelaz, B., Campos, F., 2022. Sonosensitive capsules for brain thrombolysis increase ischemic damage in a stroke model. J Nanobiotechnology 20, 46. https://doi.org/10.1186/s12951-022-01252-9

Crețu, B.E.-B., Dodi, G., Shavandi, A., Gardikiotis, I., Șerban, I.L., Balan, V., 2021. Imaging Constructs: The Rise of Iron Oxide Nanoparticles. Molecules 26, 3437. https://doi.org/10.3390/molecules26113437

Cruz-Flores, S., Rabinstein, A., Biller, J., Elkind, M.S.V., Griffith, P., Gorelick, P.B., Howard, G., Leira, E.C., Morgenstern, L.B., Ovbiagele, B., Peterson, E., Rosamond, W., Trimble, B., Valderrama, A.L., American Heart Association Stroke Council, Council on Cardiovascular Nursing, Council on Epidemiology and Prevention, Council on Quality of Care and Outcomes Research, 2011. Racial-ethnic disparities in stroke care: the American experience: a statement for healthcare professionals from the American Heart Association/American Stroke Association. Stroke 42, 2091–2116. https://doi.org/10.1161/STR.0b013e3182213e24

Dalkara, T., Arsava, E.M., 2012. Can Restoring Incomplete Microcirculatory Reperfusion Improve Stroke Outcome after Thrombolysis? Journal of Cerebral Blood Flow & Metabolism 32, 2091–2099. https://doi.org/10.1038/jcbfm.2012.139

Daniel Mihai, T., Chircov, C., Grumezescu, A., Teleanu, R., 2019. Neuronanomedicine: An Up-to-Date Overview. Pharmaceutics 11, 101. https://doi.org/10.3390/pharmaceutics11030101 de los Ríos la Rosa, F., Khoury, J., Kissela, B.M., Flaherty, M.L., Alwell, K., Moomaw, C.J., Khatri, P., Adeoye, O., Woo, D., Ferioli, S., Kleindorfer, D.O., 2012. Eligibility for Intravenous Recombinant Tissue-Type Plasminogen Activator Within a Population. Stroke 43, 1591–1595. https://doi.org/10.1161/STROKEAHA.111.645986

Debatisse J., Faruk Eker O., Wateau., Cho T-H., Wiart M., Ramonet D., Costes N., Mérida I., Léon C., Dia M., Paillard M., Confais J., Rossetti F., Langlois J-B., Troalen T., Iecker T., Le Bars D., Lancelot S., Bouchier B., Lukasziewicz A-C., Oudotte A., Nighoghossian N., Ovize M., Contamin H., Lux F., Tillement O., Canet-Soulas E., 2020. PET-MRI nanoparticles imaging of blood-brain barrier damage and modulation after stroke reperfusion. Brain Communications 2. https://doi.org/10.1093/braincomms/fcaa193

del Zoppo, G.J., Mabuchi, T., 2003. Cerebral Microvessel Responses to Focal Ischemia. Journal of Cerebral Blood Flow & Metabolism 23, 879–894. https://doi.org/10.1097/01.WCB.0000078322.96027.78

Demaerschalk, B.M., Kleindorfer, D.O., Adeoye, O.M., Demchuk, A.M., Fugate, J.E., Grotta, J.C., Khalessi, A.A., Levy, E.I., Palesch, Y.Y., Prabhakaran, S., Saposnik, G., Saver, J.L., Smith, E.E., American Heart Association Stroke Council and Council on Epidemiology and Prevention, 2016. Scientific Rationale for the Inclusion and Exclusion Criteria for Intravenous Alteplase in Acute Ischemic Stroke: A Statement for Healthcare Professionals From the American Heart Association/American Stroke Association. Stroke 47, 581–641. https://doi.org/10.1161/STR.0000000000000086

Desilles Jean-Philippe, Loyau Stephane, Syvannarath Varouna, Gonzalez-Valcarcel Jaime, Cantier Marie, Louedec Liliane, Lapergue Bertrand, Amarenco Pierre, Ajzenberg Nadine, Jandrot-Perrus Martine, Michel Jean-Baptiste, Ho-Tin-Noe Benoit, Mazighi Mikael, 2015. Alteplase Reduces Downstream Microvascular Thrombosis and Improves the Benefit of Large Artery Recanalization in Stroke. Stroke 46, 3241–3248. https://doi.org/10.1161/STROKEAHA.115.010721

Disharoon, D., Marr, D.W.M., Neeves, K.B., 2019. Engineered microparticles and nanoparticles for fibrinolysis. J Thromb Haemost 17, 2004–2015. https://doi.org/10.1111/jth.14637

Dreuille, O., Maszelin, P., Foehrenbach, H., Bonardel, G., Gaillard, J.-F., 2004. Principe et technique de la tomographie par émission de positons (TEP). Emc - Radiologie 1, 2–35. https://doi.org/10.1016/j.emcrad.2003.12.001

Dzialowski, I., Weber, J., Doerfler, A., Forsting, M., von Kummer, R., 2004. Brain tissue water uptake after middle cerebral artery occlusion assessed with CT. J Neuroimaging 14, 42–48.

Ehlerding, E.B., Chen, F., Cai, W., 2016. Biodegradable and Renal Clearable Inorganic Nanoparticles. Advanced Science 3, 1500223. https://doi.org/10.1002/advs.201500223

El Amki, M., Dubois, M., Lefevre-Scelles, A., Magne, N., Roussel, M., Clavier, T., Guichet, P.-O., Gérardin, E., Compère, V., Castel, H., 2018. Long-Lasting Cerebral Vasospasm, Microthrombosis, Apoptosis and Paravascular Alterations Associated with Neurological Deficits in a Mouse Model of Subarachnoid Hemorrhage. Mol Neurobiol 55, 2763–2779. https://doi.org/10.1007/s12035-017-0514-6

El Amki, M., Glück, C., Binder, N., Middleham, W., Wyss, M.T., Weiss, T., Meister, H., Luft, A., Weller, M., Weber, B., Wegener, S., 2020. Neutrophils Obstructing Brain Capillaries Are a Major Cause of No-Reflow in Ischemic Stroke. Cell Reports 33, 108260. https://doi.org/10.1016/j.celrep.2020.108260

Evans, M.R.B., White, P., Cowley, P., Werring, D.J., 2017. Revolution in acute ischaemic stroke care: a practical guide to mechanical thrombectomy. Practical Neurology 17, 252–265. https://doi.org/10.1136/practneurol-2017-001685

Falkstedt, D., Wolff, V., Allebeck, P., Hemmingsson, T., Danielsson, A.-K., 2017. Cannabis, Tobacco, Alcohol Use, and the Risk of Early Stroke: A Population-Based Cohort Study of 45 000 Swedish Men. Stroke 48, 265–270. https://doi.org/10.1161/STROKEAHA.116.015565

Feigin, V.L., Brainin, M., Norrving, B., Martins, S., Sacco, R.L., Hacke, W., Fisher, M., Pandian, J., Lindsay, P., 2022. World Stroke Organization (WSO): Global Stroke Fact Sheet 2022. Int J Stroke 17, 18–29. https://doi.org/10.1177/17474930211065917

Flacke, S., Fischer, S., Scott, M.J., Fuhrhop, R.J., Allen, J.S., McLean, M., Winter, P., Sicard, G.A., Gaffney, P.J., Wickline, S.A., Lanza, G.M., 2001. Novel MRI contrast agent for molecular imaging of fibrin: implications for detecting vulnerable plaques. Circulation 104, 1280–1285. https://doi.org/10.1161/hc3601.094303

Flint, A.C., Avins, A.L., Eaton, A., Uong, S., Cullen, S.P., Hsu, D.P., Edwards, N.J., Reddy, P.A., Klingman, J.G., Rao, V.A., Chan, S.L., Hartman, J., Zrelak, P.A., Nguyen-Huynh, M.N., 2020. Risk of Distal Embolization From tPA (Tissue-Type Plasminogen Activator) Administration Prior to Endovascular Stroke Treatment. Stroke 51, 2697–2704. https://doi.org/10.1161/STROKEAHA.120.029025

Fransen, P.S., Beumer, D., Berkhemer, O.A., van den Berg, L.A., Lingsma, H., van der Lugt, A., van Zwam, W.H., van Oostenbrugge, R.J., Roos, Y.B., Majoie, C.B., Dippel, D.W., 2014. MR CLEAN, a multicenter randomized clinical trial of endovascular treatment for acute ischemic stroke in the Netherlands: study protocol for a randomized controlled trial. Trials 15, 343. https://doi.org/10.1186/1745-6215-15-343

Gauberti, M., Fournier, A.P., Vivien, D., Martinez de Lizarrondo, S., 2018. Molecular Magnetic Resonance Imaging (mMRI). Methods Mol. Biol. 1718, 315–327. https://doi.org/10.1007/978-1-4939-7531-0_19

Gauberti, M., Lizarrondo, S.M. de, Orset, C., Vivien, D., 2014. Lack of secondary microthrombosis after thrombin-induced stroke in mice and non-human primates. Journal of Thrombosis and Haemostasis 12, 409–414. https://doi.org/10.1111/jth.12487

Gauberti, M., Martinez de Lizarrondo, S., Vivien, D., 2021. Thrombolytic strategies for ischemic stroke in the thrombectomy era. Journal of Thrombosis and Haemostasis 19, 1618–1628. https://doi.org/10.1111/jth.15336

Gauberti, M., Montagne, A., Marcos-Contreras, O.A., Le Béhot, A., Maubert, E., Vivien, D., 2013. Ultra-Sensitive Molecular MRI of Vascular Cell Adhesion Molecule-1 Reveals a Dynamic

Inflammatory Penumbra After Strokes. Stroke 44, 1988–1996. https://doi.org/10.1161/STROKEAHA.111.000544

Gauberti, M., Obiang, P., Guedin, P., Balossier, A., Gakuba, C., Diependaele, A.S., Chazalviel, L., Vivien, D., Young, A.R., Agin, V., Orset, C., 2012. Thrombotic stroke in the anesthetized monkey (Macaca mulatta): characterization by MRI--a pilot study. Cerebrovasc. Dis. 33, 329–339. https://doi.org/10.1159/000335309

Georgakopoulou, T., van der Wijk, A.-E., Bakker, E.N.T.P., vanBavel, E., Majoie, C., Marquering, H., van Bavel, E., Hoekstra, A., Dippel, D., Lingsma, H., van der Lugt, A., Samuels, N., Boodt, N., Roos, Y., De Meyer, S.F., Staessens, S., Vandelanotte, S., Konduri, P., Terreros, N.A., Chopard, B., Raynaud, F., Petkantchin, R., Panteleev, M., Shibeko, A., Boudjeltia, K.Z., Blanc-Guillemaud, V., Migliavacca, F., Dubini, G., Luraghi, G., Matas, J.F.R., Bridio, S., Mc Garry, P., Gilvarry, M., McCarthy, R., Moerman, K., Fereidoonnezhad, B., Dwivedi, A., Duffy, S., Payne, S., Jozsa, T., Georgakopoulou, S., Padmos, R., Azizi, V., Miller, C., van der Kolk, M., 2021. Quantitative 3D analysis of tissue damage in a rat model of microembolization. Journal of Biomechanics 128, 110723. https://doi.org/10.1016/j.jbiomech.2021.110723

Global, regional, and national burden of stroke and its risk factors, 1990–2019: a systematic analysis for the Global Burden of Disease Study 2019, 2021. . Lancet Neurol 20, 795–820. https://doi.org/10.1016/S1474-4422(21)00252-0

Goertler, M., Blaser, T., Krueger, S., Hofmann, K., Baeumer, M., Wallesch, C., 2002. Cessation of embolic signals after antithrombotic prevention is related to reduced risk of recurrent arterioembolic transient ischaemic attack and stroke. J Neurol Neurosurg Psychiatry 72, 338–342. https://doi.org/10.1136/jnnp.72.3.338

Goldstein, L.B., Adams, R., Becker, K., Furberg, C.D., Gorelick, P.B., Hademenos, G., Hill, M., Howard, G., Howard, V.J., Jacobs, B., Levine, S.R., Mosca, L., Sacco, R.L., Sherman, D.G., Wolf, P.A., del Zoppo, G.J., 2001. Primary Prevention of Ischemic Stroke. Stroke 32, 280–299. https://doi.org/10.1161/01.STR.32.1.280

Golubczyk, D., Kalkowski, L., Kwiatkowska, J., Zawadzki, M., Holak, P., Glodek, J., Milewska, K., Pomianowski, A., Janowski, M., Adamiak, Z., Walczak, P., Malysz-Cymborska, I., 2020. Endovascular model of ischemic stroke in swine guided by real-time MRI. Sci Rep 10. https://doi.org/10.1038/s41598-020-74411-3

González, R.G., 2017. Chapter 132 - MRI and MRA of Ischemic Stroke, in: Caplan, L.R., Biller, J., Leary, M.C., Lo, E.H., Thomas, A.J., Yenari, M., Zhang, J.H. (Eds.), Primer on Cerebrovascular Diseases (Second Edition). Academic Press, San Diego, pp. 695–702. https://doi.org/10.1016/B978-0-12-803058-5.00132-6

Goyal, M., Demchuk, A.M., Menon, B.K., Eesa, M., Rempel, J.L., Thornton, J., Roy, D., Jovin, T.G., Willinsky, R.A., Sapkota, B.L., Dowlatshahi, D., Frei, D.F., Kamal, N.R., Montanera, W.J., Poppe, A.Y., Ryckborst, K.J., Silver, F.L., Shuaib, A., Tampieri, D., Williams, D., Bang, O.Y., Baxter, B.W., Burns, P.A., Choe, H., Heo, J.-H., Holmstedt, C.A., Jankowitz, B., Kelly, M., Linares, G., Mandzia, J.L., Shankar, J., Sohn, S.-I., Swartz, R.H., Barber, P.A., Coutts, S.B., Smith, E.E., Morrish, W.F., Weill, A., Subramaniam, S., Mitha, A.P., Wong, J.H., Lowerison, M.W., Sajobi, T.T., Hill, M.D., ESCAPE Trial Investigators, 2015. Randomized assessment of rapid endovascular treatment of ischemic stroke. N Engl J Med 372, 1019–1030. https://doi.org/10.1056/NEJMoa1414905

Goyal, M., Kappelhof, M., McDonough, R., Ospel, J.M., 2021. Secondary Medium Vessel Occlusions. Stroke 52, 1147–1153. https://doi.org/10.1161/STROKEAHA.120.032799

Goyen, M., 2008. Gadofosveset-enhanced magnetic resonance angiography. Vasc Health Risk Manag 4, 1–9.

Gratz, P.P., Schroth, G., Gralla, J., Mattle, H.P., Fischer, U., Jung, S., Mordasini, P., Hsieh, K., Verma, R.K., Weisstanner, C., El-Koussy, M., 2015. Whole-Brain Susceptibility-Weighted Thrombus Imaging in Stroke: Fragmented Thrombi Predict Worse Outcome. AJNR Am J Neuroradiol 36, 1277–1282. https://doi.org/10.3174/ajnr.A4275

Grond, M., Stenzel, C., Schmülling, S., Rudolf, J., Neveling, M., Lechleuthner, A., Schneweis, S., Heiss, W.-D., 1998. Early Intravenous Thrombolysis for Acute Ischemic Stroke in a Community-Based Approach. Stroke. https://doi.org/10.1161/01.STR.29.8.1544

Gu, X., Zhang, Y., Sun, H., Song, X., Fu, C., Dong, P., 2015. Mussel-Inspired Polydopamine Coated Iron Oxide Nanoparticles for Biomedical Application. Journal of Nanomaterials 2015, 1–12. https://doi.org/10.1155/2015/154592

Guedj, É., 2018. L’imagerie moléculaire en médecine nucléaire, du biomarqueur au théranostique: Molecular imaging in nuclear medicine, from biomarkers to theranostics. Bulletin de l’Académie Nationale de Médecine 202, 1501–1509. https://doi.org/10.1016/S0001-4079(19)30216-X

Gutterman, D.D., Chabowski, D.S., Kadlec, A.O., Durand, M.J., Freed, J.K., Ait-Aissa, K., Beyer, A.M., 2016. The Human Microcirculation. Circulation Research 118, 157–172. https://doi.org/10.1161/CIRCRESAHA.115.305364

Hamm, B., Staks, T., Taupitz, M., Maibauer, R., Speidel, A., Huppertz, A., Frenzel, T., Lawaczeck, R., Wolf, K.J., Lange, L., 1994. Contrast-enhanced MR imaging of liver and spleen: first experience in humans with a new superparamagnetic iron oxide. J Magn Reson Imaging 4, 659–668. https://doi.org/10.1002/jmri.1880040508

Hamoudeh, M., Fessi, H., 2006. Preparation, characterization and surface study of poly-epsilon caprolactone magnetic microparticles. J Colloid Interface Sci 300, 584–590. https://doi.org/10.1016/j.jcis.2006.04.024

Hayman, L.A., Taber, K.H., Ford, J.J., Bryan, R.N., 1991. Mechanisms of MR signal alteration by acute intracerebral blood: old concepts and new theories. AJNR Am J Neuroradiol 12, 899–907.

Heid, S., Unterweger, H., Tietze, R., Friedrich, R.P., Weigel, B., Cicha, I., Eberbeck, D., Boccaccini, A.R., Alexiou, C., Lyer, S., 2017. Synthesis and Characterization of Tissue Plasminogen Activator-Functionalized Superparamagnetic Iron Oxide Nanoparticles for Targeted Fibrin Clot Dissolution. Int J Mol Sci 18, E1837. https://doi.org/10.3390/ijms18091837

Heiss, W.-D., 2011. The Ischemic Penumbra: Correlates in Imaging and Implications for Treatment of Ischemic Stroke. CED 32, 307–320. https://doi.org/10.1159/000330462

Hengerer, A., Grimm, J., 2006. Molecular magnetic resonance imaging. Biomed Imaging Interv J 2, e8. https://doi.org/10.2349/biij.2.2.e8

Higashida, R.T., Furlan, A.J., 2003. Trial Design and Reporting Standards for Intra-Arterial Cerebral Thrombolysis for Acute Ischemic Stroke. Stroke 34, e109–e137. https://doi.org/10.1161/01.STR.0000082721.62796.09

Hilal, S., Sikking, E., Shaik, M.A., Chan, Q.L., Veluw, S.J. van, Vrooman, H., Cheng, C.-Y., Sabanayagam, C., Cheung, C.Y., Wong, T.Y., Venketasubramanian, N., Biessels, G.J., Chen, C., Ikram, M.K., 2016. Cortical cerebral microinfarcts on 3T MRI: A novel marker of cerebrovascular disease. Neurology 87, 1583–1590. https://doi.org/10.1212/WNL.0000000000003110

Hinds, K.A., Hill, J.M., Shapiro, E.M., Laukkanen, M.O., Silva, A.C., Combs, C.A., Varney, T.R., Balaban, R.S., Koretsky, A.P., Dunbar, C.E., 2003. Highly efficient endosomal labeling of progenitor and stem cells with large magnetic particles allows magnetic resonance imaging of single cells. Blood 102, 867–872. https://doi.org/10.1182/blood-2002-12-3669

Hofmeister, J., Kulcsar, Z., Bernava, G., Pellaton, A., Yilmaz, H., Erceg, G., Vargas, M.I., Lövblad, K.-O., Machi, P., 2018. The Catch Mini stent retriever for mechanical thrombectomy in distal intracranial occlusions. Journal of Neuroradiology 45, 305–309. https://doi.org/10.1016/j.neurad.2018.01.051

Hoylaerts, M.F., Yamamoto, H., Nuyts, K., Vreys, I., Deckmyn, H., Vermylen, J., 1997. von Willebrand factor binds to native collagen VI primarily via its A1 domain. Biochem J 324 ( Pt 1), 185–191. https://doi.org/10.1042/bj3240185

Hu, C., Chen, Y., Tan, M.J.A., Ren, K., Wu, H., 2019. Microfluidic technologies for vasculature biomimicry. Analyst 144, 4461–4471. https://doi.org/10.1039/C9AN00421A

Huang, X., Cheripelli, B.K., Lloyd, S.M., Kalladka, D., Moreton, F.C., Siddiqui, A., Ford, I., Muir, K.W., 2015. Alteplase versus tenecteplase for thrombolysis after ischaemic stroke (ATTEST): a phase 2, randomised, open-label, blinded endpoint study. Lancet Neurol 14, 368–376. https://doi.org/10.1016/S1474-4422(15)70017-7

Huber, D., Cramer, E.M., Kaufmann, J.E., Meda, P., Massé, J.-M., Kruithof, E.K.O., Vischer, U.M., 2002. Tissue-type plasminogen activator (t-PA) is stored in Weibel-Palade bodies in human endothelial cells both in vitro and in vivo. Blood 99, 3637–3645. https://doi.org/10.1182/blood.v99.10.3637

Idicula, T.T., Naess, H., Thomassen, L., 2010. Microemboli-monitoring during the acute phase of ischemic stroke: Is it worth the time? BMC Neurol 10, 79. https://doi.org/10.1186/1471-2377-10-79

Ilium, L., Davis, S.S., Wilson, C.G., Thomas, N.W., Frier, M., Hardy, J.G., 1982. Blood clearance and organ deposition of intravenously administered colloidal particles. The effects of particle size, nature and shape. International Journal of Pharmaceutics 12, 135–146. https://doi.org/10.1016/0378-5173(82)90113-2

Johnston, S.C., Rothwell, P.M., Nguyen-Huynh, M.N., Giles, M.F., Elkins, J.S., Bernstein, A.L., Sidney, S., 2007. Validation and refinement of scores to predict very early stroke risk after transient ischaemic attack. Lancet 369, 283–292. https://doi.org/10.1016/S0140-6736(07)60150-0

Ju, K.-Y., Lee, Y., Lee, S., Park, S.B., Lee, J.-K., 2011. Bioinspired Polymerization of Dopamine to Generate Melanin-Like Nanoparticles Having an Excellent Free-Radical-Scavenging Property. Biomacromolecules 12, 625–632. https://doi.org/10.1021/bm101281b

Junghans, U., Siebler, M., 2003. Cerebral microembolism is blocked by tirofiban, a selective nonpeptide platelet glycoprotein IIb/IIIa receptor antagonist. Circulation 107, 2717–2721. https://doi.org/10.1161/01.CIR.0000070544.15890.0E

Kaesmacher, J., Maegerlein, C., Kaesmacher, M., Zimmer, C., Poppert, H., Friedrich, B., Boeckh-Behrens, T., Kleine, J.F., 2017. Thrombus Migration in the Middle Cerebral Artery: Incidence, Imaging Signs, and Impact on Success of Endovascular Thrombectomy. Journal of the American Heart Association 6, e005149. https://doi.org/10.1161/JAHA.116.005149

Kanda, T., Fukusato, T., Matsuda, M., Toyoda, K., Oba, H., Kotoku, J., Haruyama, T., Kitajima, K., Furui, S., 2015. Gadolinium-based Contrast Agent Accumulates in the Brain Even in Subjects without Severe Renal Dysfunction: Evaluation of Autopsy Brain Specimens with Inductively Coupled Plasma Mass Spectroscopy. Radiology 276, 228–232. https://doi.org/10.1148/radiol.2015142690

Kapral, M.K., Fang, J., Hill, M.D., Silver, F., Richards, J., Jaigobin, C., Cheung, A.M., Investigators of the Registry of the Canadian Stroke Network, 2005. Sex differences in stroke care and outcomes: results from the Registry of the Canadian Stroke Network. Stroke 36, 809–814. https://doi.org/10.1161/01.STR.0000157662.09551.e5

Karatas, H., Erdener, S.E., Gursoy-Ozdemir, Y., Gurer, G., Soylemezoglu, F., Dunn, A.K., Dalkara, T., 2011. Thrombotic distal middle cerebral artery occlusion produced by topical FeCl3 application: a novel model suitable for intravital microscopy and thrombolysis studies. J Cereb Blood Flow Metab 31, 1452–1460. https://doi.org/10.1038/jcbfm.2011.8

Kargiotis, O., Psychogios, K., Safouris, A., Magoufis, G., Zervas, P.D., Stamboulis, E., Tsivgoulis, G., 2019. The Role of Transcranial Doppler Monitoring in Patients with Multi-Territory Acute Embolic Strokes: A Review. J Neuroimaging 29, 309–322. https://doi.org/10.1111/jon.12602

Kasner, S.E., 2006. Clinical interpretation and use of stroke scales. The Lancet Neurology 5, 603–612. https://doi.org/10.1016/S1474-4422(06)70495-1

Kaufmann, T.J., Huston, J., Mandrekar, J.N., Schleck, C.D., Thielen, K.R., Kallmes, D.F., 2007. Complications of Diagnostic Cerebral Angiography: Evaluation of 19 826 Consecutive Patients. Radiology 243, 812–819. https://doi.org/10.1148/radiol.2433060536

Khalkhali, M., Sadighian, S., Rostamizadeh, K., Khoeini, F., Naghibi, M., Bayat, N., Habibizadeh, M., Hamidi, M., 2015. Synthesis and characterization of dextran coated magnetite nanoparticles for diagnostics and therapy. Bioimpacts 5, 141–150. https://doi.org/10.15171/bi.2015.19

Kim, J.-Y., Ryu, J.H., Schellingerhout, D., Sun, I.-C., Lee, S.-K., Jeon, S., Kim, J., Kwon, I.C., Nahrendorf, M., Ahn, C.-H., Kim, K., Kim, D.-E., 2015. Direct Imaging of Cerebral Thromboemboli Using Computed Tomography and Fibrin-targeted Gold Nanoparticles. Theranostics 5, 1098–1114. https://doi.org/10.7150/thno.11679

Kloska, S.P., Wintermark, M., Engelhorn, T., Fiebach, J.B., 2010. Acute stroke magnetic resonance imaging: current status and future perspective. Neuroradiology 52, 189–201. https://doi.org/10.1007/s00234-009-0637-1

Kolosnjaj-Tabi, J., Di Corato, R., Lartigue, L., Marangon, I., Guardia, P., Silva, A.K.A., Luciani, N., Clément, O., Flaud, P., Singh, J.V., Decuzzi, P., Pellegrino, T., Wilhelm, C., Gazeau, F., 2014. Heat-generating iron oxide nanocubes: subtle "destructurators" of the tumoral microenvironment. ACS Nano 8, 4268–4283. https://doi.org/10.1021/nn405356r

Kooi, M. e., Cappendijk, V. c., Cleutjens, K. b. j. m., Kessels, A. g. h., Kitslaar, P. j. e. h. m., Borgers, M., Frederik, P. m., Daemen, M. j. a. p., van Engelshoven, J. m. a., 2003. Accumulation of Ultrasmall Superparamagnetic Particles of Iron Oxide in Human Atherosclerotic Plaques Can Be Detected by In Vivo Magnetic Resonance Imaging. Circulation 107, 2453–2458. https://doi.org/10.1161/01.CIR.0000068315.98705.CC

Koutsiaris, A.G., Tachmitzi, S.V., Batis, N., 2013. Wall shear stress quantification in the human conjunctival pre-capillary arterioles in vivo. Microvascular Research 85, 34–39. https://doi.org/10.1016/j.mvr.2012.11.003

Krishnamurthi, R.V., Feigin, V.L., Forouzanfar, M.H., Mensah, G.A., Connor, M., Bennett, D.A., Moran, A.E., Sacco, R.L., Anderson, L.M., Truelsen, T., O'Donnell, M., Venketasubramanian, N., Barker-Collo, S., Lawes, C.M.M., Wang, W., Shinohara, Y., Witt, E., Ezzati, M., Naghavi, M., Murray, C., Global Burden of Diseases, Injuries, Risk Factors Study 2010 (GBD 2010), GBD Stroke Experts Group, 2013. Global and regional burden of first-ever ischaemic and haemorrhagic stroke during 1990-2010: findings from the Global Burden of Disease Study 2010. Lancet Glob Health 1, e259-281. https://doi.org/10.1016/S2214-109X(13)70089-5

Lamassa, M., Di Carlo, A., Pracucci, G., Basile, A.M., Trefoloni, G., Vanni, P., Spolveri, S., Baruffi, M.C., Landini, G., Ghetti, A., Wolfe, C.D.A., Inzitari, D., 2001. Characteristics, Outcome, and Care of Stroke Associated With Atrial Fibrillation in Europe. Stroke 32, 392–398. https://doi.org/10.1161/01.STR.32.2.392

Lartigue, L., Alloyeau, D., Kolosnjaj-Tabi, J., Javed, Y., Guardia, P., Riedinger, A., Péchoux, C., Pellegrino, T., Wilhelm, C., Gazeau, F., 2013. Biodegradation of Iron Oxide Nanocubes: High-Resolution In Situ Monitoring. ACS Nano 7, 3939–3952. https://doi.org/10.1021/nn305719y

Ledezma, C.J., Wintermark, M., 2009. Multi-modal CT in Stroke Imaging: New Concepts. Radiol Clin North Am 47, 109–116. https://doi.org/10.1016/j.rcl.2008.10.008

Lee, E.K., Lee, E.J., Kim, S., Lee, Y.S., 2016. Importance of Contrast-Enhanced Fluid-Attenuated Inversion Recovery Magnetic Resonance Imaging in Various Intracranial Pathologic Conditions. Korean J Radiol 17, 127–141. https://doi.org/10.3348/kjr.2016.17.1.127

Lee, H., Dellatore, S., Miller, W., Messersmith, P., 2007. Mussel-Inspired Surface Chemistry for Multifunctional Coatings. Science (New York, N.Y.) 318, 426–30. https://doi.org/10.1126/science.1147241

Lee, H., Rho, J., Messersmith, P.B., 2009. Facile Conjugation of Biomolecules onto Surfaces via Mussel Adhesive Protein Inspired Coatings. Advanced Materials 21, 431–434. https://doi.org/10.1002/adma.200801222

Lee, H., Scherer, N.F., Messersmith, P.B., 2006. Single-molecule mechanics of mussel adhesion. Proc Natl Acad Sci U S A 103, 12999–13003. https://doi.org/10.1073/pnas.0605552103

Leng, X., Fang, H., Leung, T.W.H., Mao, C., Xu, Y., Miao, Z., Liu, L., Wong, K.S.L., Liebeskind, D.S., 2016. Impact of Collateral Status on Successful Revascularization in Endovascular Treatment: A Systematic Review and Meta-Analysis. Cerebrovasc Dis 41, 27–34. https://doi.org/10.1159/000441803

Li, B., Gong, T., Xu, N., Cui, F., Yuan, B., Yuan, Q., Sun, H., Wang, L., Liu, J., 2020. Improved Stability and Photothermal Performance of Polydopamine-Modified Fe3 O4 Nanocomposites for Highly Efficient Magnetic Resonance Imaging-Guided Photothermal Therapy. Small 16, e2003969. https://doi.org/10.1002/smll.202003969

Li, Q., Yang, Y., Reis, C., Tao, T., Li, W., Li, X., Zhang, J.H., 2018. Cerebral Small Vessel Disease. Cell Transplant 27, 1711–1722. https://doi.org/10.1177/0963689718795148

Lubezky, N., Fajer, S., Barmeir, E., Karmeli, R., 1998. Duplex scanning and CT angiography in the diagnosis of carotid artery occlusion: a prospective study. Eur J Vasc Endovasc Surg 16, 133–136. https://doi.org/10.1016/s1078-5884(98)80154-8

Lundqvist, M., Stigler, J., Elia, G., Lynch, I., Cedervall, T., Dawson, K.A., 2008. Nanoparticle size and surface properties determine the protein corona with possible implications for biological impacts. Proceedings of the National Academy of Sciences 105, 14265–14270. https://doi.org/10.1073/pnas.0805135105

Ma, H., Campbell, B.C.V., Parsons, M.W., Churilov, L., Levi, C.R., Hsu, C., Kleinig, T.J., Wijeratne, T., Curtze, S., Dewey, H.M., Miteff, F., Tsai, C.-H., Lee, J.-T., Phan, T.G., Mahant, N., Sun, M.-C., Krause, M., Sturm, J., Grimley, R., Chen, C.-H., Hu, C.-J., Wong, A.A., Field, D., Sun, Y., Barber, P.A., Sabet, A., Jannes, J., Jeng, J.-S., Clissold, B., Markus, R., Lin, C.-H., Lien, L.-M., Bladin, C.F., Christensen, S., Yassi, N., Sharma, G., Bivard, A., Desmond, P.M., Yan, B., Mitchell, P.J., Thijs, V., Carey, L., Meretoja, A., Davis, S.M., Donnan, G.A., EXTEND Investigators, 2019. Thrombolysis Guided by Perfusion Imaging up to 9 Hours after Onset of Stroke. N Engl J Med 380, 1795–1803. https://doi.org/10.1056/NEJMoa1813046

Maarouf, A., Ferré, J.-C., Zaaraoui, W., Le Troter, A., Bannier, E., Berry, I., Guye, M., Pierot, L., Barillot, C., Pelletier, J., Tourbah, A., Edan, G., Audoin, B., Ranjeva, J.-P., 2016. Ultra-small superparamagnetic iron oxide enhancement is associated with higher loss of brain tissue structure in clinically isolated syndrome. Mult Scler 22, 1032–1039. https://doi.org/10.1177/1352458515607649

Mackman, N., Bergmeier, W., Stouffer, G.A., Weitz, J.I., 2020. Therapeutic strategies for thrombosis: new targets and approaches. Nat Rev Drug Discov 19, 333–352. https://doi.org/10.1038/s41573-020-0061-0

Maeda, H., 2001. The enhanced permeability and retention (EPR) effect in tumor vasculature: the key role of tumor-selective macromolecular drug targeting. Advances in Enzyme Regulation 41, 189–207. https://doi.org/10.1016/S0065-2571(00)00013-3

Marckmann, P., Skov, L., Rossen, K., Dupont, A., Damholt, M.B., Heaf, J.G., Thomsen, H.S., 2006. Nephrogenic systemic fibrosis: suspected causative role of gadodiamide used for contrast-enhanced magnetic resonance imaging. J Am Soc Nephrol 17, 2359–2362. https://doi.org/10.1681/ASN.2006060601

Marder, V.J., Chute, D.J., Starkman, S., Abolian, A.M., Kidwell, C., Liebeskind, D., Ovbiagele, B., Vinuela, F., Duckwiler, G., Jahan, R., Vespa, P.M., Selco, S., Rajajee, V., Kim, D., Sanossian, N., Saver, J.L., 2006. Analysis of thrombi retrieved from cerebral arteries of patients with acute ischemic stroke. Stroke 37, 2086–2093. https://doi.org/10.1161/01.STR.0000230307.03438.94

Martinez de Lizarrondo, S., Gakuba, C., Herbig, B.A., Repessé, Y., Ali, C., Denis, C.V., Lenting, P.J., Touzé, E., Diamond, S.L., Vivien, D., Gauberti, M., 2017. Potent Thrombolytic Effect of N-Acetylcysteine on Arterial Thrombi. Circulation 136, 646–660. https://doi.org/10.1161/CIRCULATIONAHA.117.027290

Martinez de Lizarrondo, S., Jacqmarcq, C., Naveau, M., Navarro-Oviedo, M., Pedron, S., Adam, A., Freis, B., Allouche, S., Goux, D., Razafindrakoto, S., Gazeau, F., Mertz, D., Vivien, D., Bonnard, T., Gauberti, M., 2022. Tracking the immune response by MRI using biodegradable and ultrasensitive microprobes. Sci Adv 8, eabm3596. https://doi.org/10.1126/sciadv.abm3596

May, J.E., Wolberg, A.S., Lim, M.Y., 2021. Disorders of Fibrinogen and Fibrinolysis. Hematology/Oncology Clinics of North America, Inherited Bleeding Disorders 35, 1197–1217. https://doi.org/10.1016/j.hoc.2021.07.011

McFadyen, J.D., Schaff, M., Peter, K., 2018. Current and future antiplatelet therapies: emphasis on preserving haemostasis. Nat Rev Cardiol 15, 181–191. https://doi.org/10.1038/nrcardio.2017.206

Merino, J.G., Warach, S., 2010. Imaging of acute stroke. Nat Rev Neurol 6, 560–571. https://doi.org/10.1038/nrneurol.2010.129

Molina, C.A., Chamorro, A., Rovira, À., de Miquel, A., Serena, J., Roman, L.S., Jovin, T.G., Davalos, A., Cobo, E., 2015. REVASCAT: a randomized trial of revascularization with SOLITAIRE FR device vs. best medical therapy in the treatment of acute stroke due to anterior circulation large vessel occlusion presenting within eight-hours of symptom onset. Int J Stroke 10, 619–626. https://doi.org/10.1111/ijs.12157

Monopoli, M.P., Åberg, C., Salvati, A., Dawson, K.A., 2012. Biomolecular coronas provide the biological identity of nanosized materials. Nature Nanotech 7, 779–786. https://doi.org/10.1038/nnano.2012.207

Monsour, M., Croci, D.M., Agazzi, S., 2022. Microclots in subarachnoid hemorrhage: an underestimated factor in delayed cerebral ischemia? Clinical Neurology and Neurosurgery 219, 107330. https://doi.org/10.1016/j.clineuro.2022.107330

Montagne, A., Gauberti, M., Macrez, R., Jullienne, A., Briens, A., Raynaud, J.-S., Louin, G., Buisson, A., Haelewyn, B., Docagne, F., Defer, G., Vivien, D., Maubert, E., 2012. Ultra-sensitive molecular MRI of cerebrovascular cell activation enables early detection of chronic central nervous system disorders. NeuroImage 63, 760–770. https://doi.org/10.1016/j.neuroimage.2012.07.018

Muehe, A.M., Siedek, F., Theruvath, A.J., Seekins, J., Spunt, S.L., Pribnow, A., Hazard, F.K., Liang, T., Daldrup-Link, H., 2020. Differentiation of benign and malignant lymph nodes in pediatric patients on ferumoxytol-enhanced PET/MRI. Theranostics 10, 3612–3621. https://doi.org/10.7150/thno.40606

Munich, S.A., Vakharia, K., Levy, E.I., 2019. Overview of Mechanical Thrombectomy Techniques. Neurosurgery 85, S60–S67. https://doi.org/10.1093/neuros/nyz071

Muthard, R.W., Diamond, S.L., 2013. Side view thrombosis microfluidic device with controllable wall shear rate and transthrombus pressure gradient. Lab Chip 13, 1883–1891. https://doi.org/10.1039/C3LC41332B

Myers, D.R., Lam, W.A., 2021. Vascularized Microfluidics and Their Untapped Potential for Discovery in Diseases of the Microvasculature. Annu Rev Biomed Eng 23, 407–432. https://doi.org/10.1146/annurev-bioeng-091520-025358

Ng, Y.S., Stein, J., Ning, M., Black-Schaffer, R.M., 2007. Comparison of Clinical Characteristics and Functional Outcomes of Ischemic Stroke in Different Vascular Territories. Stroke 38, 2309–2314. https://doi.org/10.1161/STROKEAHA.106.475483

Nicole, O., Docagne, F., Ali, C., Margaill, I., Carmeliet, P., MacKenzie, E.T., Vivien, D., Buisson, A., 2001. The proteolytic activity of tissue-plasminogen activator enhances NMDA receptor-mediated signaling. Nat Med 7, 59–64. https://doi.org/10.1038/83358

Nikoubashman, O., Dekeyzer, S., Riabikin, A., Keulers, A., Reich, A., Mpotsaris, A., Wiesmann, M., 2019. True First-Pass Effect. Stroke. https://doi.org/10.1161/STROKEAHA.119.025148

Nkansah, M.K., Thakral, D., Shapiro, E.M., 2011. Magnetic poly(lactide-co-glycolide) and cellulose particles for MRI-based cell tracking. Magnetic Resonance in Medicine 65, 1776–1785. https://doi.org/10.1002/mrm.22765

Nogueira, R.G., Jadhav, A.P., Haussen, D.C., Bonafe, A., Budzik, R.F., Bhuva, P., Yavagal, D.R., Ribo, M., Cognard, C., Hanel, R.A., Sila, C.A., Hassan, A.E., Millan, M., Levy, E.I., Mitchell, P., Chen, M., English, J.D., Shah, Q.A., Silver, F.L., Pereira, V.M., Mehta, B.P., Baxter, B.W., Abraham, M.G., Cardona, P., Veznedaroglu, E., Hellinger, F.R., Feng, L., Kirmani, J.F., Lopes, D.K., Jankowitz, B.T., Frankel, M.R., Costalat, V., Vora, N.A., Yoo, A.J., Malik, A.M., Furlan, A.J., Rubiera, M., Aghaebrahim, A., Olivot, J.-M., Tekle, W.G., Shields, R., Graves, T., Lewis, R.J., Smith, W.S., Liebeskind, D.S., Saver, J.L., Jovin, T.G., 2018. Thrombectomy 6 to 24 Hours after Stroke with a Mismatch between Deficit and Infarct. New England Journal of Medicine 378, 11–21. https://doi.org/10.1056/NEJMoa1706442

O’Donnell, M.J., Xavier, D., Liu, L., Zhang, H., Chin, S.L., Rao-Melacini, P., Rangarajan, S., Islam, S., Pais, P., McQueen, M.J., Mondo, C., Damasceno, A., Lopez-Jaramillo, P., Hankey, G.J., Dans, A.L., Yusoff, K., Truelsen, T., Diener, H.-C., Sacco, R.L., Ryglewicz, D., Czlonkowska, A., Weimar, C., Wang, X., Yusuf, S., 2010. Risk factors for ischaemic and intracerebral haemorrhagic stroke in 22 countries (the INTERSTROKE study): a case-control study. The Lancet 376, 112–123. https://doi.org/10.1016/S0140-6736(10)60834-3

Orset, C., Macrez, R., Young, A.R., Panthou, D., Angles-Cano, E., Maubert, E., Agin, V., Vivien, D., 2007. Mouse Model of In Situ Thromboembolic Stroke and Reperfusion. Stroke 38, 2771–2778. https://doi.org/10.1161/STROKEAHA.107.487520

Ospel, J.M., McTaggart, R., Kashani, N., Psychogios, M., Almekhlafi, M., Goyal, M., 2020. Evolution of Stroke Thrombectomy Techniques to Optimize First-Pass Complete

Reperfusion. Semin Intervent Radiol 37, 119–131. https://doi.org/10.1055/s-0040-1709153

Overoye-Chan, K., Koerner, S., Looby, R.J., Kolodziej, A.F., Zech, S.G., Deng, Q., Chasse, J.M., McMurry, T.J., Caravan, P., 2008. EP-2104R: a fibrin-specific gadolinium-Based MRI contrast agent for detection of thrombus. J Am Chem Soc 130, 6025–6039. https://doi.org/10.1021/ja800834y

Palta, S., Saroa, R., Palta, A., 2014. Overview of the coagulation system. Indian J Anaesth 58, 515–523. https://doi.org/10.4103/0019-5049.144643

Pan, Y., Shi, G., 2021. Silver Jubilee of Stroke Thrombolysis With Alteplase: Evolution of the Therapeutic Window. Frontiers in Neurology 12.

Pan, Y., Wan, W., Xiang, M., Guan, Y., 2022. Transcranial Doppler Ultrasonography as a Diagnostic Tool for Cerebrovascular Disorders. Frontiers in Human Neuroscience 16.

Pappano, A.J., Gil Wier, W., 2013. 8 - The Microcirculation and Lymphatics, in: Pappano, A.J., Gil Wier, W. (Eds.), Cardiovascular Physiology (Tenth Edition). Elsevier, Philadelphia, pp. 153–170. https://doi.org/10.1016/B978-0-323-08697-4.00008-3

Peña-Martínez, C., Durán-Laforet, V., García-Culebras, A., Cuartero, M.I., Moro, M.Á., Lizasoain, I., 2022. Neutrophil Extracellular Trap Targeting Protects Against Ischemic Damage After Fibrin-Rich Thrombotic Stroke Despite Non-Reperfusion. Front Immunol 13, 790002. https://doi.org/10.3389/fimmu.2022.790002

Perez-Balderas, F., van Kasteren, S.I., Aljabali, A.A.A., Wals, K., Serres, S., Jefferson, A., Sarmiento Soto, M., Khrapitchev, A.A., Larkin, J.R., Bristow, C., Lee, S.S., Bort, G., De Simone, F., Campbell, S.J., Choudhury, R.P., Anthony, D.C., Sibson, N.R., Davis, B.G., 2017. Covalent assembly of nanoparticles as a peptidase-degradable platform for molecular MRI. Nature Communications 8, 14254. https://doi.org/10.1038/ncomms14254

Pham, M., Kleinschnitz, C., Helluy, X., Bartsch, A.J., Austinat, M., Behr, V.C., Renné, T., Nieswandt, B., Stoll, G., Bendszus, M., 2010. Enhanced cortical reperfusion protects coagulation factor XII-deficient mice from ischemic stroke as revealed by high-field MRI. Neuroimage 49, 2907–2914. https://doi.org/10.1016/j.neuroimage.2009.11.061

Physiologie de l'hémostase [WWW Document], n.d. . MHEMO. URL https://mhemo.fr/les-pathologies/physiologie-de-lhemostase/ (accessed 9.21.22).

Pomerantz, S.R., Harris, G.J., Desai, H.J., Lev, M.H., 2006. Computed tomography angiography and computed tomography perfusion in ischemic stroke: A step-by-step approach to image acquisition and three-dimensional postprocessing. Semin Ultrasound CT MR 27, 243–270. https://doi.org/10.1053/j.sult.2006.03.001

Quenault, A., Martinez de Lizarrondo, S., Etard, O., Gauberti, M., Orset, C., Haelewyn, B., Segal, H.C., Rothwell, P.M., Vivien, D., Touzé, E., Ali, C., 2017. Molecular magnetic resonance imaging discloses endothelial activation after transient ischaemic attack. Brain 140, 146–157. https://doi.org/10.1093/brain/aww260

Rasschaert, M., 2019. Capture cérébrale de chélates de gadolinium : imagerie multimodale et analyse des conséquences neurotoxicologiques (phdthesis). Université Paris Saclay (COmUE).

Reivich, M., Kuhl, D., Wolf, A., Greenberg, J., Phelps, M., Ido, T., Casella, V., Fowler, J., Hoffman, E., Alavi, A., Som, P., Sokoloff, L., 1979. The [18F]fluorodeoxyglucose method for the measurement of local cerebral glucose utilization in man. Circ Res 44, 127–137. https://doi.org/10.1161/01.res.44.1.127

Rinne, J.O., Brooks, D.J., Rossor, M.N., Fox, N.C., Bullock, R., Klunk, W.E., Mathis, C.A., Blennow, K., Barakos, J., Okello, A.A., de LIano, S.R.M., Liu, E., Koller, M., Gregg, K.M., Schenk, D., Black, R., Grundman, M., 2010. 11C-PiB PET assessment of change in fibrillar amyloid-β load in patients with Alzheimer's disease treated with bapineuzumab: a phase 2, double-blind, placebo-controlled, ascending-dose study. The Lancet Neurology 9, 363–372. https://doi.org/10.1016/S1474-4422(10)70043-0

Roger, V.L., Go, A.S., Lloyd-Jones, D.M., Benjamin, E.J., Berry, J.D., Borden, W.B., Bravata, D.M., Dai, S., Ford, E.S., Fox, C.S., Fullerton, H.J., Gillespie, C., Hailpern, S.M., Heit, J.A., Howard, V.J., Kissela, B.M., Kittner, S.J., Lackland, D.T., Lichtman, J.H., Lisabeth, L.D., Makuc, D.M., Marcus, G.M., Marelli, A., Matchar, D.B., Moy, C.S., Mozaffarian, D., Mussolino, M.E., Nichol, G., Paynter, N.P., Soliman, E.Z., Sorlie, P.D., Sotoodehnia, N., Turan, T.N., Virani, S.S., Wong, N.D., Woo, D., Turner, M.B., American Heart Association Statistics Committee and Stroke Statistics Subcommittee, 2012. Executive summary: heart disease and stroke statistics--2012 update: a report from the American Heart Association. Circulation 125, 188–197. https://doi.org/10.1161/CIR.0b013e3182456d46

Rogosnitzky, M., Branch, S., 2016. Gadolinium-based contrast agent toxicity: a review of known and proposed mechanisms. Biometals 29, 365–376. https://doi.org/10.1007/s10534-016-9931-7

Rudroff, T., Kindred, J.H., Kalliokoski, K.K., 2015. [18F]-FDG positron emission tomography—an established clinical tool opening a new window into exercise physiology. Journal of Applied Physiology 118, 1181–1190. https://doi.org/10.1152/japplphysiol.01070.2014

Sakulkhu, U., Mahmoudi, M., Maurizi, L., Salaklang, J., Hofmann, H., 2015. Protein Corona Composition of Superparamagnetic Iron Oxide Nanoparticles with Various Physico-Chemical Properties and Coatings. Sci Rep 4, 5020. https://doi.org/10.1038/srep05020

Sanna, T., Diener, H.-C., Passman, R.S., Di Lazzaro, V., Bernstein, R.A., Morillo, C.A., Rymer, M.M., Thijs, V., Rogers, T., Beckers, F., Lindborg, K., Brachmann, J., 2014. Cryptogenic Stroke and Underlying Atrial Fibrillation. New England Journal of Medicine 370, 2478–2486. https://doi.org/10.1056/NEJMoa1313600

Saver, J.L., 2006. Time Is Brain—Quantified. Stroke 37, 263–266. https://doi.org/10.1161/01.STR.0000196957.55928.ab

Saver, J.L., Goyal, M., Bonafe, A., Diener, H.-C., Levy, E.I., Pereira, V.M., Albers, G.W., Cognard, C., Cohen, D.J., Hacke, W., Jansen, O., Jovin, T.G., Mattle, H.P., Nogueira, R.G., Siddiqui, A.H., Yavagal, D.R., Baxter, B.W., Devlin, T.G., Lopes, D.K., Reddy, V.K., du Mesnil de Rochemont, R., Singer, O.C., Jahan, R., SWIFT PRIME Investigators, 2015. Stent-retriever thrombectomy after intravenous t-PA vs. t-PA alone in stroke. N Engl J Med 372, 2285–2295. https://doi.org/10.1056/NEJMoa1415061

Schöttler, S., Becker, G., Winzen, S., Steinbach, T., Mohr, K., Landfester, K., Mailänder, V., Wurm, F.R., 2016. Protein adsorption is required for stealth effect of poly(ethylene glycol)- and poly(phosphoester)-coated nanocarriers. Nature Nanotech 11, 372–377. https://doi.org/10.1038/nnano.2015.330

Seghier, M.L., Lazeyras, F., Zimine, S., Maier, S.E., Hanquinet, S., Delavelle, J., Volpe, J.J., Huppi, P.S., 2004. Combination of event-related fMRI and diffusion tensor imaging in an infant with perinatal stroke. Neuroimage 21, 463–472. https://doi.org/10.1016/j.neuroimage.2003.09.015

Shah, A., Dobrovolskaia, M.A., 2018. Immunological Effects of Iron Oxide Nanoparticles and Iron-based Complex Drug Formulations: Therapeutic Benefits, Toxicity, Mechanistic Insights, and Translational Considerations. Nanomedicine 14, 977–990. https://doi.org/10.1016/j.nano.2018.01.014

Shapiro, E.M., Skrtic, S., Koretsky, A.P., 2005. Sizing it up: Cellular MRI using micron-sized iron oxide particles. Magnetic Resonance in Medicine 53, 329–338. https://doi.org/10.1002/mrm.20342

Shih, A.Y., Blinder, P., Tsai, P.S., Friedman, B., Stanley, G., Lyden, P.D., Kleinfeld, D., 2013. The smallest stroke: occlusion of one penetrating vessel leads to infarction and a cognitive deficit. Nat Neurosci 16, 55–63. https://doi.org/10.1038/nn.3278

Shimonaga, K., Matsushige, T., Takahashi, H., Hashimoto, Y., Mizoue, T., Ono, C., Kurisu, K., Sakamoto, S., 2020. Early venous filling after reperfusion therapy in acute ischemic stroke. Journal of Stroke and Cerebrovascular Diseases 29, 104926. https://doi.org/10.1016/j.jstrokecerebrovasdis.2020.104926

Shu, G., Chen, M., Song, J., Xu, X., Lu, C., Du, Yuyin, Xu, M., Zhao, Z., Zhu, M., Fan, K., Fan, X., Fang, S., Tang, B., Dai, Y., Du, Yongzhong, Ji, J., 2020. Sialic acid-engineered mesoporous polydopamine nanoparticles loaded with SPIO and Fe3+ as a novel theranostic agent for T1/T2 dual-mode MRI-guided combined chemo-photothermal treatment of hepatic cancer. Bioact Mater 6, 1423–1435. https://doi.org/10.1016/j.bioactmat.2020.10.020

Sivakumar, L., Camicioli, R., Butcher, K., 2014. Factors associated with cognitive decline in transient ischemic attack patients. Can J Neurol Sci 41, 303–313. https://doi.org/10.1017/s0317167100017248

Smith, E.E., Schneider, J.A., Wardlaw, J.M., Greenberg, S.M., 2012. Cerebral Microinfarcts: The Invisible Lesions. Lancet Neurol 11, 272–282. https://doi.org/10.1016/S1474-4422(11)70307-6

Soares, B.P., Chien, J.D., Wintermark, M., 2009. MR and CT Monitoring of Recanalization, Reperfusion, and Penumbra Salvage. Stroke. https://doi.org/10.1161/STROKEAHA.108.526814

Soares, B.P., Tong, E., Hom, J., Cheng, S.-C., Bredno, J., Boussel, L., Smith, W.S., Wintermark, M., 2010. Reperfusion Is a More Accurate Predictor of Follow-Up Infarct Volume Than Recanalization: A Proof of Concept Using CT in Acute Ischemic Stroke Patients. Stroke 41. https://doi.org/10.1161/STROKEAHA.109.568766

Song, Y., Huang, Z., Xu, J., Ren, D., Wang, Y., Zheng, X., Shen, Y., Wang, L., Gao, H., Hou, J., Pang, Z., Qian, J., Ge, J., 2014. Multimodal SPION-CREKA peptide based agents for molecular imaging of microthrombus in a rat myocardial ischemia-reperfusion model. Biomaterials 35, 2961–2970. https://doi.org/10.1016/j.biomaterials.2013.12.038

Sorensen, A.G., Buonanno, F.S., Gonzalez, R.G., Schwamm, L.H., Lev, M.H., Huang-Hellinger, F.R., Reese, T.G., Weisskoff, R.M., Davis, T.L., Suwanwela, N., Can, U., Moreira, J.A., Copen, W.A., Look, R.B., Finklestein, S.P., Rosen, B.R., Koroshetz, W.J., 1996. Hyperacute stroke: evaluation with combined multisection diffusion-weighted and hemodynamically weighted echo-planar MR imaging. Radiology 199, 391–401. https://doi.org/10.1148/radiology.199.2.8668784

Sporns, P.B., Jeibmann, A., Minnerup, J., Broocks, G., Nawabi, J., Schön, G., Fiehler, J., Wildgruber, M., Heindel, W., Kemmling, A., Hanning, U., 2019. Histological Clot Composition Is Associated With Preinterventional Clot Migration in Acute Stroke Patients. Stroke 50, 2065–2071. https://doi.org/10.1161/STROKEAHA.118.023314

Suchy-Dicey, A.M., Wallace, E.R., Mitchell, S.V.E., Aguilar, M., Gottesman, R.F., Rice, K., Kronmal, R., Psaty, B.M., Longstreth, W.T., 2013. Blood pressure variability and the risk of all-cause mortality, incident myocardial infarction, and incident stroke in the cardiovascular health study. Am J Hypertens 26, 1210–1217. https://doi.org/10.1093/ajh/hpt092

Sun, J.-H., Tan, L., Yu, J.-T., 2014. Post-stroke cognitive impairment: epidemiology, mechanisms and management. Ann Transl Med 2, 80. https://doi.org/10.3978/j.issn.2305-5839.2014.08.05

Suzuki, Y., Nagai, N., Umemura, K., 2011. Novel situations of endothelial injury in stroke--mechanisms of stroke and strategy of drug development: intracranial bleeding associated with the treatment of ischemic stroke: thrombolytic treatment of ischemia-affected endothelial cells with tissue-type plasminogen activator. J Pharmacol Sci 116, 25–29. https://doi.org/10.1254/jphs.10r27fm

Tang, Y.H., Vital, S., Russell, J., Seifert, H., Senchenkova, E., Granger, D.N., 2014. Transient ischemia elicits a sustained enhancement of thrombus development in the cerebral microvasculature: Effects of anti-thrombotic therapy. Exp Neurol 0, 417–423. https://doi.org/10.1016/j.expneurol.2014.07.004

Tenzer, S., Docter, D., Rosfa, S., Wlodarski, A., Kuharev, J., Rekik, A., Knauer, S.K., Bantz, C., Nawroth, T., Bier, C., Sirirattanapan, J., Mann, W., Treuel, L., Zellner, R., Maskos, M., Schild, H., Stauber, R.H., 2011. Nanoparticle Size Is a Critical Physicochemical Determinant of the Human Blood Plasma Corona: A Comprehensive Quantitative Proteomic Analysis. ACS Nano 5, 7155–7167. https://doi.org/10.1021/nn201950e

Thomalla, G., Cheng, B., Ebinger, M., Hao, Q., Tourdias, T., Wu, O., Kim, J.S., Breuer, L., Singer, O.C., Warach, S., Christensen, S., Treszl, A., Forkert, N.D., Galinovic, I., Rosenkranz, M., Engelhorn, T., Köhrmann, M., Endres, M., Kang, D.-W., Dousset, V., Sorensen, A.G., Liebeskind, D.S., Fiebach, J.B., Fiehler, J., Gerloff, C., STIR and VISTA Imaging Investigators, 2011. DWI-FLAIR mismatch for the identification of patients with acute ischaemic stroke within 4·5 h of symptom onset (PRE-FLAIR): a multicentre observational study. Lancet Neurol 10, 978–986. https://doi.org/10.1016/S1474-4422(11)70192-2

Tisserand, M., Naggara, O., Legrand, L., Mellerio, C., Edjlali, M., Lion, S., Rodriguez-Régent, C., Souillard-Scemama, R., Jbanca, C.-F., Trystram, D., Méder, J.-F., Oppenheim, C., 2014. Patient "candidate" for thrombolysis: MRI is essential. Diagnostic and Interventional

Imaging, FMC: Cerebrovascular diseases 95, 1135–1144. https://doi.org/10.1016/j.diii.2014.07.003

Tissue Plasminogen Activator for Acute Ischemic Stroke, 1995. . New England Journal of Medicine 333, 1581–1588. https://doi.org/10.1056/NEJM199512143332401

Tsivgoulis, G., Ribo, M., Rubiera, M., Vasdekis, S.N., Barlinn, K., Athanasiadis, D., Bavarsad Shahripour, R., Giannopoulos, S., Stamboulis, E., Harrigan, M.R., Molina, C.A., Alexandrov, A.V., 2013. Real-time validation of transcranial Doppler criteria in assessing recanalization during intra-arterial procedures for acute ischemic stroke: an international, multicenter study. Stroke 44, 394–400. https://doi.org/10.1161/STROKEAHA.112.675074

Uppal, R., Ay, I., Dai, G., Kim, Y.R., Sorensen, A.G., Caravan, P., 2010. Molecular MRI of intracranial thrombus in a rat ischemic stroke model. Stroke 41, 1271–1277. https://doi.org/10.1161/STROKEAHA.109.575662

van Veluw, S.J., Shih, A.Y., Smith, E.E., Chen, C., Schneider, J.A., Wardlaw, J.M., Greenberg, S.M., Biessels, G.J., 2017. Detection, risk factors, and functional consequences of cerebral microinfarcts. Lancet Neurol 16, 730–740. https://doi.org/10.1016/S1474-4422(17)30196-5

Varga-Szabo, D., Pleines, I., Nieswandt, B., 2008. Cell adhesion mechanisms in platelets. Arterioscler. Thromb. Vasc. Biol. 28, 403–412. https://doi.org/10.1161/ATVBAHA.107.150474

Viltuznik, R., Vidmar, J., Fabjan, A., Jeromel, M., Milosevic, Z.V., Kocijancic, I.J., Sersa, I., 2021. Study of correlations between CT properties of retrieved cerebral thrombi with treatment outcome of stroke patients. Radiol Oncol 55, 409–417. https://doi.org/10.2478/raon-2021-0037

von zur Muhlen, C., von Elverfeldt, D., Choudhury, R.P., Ender, J., Ahrens, I., Schwarz, M., Hennig, J., Bode, C., Peter, K., 2008. Functionalized Magnetic Resonance Contrast Agent Selectively Binds to Glycoprotein IIb/IIIa on Activated Human Platelets under Flow Conditions and Is Detectable at Clinically Relevant Field Strengths. Mol Imaging 7, 59–67.

Wang, Y.X., Hussain, S.M., Krestin, G.P., 2001. Superparamagnetic iron oxide contrast agents: physicochemical characteristics and applications in MR imaging. Eur Radiol 11, 2319–2331. https://doi.org/10.1007/s003300100908

Wardlaw, J.M., 2005. What causes lacunar stroke? Journal of Neurology, Neurosurgery & Psychiatry 76, 617–619. https://doi.org/10.1136/jnnp.2004.039982

Wintermark, M., Flanders, A.E., Velthuis, B., Meuli, R., van Leeuwen, M., Goldsher, D., Pineda, C., Serena, J., van der Schaaf, I., Waaijer, A., Anderson, J., Nesbit, G., Gabriely, I., Medina, V., Quiles, A., Pohlman, S., Quist, M., Schnyder, P., Bogousslavsky, J., Dillon, W.P., Pedraza, S., 2006. Perfusion-CT assessment of infarct core and penumbra: receiver operating characteristic curve analysis in 130 patients suspected of acute hemispheric stroke. Stroke 37, 979–985. https://doi.org/10.1161/01.STR.0000209238.61459.39

Wolfram, J., Yang, Y., Shen, J., Moten, A., Chen, C., Shen, H., Ferrari, M., Zhao, Y., 2014. The nano-plasma interface: Implications of the protein corona. Colloids and Surfaces B:

Biointerfaces, Biointerfaces: Global Perspectives 124, 17–24. https://doi.org/10.1016/j.colsurfb.2014.02.035

Wun, T.C., Capuano, A., 1987. Initiation and regulation of fibrinolysis in human plasma at the plasminogen activator level. Blood 69, 1354–1362.

Yang, P., Zhang, Yongwei, Zhang, L., Zhang, Yongxin, Treurniet, K.M., Chen, W., Peng, Y., Han, H., Wang, J., Wang, S., Yin, C., Liu, S., Wang, P., Fang, Q., Shi, Hongchao, Yang, J., Wen, C., Li, C., Jiang, C., Sun, J., Yue, X., Lou, M., Zhang, M., Shu, H., Sun, D., Liang, H., Li, Tong, Guo, F., Ke, K., Yuan, H., Wang, G., Yang, W., Shi, Huaizhang, Li, Tianxiao, Li, Z., Xing, P., Zhang, P., Zhou, Y., Wang, H., Xu, Y., Huang, Q., Wu, T., Zhao, R., Li, Q., Fang, Y., Wang, Laixing, Lu, J., Li, Y., Fu, J., Zhong, X., Wang, Y., Wang, Longde, Goyal, M., Dippel, D.W.J., Hong, B., Deng, B., Roos, Y.B.W.E.M., Majoie, C.B.L.M., Liu, J., 2020. Endovascular Thrombectomy with or without Intravenous Alteplase in Acute Stroke. N Engl J Med 382, 1981–1993. https://doi.org/10.1056/NEJMoa2001123

Yang, Yidong, Yang, Yuhui, Yanasak, N., Schumacher, A., Hu, T.C.-C., 2010. Temporal and noninvasive monitoring of inflammatory-cell infiltration to myocardial infarction sites using micrometer-sized iron oxide particles. Magn Reson Med 63, 33–40. https://doi.org/10.1002/mrm.22175

Ye, Y., Perez-Polo, J.R., Birnbaum, Y., 2010. Protecting against ischemia-reperfusion injury: antiplatelet drugs, statins, and their potential interactions. Annals of the New York Academy of Sciences 1207, 76–82. https://doi.org/10.1111/j.1749-6632.2010.05725.x

Yu, Z., Lin, L., Wang, X., 2017. Chapter 24 - Pathophysiology of Ischemia-Reperfusion Injury and Hemorrhagic Transformation in the Brain, in: Caplan, L.R., Biller, J., Leary, M.C., Lo, E.H., Thomas, A.J., Yenari, M., Zhang, J.H. (Eds.), Primer on Cerebrovascular Diseases (Second Edition). Academic Press, San Diego, pp. 121–124. https://doi.org/10.1016/B978-0-12-803058-5.00024-2

Yuki, I., Kan, I., Vinters, H.V., Kim, R.H., Golshan, A., Vinuela, F.A., Sayre, J.W., Murayama, Y., Vinuela, F., 2012. The impact of thromboemboli histology on the performance of a mechanical thrombectomy device. AJNR Am J Neuroradiol 33, 643–648. https://doi.org/10.3174/ajnr.A2842

Zaidat, O.O., Bozorgchami, H., Ribó, M., Saver, J.L., Mattle, H.P., Chapot, R., Narata, A.P., Francois, O., Jadhav, A.P., Grossberg, J.A., Riedel, C.H., Tomasello, A., Clark, W.M., Nordmeyer, H., Lin, E., Nogueira, R.G., Yoo, A.J., Jovin, T.G., Siddiqui, A.H., Bernard, T., Claffey, M., Andersson, T., 2018. Primary Results of the Multicenter ARISE II Study (Analysis of Revascularization in Ischemic Stroke With EmboTrap). Stroke 49, 1107–1115. https://doi.org/10.1161/STROKEAHA.117.020125

Zenych, A., Jacqmarcq, C., Aid, R., Fournier, L., Forero Ramirez, L.M., Chaubet, F., Bonnard, T., Vivien, D., Letourneur, D., Chauvierre, C., 2021. Fucoidan-functionalized polysaccharide submicroparticles loaded with alteplase for efficient targeted thrombolytic therapy. Biomaterials 277, 121102. https://doi.org/10.1016/j.biomaterials.2021.121102

Zhang, Z., Guan, J., Jiang, Z., Yang, Y., Liu, J., Hua, W., Mao, Y., Li, C., Lu, W., Qian, J., Zhan, C., 2019. Brain-targeted drug delivery by manipulating protein corona functions. Nat Commun 10, 3561. https://doi.org/10.1038/s41467-019-11593-z

Zhong, X., Yang, K., Dong, Z., Yi, X., Wang, Y., Ge, C., Zhao, Y., Liu, Z., 2015. Polydopamine as a Biocompatible Multifunctional Nanocarrier for Combined Radioisotope Therapy and Chemotherapy of Cancer. Advanced Functional Materials 25, 7327–7336. https://doi.org/10.1002/adfm.201503587

Zhou, J., Guo, D., Zhang, Y., Wu, W., Ran, H., Wang, Z., 2014. Construction and evaluation of $Fe_3O_4$-based PLGA nanoparticles carrying rtPA used in the detection of thrombosis and in targeted thrombolysis. ACS Appl Mater Interfaces 6, 5566–5576. https://doi.org/10.1021/am406008k

Zmerli, I., Michel, J.-P., Makky, A., 2020. Bioinspired polydopamine nanoparticles: synthesis, nanomechanical properties, and efficient PEGylation strategy. J. Mater. Chem. B 8, 4489–4504. https://doi.org/10.1039/C9TB02769F

Zong, W., Hu, Y., Su, Y., Luo, N., Zhang, X., Li, Q., Han, X., 2016. Polydopamine-coated liposomes as pH-sensitive anticancer drug carriers. J Microencapsul 33, 257–262. https://doi.org/10.3109/02652048.2016.1156176

Titre : **Mise au point d'un outil de diagnostic pour révéler les microthrombi**

# Résumé

Les traitements actuels de l'AVC ischémique ont pour but la restauration de la perfusion cérébrale en éliminant le thrombus qui occlut l'artère par injection d'un agent thrombolytiques (thrombolyse) ou mécaniquement, en retirant le caillot par voie endovasculaire (thrombectomie). Les études cliniques ont montré la présence de thrombi au niveau de la microcirculation chez les patients, même après une recanalisation réussie de l'artère occlue. Ce phénomène est par ailleurs associé à l'apparition de déclins cognitifs et de démences. Cependant les outils de diagnostics habituellement utilisés dans l'imagerie à la phase aigüe de l'AVC ne permettent pas d'établir précisément la présence et l'étendue de cette microthrombose. Nous proposons, dans ce travail de thèse, l'utilisation de l'IRM moléculaire pour le diagnostic de la microthrombose. Nous avons développé un agent de contraste basé sur des nanoparticules superparamagnétiques d'oxydes de fer conglomérées dans une matrice de polydopamine biodégradable. Nos résultats suggèrent un ciblage spécifique de l'agent de contraste au microthrombi *in vitro,* sur des microthrombi formés à partir de sang humain de volontaires sains, et *in vivo* sur un modèle d'AVC thromboembolique murin. Nous avons montré son efficacité pour l'IRM moléculaire de la microthrombose en préclinique, et mis en évidence l'apport diagnostic que représente le suivi des microthrombi dans le cadre de la thrombolyse. Nous avons enfin observé la biodégradabilité de ce nouvel agent de contraste, ce qui nous permet d'envisager la translation de cette approche en clinique, pour améliorer la prise en charge des patients victimes d'AVC ischémique.

Mots-Clés : Microparticules d'Oxydes de Fer ; IRM ; modèle murin d'AVC ; Microthrombi

# Summary

Current treatments of ischemic stroke consist in restoring cerebral perfusion by removing the thrombus occluding the artery with a thrombolytic agent injection (thrombolysis) or mechanically with an endovascular approach (thrombectomy). Clinical studies have demonstrated the presence of thrombi localized in the microcirculation, even after a successful recanalization. Those microthrombi are associated with further dementia and cognitive decline. Unfortunately, current imaging tool for the diagnosis of acute stroke cannot provide information on this microthrombosis. In this work, we propose to use molecular MRI for the diagnosis of microthrombosis and, to this end, we developed a superparamagnetic iron oxide-based contrast agent clusterized in a polydopamine matrix. Our results shows specific targeting of the contrast agent *in vitro* to microthrombi formed with human blood, and *in vivo* in a thromboembolic mouse model. We demonstrated the efficacy of the contrast agent to provide molecular MRI of microthrombosis, and highlighted its ability to follow-up microthrombi degradation during thrombolysis. Finally, we observed the biodegradation of the contrast agent, allowing us to consider a future clinical translation to improve stroke patient care.

Keywords : Microparticles of Iron Oxide ; MRI ; Mouse Model of Stroke ; Microthrombi